UNIVERSITÉ DU QUEBEC À CHICOUTIMI

THÈSE PRÉSENTÉE À
L'UNIVERSITÉ DU QUÉBEC À CHICOUTIMI
COMME EXIGENCE PARTIELLE
DU DOCTORAT EN INGÉNIERIE

par
YAŞAR S. KOCAEFE

MODÉLISATION ET OPTIMISATION DES FOURS À PUITS LATÉRAL

(MODELLING AND OPTIMISATION OF SIDEWELL FURNACES)

Mai 2003

Bibliothèque
Paul-Émile-Boulet

UQAC
Université du Québec
à Chicoutimi

Mise en garde/Advice

Afin de rendre accessible au plus grand nombre le résultat des travaux de recherche menés par ses étudiants gradués et dans l'esprit des règles qui régissent le dépôt et la diffusion des mémoires et thèses produits dans cette Institution, **l'Université du Québec à Chicoutimi (UQAC)** est fière de rendre accessible une version complète et gratuite de cette œuvre.

Motivated by a desire to make the results of its graduate students' research accessible to all, and in accordance with the rules governing the acceptation and diffusion of dissertations and theses in this Institution, the **Université du Québec à Chicoutimi (UQAC)** is proud to make a complete version of this work available at no cost to the reader.

L'auteur conserve néanmoins la propriété du droit d'auteur qui protège ce mémoire ou cette thèse. Ni le mémoire ou la thèse ni des extraits substantiels de ceux-ci ne peuvent être imprimés ou autrement reproduits sans son autorisation.

The author retains ownership of the copyright of this dissertation or thesis. Neither the dissertation or thesis, nor substantial extracts from it, may be printed or otherwise reproduced without the author's permission.

À ma famille

Duygu, Burcu Suzan et Aylin Kocaefe

et

à mes parents

Leman et Ahmet Kocaefe

ACKNOWLEDGEMENTS

Prof. R.T. Bui is an inspiring supervisor, and I benefited enormously from working with a person of exceptional qualities. I would like to express my deepest gratitude for everything.

I am also grateful to my co-supervisors Prof. A. Charette (UQAC) and Prof. H.A. Becker (Queen's University) for their guidance. I would like to thank Prof. L. Kiss (UQAC) for his suggestions for measurements in water model and Prof. L. Tikasz (UQAC) and Dr. J. Perron (ALCAN) for their contributions to the development of the dynamic model.

The sidewell furnace simulator was a result of the group work from LECAP. I would like to thank V. Villeneuve, B.S. Kocaefe, C. Charette, C. Fillion, S. Doyon, J. Sasseville, D. Desrosiers and M. Mirchi from LECAP for their contributions.

The project would not have been successful without the collaboration of G. Riverin, T. Bourgeois, W. Stevens and G. Dubé from ARDC (ALCAN) as well as the personnel in plants where the industrial tests were carried out.

I would like to express my appreciation for some of the testing and simulations done by T. Rivard and J.M. Dubé from UQAC.

I am grateful to the many workers from the research groups GRIPS and CHIP (UQAC) for the warm and friendly atmosphere they created.

Above all, I thank my wife Duygu and my daughters Burcu Suzan and Aylin for their patience and understanding. As always, Duygu has been very supportive and helpful during the entire project.

The funding provided for the project by the National Science and Engineering Research Council of Canada (NSERC), le Centre Québecois de recherche et de développement sur l'aluminium (CQRDA), Alcan International Ltd. (ALCAN), and la Fondation de l'Université du Québec à Chicoutimi (FUQAC) is greatly appreciated.

RÉSUMÉ

Le recyclage de l'aluminium a de multiples effets positifs sur l'économie et l'environnement. Il aide à conserver les ressources, réduire les dépenses d'énergie de 95% et le coût de l'aluminium. Aujourd'hui, le recyclage est une composante majeure de l'industrie de l'aluminium. Les canettes de boisson constituent la catégorie de recyclables la plus importante en quantité et en qualité. En général, on effectue la refonte des canettes dans les fours à puits latéral.

L'industrie du recyclage croît très rapidement, et pour demeurer compétitive, elle doit optimiser son efficacité en diminuant les coûts d'énergie et maximisant la productivité. Dans cette optique, un projet a été entrepris pour le développement des modèles du four à puits latéral. À l'aide de ces modèles, on peut améliorer et optimiser le design et l'opération de ces fours. L'objectif du projet est de développer des outils pour les travaux d'amélioration et d'optimisation requis des fours à puits latéral :

- Un modèle mathématique général en 3D pour des études détaillées comme la meilleure géométrie du four, et la meilleure position de la pompe et de l'hélice pour optimiser la fusion et la circulation du métal,
- Un modèle mathématique dynamique simplifié pour des études de contrôle et d'opération.

Le four est composé de deux parties : un puits latéral dans lequel les copeaux de canettes déchiquetées sont alimentés et une chambre principale dans laquelle la chaleur est introduite. Des arches d'entrée et de sortie assurent la circulation du métal entre ces deux parties à travers le mur de séparation. Dans le puits latéral, on installe une hélice pour submerger les copeaux, à laquelle on adjoint un muret pour favoriser la circulation du métal chaud. Certaines usines ajoutent une pompe à injection de métal dans la chambre principale pour obtenir un meilleur brassage dans le bain de métal liquide.

La performance d'un four de refonte peut être caractérisée par le rendement énergétique et le taux de refonte. Ces paramètres dépendent du transfert effectif de la chaleur entre la chambre de combustion où elle est générée et les points d'utilisation. La chaleur est requise pour maintenir le métal liquide à une certaine température et pour fondre les copeaux introduits dans le puits latéral et le métal solide admis dans la chambre principale.

Le projet consiste en quatre parties. La première partie est le développement d'un modèle en 3D pour le calcul de l'écoulement isotherme dans le bain de métal. On solutionne les équations différentielles de la continuité, de la quantité de mouvement en trois directions, et de la turbulence en utilisant le logiciel CFX. Un grand nombre de simulations ont été effectuées pour étudier l'effet des paramètres sur l'écoulement. À partir des résultats, on a optimisé les positions de l'hélice et de la pompe, la longueur et le type du muret, les grandeurs des arches, la largeur du puits, et la géométrie de la chambre principale pour obtenir la meilleure circulation du métal liquide dans le bain.

La deuxième partie est la modélisation de la chambre de combustion. Un modèle à une zone de gaz est développé pour calculer le transfert de chaleur au métal (aussi aux réfractaires) par rayonnement et par convection. Ce modèle ne donne pas tous les détails concernant les distributions de la température et de la densité de flux de chaleur, mais il est

simple et il tient compte de tous les phénomènes importants. De plus, le temps de calcul est très court. Une étude paramétrique a été déjà effectuée pour déterminer les effets des différents facteurs sur le transfert de chaleur au métal. Les résultats montrent qu'on peut améliorer le transfert de chaleur au métal en augmentant le débit du carburant et la température de l'air de combustion. Le débit du carburant a un impact significatif, mais le rendement du four diminue avec une augmentation du débit. La température de l'air de combustion est le paramètre le plus important et le plus facile à ajuster. Le préchauffage de l'air augmente le transfert de chaleur ainsi que le rendement du four. Aussi, il est important de mélanger le bain de métal pour maintenir la température de la surface la plus basse possible pour que le transfert de chaleur au métal soit favorisé.

La troisième partie est la modélisation globale du four en 3D. Étant donné le caractère transitoire du procédé, le transfert de chaleur dans le métal liquide est aussi incorporé dans le modèle du bain de métal, et il est couplé avec le modèle de la chambre de combustion. Pour optimiser le temps de calcul, le champ de vitesse est déterminé en régime établi, et ce champ de vitesse est utilisé pour solutionner l'enthalpie en régime transitoire. Les résultats montrent que l'écoulement forcé est le facteur le plus important. Le gradient de température diminue avec la circulation du métal à travers les arches et le brassage dans la chambre principale. On voit que le gradient moyen de la température dans la chambre principale diminue de 50% (d'environ 80°C à 40°C) en ajoutant un muret et de 80-90% (d'environ 80°C à 10°C) avec un muret et une pompe.

La quatrième partie est le développement du modèle dynamique du four pour améliorer le contrôle du procédé. Le four à puits latéral est un système très dynamique et tout varie en fonction du temps. Pour étudier l'aspect d'opération, il faut un modèle dynamique. La modélisation est faite de façon modulaire en deux parties représentant le métal et la chambre de combustion. Les deux parties sont construites séparément puis sont couplées ensemble afin d'obtenir un outil intégré. L'interface pour le couplage est la surface du bain de métal. C'est un modèle simplifié, mais il tient compte de tous les phénomènes et tous les événements du procédé. Ce modèle sert comme un four virtuel. Un émulateur de contrôle est ajouté et un simulateur pour fours à puits latéral est ainsi obtenu. Le simulateur qui est utilisé à partir d'une interface-usager est transféré à l'industrie pour des applications. Plusieurs études ont été déjà effectuées en utilisant ce simulateur. On a étudié les effets des positions des thermocouples d'opération (contrôle), de la température maximale des réfractaires permise, des préchauffages des métaux alimentés et de l'air de combustion sur la performance du four. Les améliorations ont été apportées au procédé à partir des résultats obtenus.

Tous les modèles sont validés en utilisant les données expérimentales disponibles du laboratoire et des usines. Tous les résultats du modèle mathématique sont confirmés par les observations en usine.

(Summary in English is given in Appendix 1)

PREFACE

Practically all sidewell furnaces in operation are located either in the United States or in England. Throughout the project, almost all the documentation and reports were written in English in order to make the models and the results available not only to researchers in the CRDA (Alcan), Québec, but also to all parties of interest worldwide. For the same reasons, the thesis is also written in English.

The programming work, in general, was done in SI units. Some of the results are also presented in SI units, which is the system of choice in plants such as Latchford in England. However, the plants in the United States use a system of mixed units: for example, the temperature is in °C, but the shred feed rate is in lbs/h. For this reason, the input and output files were prepared to accommodate the mixed units used in those plants. This is, of course, of utmost importance for the use and application of the project results and products by the industry. Consequently, some results are presented in mixed units as well.

A large number of computer programmes in Fortran was written for different models of the project. All together they add up to about 15,000 lines. In order to avoid having excessive number of pages, these are not presented in the thesis.

TABLE OF CONTENTS

LISTE OF FIGURES

LISTE OF TABLES

CHAPTER 1

INTRODUCTION

1.1 Statement of the Problem

Energy conservation and environmental protection incentives promoted recycling in many areas in the last few decades. In aluminum industry, recycling always had a strong presence and, recently, has become an important component of the overall production[1-6]. There are many advantages in recycling: conservation of natural resources, reduction in waste and pollution, lower energy costs, and, consequently, lower production costs.

Beverage cans constitute the most important category of recycled material in quantity and quality in aluminum industry. Estimated amount of recycled aluminum cans is about one million tons per year. Recently, they became the most important source of revenue among the recycled solids[3,5]. The cans are shredded and fed to a unit where the oil and paint are removed by burning off. Then the shreds are melted and treated in various furnaces for alloy preparation and casting. The recycled alloy composition is not far from what is needed in the final product. Such a high alloy quality makes the metal treatment easier and cost-effective. The energy consumption for the production of cans from recycled material is about 5% of the energy consumption if the cans are produced starting from the ore (bauxite).

Many different types of furnaces are used for melting and treating the metal. The sidewell furnaces are commonly used for shred melting[7-10]. These furnaces consist of two sections: a main hearth and a side well from which the name "sidewell" is derived (see Figure 1.1). The liquid metal circulates between the main hearth and the side well through two arches located in the wall, called hotwall, separating these two sections. The shred is fed to the side well continuously without interrupting the operation of the furnace. However, these furnaces have lower energy efficiencies compared to conventional ones. The operation and characteristics of the sidewell furnaces will be discussed in Section 1.3 in more detail.

It is important for the recycling industry to lower the cost and to increase the productivity. Sidewell furnaces are an important part of the recycling plants, and their operation has to be improved. A project was undertaken to develop modelling tools for this purpose (see Figure 1.2).

1.2 Objectives of the Current Research Project

The general objective was to develop tools which could be used to study the phenomena occurring in the sidewell furnaces and, consequently, to improve their performance (see Figure 1.2). In order to meet this objective, the following models were to be developed:

- A three-dimensional general mathematical model to study the effects of various design and operational factors such as the geometry, the impeller and pump positions which would give optimum melt rate and metal circulation.

- A dynamic model including a control emulator to simulate the actual operation of sidewell furnaces to improve their operation and control.

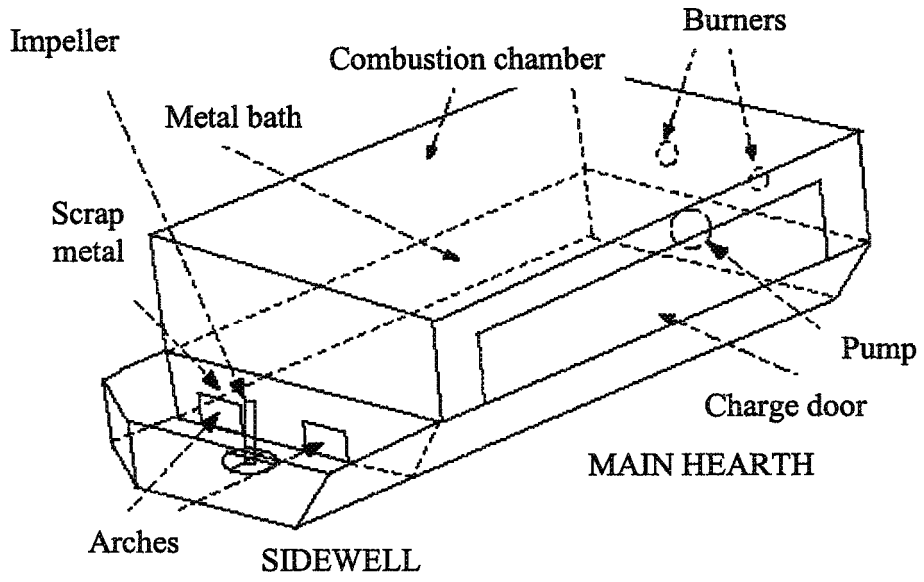

Figure 1-1 : A Schematic Diagram of the Sidewell Furnace

1.3 Sidewell Furnaces

Cans are chopped into small pieces called shreds. Then they are treated in a furnace where the paint and the oil are removed at about 500°C before they are sent to the sidewell furnaces. The advantage of sidewell furnaces is to be able to melt shreds continuously by feeding them into the side well as opposed to conventional furnaces where the furnace operation has to be stopped in order to feed the charge into the hearth. There is also an impeller in the side well where the shreds are fed which provides a quick submergence

minimizing the oxidation of aluminum alloy. Typical dimensions of a sidewell furnace are given in Table 1.1.

The cans are made from three different alloys. The sides contain about 1% magnesium, and the top is made of two alloys containing 3% and 5% magnesium. Large quantities of the alloy for the sides are needed, and furnaces treating the alloy containing 1% magnesium were studied in this project. When the shreds melt, the liquid metal contains over 1% magnesium. Blocks of pure aluminum, called sows, are charged into the main hearth to reduce the concentration of magnesium to 1%. For this operation, the burners are turned off to be able to open the charge doors.

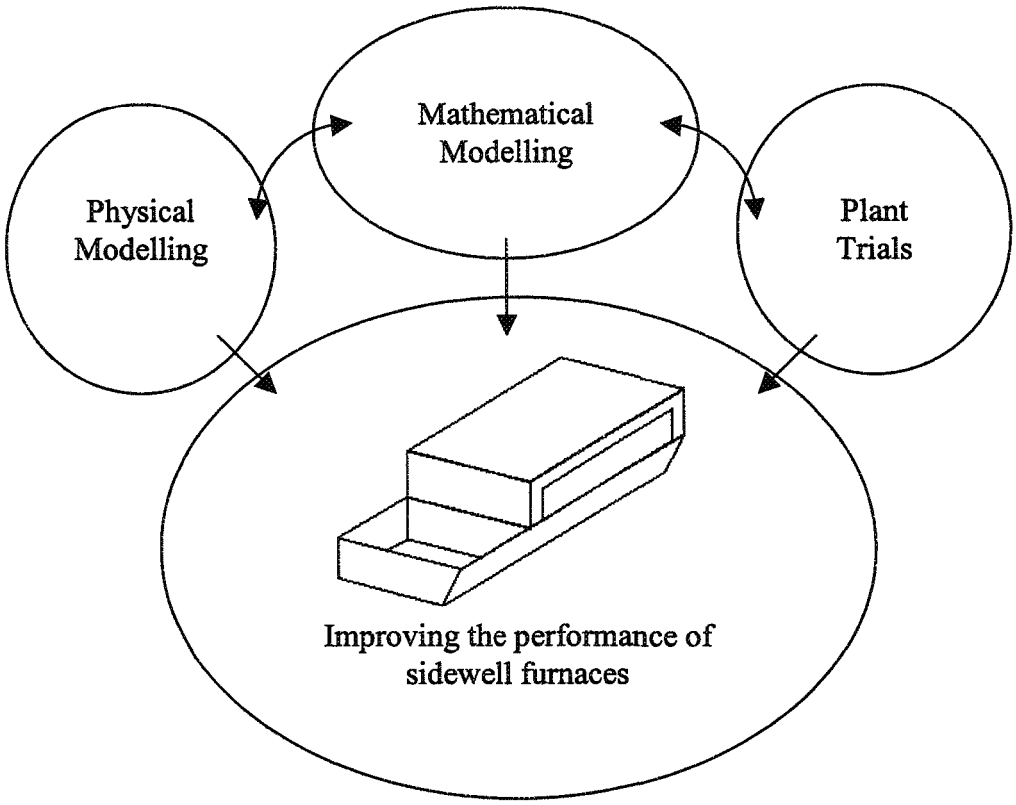

Figure 1-2 : Objectives and Overall View of the Project

The main function of the impeller is the submergence of shreds; however, it also provides some circulation between the main hearth and the side well through the arches[11]. It is important to position the impeller properly to maximize this circulation. In some furnaces, there is also a pump in the main hearth directed towards the inlet arch where the metal enters the side well from the main hearth[11]. The pump increases mixing of the liquid metal in the main hearth as well as the circulation to the side well. These are discussed in more detail in Chapter 2.

A typical furnace with the dimensions given in Table 1 contains about 110 tonnes of metal. Approximately 30 tonnes of metal is melted within a period of four to five hours. A certain amount of metal is always maintained in the furnace, and this is called the heel. When the furnace is almost full, about 25% to 30% of the metal is transferred to a holding tank for further alloy preparation and casting. This occurs approximately once every four to five hours. There might be slight variations from one plant to another in the sequence of events and cycle time.

The combustion chamber provides the heat necessary for maintaining the liquid at a certain temperature and melting the solids (sows and shreds). Usually, regenerative burners are used in sidewell furnaces. These burners are coupled, and when one is on, the other is off. Behind each burner, there is a bed of particles (ceramic or alumina). Part of the exhaust gas passes through the off-burner and the bed behind it for heating the particles. The combustion air for the other burner passes through the bed of particles of that burner for preheating. After a period of time, this arrangement is switched. The cycle is in the order of

20 to 40 seconds. Preheating air is very important for energy conservation and improved heat transfer in the combustion chamber as will be demonstrated in Chapters 3 and 5.

The process is controlled by a cascade controller. The liquid metal has to be maintained at a certain temperature level. The refractory temperature should not exceed a certain value to prevent refractory failure. The fuel flow rate is controlled based on the thermocouple signals from the metal and the refractory as well as the air flow rate. The control is discussed in more detail in Chapter 5.

Table 1-1 : Typical Dimensions of a Sidewell Furnace

	Dimension
Height of liquid metal	0.94 m (3' 1")
Width of main hearth	5.84 m (19' 2")
Width of sidewell	2.08 m (6' 10")
Overall length of furnace	9.65 m (31' 8")
Length of main hearth	6.96 m (22' 10")
Height of combustion chamber	1.52 m (5')
Width of hot wall	0.61 m (2')
Height of inlet arch	0.38 m (15")
Height of outlet arch	0.28 m (11")
Width of both arches	0.91 m (3')
Impeller diameter	0.91 m (36")
Impeller shaft diameter	0.1 m (4")
Blade height	0.19 m (7.5")
Impeller speed	50-80 rpm

1.4 Mathematical Modelling and Experimental Testing

There are two ways of studying the phenomena occurring in any system: experimental testing and mathematical modelling. Experimental work can be done in the

plant on the actual unit. However, this is a very costly option and could affect the production unfavourably. Due to production restrictions and high risks involved, a very limited number of tests are usually carried out in plants. These data are highly useful for the calibration of mathematical models. It is also possible to build a physical model of the system in the laboratory and do the testing on that unit. One of the major problems in physical modelling is respecting the similarity parameters (geometrical, kinematic, and dynamic). Usually, it is difficult to respect all of them; therefore, one has to choose the ones that are essential and use those in the experimental study[12].

Measurements carried out during experimental studies vary in nature. Some involve intrusive methods such as the use of pitot tubes and suction pyrometers. When such a probe is introduced into a system, it modifies the conditions surrounding it. Therefore, it is very crucial to take this into account in estimating the accuracy of the measurements. In many cases, correction has to be made to the original data[13]. These methods are in use since many decades. With the advancement in the capacity (memory and computational speed) of computers, many non-intrusive measurement techniques such as laser Doppler anemometer have been developed in the past few decades. These types of measurements require collecting and processing a large amount of data. With today's computers, this is not a problem anymore. However, most of the non-intrusive techniques are limited to laboratory use. Usually, the large size of the industrial units and the environment in the plants (pollution, vibration, etc.) are not favourable for their use[13].

Mathematical modelling has many advantages. Many different options can be tested without any risk or interference with the production. Once a modelling tool is developed,

the cost of testing various options is very low. The model can be installed on different computers, and many people can use it independently. There are two points that are very important in mathematical modelling. First is the validation of the mathematical model which requires the comparison of model predictions with experimental data in order to establish how reliable the model is and how well the model represents the system. Second is the representation of the physical phenomena by appropriate mathematical equations in the model. For this, a fundamental understanding of each phenomenon occurring in the system is needed which can be accomplished by mainly experimental work. Therefore, it is of utmost importance to complement the mathematical modelling with experimental testing which is the case in the current project.

Increase in the speed and memory of computers led to substantial developments in numerical methods for the solution of complex and non-linear partial differential equations[14-15]. A number of commercial codes have been developed for modelling many different systems[16]. Today these codes serve as highly valuable tools to analyse almost any phenomena and significant advancements are being reported continuously. It is important to note, though, the commercial codes are nothing but tools which help the user make a better assessment of the system of interest. It is not given that the results produced are always useful or right unless the codes are used properly. Mathematical modelling is still very much a state-of-the-art business, especially, when it comes to modelling industrial systems.

Industries have realized the potential the commercial codes offer as valuable tools for analysis, development, control, and optimization of processes. In recent years, they have

paid much attention to mathematical modelling, and significant increase has been seen in their use for research and development. A number of articles indicate this trend clearly[17-20].

The focus of the current project was the development of mathematical models as tools to study the phenomena occurring in sidewell furnaces in order to be able to improve their performance and operation. These models were validated using the data from a pilot-size system and various data and observations from the plant trials. Due to the difficulty of obtaining a complete set of detailed data on such systems, partial validations were carried out. These will be explained in the relevant sections.

1.5 Mathematical Modelling of Sidewell Furnaces

A sidewell furnace consists of a side well and a main hearth which includes the combustion chamber. From the mathematical modelling point of view, it is better to divide it into two parts as follows: liquid metal bath and combustion chamber. Liquid metal bath covers the metal in both the side well and the main hearth. These two parts have completely different properties (physical, thermodynamic, etc.), and it is much easier to model them separately. Different methods, numerical solution techniques, or commercial codes could be used to model each part. This allows great flexibility for the modeller.

The modular approach is very important in modelling. Separate models should be built for different parts of a system that display different characteristics, and then they should be coupled through interfaces. This was done in the current project. Separate models are built for the liquid metal and the combustion chamber. Then they are coupled through an interface located at the surface of the metal bath in the main hearth (see Figure 1.3). The

modular modelling also has a great advantage if only one part of the system is to be studied. The model of interest can be used exclusively by imposing appropriate boundary conditions on the surface where the interface is located. In this project, the liquid metal bath and the combustion chamber were studied separately as will be seen in the following chapters. Further details of the models will be explained in the relevant chapters.

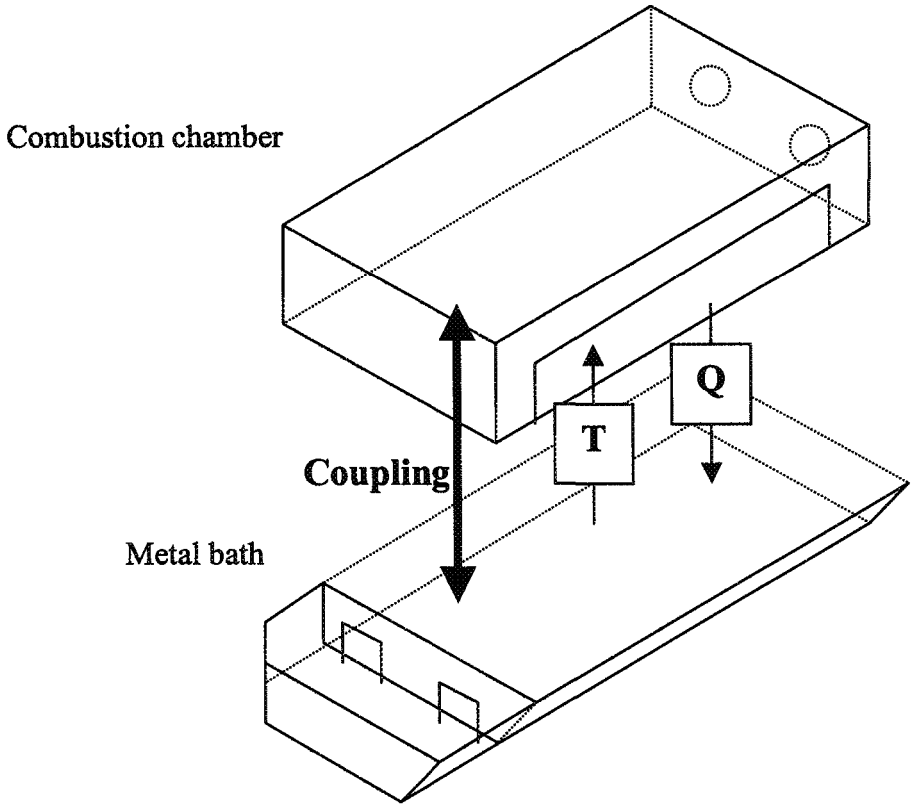

Figure 1.3 : Coupling Between the Models of Combustion Chamber and the Metal Bath (T: temperature, in K; Q: heat flow rate, in W).

1.6 Literature Review on Sidewell Furnaces

Many physical phenomena are occurring in sidewell furnaces ranging from melting of the solid scrap in the liquid metal to radiative heat transfer in the combustion chamber. Large numbers of studies are available in the literature on all of these phenomena. Also, studies reported on modelling of different types of furnaces and combustion systems are numerous. However, very few papers are available in the literature dealing with sidewell furnaces[7-11, 21-24]. Those that are reported are mostly from the research group of the author or their collaborators in Alcan. Due to the presence of a side well where the charge is fed while the source of heat is in the main hearth section, these furnaces have many different characteristics compared to the conventional ones. The current project is a detailed study of sidewell furnaces, and the results have been used to improve their performance and the process significantly.

Literature reviews on fundamental physical phenomena as well as on mathematical modelling of combustion systems are presented in the relevant sections later on.

1.7 Scope of the Current Work

Different models were developed to study different aspects of the sidewell furnaces:

1. A three-dimensional steady-state model was built using the commercial CFD code CFX[15] to calculate the flow field in the liquid metal. The flow pattern in the metal bath gives a good indication of how well the heat is transferred from the combustion chamber to different sections of the liquid metal. After validation, this model was used to study many geometrical factors such as furnace dimensions, arch sizes, and optimum

impeller and pump positions. The details of the model and the results are discussed in Chapter 2.

2. A model for the combustion chamber was developed based on the one-gas-zone-model concept. This is essentially a heat-transfer model. A parametric study was carried out to determine the effects of various parameters in the combustion chamber. The model and the results are presented in Chapter 3.

3. A three-dimensional transient heat-transfer model was built for the liquid metal using CFX. The flow field calculated by the three-dimensional flow model of Part 1 above was imposed. Then, this is coupled with the combustion chamber heat transfer model of Part 2 above. The temperature distribution in the liquid metal was calculated for a number of cases. This model is described and the results are discussed in Chapter 4.

4. Originally, a more detailed combustion chamber model was to be developed for optimization of parameters such as burner position. However, it was realized that studying the dynamic operation of the furnace with the control emulator incorporated was more important. Consequently, a dynamic model was developed including both the metal and the combustion chamber. It was used to study various operational scenarios, and recommendations were made to Alcan. Also, combining the model with a user-friendly interface, a sidewell furnace simulator was built and transferred to the industry. The technique used for dynamic modelling is original and gives detailed information in the liquid metal. The details are explained in Chapter 5.

Each of the above models is used for different purposes. For this reason, the results of each model are discussed in the relevant chapter, and there is no separate chapter on

results and discussion. Overall conclusions and recommendations are given in Chapter 6. The assumptions used in the models are summarised in Appendix 7. The modelling work and strategies carried out in the current project can easily be extended or adapted to other industrial furnaces.

CHAPTER 2

3D MATHEMATICAL MODELLING OF THE FLOW PATTERN IN THE METAL

2.1 Introduction

The performance of a melting furnace can be characterized by the melt rate and the energy efficiency. Both of these parameters depend on the efficient transfer of heat from the source to the point of utilization. The source is the hot combustion gases produced by burning the fuel in the combustion chamber. The heat is required:

- to maintain the liquid metal at a proper temperature,
- to melt the shred charged to the sidewell, and
- to melt the solid charge (sows) placed in the main hearth.

2.1.1 Heat Transfer Mechanisms

Different modes of heat transfer are important in different sections of the furnace. In the combustion chamber, heat is transferred from the hot gases to the metal surface mainly by radiation and convection. Radiative transfer takes place either directly from the flame to the metal surface or indirectly through absorption and re-emission by the refractory surfaces. In liquid metal, conduction and convection are important. Aluminum has a high thermal conductivity which makes the conduction one of the two major mechanisms. Due to temperature gradient in the liquid metal, natural convection also occurs. However, neither conduction nor natural convection provides means for efficient heat transfer (see

Figure 2.1). Forced convection provided by various devices such as pumps or impellers has a considerable effect on the performance.

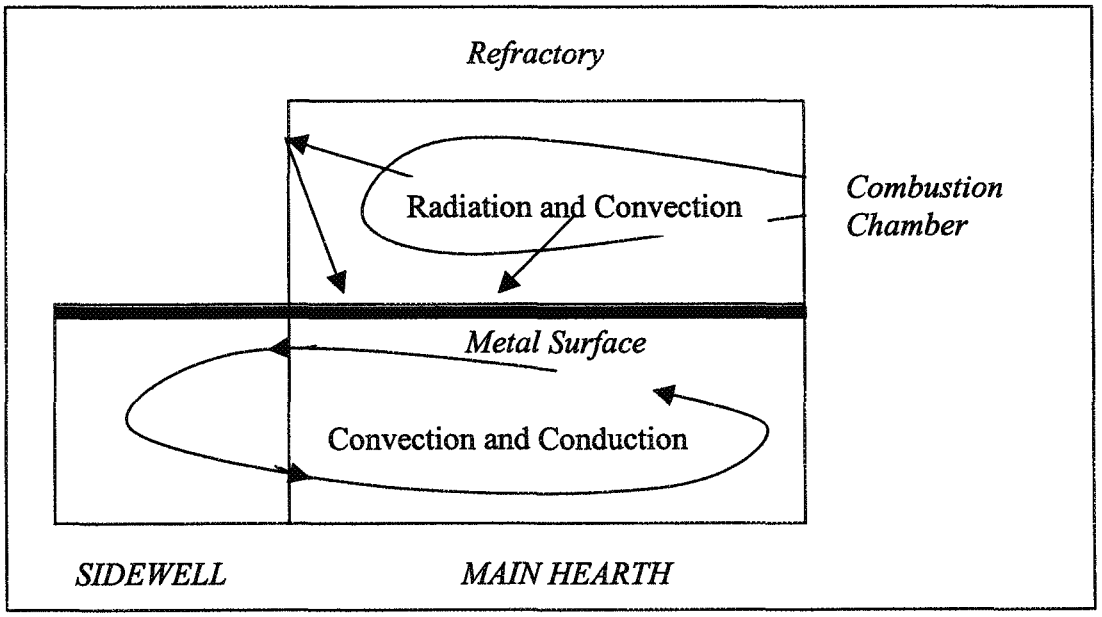

Figure 2.1 : Heat Transfer Mechanisms Occurring in the Two Sections of the Furnace.

2.1.2 Relationship Between Metal Flow and Heat Transfer

Heat transfer in the combustion chamber depends mainly on the liquid metal area, refractory and metal surface emissivities, and the difference between the average combustion chamber temperature and the average metal surface temperature. The emissivities are usually difficult to control or modify and are function of material characteristics. The metal surface area can be increased by changing the design for new furnaces; however, physically there are limitations to how much this variable can be changed. For existing furnaces, the area is fixed.

The temperature difference is probably the most convenient variable that can be modified through changes in operating conditions. The larger this difference is, the more favorable the heat transfer is from the combustion chamber to the metal surface. The

temperature difference can be increased by either increasing the fuel flow rate to the combustion chamber or by stirring the liquid metal. Increased fuel flow rate leads to higher combustion temperatures. Stirring reduces the average metal surface temperature by decreasing the temperature gradient in the liquid metal[11, 22-24]. Either one or a combination of these two actions may be required to increase the heat transfer.

The melt rate in the side well depends on the energy available in the liquid metal coming from the main hearth (see Figure 2.2). This is a function of the mass flow rate and the temperature level of the metal. In general, increase in the metal flow rate through the arches should lead to increased melting capacity. Extremely high flow rates may not be desirable though since this may cause the cooling of liquid metal in the main hearth if the heat transfer from the combustion chamber to the metal is limited and less than the heat carried from the main hearth to the side well by the metal flow.

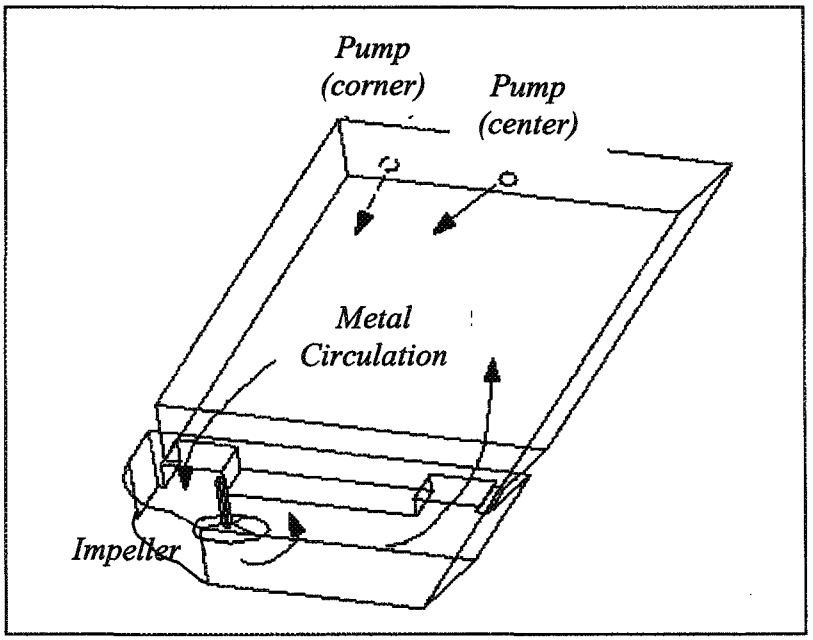

Figure 2.2 : Circulation of Metal Between the Main Hearth and the Side Well.

Increasing both the metal flow through the arches (arch flow) and the stirring in the main hearth (main hearth circulation) should improve furnace performance by favoring more efficient heat transfer (see Figure 2.3):

- between the combustion chamber and the liquid metal in the main hearth, and
- between the main hearth and the side well within the metal bath.

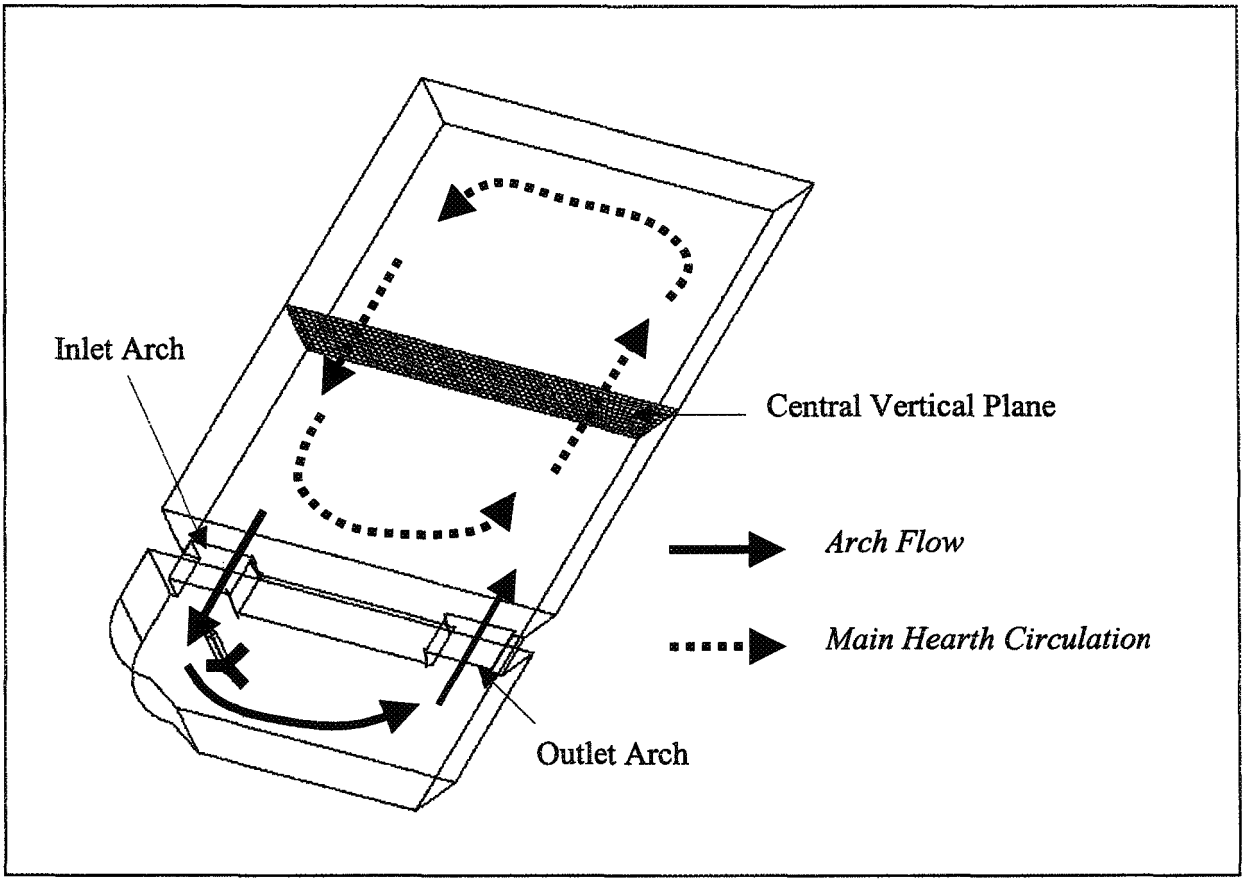

Figure 2.3 : Arch Flow and Main Hearth Circulation in the Furnace.

2.1.3 Stirring and Submergence Devices

Salt is added to side well to help remove oxides and inclusions coming from the scrap metal. Normally, these form a dross layer floating on the liquid metal surface which

is removed from the furnace at regular time intervals. Significant amount of liquid aluminum is usually found trapped in the dross layer. In the side well, the dross can be collected in the form of balls. The dross balls are easier to remove and contain relatively smaller amount of trapped aluminum.

The main function of impellers is to submerge the scrap metal fed to the side well. They also help circulate the dross balls and mix the salt within the liquid metal. In addition, they provide some metal circulation between the side well and the main hearth as well as mixing in the main hearth. However, these metal flow rates depend strongly on the position, diameter, and rotational speed of the impeller[11, 22-24].

Pumps can be used either in the side well or in the main hearth[25-26]. If placed in the side well, their function is limited to increasing metal circulation. If placed in the main hearth as shown in Figure 2.2, they could perform both functions: stirring the metal bath in the main hearth and increasing the metal circulation between the two sections of the furnace.

In order to improve the side well furnace performance, it is important to optimize the metal flow. This could be achieved by combining and properly positioning the stirring and submergence devices.

2.2 Mathematical Model

A three-dimensional mathematical model has been developed for the flow in the metal bath for sidewell furnaces. The flow was used to study the effect of various geometrical factors. Also the calculated flow fields were used in subsequent models as will be seen in the following chapters.

The governing differential equations for flow were solved using the commercial CFD code CFX[15] (formerly CFDS-FLOW3D). The equations are: the continuity equation, the momentum conservation equations in three directions (the three velocity components) and the K-ε turbulence equations. These equations are presented in Appendix 2. Complex geometry of the furnace is easily handled using the block structure of the code. The number of cells used for different furnaces range from about 45,000 to 75,000 cells. Figure 2.4 shows the grid used for the furnace for which the dimensions are given in Table 1. The computation time for each run is about 5 hours on a SUN ULTRA1 (200MHz) workstation for 56,000 cells (12 hours on a HP730 workstation). Depending on the number of cells, the computation time increases or decreases proportionally.

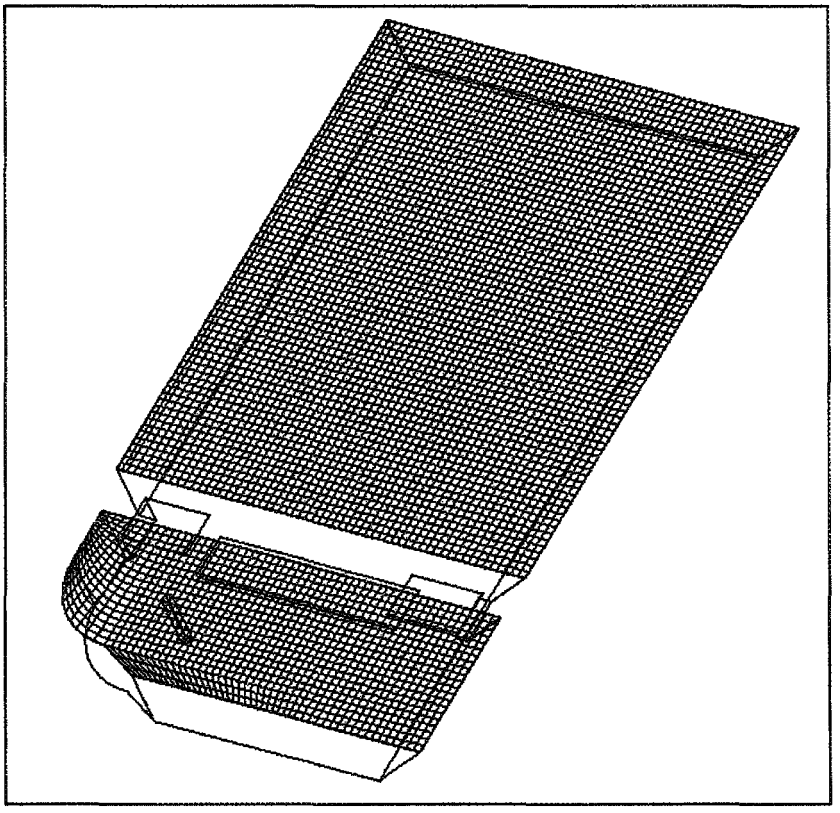

Figure 2.4 : A Typical Grid Used for the Furnace.

The force applied onto the fluid by the blades of the impeller is represented by a source term in the momentum equations. This approach has been used successfully to simulate the impeller action in other systems and has the advantage of allowing the user to maintain coarser grid and reasonable computation times[27-29]. Detailed geometrical representation of the impeller is also possible; however, this would require much finer grid resulting in very large computation times. The representation of impeller within the source term of the momentum equations is described in Appendix 3.

The pump action is represented by a mass inlet term at the boundary where it is located. The mass flow rate is the product of discharge velocity, area normal to velocity, and density. The discharge diameter (pump discharge area) and discharge velocity as well as the flow direction are introduced directly into the model. Since this is a steady-state model and the liquid level is not allowed to vary, a mass outlet is needed. The mass outlet is placed above the mass inlet position at a much higher level through an area of nine times that of the inlet. In this way, the effect of the mass outlet on the flow pattern in the liquid metal becomes negligible as confirmed by the results. The pump and the impeller can be placed at various positions in the furnace.

The metal surface is assumed flat in order to create a model manageable from the point of view of number of cells, number of phases and computation time. As a consequence, the vortex formation around the impeller or the waves created by excessive flow rates cannot be represented by the model. Nevertheless, the velocity field around the impeller shaft near the metal surface gives a good indication of the possible vortex formation and its strength. In simulations, the surface is treated as a symmetry plane.

In the model, most design and operational parameters can be varied. Numerous simulations have been carried out to calculate the metal flow under different conditions. The results of these simulations and model validation will be presented in the following sections.

2.3 Model Validation

For the validation of the mathematical model, a pilot model of the furnace at 0.3 scale was built[30-31]. Since it is almost impossible to use aluminum for flow measurements, the working fluid was water which has a kinematic viscosity similar to that of aluminum (1.0×10^{-6} m^2/s for water at 25°C, and 1.8×10^{-6} m^2/s for aluminum at 700°C). Then the pilot laboratory unit was simulated using the above flow model. Predictions of the mathematical model were very similar to those measured in the pilot model of the furnace. A comparison of the velocity field at 0.085 m from the bottom (total liquid height is 0.267 m) is shown in Figure 2.5. All the tendencies measured in the pilot model and all the plant observations were similar to those predicted by the model. Design of the pilot model and similarity criteria are discussed in Appendix 4.

Figure 2.5 shows clearly the good agreement between the results. The magnitude and the direction of velocities are very similar. The low-velocity zone is predicted accurately by the mathematical model. Maximum velocity (located at the exit of the outlet arch) is 0.141 m/s in both cases. The average velocity predicted by the mathematical model over the shown section is 0.074 m/s, and the calculated value from the measurements is about 0.075 m/s. Averages were determined arithmetically since the cell sizes are similar in the model and the measurements were done over equidistant positions in the water model.

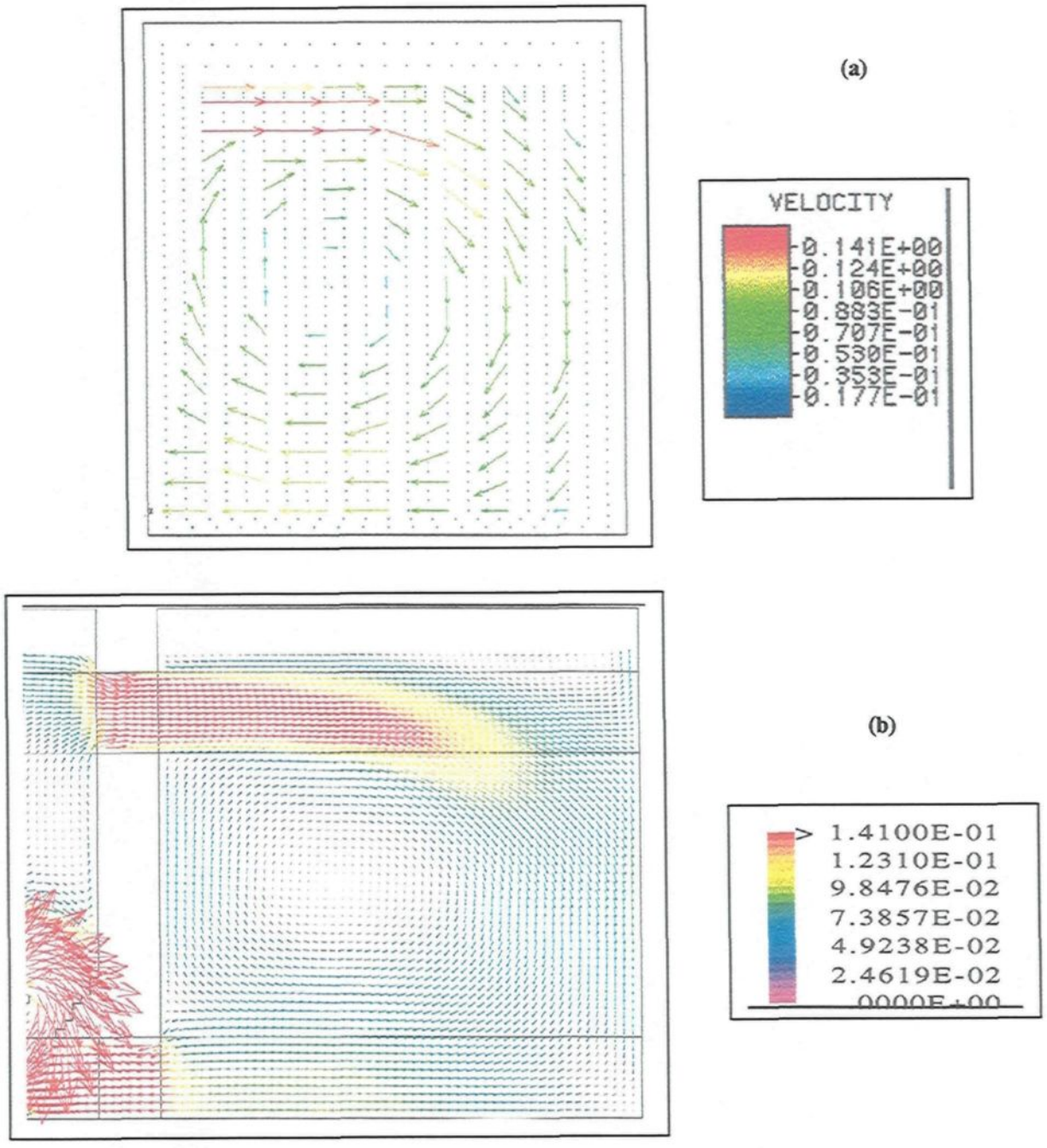

Figure 2.5 : Comparison of Mathematical Model Results with Measurements on the Pilot Model (Velocities are in m/s): (a) Velocities Measured in the Pilot Model, (b) Velocities Predicted by the Mathematical Model.

2.4 Results and Discussions

The flow model has been used to determine the flow field for a large number of cases. Various indices have been calculated and investigated to characterize the flow in a furnace[32-33]. As mentioned previously, the metal flow through the arches (arch flow) and the metal circulation rate in the main hearth (main hearth circulation) appear to be the most suitable indices for the purpose of quantitatively comparing different cases. The arch flow is directly related to the melting rate of shreds, and the main hearth circulation gives an indication of the heat transfer efficiency between the combustion chamber and the liquid metal.

Each of the following sections presents and compares the results for one given aspect of the metal flow. In each section, only one parameter is changed keeping all others constant so that the furnace performance could be compared on the same basis. Only the arch flow is given in some sections depending on the relevance of that parameter to the furnace operation.

2.4.1 Effect of Baffle Type and Length

Table 2.1 and Figures 2.6-2.8 presents the results (calculated by the model) for cases with and without baffle in the side well as well as the effects of baffle type and length. The three configurations (without baffle, with rectangular baffle and with triangular baffle) are given in Figure 2.6. The distance "d" between the impeller and the hotwall is also shown in the same figure. This distance is also equal to the length of the baffle when a baffle is present. In all of these cases the impeller is aligned with the inlet arch.

Without baffle, the arch flow is higher when the impeller is closer to the hotwall. As it is moved away, it can withdraw less and less metal from the main hearth (see Figure 2.7). With the addition of a baffle, the arch flow increases significantly. The optimum baffle length is about 25-30% of the side-well width. When the length is shorter or longer, the arch flow decreases (see Figure 2.7). This decrease is more significant when the baffle length is increased (234.3 to 209.7 kg/s for a rectangular baffle, and 206.7 to 154.1 kg/s for a triangular baffle).

Table 2.1 : Arch Flow (kg/s) for Different Baffle Configurations.

Distance between the hotwall and the impeller (d in Figure 2.6)	No baffle	Rectangular baffle	Triangular baffle
0.1 m (3.9")	80.3	-	-
0.3 m (11.7")	**82.4**	224.7	-
0.5 m (19.4 ")	76	**234.3**	**206.7**
0.6 m (23.3")	-	-	200.1
0.7 m (27.2")	-	209.7	154.1
0.9 m (35")	45	-	-

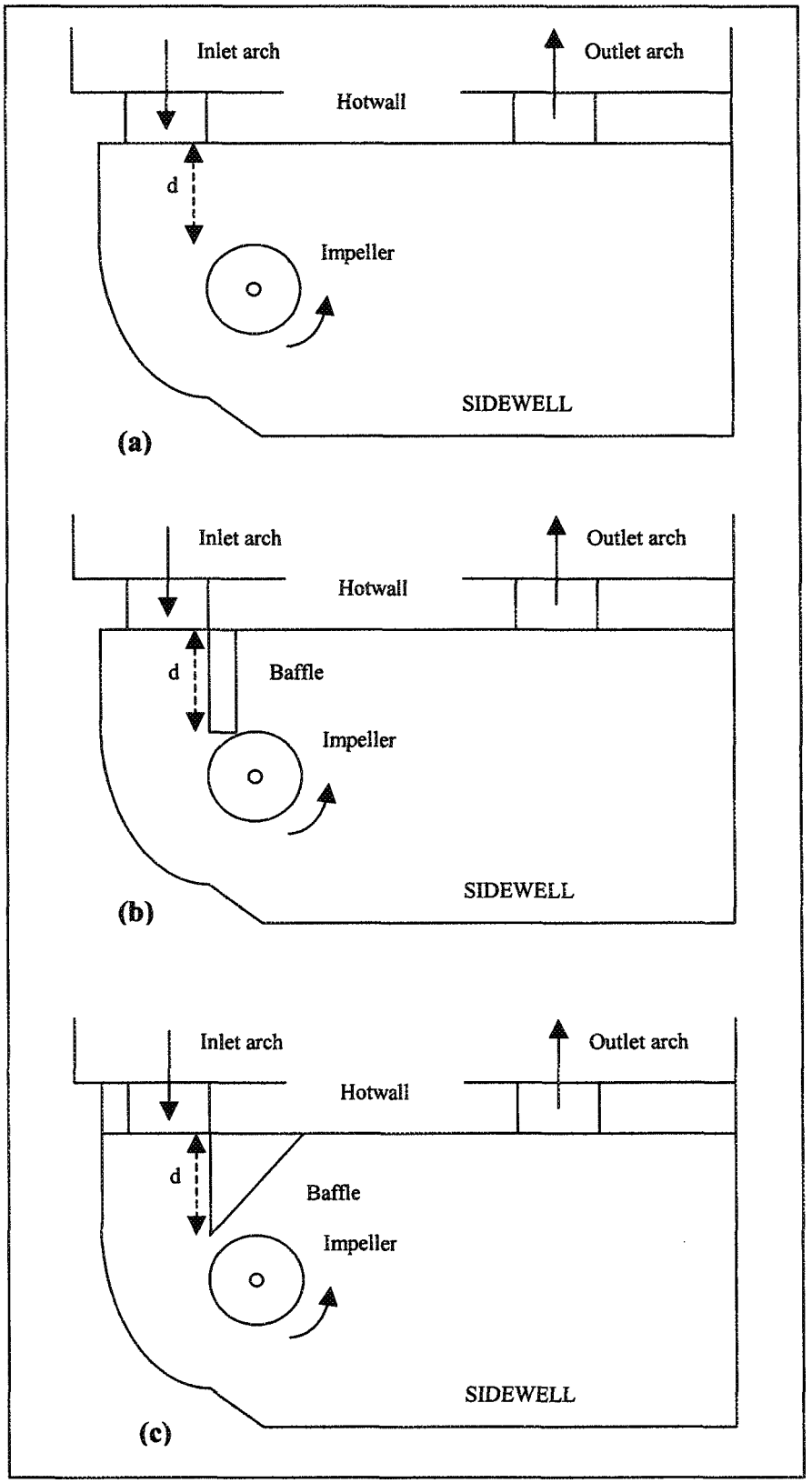

Figure 2.6 : The Side Well Configurations for Cases: (a) Without Baffle, (b) With a Rectangular Baffle, and (c) With a Triangular Baffle.

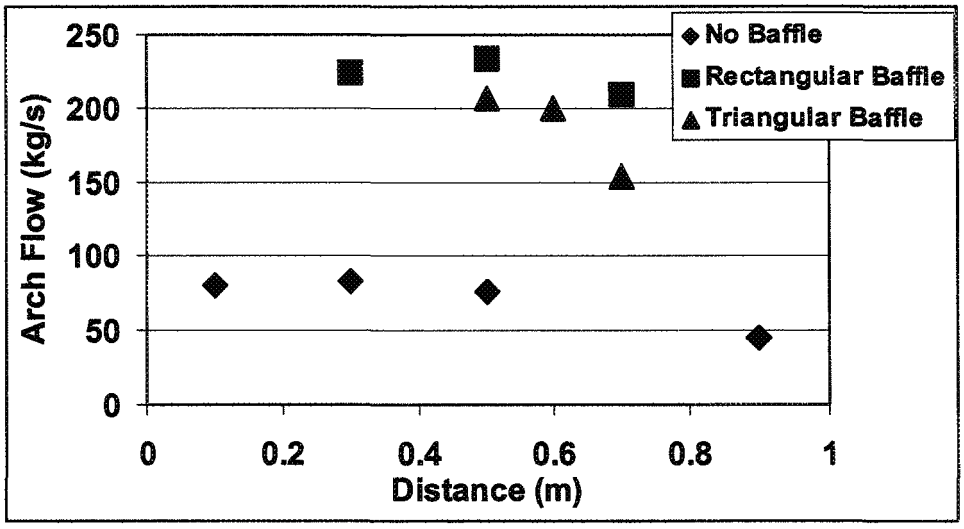

Figure 2.7 : Arch Flow for Different Baffle Configurations as a Function of Distance Between Impeller and Hotwall.

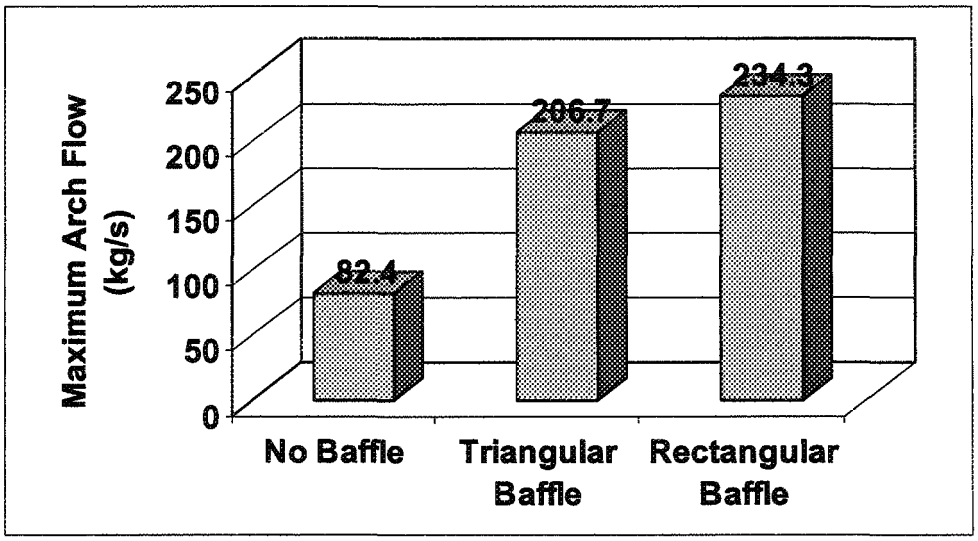

Figure 2.8 : Comparison of Maximum Arch Flow Rates for Different Baffle Configurations.

Table 2.1 also shows that when the baffle length is not optimum, the decrease in flow is more pronounced for a triangular baffle. Rectangular baffle gives a better performance both in terms of arch flow (see Figure 2.8) as well as reducing the effect of non-optimum baffle lengths on the metal flow.

2.4.2 Effect of Mal-positioning the Impeller

Table 2.2 presents the results for the effect of mal-positioned impeller for a number of side-well configurations. In all of these cases, the impeller is shifted towards the outlet arch. The letters in parentheses refer to the configuration given in Figure 2.9. The percentages represent the reduction in arch flow in comparison with the ones obtained when the impeller is aligned with the inlet arch as given by Table 2.1 (not with respect to arch flow at the optimum impeller position).

These results clearly show that when the impeller is not well positioned, the arch flow decreases. This effect is significantly more important when there is no baffle. Comparison of the two baffles indicates that the reduction in arch flow is higher for the triangular baffle. The percentages would be even higher if the comparison was made with respect to the arch flow for the optimum impeller position in which case the baffle length is about 0.5 m. The rectangular baffle gives a better performance in terms of countering the negative effects of non-optimum or mal-positioned impellers.

The 88% decrease in the arch flow for case without baffle is due to the formation of a recirculation zone in the inlet arch. Most of the metal returns back to the main hearth without even entering the sidewell. A badly positioned impeller may yield such undesirable

flow patterns. Figure 2.10 compares the flow through the inlet arch for both favorable and unfavorable conditions.

Table 2.2 : Effect of Mal-positioned Impeller on Arch Flow (kg/s). Parentheses Containing Letters Show the Side-Well Configurations in Figure 2.9. The Percentages in Parenthesis Represent the Reduction in Arch Flow in Comparison with the Ones Obtained When the Impeller is Aligned with the Inlet Arch as Given by Table 2.1 (not with Respect to Arch Flow at the Optimum Impeller Position).

Distance d in Figure 2.9	No baffle	Rectangular baffle	Triangular baffle
0.3 m (11.7")	(A) 9.6 (88%)	-	-
0.5 m (19.4")	-	(B1) 210.8 (10%)	(C1) 178.7 (14%)
	-	(B2) 226.8 (3.2%)	(C2) 176.6 (15%)
	-	(B3) 221.5 (5.5%)	-
0.7 m (27.2")	-	-	(C1) 114.5 (26%)

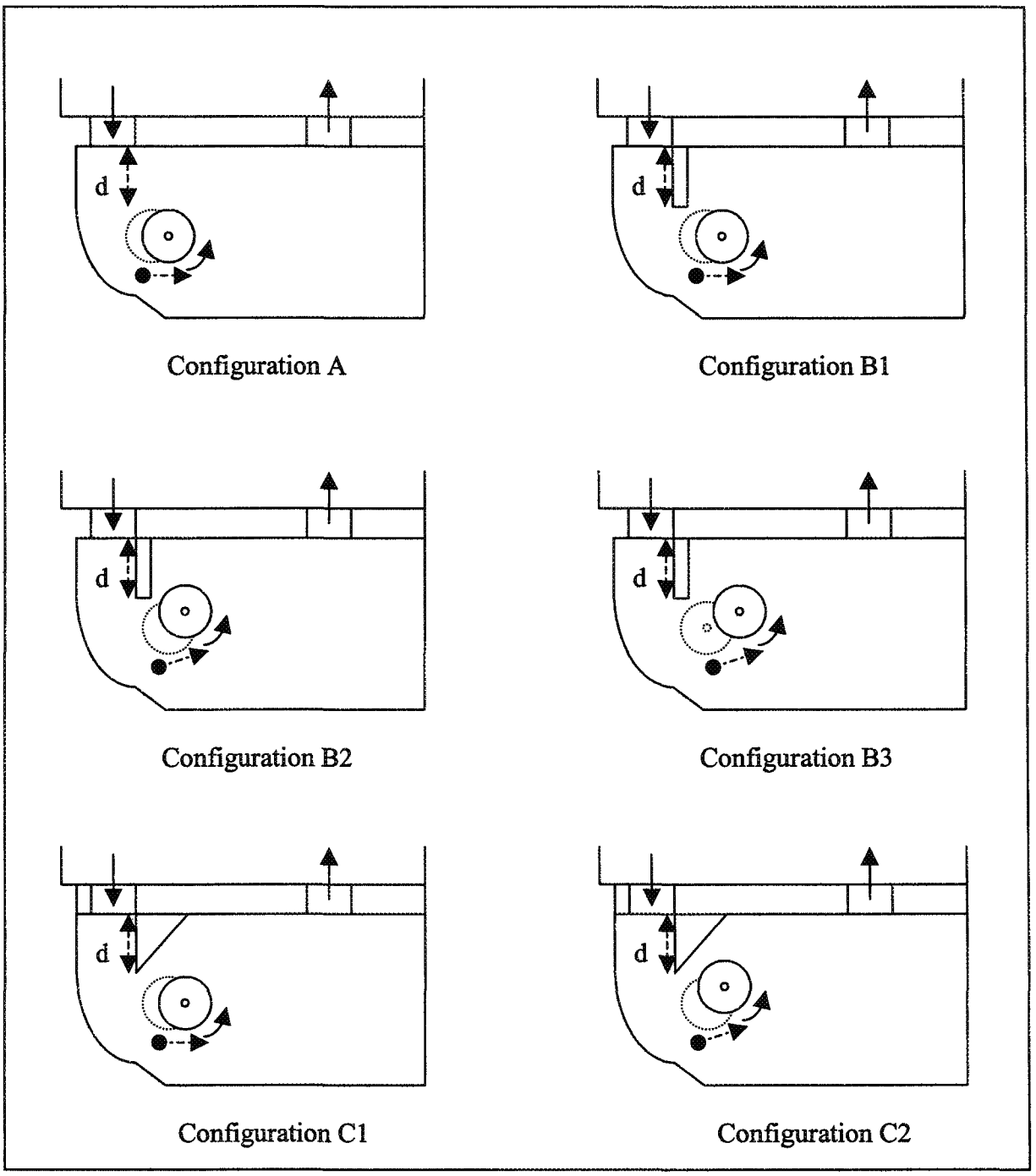

Figure 2.9 : Side-Well Configurations for Table 2.2 Showing How the Impeller is Moved Away from Its Position Where It Was Aligned With the Inlet Arch.

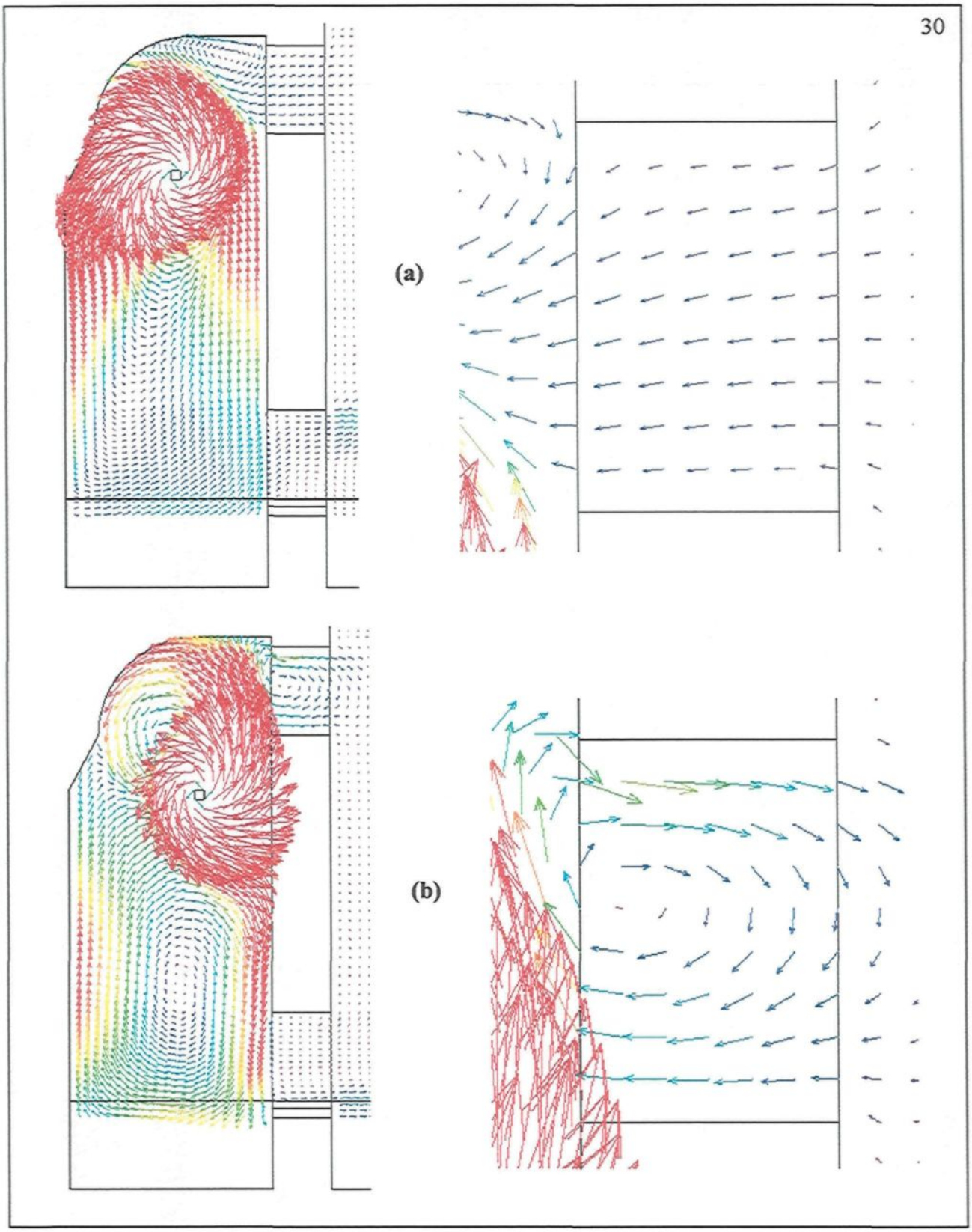

Figure 2.10 : Flow Field (0.24m from Bottom) Within the Inlet Arch for (a) Well-positioned Impeller, and (b) Mal-positioned Impeller.

2.4.3 Effect of Pump on Arch Flow

Pumps can be placed in a number of different locations around the furnace; however, the most suitable area in the main hearth is usually the opposite side across from the side well as shown in Figure 2.2. The central position seems to be the preferred one since it does not interfere with the other parts of the furnace such as charge door and burners, and at the same time, the pump can be directed towards the inlet arch with ease. For these cases, the angle of the pump is 16° (see Figure 2.13) and the discharge velocity is 5.5 m/s giving a mass flow rate of 110 kg/s at the pump outlet.

Table 2.3 presents the arch flow rates for the three configurations shown in Figure 2.6 as a function of the distance "d". The percentages in parentheses show the increase in arch flow with respect to the ones without any pump in Table 2.1. Results for the distance d equal to 0.5m are given in Figure 2.11. When there is no baffle, the effect of the pump is quite significant. If there is a baffle, the increase is still important, but not as much as going from a "no-baffle" case to a "with-baffle" case. With the rectangular baffle, the flow is already high; the addition of a pump has a smaller effect compared to other cases (see Figure 2.11).

Table 2.3 : Effect of Centrally Located Pump (See Figure 2.2) on Arch Flow (kg/s) for the Three Side-Well Configurations Shown in Figure 2.6. The Percentages in Parentheses Show the Increase in Arch Flow with Respect to the Ones Without Any Pump in Table 2.1.

Distance d	No baffle	Rectangular baffle	Triangular baffle
0.3 m (11.7")	144.5 (75%)	272.9 (21%)	-
0.5 m (19.4")	186.2 (145%)	279.2 (19%)	261.3 (26%)

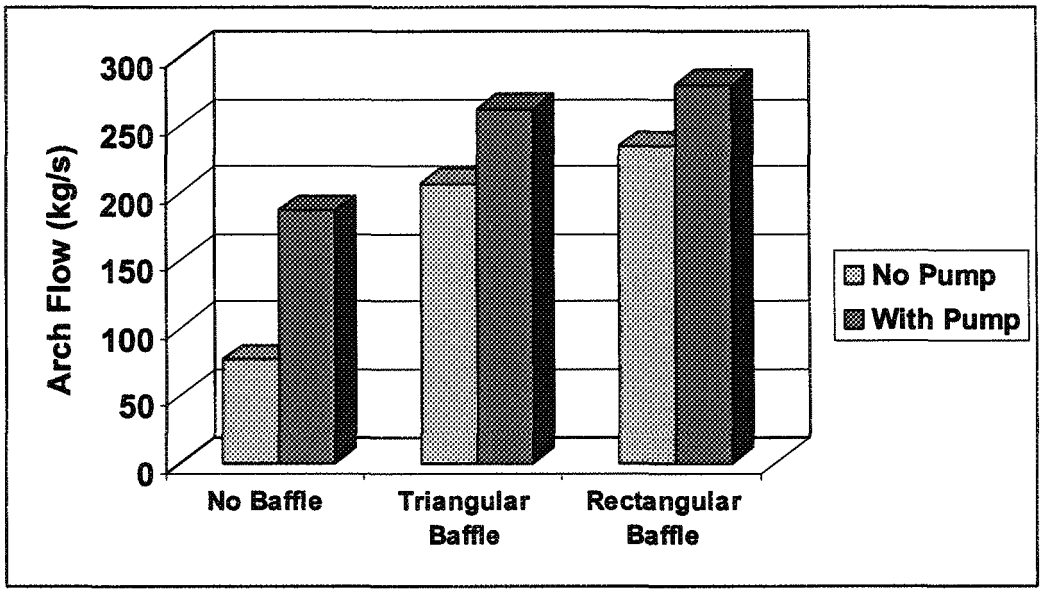

Figure 2.11 : Effect of Pump on Arch Flow Rate for Different Baffle Configurations for the Distance d Equal to 0.5 m.

Figure 2.2 also shows an alternative position for the pump, at the corner facing the inlet arch. Table 2.4 compares the arch flow rates obtained for the two pump positions of Figure 2.2 using the same pump described above (see also Figure 2.12). The percentages in parentheses show the increase in arch flow with respect to the case without any pump (234.3 kg/s in Table 2.1) for a rectangular baffle of 0.5 m length. Corner position gives a much higher rate due to its location being right opposite the inlet arch. Some furnaces are equipped with regenerative burners. The heat recuperation units are usually located right below the burners in which case the corner position cannot be used for placing pumps.

Table 2.4 : Effect of Pump Position on Arch Flow (kg/s). The Percentages in Parentheses Show the Increase in Arch Flow with Respect to the Case Without Any Pump (234.3 kg/s in Table 2.1) for a Rectangular Baffle of 0.5 m Length.

Distance d for rectangular baffle	Central position	Corner position
0.5 m (19.4")	279.2 (19%)	329.6 (41%)

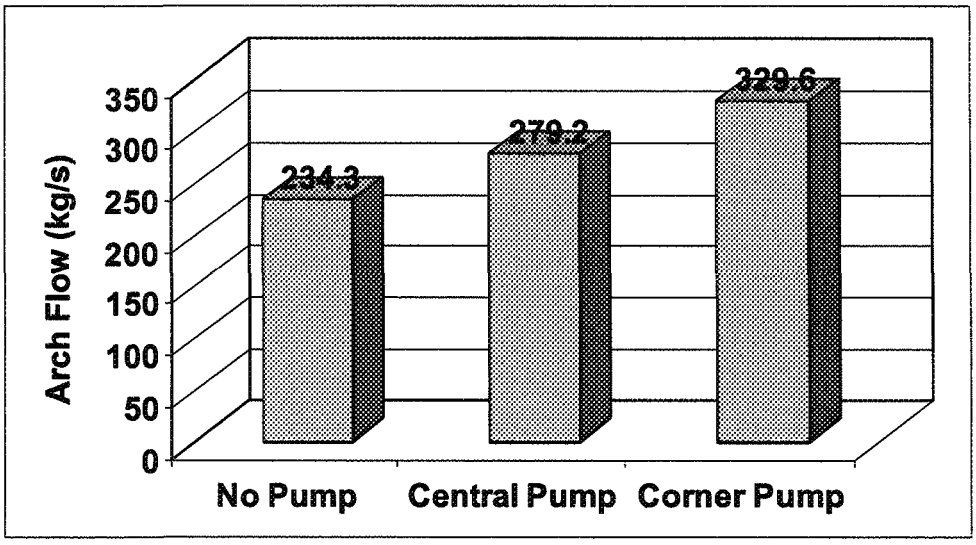

Figure 2.12 : Effect of Pump Position on Arch Flow Rate.

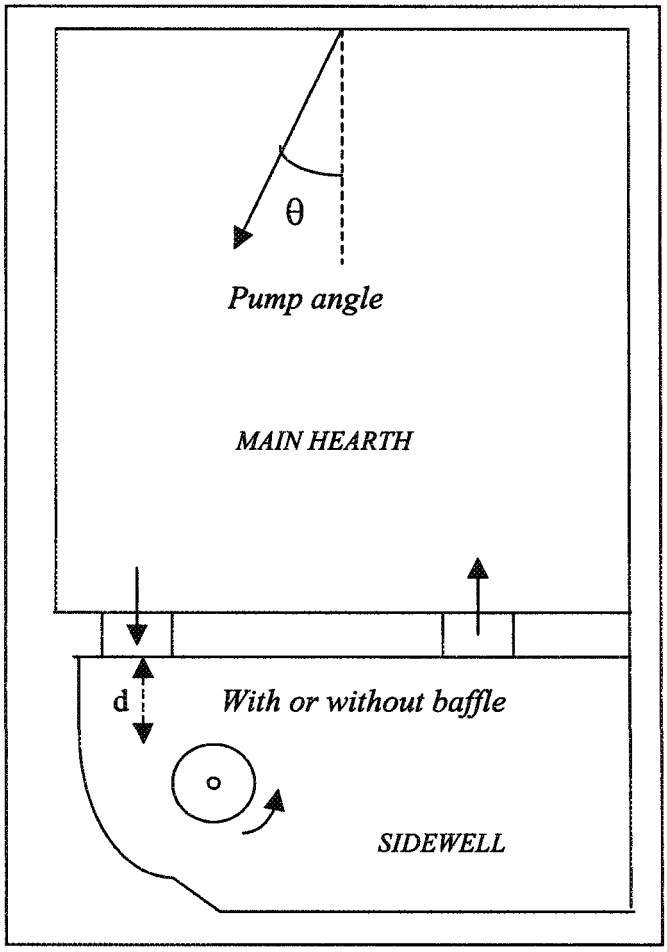

Figure 2.13 : Central Position for a Pump Located in the Main Hearth.

Figure 2.14 shows the flow field in the form of velocity vectors for the two cases given in Table 2.4 on a horizontal plane 0.7 m from the metal surface (0.24 m from the bottom) where the impeller is located. When the pump is at the center position, a low velocity zone forms in the middle of the main hearth. Also a second smaller low velocity zone is seen at the corner behind the jet created by the pump. For the pump located at the corner, the low velocity zone in the middle of the main hearth is larger; however, the secondary low velocity zone at the corner no longer exists. Low velocity regions are usually less favorable for the heat transfer process in the liquid metal. Without heat transfer analysis, it is difficult to judge which of these cases is more advantageous.

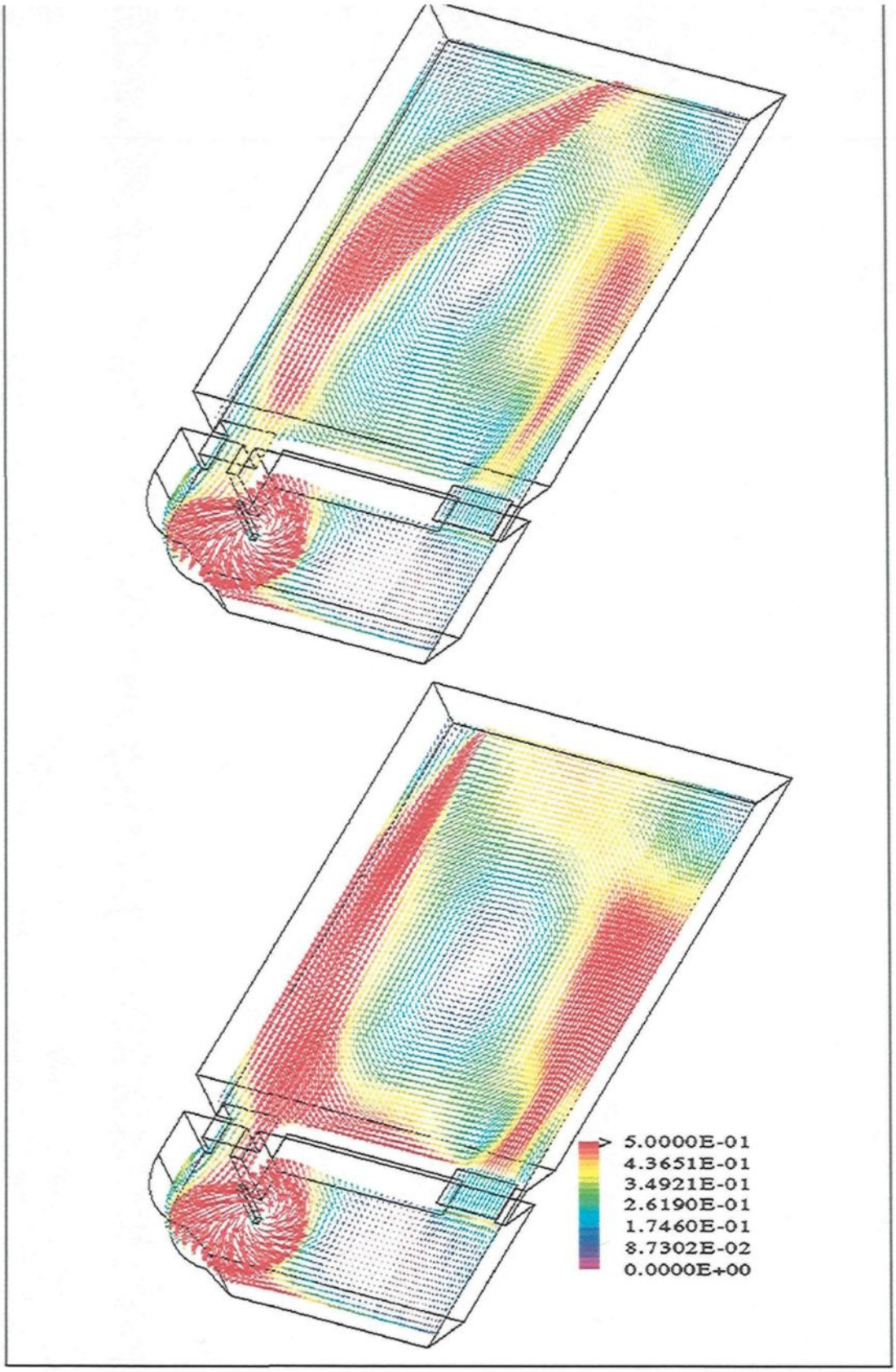

Figure 2.14 : Velocity Vectors (in m/s at 0.24m from Bottom) Showing the Flow Field for Central and Corner Pump Positions.

2.4.4 Effects of Pump Discharge Area and Velocity

Two series of simulations were carried out to determine the effects of pump discharge area and pump discharge velocity as function of pump angle (see Figure 2.13 for pump angle). The product of the velocity and the area gives the volumetric flow rate of the liquid metal being forced through the pump. In these simulations, a rectangular baffle and an impeller are present in the side well.

In the first series, the area was kept constant, and the discharge velocity was varied. The results are given in Table 2.5 and Figures 2.15-2.17. They clearly convey a number of conclusions. When the pump is directed towards the inlet arch (16°), the arch flow increases slowly with increasing velocity up to about 4 m/s, then rapidly above this value (see Figure 2.15). For larger angles, as the pump is directed closer to the wall, increase in pump discharge velocity may have an adverse effect on the arch flow. For example, at 19°, an increase from 5.5 to 7 m/s causes a decrease in arch flow (see Figure 2.17).

For each pump discharge velocity, there is an optimum angle (21° for 3 m/s, 19° for 4 m/s, 18° for 5.5 m/s and 17-18° for 7 m/s) to attain maximum arch flow (see Figures 2.16-2.17). The main hearth circulation rates depend on the pump angle as well, and there seems to be an optimum angle (at 5.5m/s, 19° gives the maximum rate). However they are, in general, very high; therefore, the pump angle is less of a concern for the main hearth circulation rate within a certain range of angles (about 14° to 22°).

Table 2.5 : Effect of Pump Discharge Velocity at Constant Discharge Area (0.009 m^2).

Pump disch. vel.►	1 m/s		3m/s		4m/s		5.5 m/s		7 m/s	
Angle (°) ▼	Arch flow (kg/s)	Main hearth circ. (kg/s)	Arch flow (kg/s)	Main hearth circ. (kg/s)	Arch flow (kg/s)	Main hearth circ. (kg/s)	Arch flow (kg/s)	Main hearth circ. (kg/s)	Arch flow (kg/s)	Main hearth circ. (kg/s)
0	-	-	-	-	-	-	173	1327	-	-
10	-	-	-	-	-	-	208.2	1628	-	-
14	-	-	-	-	-	-	225.4	1860	-	-
16	236.8	591.8	238.3	1372	247.5	1638	279.2	1996	317.2	2432
17	-	-	-	-	255.8	1626	290.8	2016	**326.8**	2506
18	-	-	-	-	264.5	1604	**299.3**	2031	**326.8**	2565
19	-	-	251.3	1324	**275**	1566	281	2060	277.3	2617
20	-	-	258.4	1307	271.5	1555	253.3	2020	-	-
21	-	-	**262.1**	1290	-	-	-	-	-	-
22	-	-	259.8	1269	-	-	-	-	-	-
25	-	-	-	-	-	-	231	1791	-	-
40	-	-	-	-	-	-	224.1	913	-	-

With impeller and rectangular baffle (no pump):
Arch flow = 234.3 kg/s Main hearth circ. = 568 kg/s

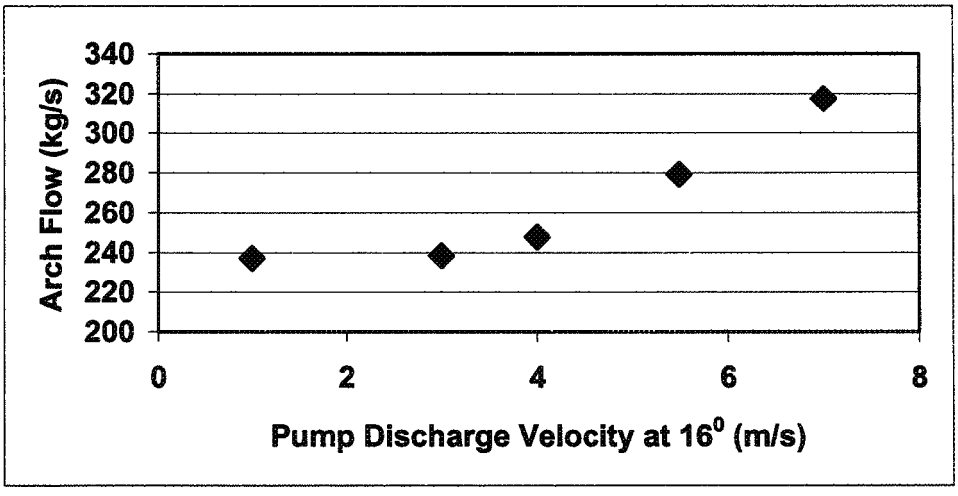

Figure 2.15 : Effect of Pump Discharge Velocity on Arch Flow Rate.

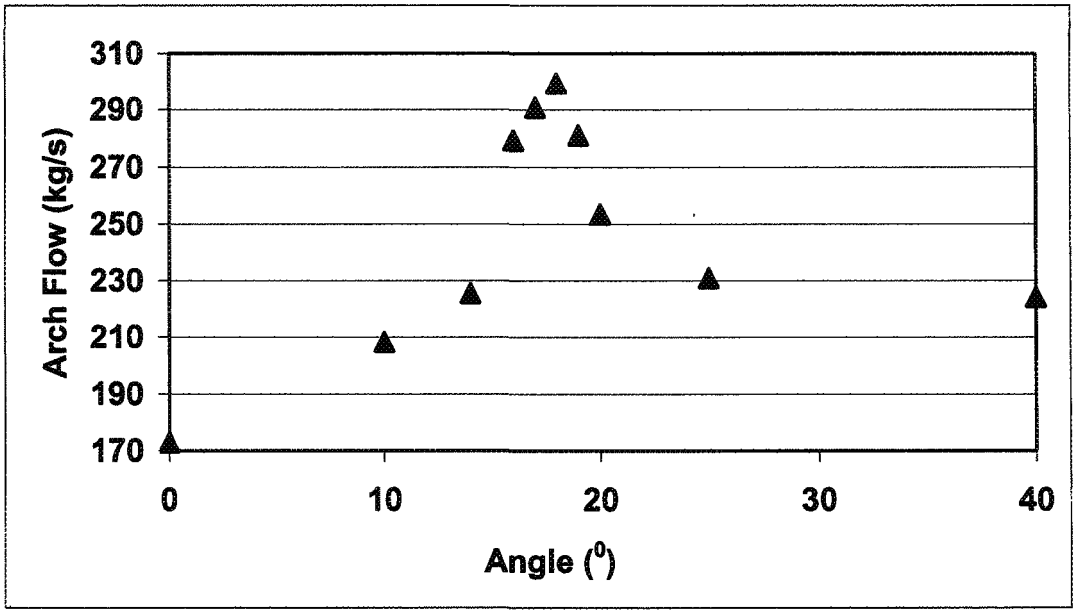

Figure 2.16 : Effect of Pump Angle on Arch Flow for 5.5 m/s Discharge Velocity

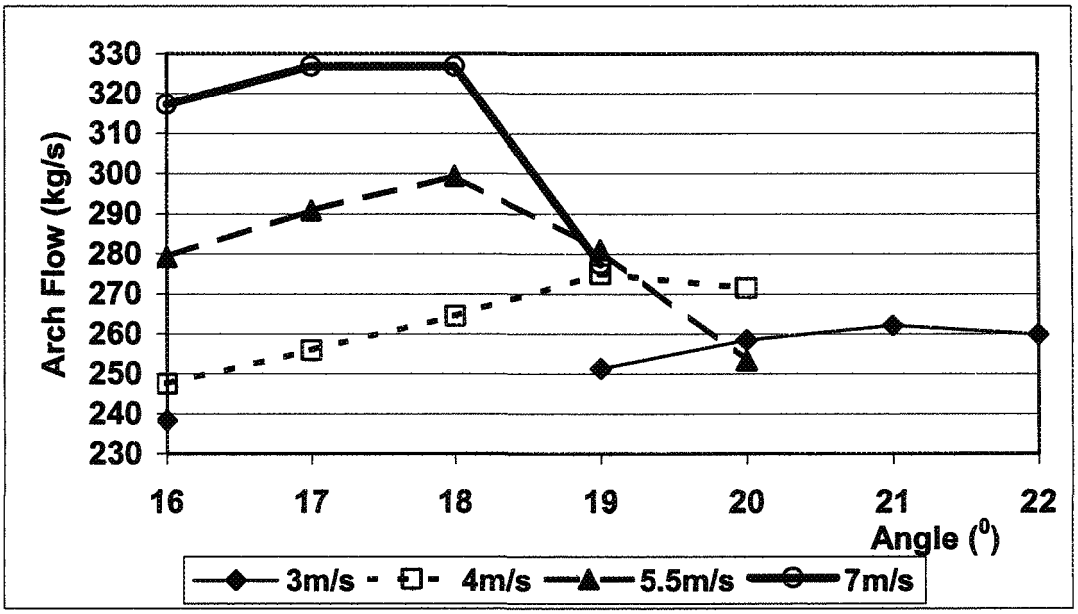

Figure 2.17 : Effect of Pump Angle on Arch Flow for Different Discharge Velocities.

In the second series, the velocity was kept constant, and the area was increased. The results are given in Table 2.6 and Figure 2.18. For each area, there is an optimum pump

angle to maximize the arch flow (see Figure 2.18). This angle increases with the increase in area. Also, there seems to be an optimum angle that gives the maximum main hearth circulation rate. The two optimum angles are not necessarily the same (for example, 18° for maximum arch flow and 19° for maximum main hearth circulation in the case of 0.009 m^2 area). As mentioned previously, the latter is less important since the main hearth circulation rates are very high in all cases.

Table 2.6 : Effect of Pump Discharge Area at Constant Discharge Velocity (5.5 m/s).

Pump disch. area ▶	0.009 m^2		2×0.009 m^2		4×0.009 m^2	
Angle (°) ▼	Arch flow (kg/s)	Main hearth circulation (kg/s)	Arch flow (kg/s)	Main hearth circulation (kg/s)	Arch flow (kg/s)	Main hearth circulation (kg/s)
0	173	1327	-	-	-	-
10	208.2	1628	-	-	-	-
14	225.4	1860	-	-	-	-
16	279.2	1996	-	-	-	-
17	290.8	2016	219	2905	-	-
18	**299.3**	2031	224.9	2976	224	3740
19	281	2060	233.7	2957	-	-
20	253.3	2020	246	2948	-	-
20.5	-	-	249.7	2925	-	-
21	-	-	**285.5**	2781	228	4060
21.5	-	-	265.6	2462	-	-
22	-	-	261.5	2416	-	-
23	-	-	-	-	256.4	4053
24	-	-	-	-	**309**	3576
25	231	1791	240	2056	280.9	3403
40	224.1	913	-	-	-	-

With impeller and rectangular baffle (no pump):
Arch flow = 234.3 kg/s Main hearth circ. = 568 kg/s

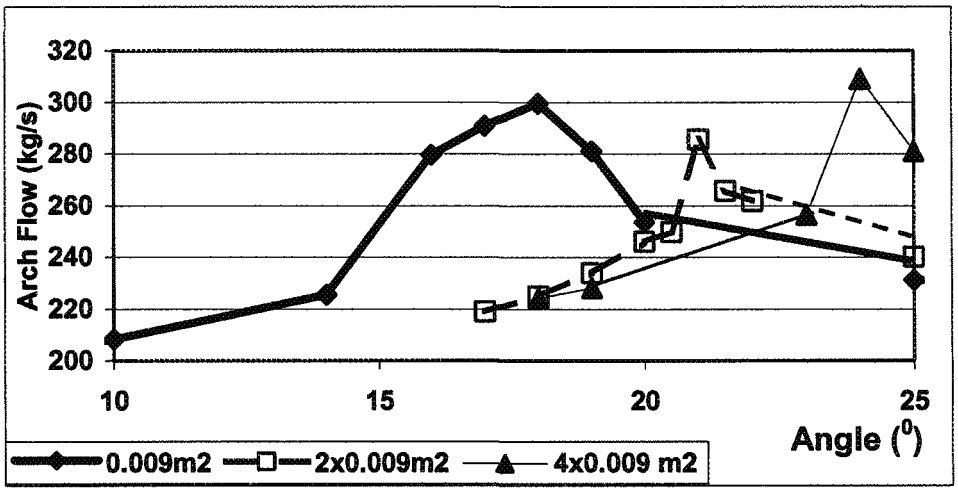

Figure 2.18 : Effect of Pump Discharge Area on Arch Flow.

2.4.5 Effect of the Liquid Metal Height

Liquid metal height varies in the furnace with time. As the melting is carried out, the metal level increases. At a regular time interval (about every 4-5 hours), approximately 25-30% of the metal is transferred to a holding furnace which means a drop in the metal level in the same order of magnitude (this drop in height is not always proportional to the percentage of metal removed because of the furnace geometry). For an industrial furnace, a number of simulations were carried out at two different metal levels and for three impeller positions in the vertical direction. The results are given in Table 2.7. Figure 2.19 shows the 6" and 12" impeller positions. Figure 2.20 gives a schematic diagram of the furnace.

Table 2.7 : Effect of Liquid Metal Height and Impeller Position on Arch Flow.

Metal height (see Figure 2.19)	Impeller distance from the bottom (see Figure 2.19)	Arch flow (kg/s)
30" (no pump)	6"	137
	9"	129.5
	12"	105*
24" (no pump)	6"	122
30" (with pump)	6"	208.7
	12"	197*
*There is recirculation in the inlet arch near the bottom.		

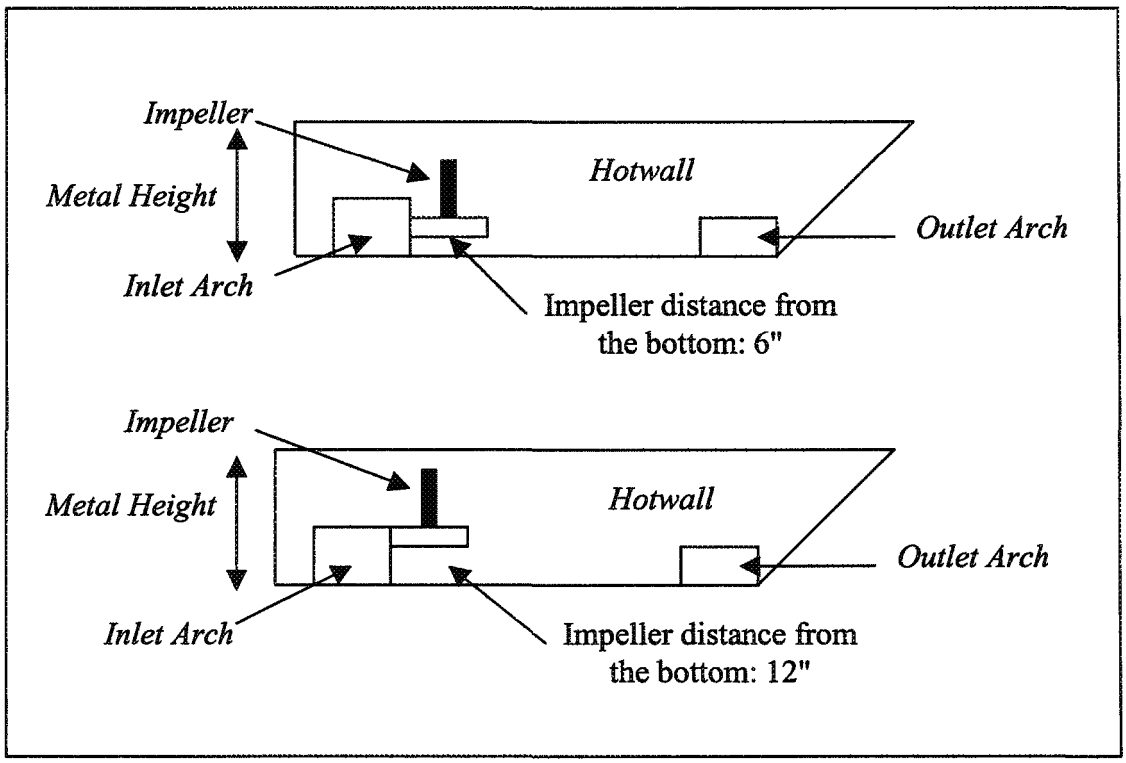

Figure 2.19 : Impeller Positions in the Vertical Direction.

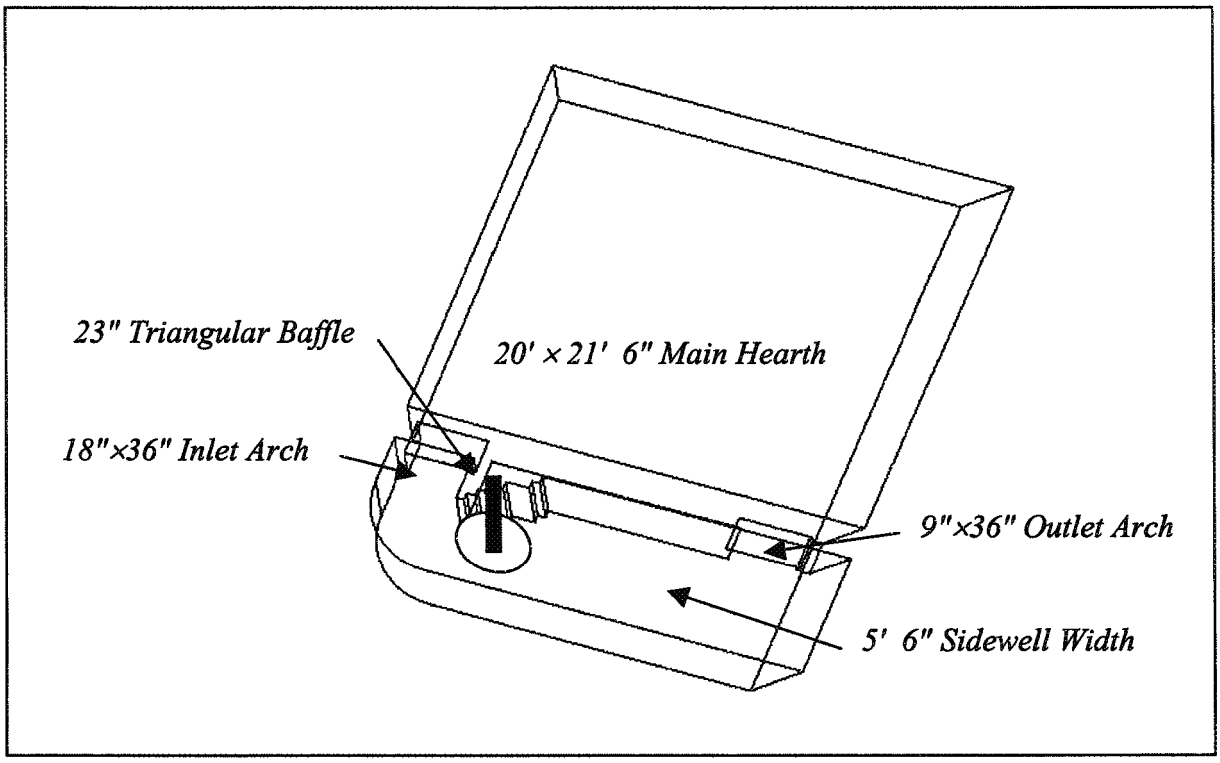

Figure 2.20 : Furnace Used to Study the Effect of Liquid Level.

When the liquid metal level decreases, there is also a decrease in the arch flow for the same impeller position. However, the decrease in arch flow is proportionately less than the decrease in the volume of liquid metal. For example, the arch flow decreases from 137 to 122 kg/s (11%) compared to about 21% decrease (30" to 24") in liquid volume for 6" impeller distance. This gives higher velocities throughout the furnace. If a pump is used in the main hearth and directed towards the inlet arch, the arch flow increases significantly (52%).

Sometimes the impeller is moved upwards to submerge the shred quickly and to prevent the accumulation of chips on the liquid surface. This has to be done carefully. As seen in Table 2.7, if the impeller is moved to a position of 12" from the bottom (see Figure

2.19), some return (about 10%) of the metal is observed through the inlet arch. This is not desirable. It may cause the transfer of certain components such as dross to the main hearth. It also reduces the melt rate due to the return of the hot metal.

2.4.6 Effects of Separator Wall and Blockage Above the Inlet Arch in the Sidewell

Simulations were carried out to determine the effect of a separator wall in the sidewell and a blockage above the inlet arch. A schematic diagram of the furnace is shown in Figure 2.21, and the results are given in Table 2.8. There is also an impeller and a triangular baffle in the side well. The length of the blockage is the same as the length of the baffle. The additional arch in the side-well separator wall is 30" wide and 22" high.

With only a triangular baffle and an impeller (80 rpm), the arch flow is 206.7 kg/s. Addition of a pump increases this value significantly as discussed previously. When a blockage is added on top of the inlet arch without the pump, the arch flow slightly decreases (to 199 kg/s, 3.7%). Onto this, if a separator wall is added in the side well, a considerable increase from 199 kg/s to 262.5 kg/s is obtained. The separator wall with an additional arch acts in a way similar to the baffle. The arch flow increases due to the new configuration, which gives direction to liquid metal, resulting in more favorable flow conditions.

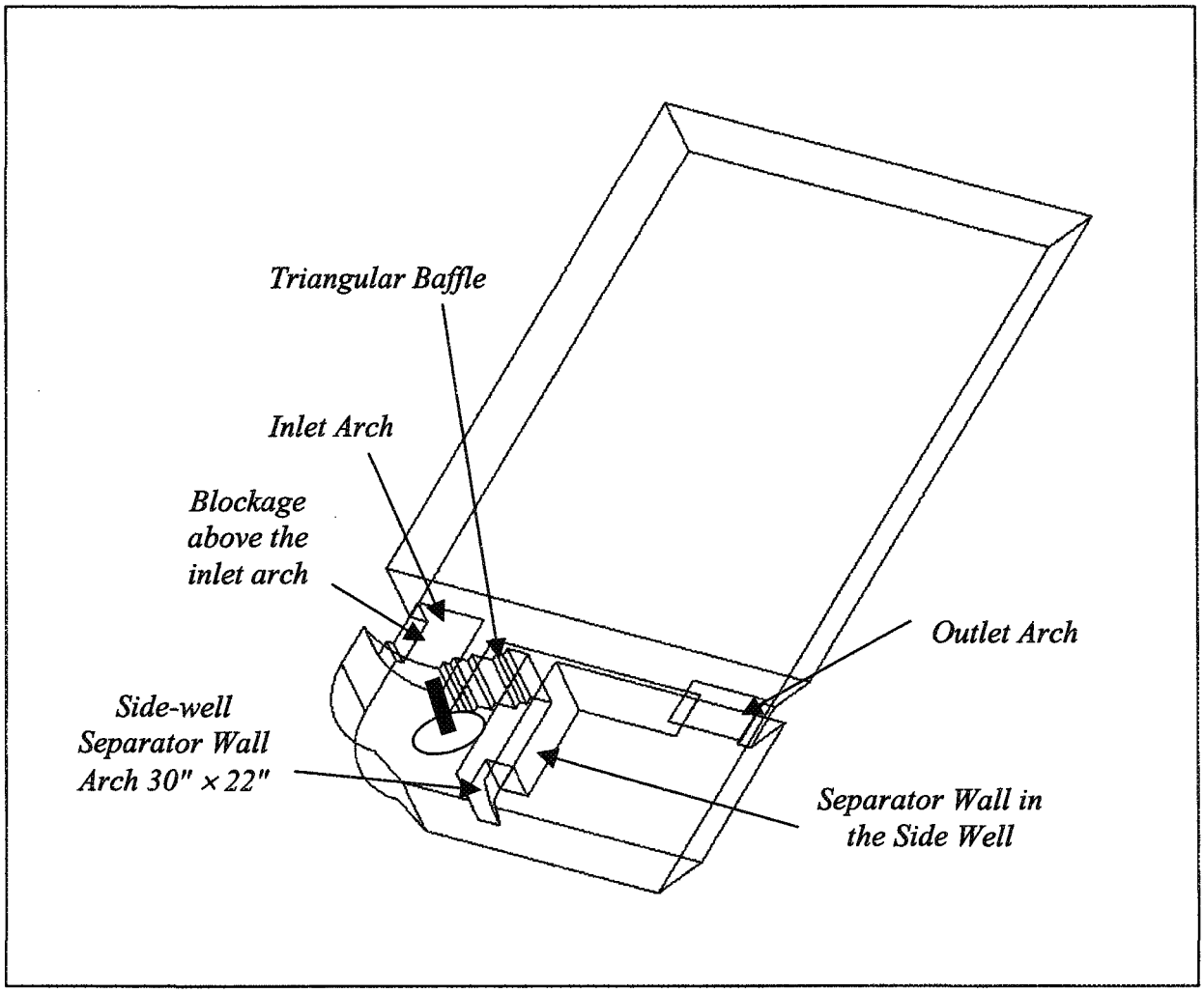

Figure 2.21 : A Schematic Diagram of the Furnace Used to Study the Effects of Side-Well Separator Wall and the Blockage Above the Inlet Arch.

Table 2.8 : Effects of Separator Wall and Blockage Above the Inlet Arch in the Side Well.

Configuration	Arch flow (kg/s)	Main hearth circulation (kg/s)
Triangular baffle, Impeller (80rpm)	206.7	487
Triangular baffle, Impeller (80rpm) Pump (5.5 m/s, 16°)	261.3	1900
Triangular baffle, Impeller (80rpm) Blockage above inlet arch	199	472
Triangular baffle, Impeller (80rpm) Blockage above inlet arch Separator wall in side well	262.5	617
Triangular baffle, Impeller (50rpm) Blockage above inlet arch Separator wall in side well	163.7	385
Triangular baffle, Impeller (80rpm) Blockage above inlet arch Separator wall in side well Pump (5.5 m/s, 16°)	293.8	2040
Triangular baffle, Impeller (50rpm) Blockage above inlet arch Separator wall in side well Pump (5.5 m/s, 16°)	232.9	1846
Triangular baffle, Impeller (80rpm) Blockage above inlet arch Separator wall in side well Pump (5.5 m/s, 18°)	269.8	1989
Triangular baffle, Impeller (80rpm) Blockage above inlet arch Separator wall in side well Scrap metal	277	667
Triangular baffle, Impeller (80rpm) Blockage above inlet arch Separator wall in side well Scrap metal Pump (5.5 m/s, 16°)	299	2112

The results also indicate that when a pump is added, the arch flow increases. The impeller rotational speed is important; when it is decreased to 50rpm from 80rpm, significant reduction in arch flow is observed. Addition of solid charge (scrap) in the side

well increases the arch flow slightly (from 262.5 kg/s to 277 kg/s) by reducing the area for metal flow without increasing the resistance.

2.4.7 Effect of Inlet Arch Size

Simulations were done to determine the effect of inlet arch dimensions on metal flow. The results are given in Table 2.9 and Figure 2.22. The area of the arch is the determining factor in arch flow: the larger the area the higher the flow. The resistance to flow decreases as the area increases. A width of 36 inches (914 mm) seems reasonable, given the typical dimensions of a furnace. Therefore, the height can be increased to enlarge the area. However, this has to be done with caution. If the arch is too high, the impeller position may become critical as discussed previously. When the impeller is moved too high in such a situation, there may be a return to main hearth from the side well through the inlet arch. Table 2.9 and Figure 2.22 also show that the main hearth circulation increases with the arch flow as expected.

Table 2.9 : Effect of the Inlet Arch Size on Metal Flow.

Arch dimensions	Arch flow (kg/s)	Main hearth circulation (kg/s)
36"×12" (0.279 m^2)	204.8	498
36"×18" (0.418 m^2)	237.8	581
36"×24" (0.557 m^2)	264.7	647
24"×18" (0.279 m^2)	201.7	492

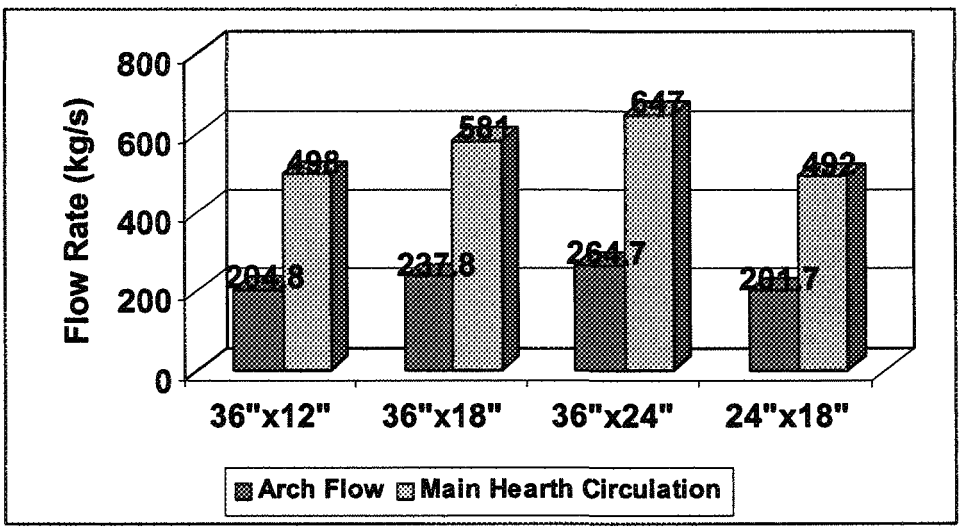

Figure 2.22 : Effect of Inlet Arch Size on Arch Flow and Main Hearth Circulation.

2.4.8 Effect of Outlet Arch Size

The results are presented in Table 2.10 and are similar to those obtained in the previous section. As the area increases, the arch flow increases due to reduced resistance to flow. It is important to have a modest outlet arch height to minimize the transfer of salt and dross from the side well to the main hearth. Therefore, the width could be increased to compensate for a decrease in height. There is a limit, however, as to what extent this can be done. If the height is too small, the metal emerging from the outlet arch will go through the lower and colder section of the metal in the main hearth. This may lead to colder metal temperatures for the flow entering the inlet arch, consequently, lower melting rates or increased metal temperature in the main hearth. The flow fields for four cases in Table 2.10 are shown in Figure 2.24.

Table 2.10 : Effect of the Outlet Arch Size on Metal Flow (Letters in Parentheses Refer to the Cases in Figure 2.24).

Arch dimensions	Arch flow (kg/s)	Main hearth circulation (kg/s)
(A) 36"×14" (0.325 m^2)	237.8	581
36"×9" (0.209 m^2)	166.8	493
(B) 36"×12" (0.279 m^2)	203.1	540
(C) 24"×16" (0.248 m^2)	176.5	524
(D) 48"×9" (0.279 m^2)	208.6	500
24"×9" (0.139 m^2)	100.6	379

2.4.9 Effect of Side-Well Width

One of the important geometrical factors is the width of the side well. The larger the side well is, the more shred could be fed into it. At the same time, larger width means increased surface area and heat loss. Some of the reasonable dimensions have been simulated and the results are given in Table 2.11 and Figure 2.23. These clearly indicate that increase in width increases the arch flow. Narrow side wells (less than approximately 6') do limit the arch flow significantly. Above this value, the effect of width on arch flow is rather moderate (an increase from 6' to 8' in width gives 9.5% increase in arch flow). The main hearth circulation also increases in proportion with the arch flow as well. The flow fields for two cases in Table 2.11 are shown in Figure 2.25.

Table 2.11 : Effect of the Side-Well Width on Metal Flow (Letters in Parentheses Refer to the Cases in Figure 2.25).

Sidewell width	Arch flow (kg/s)	Main hearth circulation (kg/s)
5'	172.1	460
6' (A)	233	567
6' 10"	237.8	581
8' (B)	255.1	623

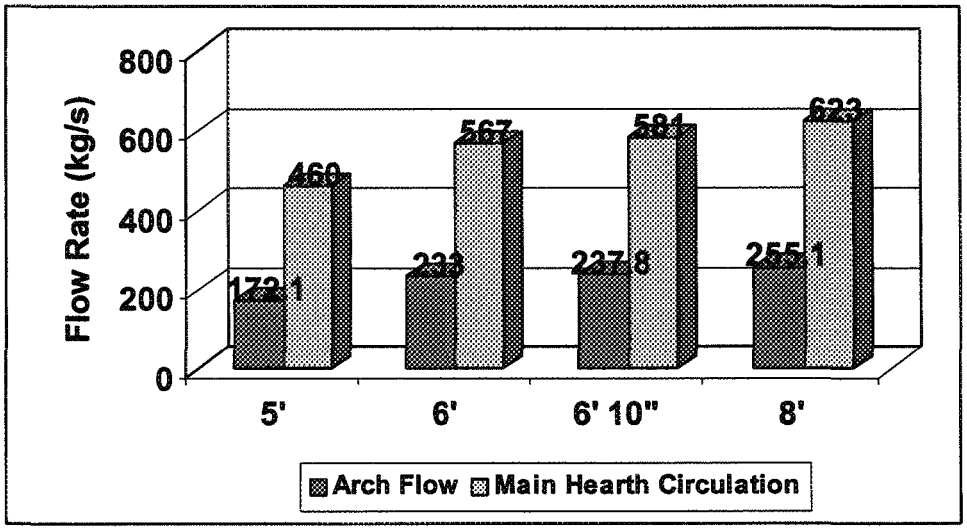

Figure 2.23 : Effect of Side-Well Width on Arch Flow and Main Hearth Circulation.

2.4.10 Effect of the Dimensions of the Main Hearth

Different sizes for the main hearth are used in different plants. In order to study the main hearth dimensions, the simulations in Table 2.12 were carried out. The side-well dimensions were also changed depending on those of the main hearth. The results show that a width-to-length ratio between 0.85 and 1.2 does not seem to affect much the metal flow.

This means that depending on the space available or the need, different main hearth dimensions can be used. When the furnace is square, the main hearth circulation is somewhat higher than in the other cases. When there is no pump in the main hearth, a low velocity zone forms in the center. A square furnace appears to minimize this zone. A long main hearth has approximately the same arch flow as the others, however the main hearth circulation rate is lower (412 kg/s). This is normal since there is more liquid metal (in proportion to the length) in the main hearth. The flow fields for three cases in Table 2.12 are shown in Figure 2.26.

Table 2.12 : Effect of the Dimensions of the Main Hearth on Flow Conditions (Letters in Parentheses Refer to the Cases in Figure 2.26).

Main hearth dimensions (width × length)	Arch flow (kg/s)	Main hearth circulation (kg/s)
19' 2" × 22' 10" (A)	237.8	581
20' 11" × 20' 11" (B)	239	619
22' 10" × 19' 2" (C)	239.6	607
19' 2" × 30'	236.3	412

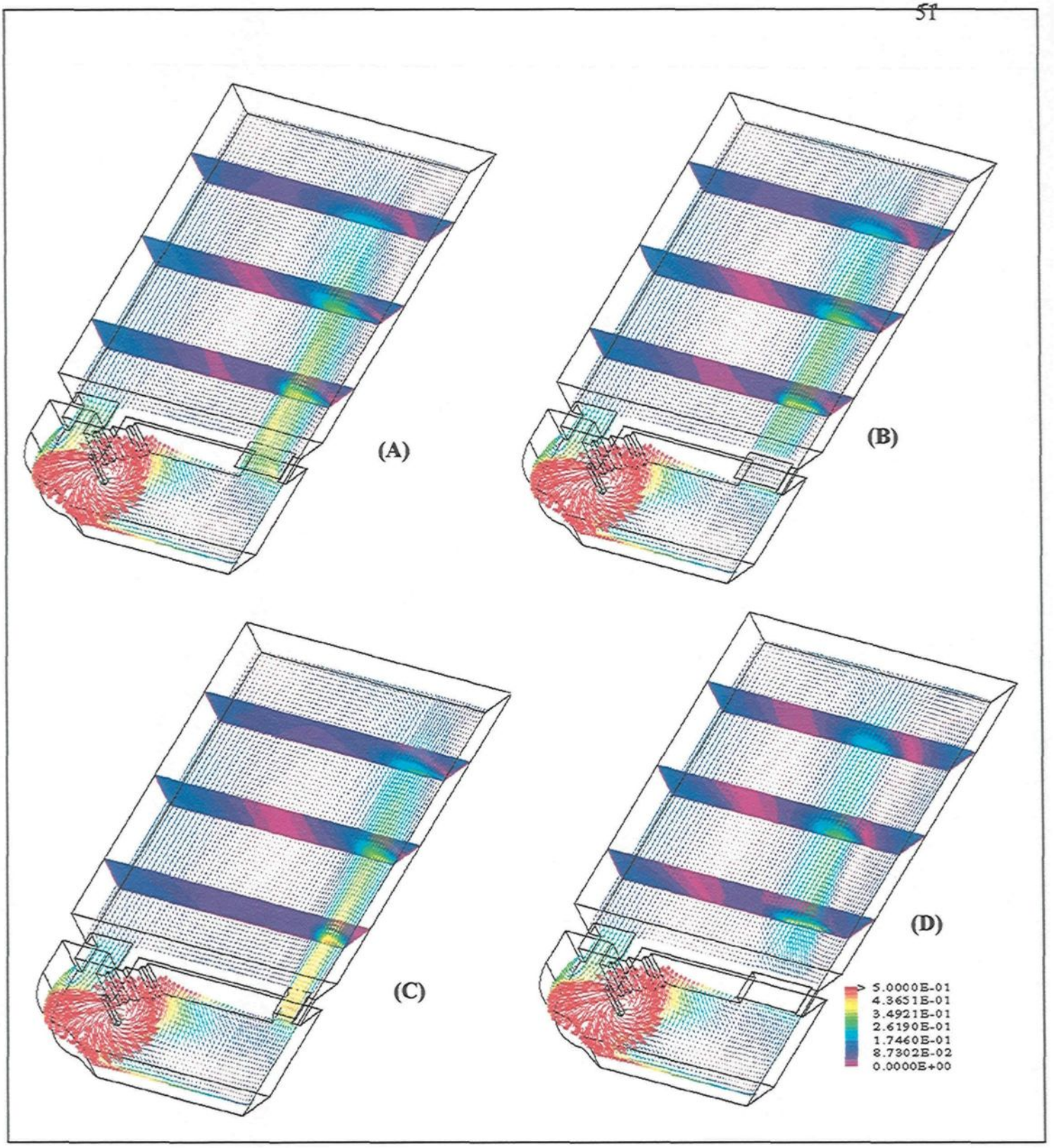

Figure 2.24 : Effect of the Outlet Arch on the Flow Field at 0.24m from Bottom (Letters Indicate the Cases Given in Table 2.10 and Velocities are in m/s).

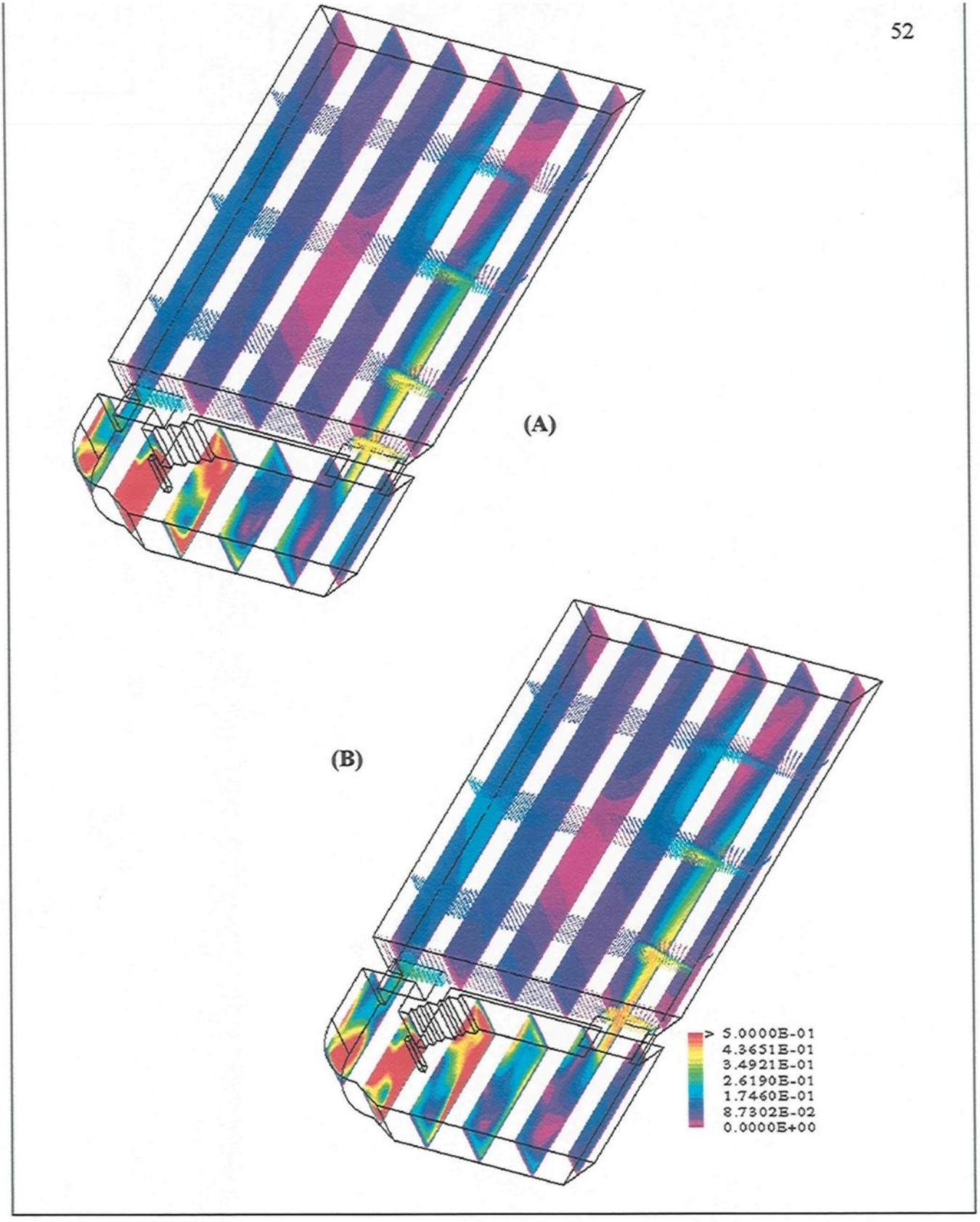

Figure 2.25 : Effect of the Side-Well Width on the Flow Field (Letters Indicate the Cases Given in Table 2.11 and Velocities are in m/s).

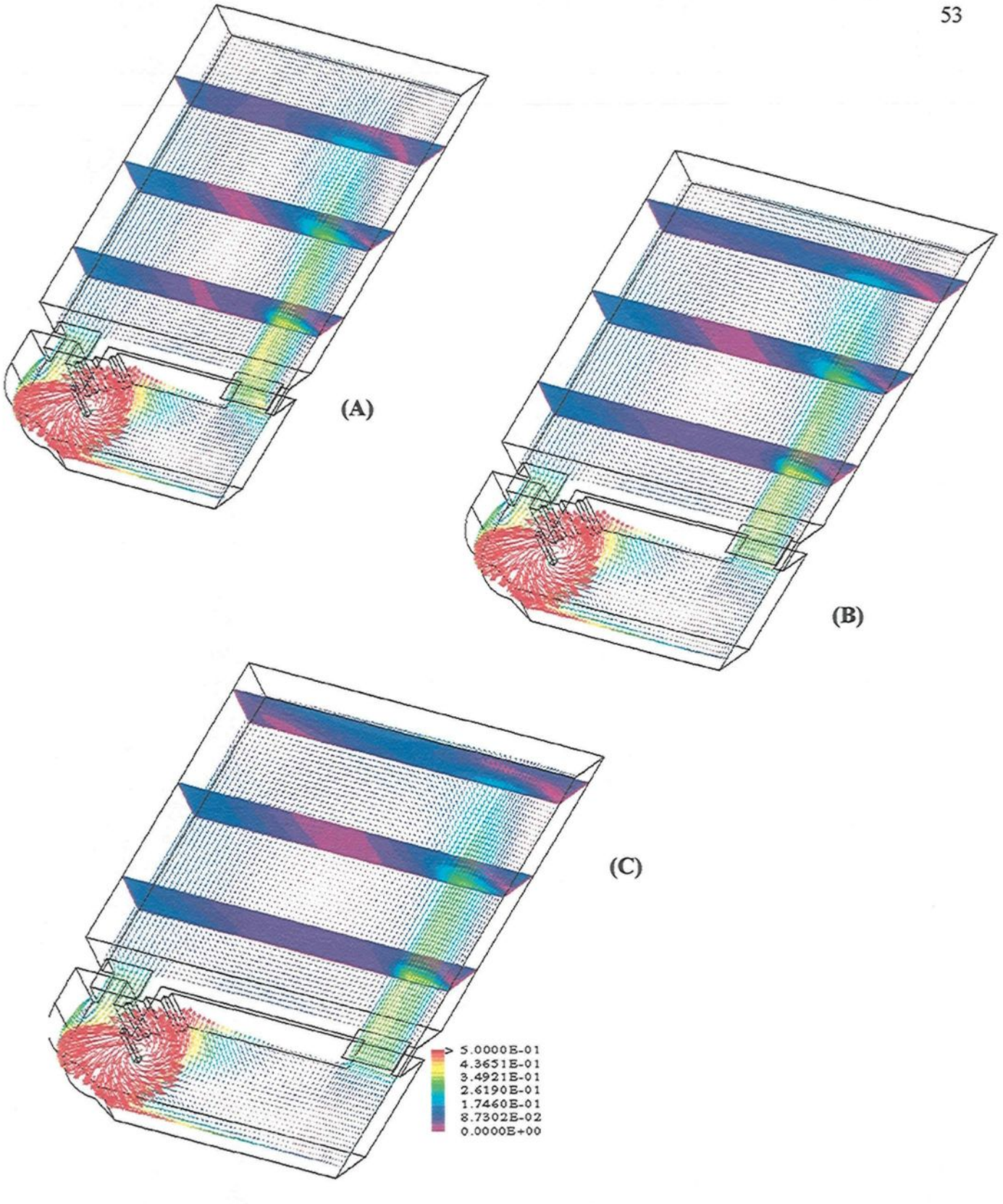

Figure 2.26 : Effect of the Main Hearth Dimensions on the Flow Field at 0.24m from Bottom (Letters Indicate the Cases Given in Table 2.12 and Velocities are in m/s).

2.4.11 Effect of the Sidewell Configuration

Two modifications to side-well geometry were simulated. These are shown in Figure 2.27, and the results are presented in Table 2.13. In the first one, the expanding section of the side well was removed (see Figure 2.27 a). The dotted line shows the original configuration and the solid line the modified one. This results in a decrease in the metal flow through the arches, however, the decrease is not significant (3.6%). Removal of the expanding section effectively reduces the side-well width from 6' 10" to 6'. Such a reduction has little effect on the arch flow as discussed in Section 2.4.9 (see also Table 2.11). Therefore, as long as the side well is large enough, an expending section does not appear to contribute much to the furnace performance.

The second modification tested was the round corner on the metal inlet side as shown in Figure 2.27 b. Again, the dotted line shows the original configuration and the solid line the modified one which is the square geometry. Here the reduction is quite significant (12.3%). The round entry clearly results in more favorable flow conditions.

Table 2.13 : Effect of Side-Well Configuration on Metal Flow Through the Arches (kg/s). The Percent Decrease With Respect to the Original Configuration is Shown in Parentheses.

Length of rectangular baffle	Original configuration	Without expansion (Figure 2.27 a)	Square corner (Figure 2.27 b)
0.5 m (19.4")	234.3	225.8 (3.6%)	205.4 (12.3%)

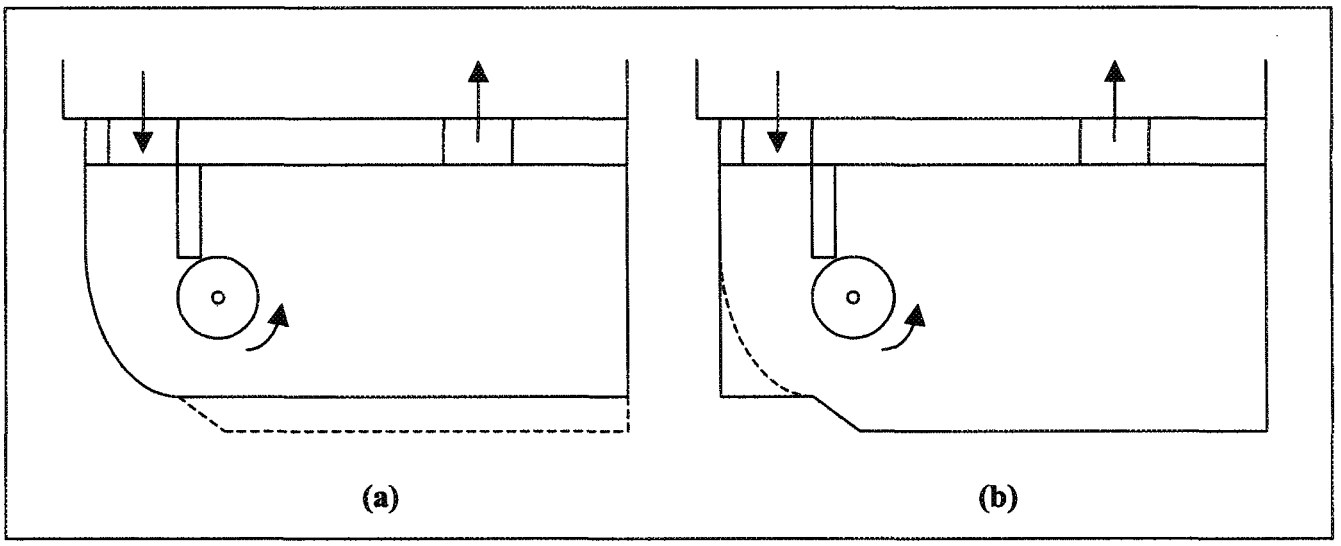

Figure 2.27 : Modifications to Side-Well Geometry: (a) Removal of Expanding Section, and (b) Square Corner Instead of Round One.

2.5. Conclusions

A three-dimensional model has been developed to simulate the metal flow in sidewell furnaces. The following conclusions can be drawn from the various simulation results:

2.5.1 For the impeller and the baffle

1. There is an optimum position for the impeller. When the impeller is shifted away from this position, the metal flow rate through the arches decreases. Even a partial reversal of flow in the inlet arch may occur at certain positions.
2. There is also an optimum baffle length which is about one third of the width of the side well. The metal flow through the arches decreases if the baffle length is shorter or longer than the optimum value.
3. The metal flow rate through the arches is higher for the rectangular baffle compared to the triangular baffle. Also, when the impeller is not in its optimum position, the penalty (decrease in metal flow) is higher when the triangular baffle is used.

2.5.2 For the arches

1. The flow field in the main hearth may be modified by changing the arch design (the height and width).
2. The metal flow through the arches depends on the arch sizes: the larger the arch (inlet or outlet) the higher the flow. This is a direct result of the resistance created by the arch size.
3. Too high an inlet arch may favor partial flow reversal within the inlet arch if the impeller is shifted up to a high level.

4. When the level of the liquid bath is lower, the metal flow rate through the arches decreases. However, the relative decrease in this flow rate is less than the relative decrease in the liquid volume in the main hearth. Therefore, the stirring in the main hearth somewhat increases as the liquid level drops.

2.5.3 For the pump

1. With the addition of a pump, the metal flow through the arches increases, and this increase depends on the momentum provided by the pump. The major impact of the pump is the significant increase of stirring in the main hearth.

2.5.4 For the overall dimensions of the furnace

1. The increase in the width of side well increases the metal flow through the arches.
2. The length-to-width ratio of the main hearth does not affect the metal flow significantly, if this ratio is not too far from one (0.85 to 1.2).

When all the simulation results are considered, clearly the trends predicted by the model are similar to those observed in the plant (plant tests) and in the laboratory (water model).

CHAPTER 3

COMBUSTION CHAMBER MODELLING

3.1 Introduction

Many physical processes occur in a combustion chamber. Energy released by the combustion of fuel heats up the product gas to high temperatures. Then heat is transferred from these hot combustion products to cold sink surfaces by conduction, convection and more importantly by radiation. The flow field plays an important role in determining the combustion rate and, consequently, the temperature and heat flux distributions. At the same time, combustion and heat transfer processes affect the flow field. In order to analyse such systems, all these mechanisms have to be considered simultaneously.

The above phenomena and their interactions are governed by the design of the system and the operating conditions. A rigorous combustion chamber analysis requires detailed modelling of the momentum, heat and mass transfer processes with special attention to turbulent combustion and radiative heat transfer[34-36]. These models give detailed information, but they usually require longer computation times. Many engineering problems call for much simpler models which could yield answers in a relatively short time. The approach to be used depends on the purpose of the modelling work.

In simple models, the complex reacting flow is simplified by assuming a well-mixed or a plug-flow system. The plug flow assumption can be used only for very long

furnaces. The well-mixed furnace model, however, can be applied to many industrial furnaces after certain modifications which allow for more realistic simulations.

In the well-mixed furnace model, it is assumed that the combustion gas in the enclosure is completely mixed, therefore no gradient exists in the gas and gas properties are uniform throughout the system. In furnaces with vigorous mixing (due to high momentum air or fuel jets) and dimensions not too different from each other (similar length, height and width), the conditions may approach those of a well-mixed chamber. In this case, the exit gas temperature is the same as the radiating gas temperature. However, the well-mixed model underpredicts the heat transfer since the actual radiating gas temperature is normally much higher than the exit gas temperature. This problem can be improved by differentiating the two temperatures and assigning a higher value to the radiating gas temperature. The model can be further extended to systems containing different types of walls by making allowance for heat transfer to more than one heat sink surface[37-38]. The well-mixed furnace models with such modifications which lead to more realistic predictions are usually referred to as the "one-gas-zone models".

In sidewell furnaces, there are two different types of surfaces: the metal surface and the refractory surface. The refractories re-radiate most of the heat they absorb and a relatively small percentage is lost to the surroundings. In this project, a one-gas-zone model was developed and adapted to sidewell furnaces. The model is presented in the next section. A more detailed discussion on combustion chamber modelling is given in Appendix 5.

3.2 One-Gas-Zone Model

In this model, the gas is assigned an average radiation temperature, and it takes a value between the adiabatic flame temperature ($T_{ad.fl.}$) and the gas exit temperature (T_e) based on a weighting factor (a_T):

$$T_g = a_T\, T_e + (1 - a_T)\, T_{ad.fl.} \qquad [3.1]$$

When a_T=1, the gas is well mixed and the gas exit temperature becomes equal to the radiating gas temperature. If a_T=0, there is no mixing and the gas radiates at the adiabatic flame temperature which, of course, is not possible. The weighting factor depends on the furnace design and the operating conditions; therefore, it is furnace specific. In the present study, a value of 0.75 for a_T gave reasonable predictions for the sidewell furnaces.

Total heat input to the furnace (Q_{in}) is given by (fuel is natural gas which was considered as methane):

$$Q_{in} = m_f\, \Delta H_{fuel} + m_f\, C_{p,f}\, (T_{fuel} - T_{amb}) + m_{air}\, C_{p,air}\, (T_{air} - T_{amb}) \qquad [3.2]$$

T_{amb} is also used as the reference temperature. The air flow rate is determined from the percent excess air and the stoichiometry of the combustion reaction. The adiabatic flame temperature is calculated from:

$$Q_{in} = m_{prod}\, C_{p,prod}\, (T_{ad.fl.} - T_{amb}) \qquad [3.3]$$

The overall energy balance for the gas in the enclosure is:

$$Q_{in} = Q_{ref} + Q_{dir} + Q_{exit} \qquad [3.4]$$

Q_{ref} is the heat transferred to the refractory surface by convection ($Q_{ref,con}$) and radiation ($Q_{ref,rad}$); Q_{dir} is the heat transferred directly from gas to the metal surface by radiation ($Q_{dir,rad}$) and convection ($Q_{dir,con}$); and Q_{exit} is the heat loss at the chimney due to the combustion products leaving the system. The energy balance for the refractory surface is given by:

$$Q_{ref} = Q_{ind} + Q_{loss} \qquad [3.5]$$

The heat absorbed by the refractory is partly lost through the wall (Q_{loss}), and the rest is transferred to the metal surface by radiation (Q_{ind}). The transient effects were not taken into account. However, transient effects can be neglected for the purpose of this part of the project which is to carry out a parametric study in the combustion chamber. The transient effects are significant when the temperature variation is important and have to be considered in the energy balance.

The model solves the above equations simultaneously to calculate the variables given in Figure 3.1 and Table 3.1. Total heat transfer to the metal surface Q_{met} is the sum of direct and indirect components:

$$Q_{met} = Q_{ind} + Q_{dir} \qquad [3.6]$$

The overall energy balance for the furnace requires that:

$$Q_{in} = Q_{met} + Q_{exit} + Q_{loss} \qquad [3.7]$$

The thermal efficiency of the furnace is defined as the total heat transferred to metal surface divided by the total heat input:

$$\eta = Q_{met} / Q_{in} \qquad [3.8]$$

Simulations have been carried out to determine the effects of different parameters on furnace performance based on the above model[39]. The values for the Base Case are given in Table 3.1. The results are presented in Table 3.2 and discussed in the next section. The details of the one-gas-zone model are presented in Appendix 5.

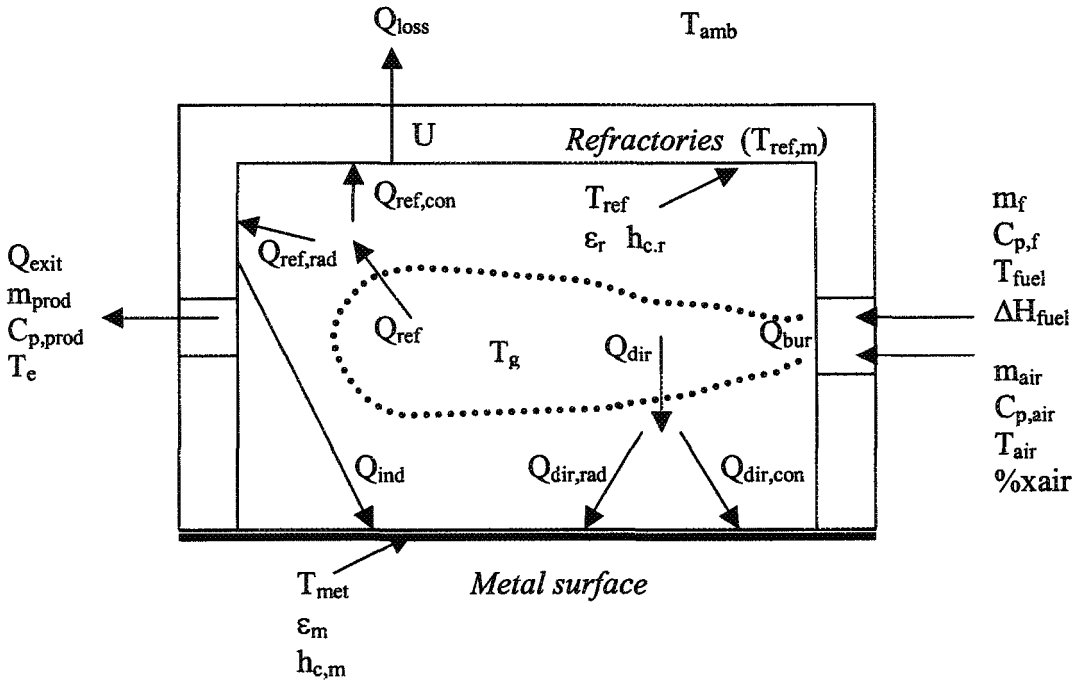

Figure 3. 1: Schematic Representation of the Combustion Chamber and Model Parameters (Definitions are Given in Table 3.1)

Table 3.1 : Description of the Model Parameters for the Combustion Chamber, Values for the Base Case, and Definitions of Some of the Variables Given in Table 3.2.

- Mass flow rate of fuel (m_f) : 0.1 kg/s
- Heat of combustion (ΔH_{fuel}) : 40 MJ/kg of CH_4
- Chamber dimensions : 6.96 × 5.84 × 1.5 m
- Emissivity of refractory (ϵ_r) : 0.6
- Emissivity of metal surface (ϵ_m) : 0.6
- Overall heat transfer coefficient (U) : 2 W/m^2 K (for heat loss between the inside surface temperature of the refractory and the ambient temperature)
- Convective heat transfer coefficient ($h_{c,m}$) : 20 W/m^2 K (for metal surface)
- Convective heat transfer coefficient ($h_{c,r}$) : 10 W/m^2 K (for refractory surface)
- Maximum refractory temperature ($T_{ref,m}$) : 1100°C
- Metal surface temperature (T_{met}) : 750°C
- Inlet air temperature (T_{air}) : 27°C
- Inlet fuel temperature (T_{fuel}) : 27°C
- % excess air (%xair) : 10%
- Burner power (Q_{bur}) : $m_f \times \Delta H_{fuel}$ (MW)
- Percent direct radiative transfer to metal, $\%Q_{dir,rad}/Q_{dir}$
- Percent total radiative transfer to metal, $\%(Q_{dir,rad}+Q_{ind})/Q_{met}$
- Percent direct component of total heat transfer to metal, $\%Q_{dir}/Q_{met}$
- Percent chimney loss based on total heat input, $\%Q_{exit}/Q_{in}$
- Percent heat loss to surroundings based on total heat input, $\%Q_{loss}/Q_{in}$
- Percent heat loss to surroundings based on heat transfer to refractories, $\%Q_{loss}/Q_{ref}$
- Percent convective transfer to refractories, $\%Q_{ref,con}/Q_{ref}$
- Gas radiation temperature (T_g)
- Refractory temperature (T_{ref})
- Exit gas temperature (T_e)
- Adiabatic flame temperature ($T_{ad.fl.}$)
- Heat flux on the metal surface (q_{met}) : Q_{met}/(metal surface area) (W/m^2)
- Percent difference from Base Case: $\%(Q_{met(Case\ i)}-Q_{met(Base\ Case)})/\ Q_{met(Base\ Case)}$
  A negative value indicates a lower heat transfer to the metal surface, and a positive value shows a higher heat transfer to the metal surface.

3.3 Results and Discussion

The simulation results are presented in Table 3.2. Due to the large number of variables, the table is given in three parts. Some of the columns are repeated to be able to compare the results better. Each series of simulations is separated by darker solid lines. The refractory temperature T_{ref} is the average value for the entire refractory surface. The temperature $T_{ref,m}$ is the maximum set value and, in plants, it is measured by a thermocouple placed in the roof of the combustion chamber (the roof is hotter than the rest of the refractory). In the model, T_{ref} is constrained to an upper limit at 50°C below $T_{ref,m}$. This accounts for the temperature distribution on refractory surface. If the refractory exceeds the maximum temperature, the fuel flow rate is reduced untill the refractory temperature is reduced to allowable maximum level. The overall energy balance is checked after the calculations are done; the error in above simulations is less than 0.2%. This error can be reduced by simply decreasing the error tolerance. Further accuracy is not of interest for the present project.

In Cases 2 to 4, the effect of convective heat transfer coefficient is studied (see Figure 3.2). For the Base Case, the coefficient for the metal surface is taken as 20 W/m^2K. Values varying between 15 to 20 W/m^2K were found from different correlations. Since the burner is usually directed towards the metal surface, the higher value was chosen. It is seen in these cases that a significant increase in the coefficients yields only a marginal increase in heat transfer to metal. It should also be noted that it is not easy to achieve such increases in the convective heat transfer coefficients without making considerable changes in design.

Cases 5 and 6 examine the effect of percent excess air (see Figure 3.3). When excess air is reduced to zero, 13% increase in heat transfer to metal is obtained. In practice, excess air is always needed to achieve complete combustion in the chamber. Too much excess air reduces the heat transfer (12.3% decrease for an increase from 10 to 20% excess air). Evidently, the excess air should be reduced as much as possible.

Case 7 looks at the effect of metal surface temperature (see Figure 3.4). When it is increased by 50°C, the heat transfer to metal decreases by 5.7%. This is due to the decrease in the temperature difference between the gas and metal surface which is the driving force for the heat transfer. It also shows the importance of maintaining a well-mixed liquid metal bath with as little vertical temperature gradient as possible so as to yield a lower surface temperature.

Cases 8 and 9 show the effect of increasing the surface emissivities (see Figure 3.5). Increase in metal surface emissivity has an important impact on heat transfer to metal (6% for an increase from 0.6 to 0.8). The refractory emissivity has a marginal effect. The same increase in refractory emissivity (an increase from 0.6 to 0.8) results in only 0.1% increase in heat transfer to metal. It is very difficult to change these variables in practice.

In Cases 10 to 12, the fuel flow rate is increased (see Figure 3.6). The heat transfer to the metal surface increases considerably (31.2%, 56.1% and 76.2% for 50%, 100% and 150% increase in fuel flow rates, respectively), however the thermal efficiency of the furnace decreases.

In Cases 13 to 16, the air temperature is 627°C instead of 27°C (see Figure 3.7). The heat transfer to the metal as well as the furnace thermal efficiency increase significantly.

This shows the importance of preheating the combustion air which is the case with regenerative burners. Such augmentation in heat transfer is achieved due to the increase in the gas temperature. The refractory temperature increases along with the gas temperature and may reach the maximum limit which, in turn, restricts the fuel flow rate. This is seen in Cases 14 and 15; the fuel flow rate is less than the initially specified value. Therefore, it is important to set this limit as high as physically possible to be able to increase fuel flow rate if necessary.

Cases 17 and 18 show the effect of overall heat transfer coefficient through the refractory wall (see Figure 3.8). Doubling the coefficient reduces the heat transfer to metal by 6.7%. Obviously, the walls should be insulated as much as possible to reduce this heat loss. If there were no heat loss, the heat transfer to metal would increase by the same percentage.

In Cases 19 to 21, the combustion chamber is larger (the surface area was increased and the height was kept constant). Larger surface area gives higher heat transfer rate to metal. Thermal efficiency of the furnace increases. The heat flux, though, decreases. Larger combustion chamber means more fuel can be burned. This, again, is a question of changing design and increasing furnace size.

In Table 3.2, the temperatures and the components of heat transfer (in percentages) are presented in detail. The results indicate that direct transfer from the gas to the metal is in the order of 60 %. The remaining 40% comes via the refractories indirectly. This shows that both components are significant. Also the radiation accounts for ~75-80% of direct transfer and ~85-90% of total transfer to the metal surface. Heat loss through the refractory

walls is about 3-4% of the total heat input. Wall heat loss as percent of the total heat transfer (convection and radiation) to the refractory surfaces is in the order of 10-14%. This value is similar to the heat transfer from the gas to the refractory surfaces by convection as expected. Figure 3.9 shows the heat transfer rates based on a burner input (energy input) of 100% as the basis for a typical condition. Depending on the operating conditions, these percentages changes as shown by the Table 3.2.

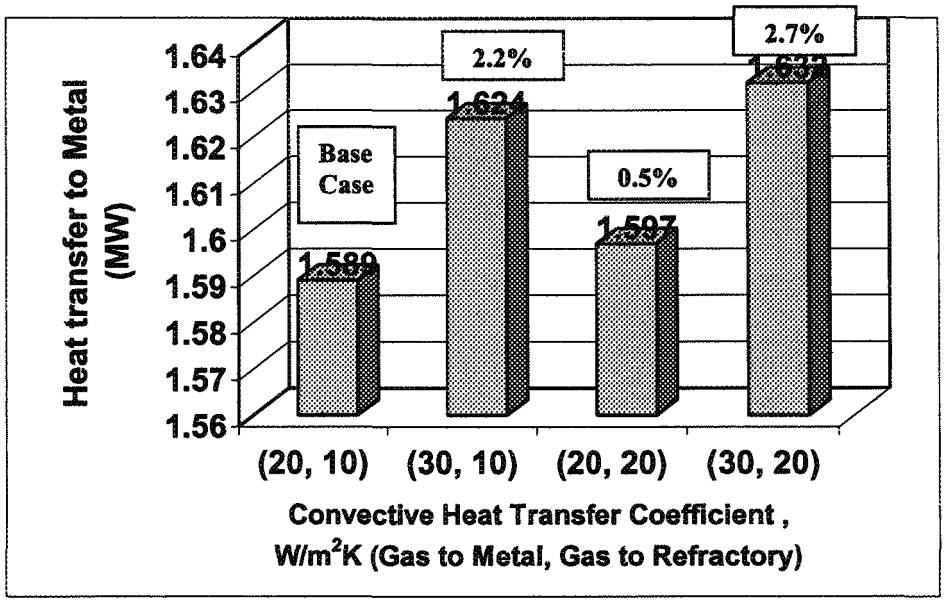

Figure 3.2 : Effect of Convective Heat Transfer Coefficient on Heat Transfer to Metal (Numbers in Parentheses Indicate the Coefficients: First One Gas to Metal, Second One Gas to Refractory)

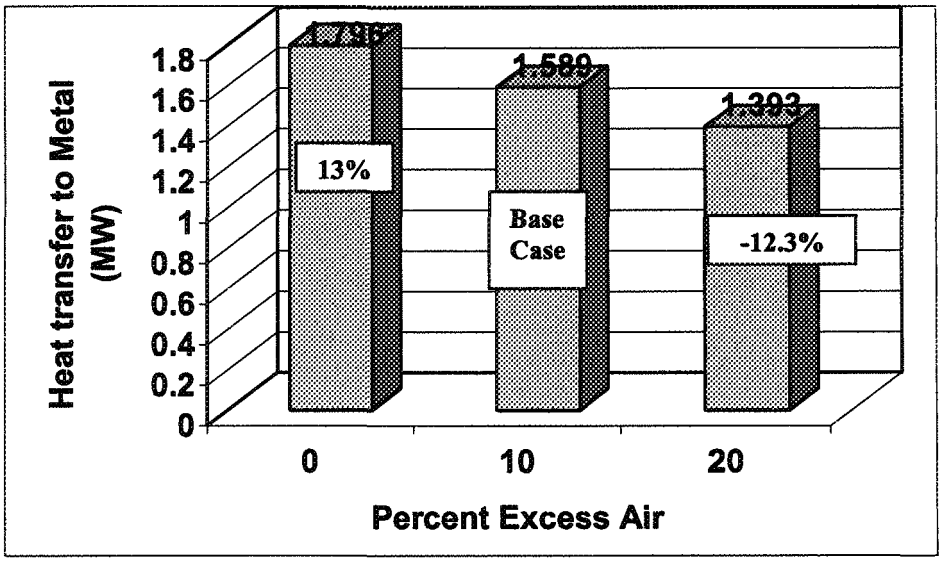

Figure 3.3 : Effect of Percent Excess Air on Heat Transfer to Metal

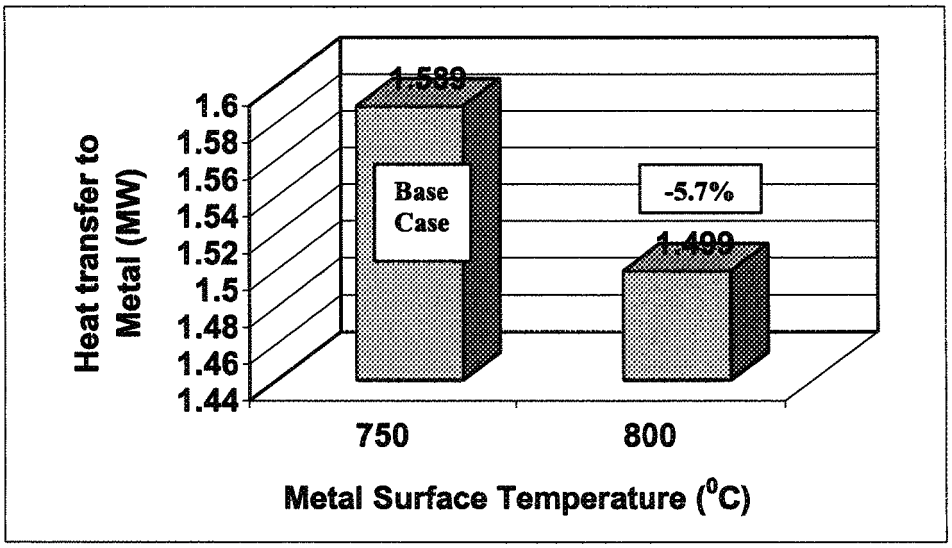

Figure 3.4 : Effect of Metal Surface Temperature on Heat Transfer to Metal

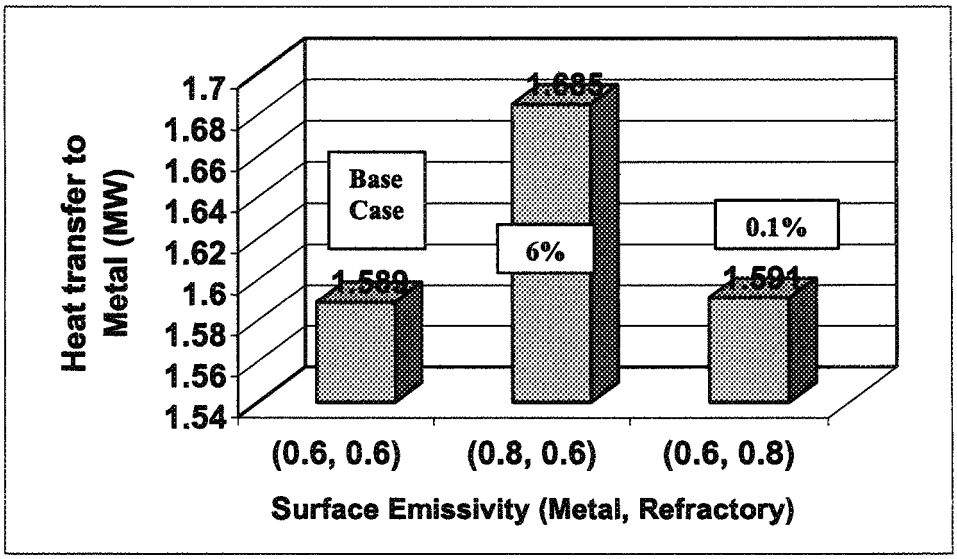

Figure 3.5 : Effect of Surface Emissivity on Heat Transfer to Metal (Numbers in Parentheses Indicate the Emissivities: First One is the Metal Surface Emissivity, Second One is the Refractory Surface Emissivity).

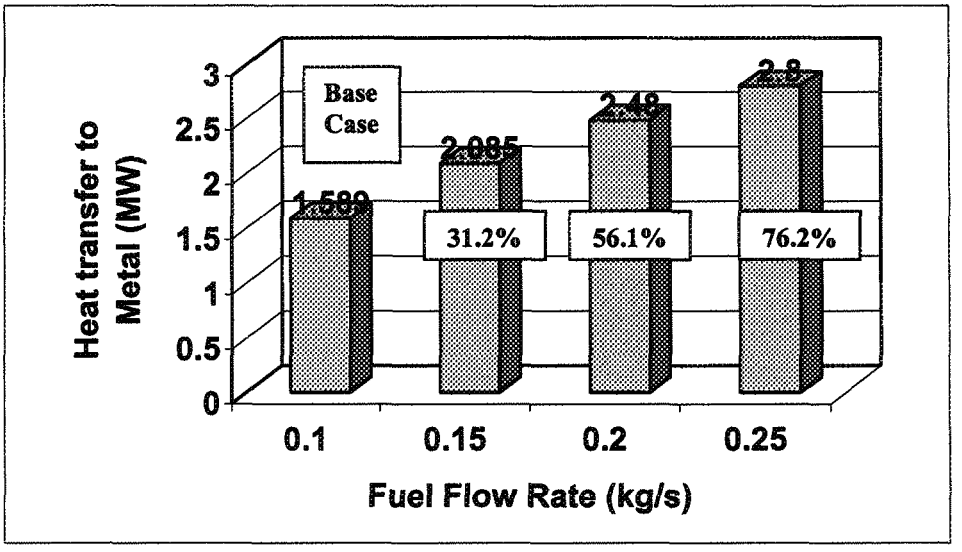

Figure 3.6 : Effect of Fuel Flow Rate on Heat Transfer to Metal

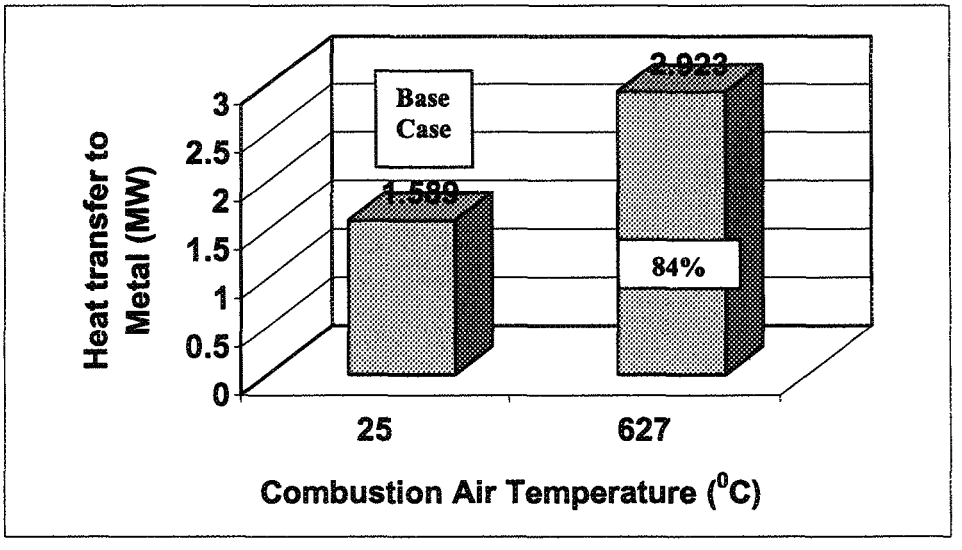

Figure 3.7 : Effect of Combustion Air Temperature (i.e. Preheating Air) on Heat Transfer to Metal

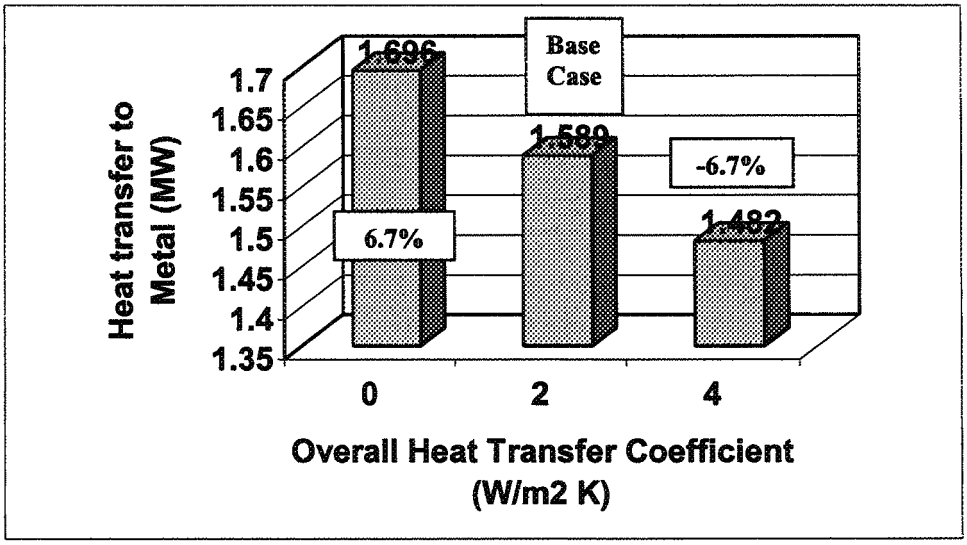

Figure 3.8 : Effect of Overall Heat Transfer Coefficient on Heat Transfer to Metal

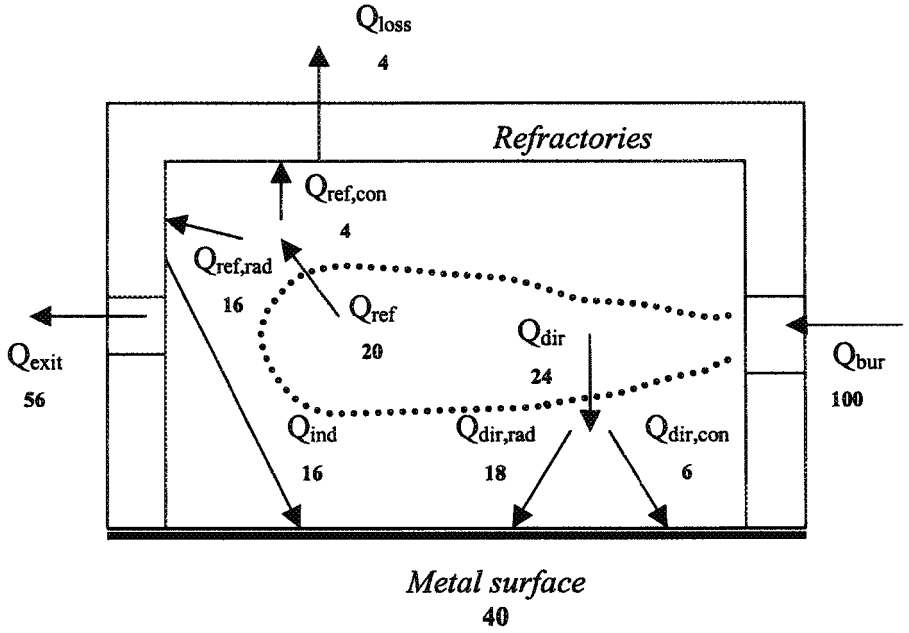

Figure 3.9 : Various Heat Transfer Rates in the Combustion Chamber Based on 100% as the Heat Input by the Burner for a Typical Operation (These Percentages Vary Depending on the Conditions).

Table 3.2 : Results of the Simulations.

Case no.	Difference in specifications	Q_{met} (MW)	% difference from Base Case	q_{met} (W/m^2)	η(%)	m_f (kg/s) (allowed by model based on max. ref. temperature)	T_{ref} (°C)
1	Base	1.589	0.0	39070	39.7	0.1	909
2	$h_{c,m}$=30	1.624	+2.2	39940	40.6	0.1	903
3	$h_{c,r}$=20	1.597	+0.5	39280	39.9	0.1	913
4	$h_{c,m}$=30 $h_{c,r}$=20	1.632	+2.7	40140	40.8	0.1	907
5	%xair=0	1.796	+13.0	44180	44.9	0.1	927
6	%xair=20	1.393	-12.3	34260	34.8	0.1	891
7	T_{met}=800	1.499	-5.7	36870	37.5	0.1	936
8	ϵ_m=0.8	1.685	+6.0	41430	42.1	0.1	876
9	ϵ_r=0.8	1.591	+0.1	39120	39.8	0.1	909
10	m_f=0.15	2.085	+31.2	51270	34.7	0.15	948
11	m_f=0.20	2.480	+56.1	60990	31.0	0.2	977
12	m_f=0.25	2.800	+76.2	68860	28.0	0.25	999
13	T_{air}=627	2.923	+84.0	71890	53.4	0.1	1007
14	T_{air}=627 m_f=0.15*	3.606	+126.9	88680	49.5	*0.133	1050 max
15	T_{air}=627 m_f=0.15* $T_{ref,m}$=1050	2.804	+76.5	68960	54.1	*0.095	1000 max
16	T_{air}=627 m_f=0.15 $T_{ref,m}$=1150	3.916	+146.4	96300	47.7	0.15	1068
17	U=0	1.696	+6.7	41700	42.4	0.1	924
18	U=4	1.482	-6.7	36440	37.0	0.1	892
19	8×6.5×1.5 m_f=0.1	1.698	+6.9	32660	42.5	0.1	885
20	8×6.5×1.5 m_f=0.125	2.002	+26.0	38500	40.0	0.125	906
21	8×6.5×1.5 m_f=0.15	2.278	+43.4	43810	38.0	0.15	923

Case no.	Difference in specifications	Q_{met} (MW)	q_{met} (W/m^2)	$T_{ad.fl.}$ (°C)	T_g (°C)	T_e (°C)	T_{ref} (°C)
1	Base	1.589	39070	1422	1012	875	909
2	$h_{c,m}$=30	1.624	39940	1422	1004	864	903
3	$h_{c,r}$=20	1.597	39280	1422	1010	872	913
4	$h_{c,m}$=30 $h_{c,r}$=20	1.632	40140	1422	1001	861	907
5	%xair=0	1.796	44180	1529	1034	869	927
6	%xair=20	1.393	34260	1330	990	877	891
7	T_{met}=800	1.499	36870	1422	1033	903	936
8	ϵ_m=0.8	1.685	41430	1422	991	847	876
9	ϵ_r=0.8	1.591	39120	1422	1011	874	909
10	m_f=0.15	2.085	51270	1422	1070	953	948
11	m_f=0.20	2.480	60990	1422	1113	1009	977
12	m_f=0.25	2.800	68860	1422	1144	1052	999
13	T_{air}=627	2.923	71890	1876	1156	916	1007
14	T_{air}=627 m_f=0.15*	3.606	88680	1876	1218	998	1050 **max**
15	T_{air}=627 m_f=0.15* $T_{ref,m}$=1050	2.804	68960	1876	1145	901	1000 **max**
16	T_{air}=627 m_f=0.15 $T_{ref,m}$=1150	3.916	96300	1876	1244	1033	1068
17	U=0	1.696	41700	1422	1019	884	924
18	U=4	1.482	36440	1422	1006	867	892
19	8×6.5×1.5 m_f=0.1	1.698	32660	1422	980	832	885
20	8×6.5×1.5 m_f=0.125	2.002	38500	1422	1010	873	906
21	8×6.5×1.5 m_f=0.15	2.278	43810	1422	1037	908	923

Case no.	Difference in specifications	$\%Q_{dir,rad}/Q_{dir}$ (dirct radiationto metal)	$\%(Q_{dir,rad}+Q_{ind})/Q_{met}$ (total radiation to metal)	$\%Q_{dir}/Q_{met}$ (direct component of the total tr. to metal)	$\%Q_{exit}/Q_{in}$ (chimney loss)	$\%Q_{loss}/Q_{in}$ (heat loss to env. based on total heat input)	$\%Q_{loss}/Q_{ref}$ (heat loss to env. based on heat tr. to refractories)	$\%Q_{ref,con}/Q_{ref}$ (convection to refrac.)
1	Base	77.9	86.4	61.5	57.0	3.5	14.3	11.0
2	$h_{c,m}$=30	69.9	80.7	64.1	56.1	3.5	13.3	11.1
3	$h_{c,r}$=20	77.8	86.6	60.4	56.7	3.5	14.5	19.8
4	$h_{c,m}$=30 $h_{c,r}$=20	69.6	81.6	63.0	55.9	3.5	13.5	20.0
5	%xair=0	78.9	87.0	61.7	51.7	3.6	12.8	10.3
6	%xair=20	76.9	85.8	61.4	61.9	3.4	16.0	11.7
7	T_{met}=800	79.1	87.3	60.9	59.1	3.6	15.7	10.5
8	ϵ_m=0.8	81.7	88.2	64.4	54.9	3.4	12.4	12.5
9	ϵ_r=0.8	74.8	86.5	53.8	56.9	3.5	16.3	9.31
10	m_f=0.15	79.0	87.3	60.7	62.9	2.4	11.5	10.1
11	m_f=0.20	79.8	87.9	60.2	67.3	1.9	10.1	9.5
12	m_f=0.25	80.4	88.3	59.8	70.6	1.5	9.2	9.0
13	T_{air}=627	80.6	88.4	59.7	43.9	2.8	8.9	8.9
14	T_{air}=627 m_f=0.15*	81.5	89.1	59.1	48.5	2.2	7.6	8.1
15	T_{air}=627 m_f=0.15* $T_{ref,m}$=1050	80.4	88.3	59.8	43.0	3.0	9.2	9.0
16	T_{air}=627 m_f=0.15 $T_{ref,m}$=1150	81.9	89.4	58.8	50.5	2.0	7.1	7.9
17	U=0	78.0	87.0	59.4	57.6	0.0	0.0	10.8
18	U=4	77.8	85.8	63.9	56.4	6.8	28.9	11.2
19	8×6.5×1.5m m_f=0.1	77.4	85.8	62.9	53.7	4.1	15.4	11.4
20	8×6.5×1.5m m_f=0.125	78.1	86.3	62.4	56.8	3.4	13.4	10.9
21	8×6.5×1.5m m_f=0.15	78.6	86.7	62.0	59.5	2.9	12.1	10.5

3.4 Conclusions

A one-gas-zone model has been developed to calculate the heat transfer in the combustion chamber of the sidewell furnace. The model has been used to determine the effects of various parameters on the heat transfer to the liquid metal bath surface.

1. Increasing the surface area and emissivity of the metal increases the heat transfer. However, it is very difficult to vary the emissivity, and any change in surface area requires modifying the furnace design (size and, perhaps, capacity). Certainly, higher convection means better heat transfer, but, again, it is not easy to realize this without significant changes in design (burner position and design).
2. Varying surface emissivity and convection on refractories has a marginal effect. It is also very difficult to modify these parameters.
3. Metal surface temperature has a direct impact on heat transfer. The lower the surface temperature, the higher the temperature difference between the gas and the surface temperatures, and, consequently, the higher the heat transfer rate. Mixing in the liquid bath reduces the vertical temperature gradient and the surface temperature. Therefore, it is important to promote conditions which favor mixing in the metal bath.
4. It is also important to insulate the walls and to reduce the excess air (and air infiltration) as much as possible to decrease losses from the combustion chamber.
5. The heat transfer to the metal surface can be increased significantly by increasing the fuel flow rate. However, this increase is realized at the expense of the furnace efficiency. That is, of the additional heat input, a higher portion is lost through the chimney.

6. The parameter that appears to have the greatest impact is the inlet air temperature. This shows the importance of preheating the combustion air which results in higher gas temperatures and, consequently, better heat transfer rates. Recuperation of heat also increases the furnace efficiency. Higher gas temperature means, of course, higher refractory temperature which may attain the maximum value easily. With air preheating, it is important to set the maximum refractory temperature as high as possible.
7. The model accounts for all the important phenomena. It is also flexible enough to be used to determine the effects of various parameters on furnace performance.

CHAPTER 4

3D MATHEMATICAL MODELLING OF THE TRANSIENT HEAT TRANSFER IN METAL

4.1 Introduction

The sidewell furnace is a dynamic system. As the melting occurs or as the metal is transferred to a holding furnace, the metal level increases or decreases accordingly. These changes in the heights of the metal bath and the combustion chamber lead to continuous variations in heat transfer and flow patterns. Since the metal height increases very slowly during melting, it can be assumed to a certain degree that the flow pattern remains approximately the same. When the metal is transferred to a holding furnace, the procedure takes about 10 to 15 minutes. The flow pattern should be affected significantly during this period; however, it can be assumed that the normal flow pattern re-establishes quickly afterwards as long as there is circulation in the main hearth and between the two sections of the furnace. Therefore, the flow could be taken steady based on above assumptions.

Heat transfer has to be calculated in transient mode in the metal due to continuous changes in metal temperature including heat losses from the metal through the refractories and to the environment as well as the melting of the solids (sows and shreds).

The gas in the combustion chamber can be assumed steady as well due to its very low residence time (in seconds) in the system. The heat transfer in refractories of the

combustion chamber should normally be calculated under transient conditions. If the system is in operation for a long time and the changes in refractory temperature are slow, as a rough approximation, they can be treated as steady.

Based on these assumptions, a 3D heat transfer model was built using CFX for the metal bath. The model is explained in the next section.

4.2 Mathematical Model

A model that treats every phenomenon in transient mode can be built in 3D. However, the level changes would require mesh variation with time, the flow would have to be re-calculated at every time step along with the heat transfer. Even though it is possible to do this, the memory and computation time requirements would be so high that it would be impracticle to run such a model. Therefore, with the above assumptions, a 3D model for only the heat transfer part of the metal was developed based on CFX platform.

The combustion chamber was represented by the model described in Chapter 3. The flow pattern in the liquid metal was assumed steady, and the flow fields (calculated by the 3D flow model of Chapter 2) were imposed directly in the heat transfer calculations. The heat transfer in the liquid metal was solved in detail to determine the temperature fields and heat flux distributions under different conditions. The overall view of the model is shown in Figure 4.1. The two models (the combustion chamber and the metal bath) are coupled through the interface located at the metal surface. The metal surface temperature calculated by the metal model is fed to the combustion chamber model as the boundary condition at the interface. The heat flux calculated by the combustion chamber model is transferred to

the metal model and is used as the boundary condition at the interface. A number of simulations are carried out and the results are presented in the next section.

There is no controller incorporated into this model. A few simple control strategies were used to be able to compare different cases. These control strategies are described in the following section as well. The transient enthalpy equation solved by the CFX code is presented in Appendix 2 along with the flow equations.

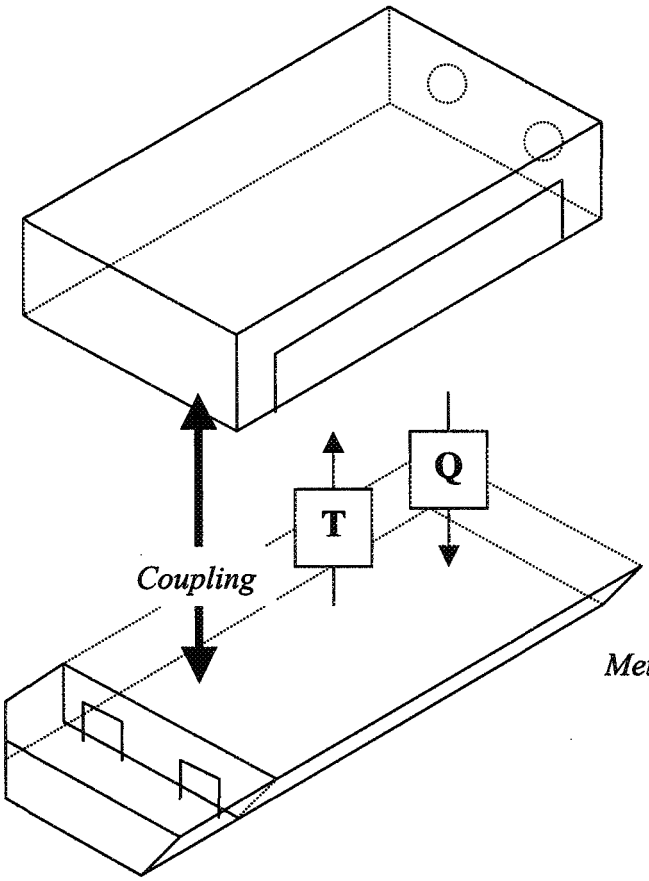

Combustion chamber:

- *Steady state*
- *Fuel flow limited by maximum refractory temperature*
- *Calculated by the model described in Chapter 3*

Metal bath:

- *Transient heat transfer*
- *Flow imposed (calculated by the model described in Chapter 2)*

Figure 4.1 : Coupling of the Models of the Combustion Chamber and the Metal Bath (T: temperature, in K; Q: heat flow rate, in W).

In the second control strategy, the shred flow rate is constant. The burner power decreases going from Case (a) to Case (c) as demonstrated in Figure 4.4. This means that the same production can be maintained using lower burner power (fuel flow rate) resulting in lower energy costs. Concerning the temperature difference between the inlet and outlet arch as well as the average temperature gradient in the main hearth (see Figure 4.5), the same trends are obtained.

The results clearly indicate that it is very important to provide a good mixing in the main hearth and a good metal circulation rate between the main hearth and the side well in order to have an efficient heat transfer. Higher heat transfer rates can be used to increase the production if necessary.

Due to the highly dynamic nature of the sidewell furnace, this model was not pursued any further as it would require unrealistic computation time. Instead, a fully dynamic model was built, based on further simplifications on geometry and discretization, to simulate the operation of the furnace including the controller. The dynamic model is presented in the following chapter.

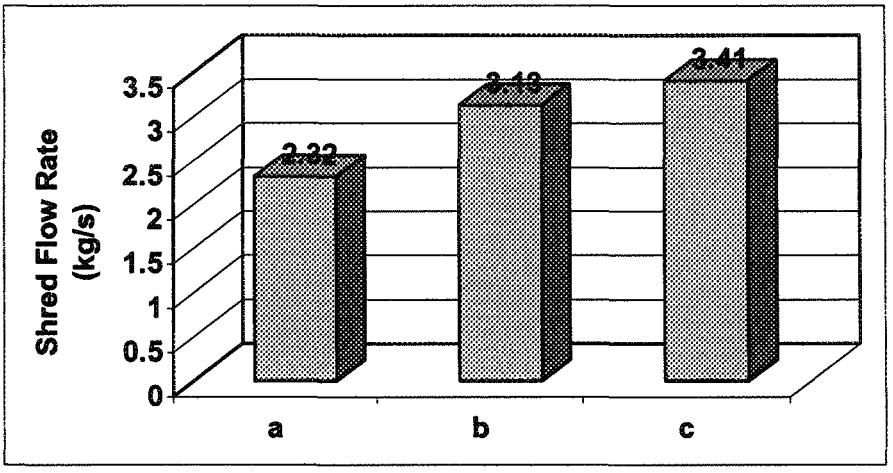

Figure 4.2 : Increase in Melting Rate (Shred Flow Rate) Depending on the Furnace Configuration Using Control Strategy 1 (a) Impeller, (b) Impeller and Baffle, (c) Impeller, Baffle, and Pump

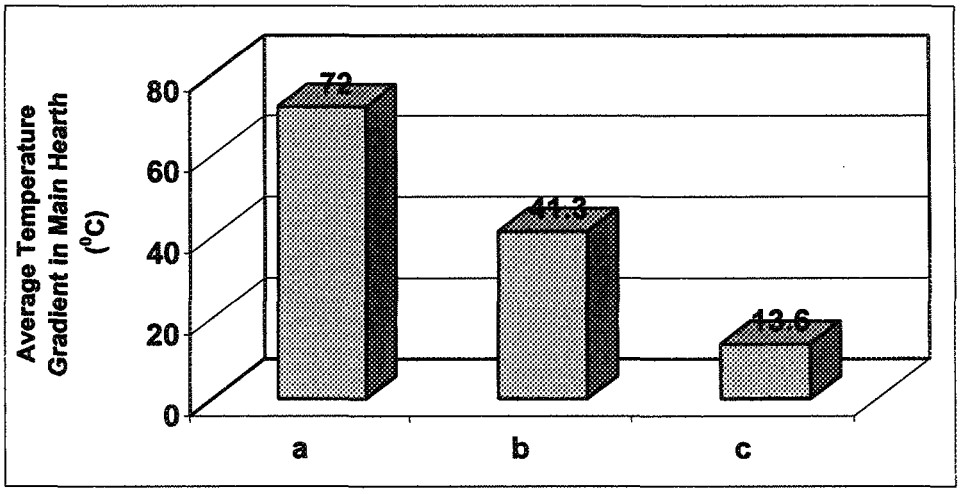

Figure 4.3 : Decrease in Average Temperature Gradient in the Main Hearth Depending on the Furnace Configuration Using Control Strategy 1 (a) Impeller, (b) Impeller and Baffle, (c) Impeller, Baffle, and Pump

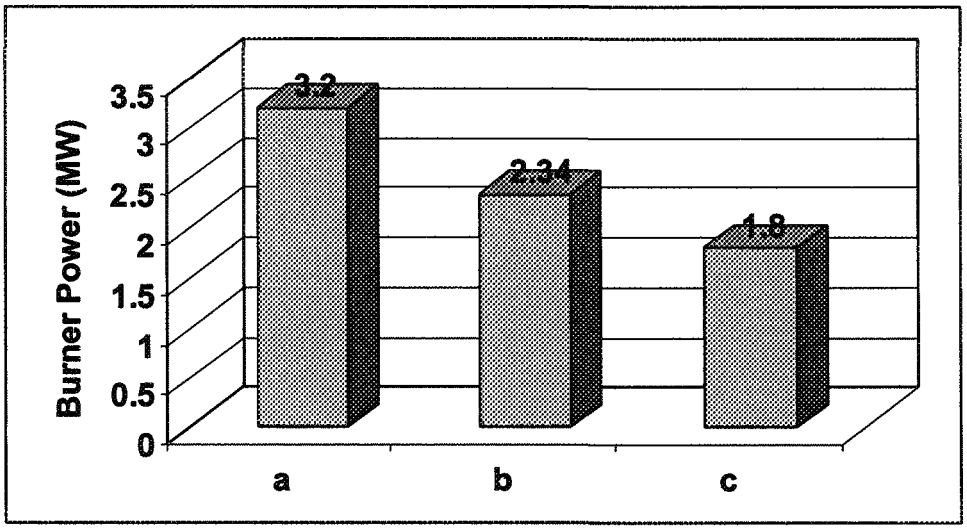

Figure 4.4 : Decrease In Burner Power for Melting 1.9 kg/s Shred Depending on the Furnace Configuration Using Control Strategy 2 (a) Impeller, (b) Impeller and Baffle, (c) Impeller, Baffle, and Pump

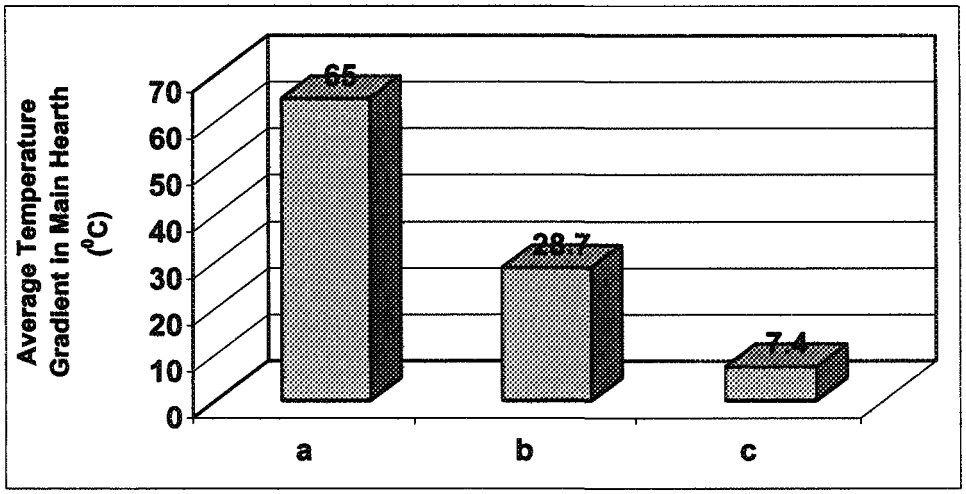

Figure 4.5 : Decrease in Average Temperature Gradient in the Main Hearth Depending on the Furnace Configuration Using Control Strategy 2 (a) Impeller, (b) Impeller and Baffle, (c) Impeller, Baffle, and Pump

Table 4.1 : Description of the Parameters, Cases and Control Strategies for the Variables Given in Table 4.2.

Parameters:

- Mass flow rate of fuel (m_f): 0.15 kg/s (maximum)
- Heat of combustion: 40 MJ/kg of CH_4
- Chamber dimensions: 6.96 × 5.84 × 1.5 m
- Emissivity of refractory (ϵ_r): 0.6
- Emissivity of metal surface (ϵ_m): 0.6
- Overall heat transfer coefficient (U): 2 W/m^2 K (heat loss from the chamber)
- Convective heat transfer coefficient ($h_{c,m}$): 20 W/m^2 K
- Convective heat transfer coefficient ($h_{c,r}$): 10 W/m^2 K
- Maximum refractory temperature ($T_{ref,m}$): 1100°C
- Inlet fuel temperature (T_{fuel}): 27°C
- % excess air (%xair): 10%
- Heat loss from the sides of liquid section: 3750 W/m^2
- Heat loss from the top of side well: 17500 W/m^2
- Initial metal temperature: 720°C
- Shred entrance temperature: 427°C

Cases:

- (a) With Impeller
- (b) With Impeller + Baffle
- (c) With Impeller + Baffle + Pump (110 kg/s)

Simulations were carried out for two hours.

Simplified Control Strategies (CS):

- ***CS1*:**
  If the control temperature >750°C: Decrease fuel flow rate and increase shred flow rate
  If the control temperature <750°C: Increase fuel flow rate and decrease shred flow rate
  Initial shred flow rate: 1.9 kg/s (15,000 lbs/h)
  Inlet air temperature: 627°C

- ***CS2*:**
  Shred flow rate constant at 1.9 kg/s (15 000 lbs/h)
  If the control temperature >750°C: Decrease fuel flow rate
  If the control temperature <750°C: Increase fuel flow rate

Control temperature is the metal temperature at the corner (burner side) near bottom.

Table 4.2 : Results of the Simulations.

	(a) Impeller		(b) Impeller + Baffle		(c) Impeller + Baffle + Pump	
	CS1	**CS2**	**CS1**	**CS2**	**CS1**	**CS2**
Arch flow rate (kg/s)	38		120		219	
Shred flow rate (kg/s)	2.32	(1.9)	3.13	(1.9)	3.41	(1.9)
Burner power (MW)	2.80	3.20	3.91	2.34	4.31	1.8
Q to metal (MW)	2.05	2.27	2.73	1.83	2.98	1.5
Refractory temperature (°C)	1028	1050 max	1050 max	977	1050 max	969
Outlet arch temperature (°C)	720	724	720	741.5	720	742.5
Inlet arch temp (°C)	759.5	759.4	739	754	731.7	749.8
Temperature difference between the inlet and outlet arches (°C)	40	35	19	12.5	11.7	7.3
Average temperature in main hearth (°C)	768	768	741	755	732	749.4
Average temperature gradient in main hearth (°C)	72	65	41.3	28.7	13.6	7.4

4.4 Conclusions

A 3D transient model for the liquid metal bath was developed using CFX. The flow was imposed based on the flow patterns calculated by the 3D flow model presented in Chapter 2. The heat transfer in the combustion chamber was solved using the model discussed in Chapter 3. The two models were coupled through an interface located at the metal surface. Various cases were studied in order to determine the effect of metal circulation (in the main hearth as well as between the two sections of the furnace) on heat transfer in the liquid metal. Results indicate the following:

1. Increased metal circulation gives lower temperature gradients and smaller temperature differences between the inlet and outlet arches.
2. Increased metal circulation leads to more efficient heat transfer in the furnace. If the shred flow rate is kept constant, the same production (melt rate) can be achieved using less fuel (lower burner power) leading to energy conservation. Also, with good mixing, it is possible to maintain higher burner power and increase the shred flow rate if it becomes necessary.

This model can be further exploited by converting the steady-state combustion chamber model to a transient one. However, consideration of the metal level changes in such a 3D model is still impractical, especially from the computation time point of view.

CHAPTER 5

DYNAMIC SIDEWELL FURNACE MODEL

5.1 Description of the Model

The sidewell furnace is a highly dynamic system. Metal level varies continuously due to the addition of solid charges to different parts of the system, melting, and removal of metal by skimming and tapping. Firing rate of the burner always changes depending on the controller (the controlling variables are the metal and refractory temperatures). Appropriate and realistic analysis of the operation and control of such systems, in which everything is transient, can be carried out only using dynamic models. In order to avoid excessive computation times, simplifications have to be made in the representation of the geometry and the discretization of the calculation domain. This has to be done without compromising accuracy.

In the current project, one dynamic model was developed for the combustion chamber and one dynamic model for the metal bath. The overall model is made up of these two models. The two parts interact with each other through the interface which is located at the top surface of the dross layer similar to the coupling explained in Chapter 4 for the transient metal heat transfer model. This is a fully dynamic model accounting for all the important phenomena taking place in the furnace[40-41]. Each model will be explained briefly in the following sections. Further details are given in Appendix 6.

5.1.1 Combustion Chamber Model

The combustion chamber includes the refractories and the gas as shown below. Heat generated by the combustion reaction is partly transferred to the metal directly and indirectly via refractories by radiation and convection. The combustion chamber model calculates the entire heat transfer process.

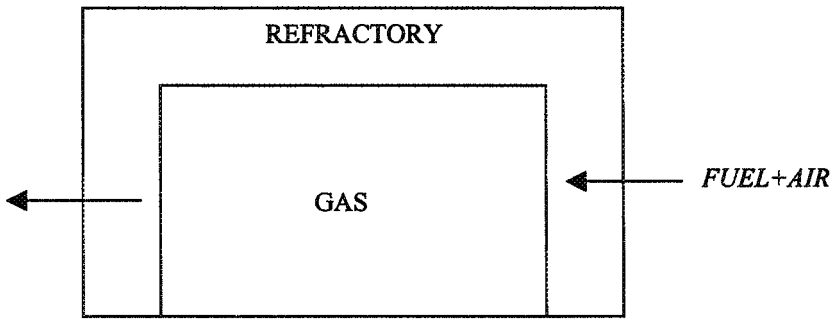

Figure 5.1 : Combustion Chamber

Refractories: One-dimensional transient conduction equation with boundary conditions of radiation and convection is solved for the entire refractory wall considering all five refractory walls as one large slab. The equation is given by:

$$\frac{1}{\alpha}\frac{\partial T}{\partial t} = \frac{\partial^2 T}{\partial x^2} \qquad [5.1]$$

where T is the temperature, x is the distance, t is time and α is the thermal diffusivity.

Gas: Gas in the combustion chamber is analyzed under steady-state conditions due to its small time constant (low residence time). However, variations with time (the transient effects) are taken into account by repeating the calculation at every time step. One-gas-zone

model described in Chapter 3 is used for the heat transfer calculations within the gas coupled with transient heat transfer in the refractories.

5.1.2. Dross Layer

Heat transfer through the dross layer is also analyzed based on the steady-state one-dimensional conduction. However, the dross thickness increases linearly as a function of the amount of metal melted which, of course, varies with time. When skimming is done, the dross layer thickness is set to zero. The heat flow rate is assumed continuous through this layer, and there is no accumulation. The steady-state conduction equation is given by:

$$Q = -k\frac{dT}{dx} = -k\frac{\Delta T}{\Delta x} \qquad [5.2]$$

where Δx is the thickness which could vary with time (Δx = f(time), empirical), and ΔT is the temperature difference between the top and bottom of the dross layer. The dross layer constitutes the interface between the two models.

5.1.3 Liquid Metal Bath Model

The dynamic model for the liquid metal bath includes the refractories and the liquid metal. Also, there are two sections, namely the main hearth and the side well, which are connected by the inlet and outlet arches. These arches allow the circulation of metal between the two sections.

Refractories: Heat transfer in the nine refractory walls shown in Figure 5.2 was calculated based on the one-dimensional transient conduction with appropriate boundary conditions as given by Equation 5.1. Outside the furnace where the refractories are in contact with ambient air, radiation and natural convection are considered. Inside the furnace

where the refractories are in contact with the liquid metal, only convection is considered (the conduction is also included in the governing differential equation). The boundary condition on the outside of the refractory at the bottom of the furnace (that is, in contact with the foundation) is treated similar to a convection type boundary but with a very low convective heat transfer coefficient.

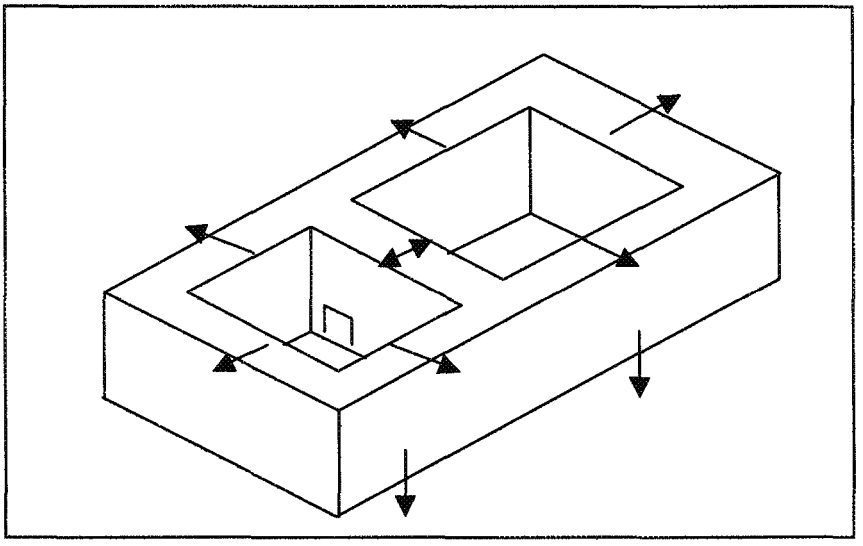

Figure 5.2 : Refractories Surrounding the Liquid Metal Bath

Liquid Metal: The liquid metal is divided into a number of divisions called cells. Transient heat and mass balances are solved for each cell. The side well is divided into (2×4×3) 24 cells and the main hearth into (5×3×3) 45 cells as shown below in Figure 5.3.

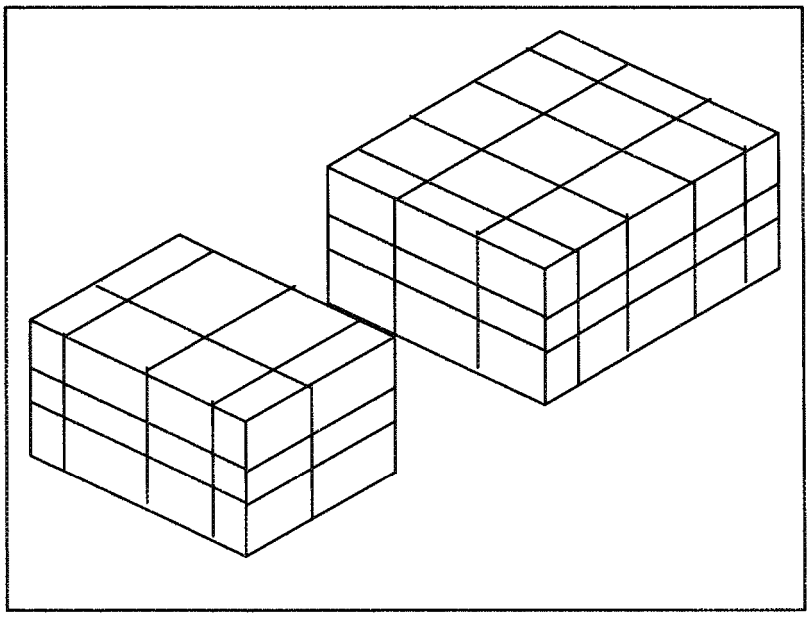

Figure 5.3 : Division of the Side Well and Main Hearth into Cells for Dynamic Heat and Mass Balance Calculations

Mass and heat balances for each cell are written as:

$$\frac{\partial m}{\partial t} = \sum m_{in} - \sum m_{out} = \frac{\partial (V\rho)}{\partial t} \qquad [5.3]$$

$$\frac{\partial}{\partial t}(V\rho CpT) = \nabla Q_{conduction} + \sum Q_{in} - \sum Q_{out} \qquad [5.4]$$

where V is the metal volume,V=f(h), h: liquid level which varies with time, Q_{in} is the heat input from all sources (such as from combustion chamber and due to flow into the cell, depending on the location of the cell), Q_{out} is the heat leaving the cell (such as from heat loss to environment, due to flow out of the cell, and melting of various charges, again depending on the location of the cell).

The flow field is imposed based on the detailed calculation from the three-dimensional flow model described in Chapter 2. A controller is incorporated into the model. This part of the model, which simulates the controller, is called the control emulator. Also an interface is built which allows inputting the data through a number of files and running the program in a user-friendly way. All the results are displayed in Excel format. The flow charts for the programme and the control emulator are shown in Figures 5.4 and 5.5, respectively. The interactions between different parts of the model are also shown in these figures.

The sidewell furnace simulator runs on PC. The computation time on a 450 MHz computer is about 10 to 15 seconds for the simulation of 5-hour furnace operation. A user manual and tutorial accompanies the CD containing the simulator.

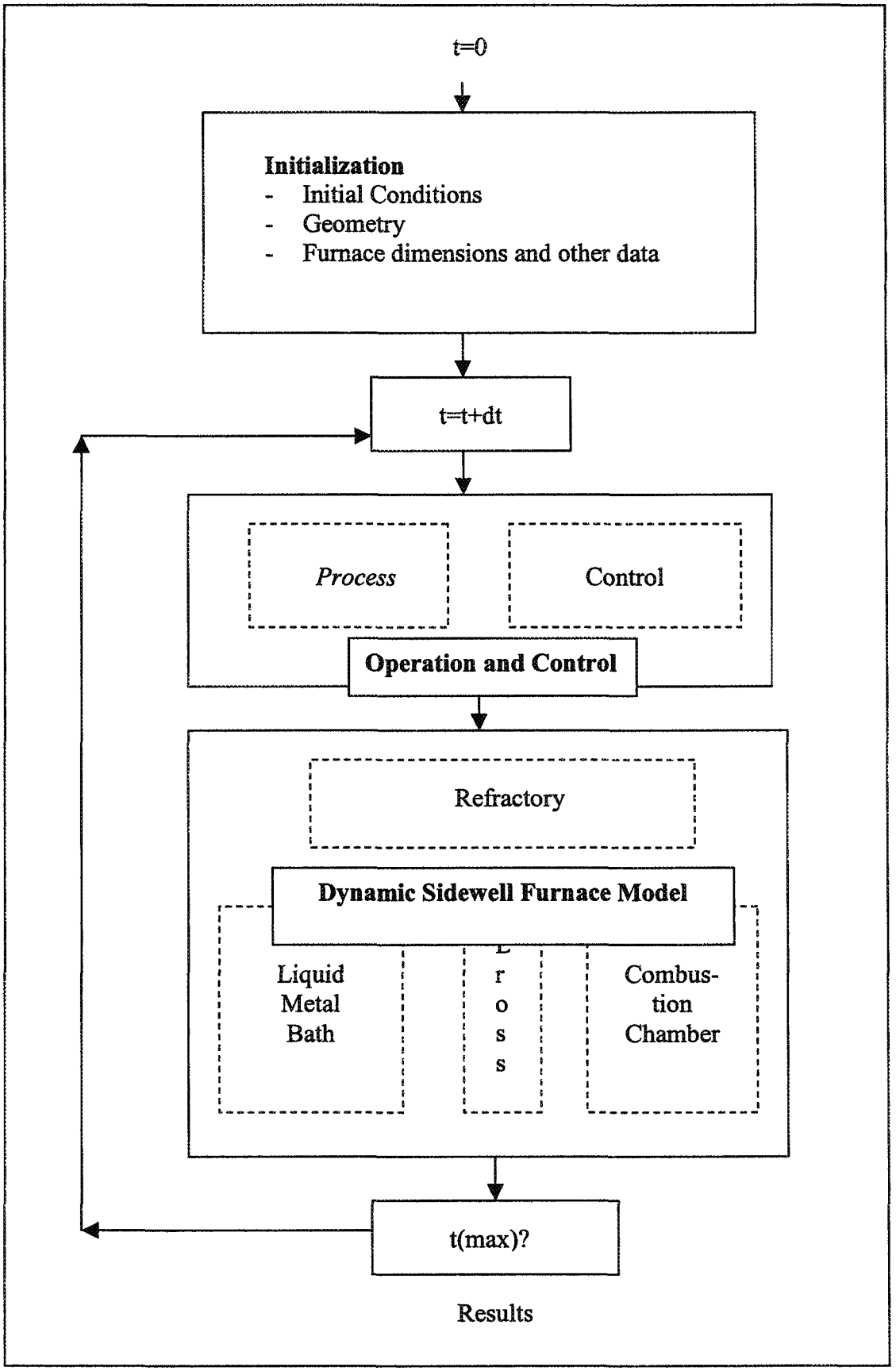

Figure 5.4 : Program Flowchart

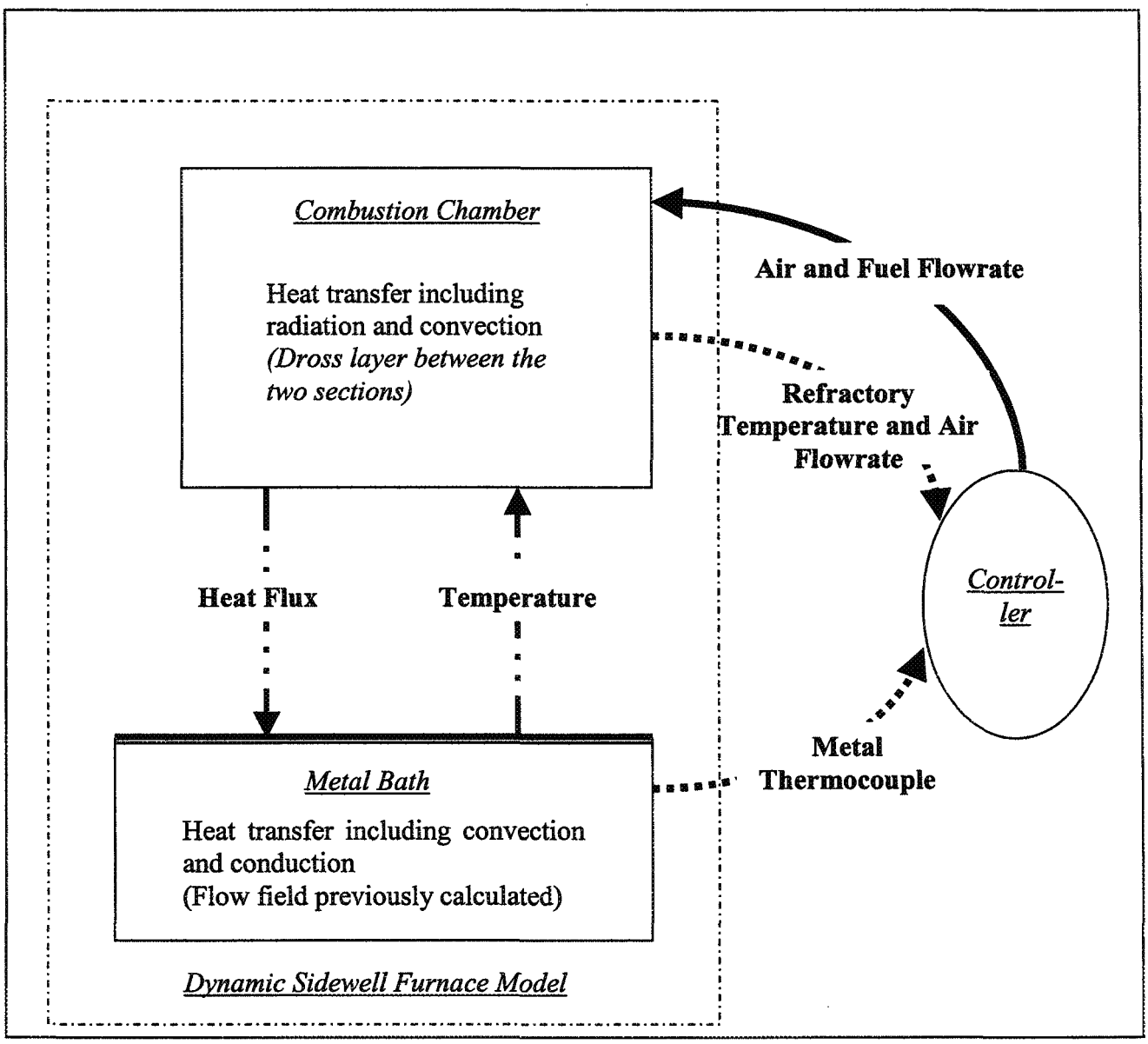

Figure 5.5 : Dynamic Sidewell Furnace Model with the Control Emulator

The numerical solution of the above equations is described in Appendix 6. Also the interface is briefly presented along with the input files and the results displayed at the end of the run. A typical run is demonstrated in the same Appendix. A few typical results are shown in the following section. The model was validated by comparing the model predictions with the plant data. The validation work for two sets of data is presented in Sections 5.3 and 5.4[40-41].

5.2 Example of a Simulation

A simulation was carried out to demonstrate the use of the model. Some of the results are given in Figure 5.6 (a-d). Various events are marked on the figures. In this simulation, the fuel and shred flow rates were fixed (2 kg/s shred flow rate, i.e. 16,000 lbs/h; 0.1 kg/s fuel flow rate, i.e. 4MW burner power). These usually vary during the operation and are determined by the conditions in the plant. The shred flow rate depends on the de-coating unit and the availability of the recycled cans. The fuel flow rate is regulated by the controller. During skimming, the burner is turned off. After skimming, the burner is turned on again.

Figure 5.6 shows (a) the average metal temperature in the main hearth, (b) the metal level, (c) the total amount of metal melted, and (d) the dross thickness. Temperatures at any position can be extracted from the model.

In these figures, the SI units are used. Some of the variables are more convenient and easily understandable in other units for a number of users. The program is available for both SI and US units (US is the set of mixed units used in the US plants).

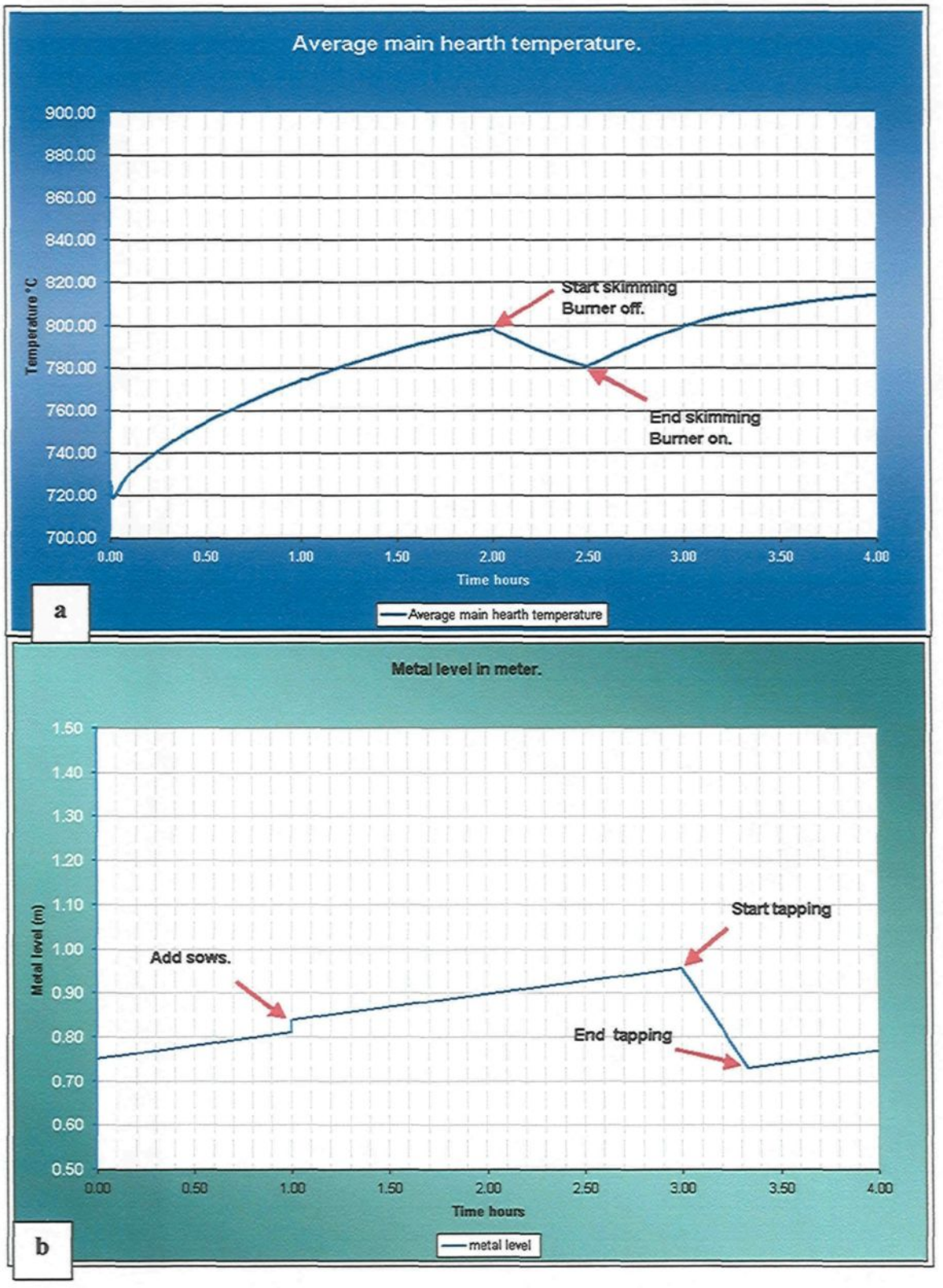
Average main hearth temperature.
900.00
880.00
860.00
840.00
820.00
800.00
780.00
760.00
740.00
720.00
700.00
Temperature °C
0.00
0.50
1.00
1.50
2.00
2.50
3.00
3.50
4.00
Time hours
Start skimming
Burner off.
End skimming
Burner on.
Average main hearth temperature
a
Metal level in meter.
1.50
1.40
1.30
1.20
1.10
1.00
0.90
0.80
0.70
0.60
0.50
Metal level (m)
Add sows.
Start tapping
End tapping
Time hours
metal level
b

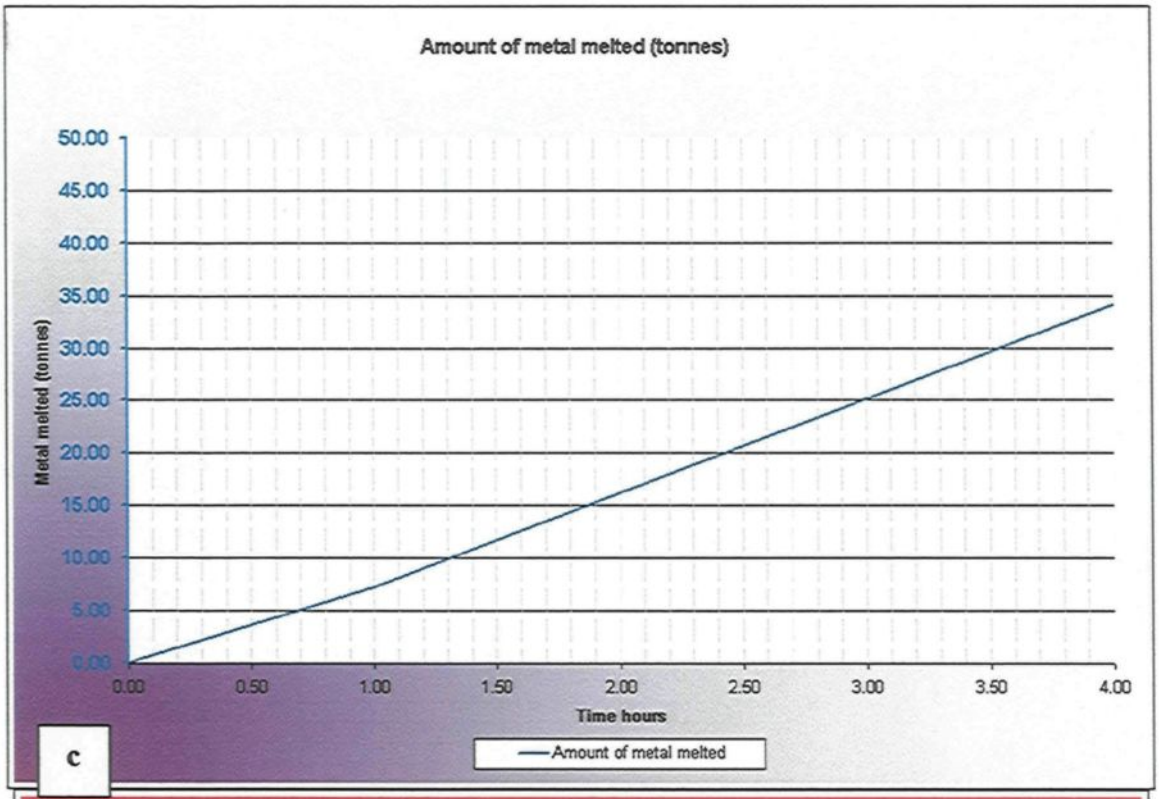

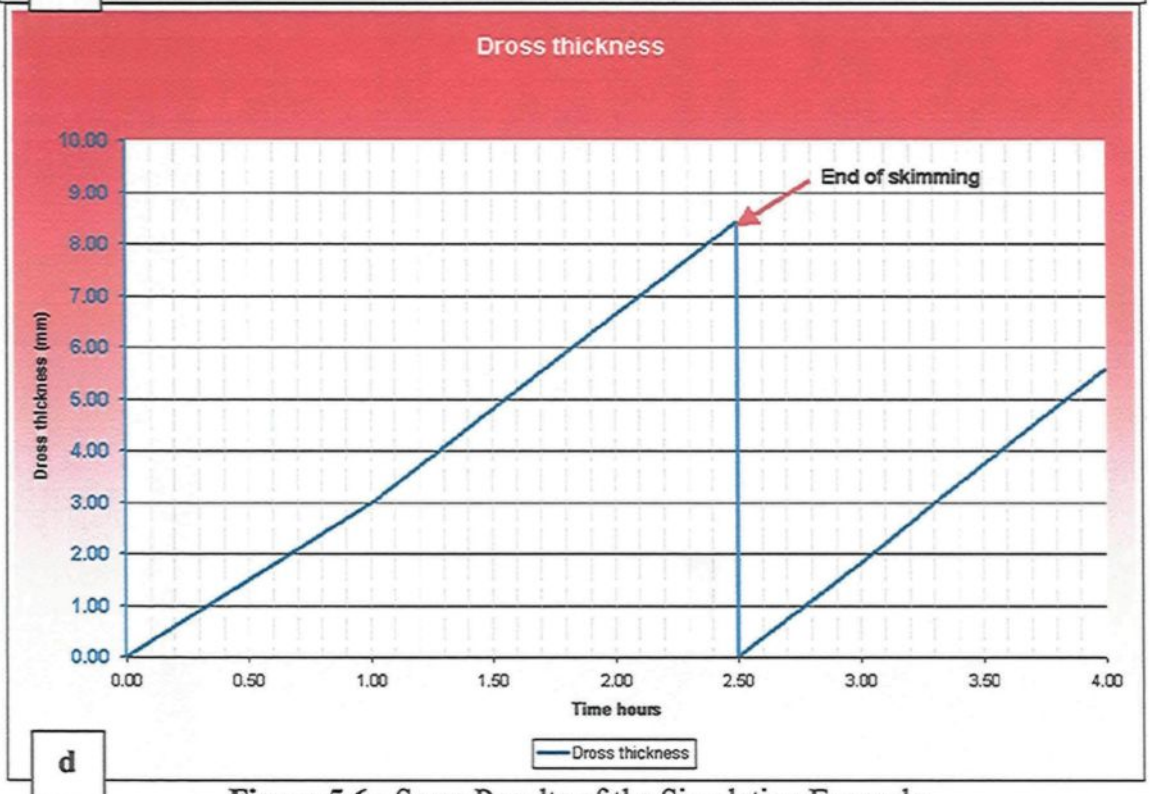

Figure 5.6 : Some Results of the Simulation Example

5.3 Validation with the Test A on the 2A Berea Furnace

A validation work was done based on the plant data taken during the week of June 12, 2000 on Furnace 2A in the Berea plant (Alcan, Kentucky, USA). Four tests were performed (Tests A, B, C and D). The details are given in a technical letter[42]. Test A was done on June 13 before noon. For the validation, the period from 10:30 to 11:30 a.m. (the second hour of the test shown in Figures 5.7 (a) and (b)) was used. In this test, there is only shred melting as the only event and no other complication is involved; therefore, it is a good starting point to test the model. The results of the validation work using Test A are presented in this section.

In this validation, there is no control emulator in the model. The shred flow rate, the fuel flow rate and impeller rpm were taken directly from the plant data. Figures 5.7 (a) and (b) show the plant data and the data used in the model for these variables. Since the model and plant data are the same, the curves overlap in the second hour of the test in these figures. Consequently, the control action on the furnace was implicitly included in the model. Initial values of a number of parameters such as the metal level were taken from the plant data as well. Initial conditions in the furnace are crucial for the success of the simulation. The plant data were studied in detail in an effort to understand the conditions in the furnace at the beginning of the test. Some of the discrepancies between the model predictions and the plant data may be due to difficulty in specifying the initial conditions. Further improvements may be possible with better specification of initial conditions.

Some of the results are shown in Figure 5.7 (b) metal level, (c) metal temperature in the main hearth at 24-inch depth, (d) inlet and outlet arch temperatures, and (e) four

temperatures from different positions in the furnace. The metal level is underestimated by about one inch at the end of one hour (Figure 5.7 b). This corresponds to 2-3% of the metal in the furnace and it is significant. The source of error might be in the model or in the measurement itself when the level is high. The metal temperature predictions are reasonable (Figure 5.7 c); however, the thermocouple indicates slight cooling as opposed to slight heating predicted by the model in the second half hour. The predicted temperature difference between the inlet and outlet arch temperatures is around 9°C compared to about 6°C measured in the plant (Figure 5.7 d). The last figure (Figure 5.7e) clearly shows that gradients exist both horizontally and vertically in the liquid metal. This indicates that the position of the thermocouple used for the furnace control is of utmost importance. A well-positioned thermocouple will give a good indication of the heat content of the metal. Otherwise, the thermocouple reading may not be representative of what is occurring in the liquid metal resulting in overheating or underheating of the metal. Overheating will increase aluminum oxidation and energy waste. Underheating will lead to low metal temperature and, consequently, loss of production due to reduction in the shred flow rate.

In a dynamic model, it is very important to specify the initial conditions properly. Otherwise, significant discrepancies could occur between the predictions and data. The discrepancies in the present case may be due to this reason because it is very difficult to determine the initial conditions in such an industrial system.

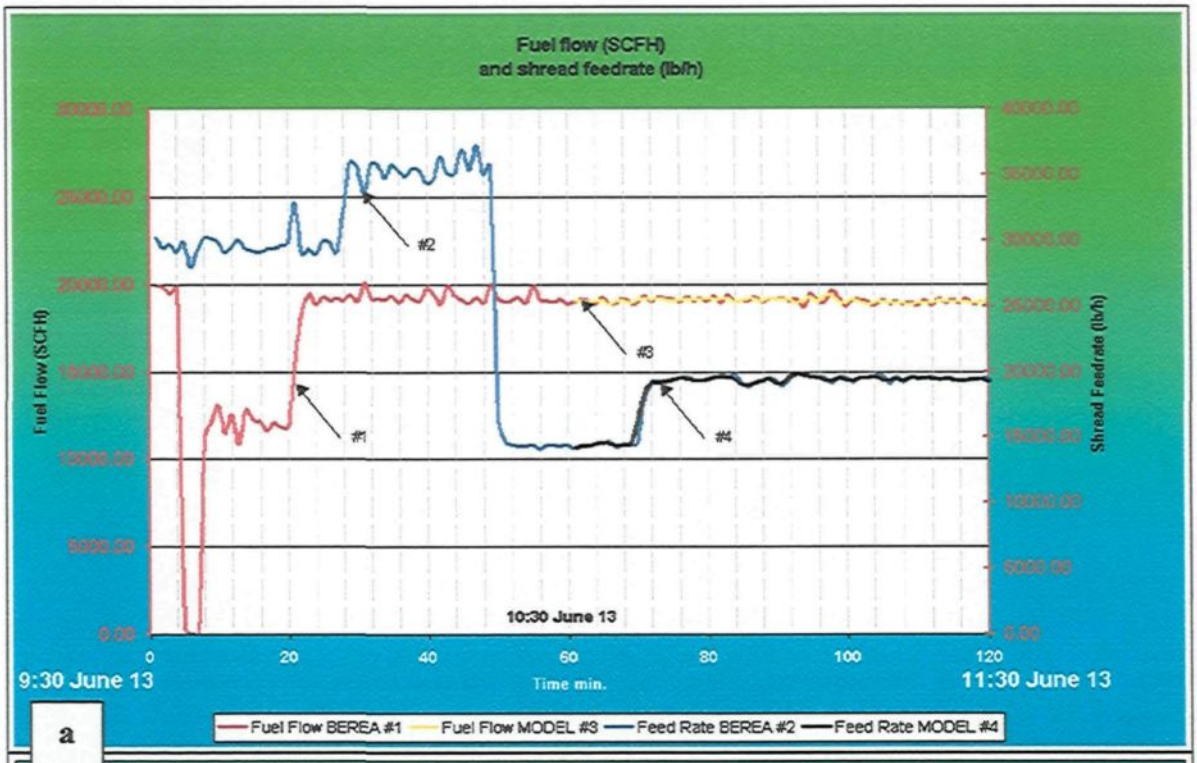
Fuel flow (SCFH)
and shread feedrate (lb/h)
Fuel Flow (SCFH)
Shread Feedrate (lb/h)
#1
#2
#3
#4
10:30 June 13
9:30 June 13
Time min.
11:30 June 13
Fuel Flow BEREA #1
Fuel Flow MODEL #3
Feed Rate BEREA #2
Feed Rate MODEL #4

a

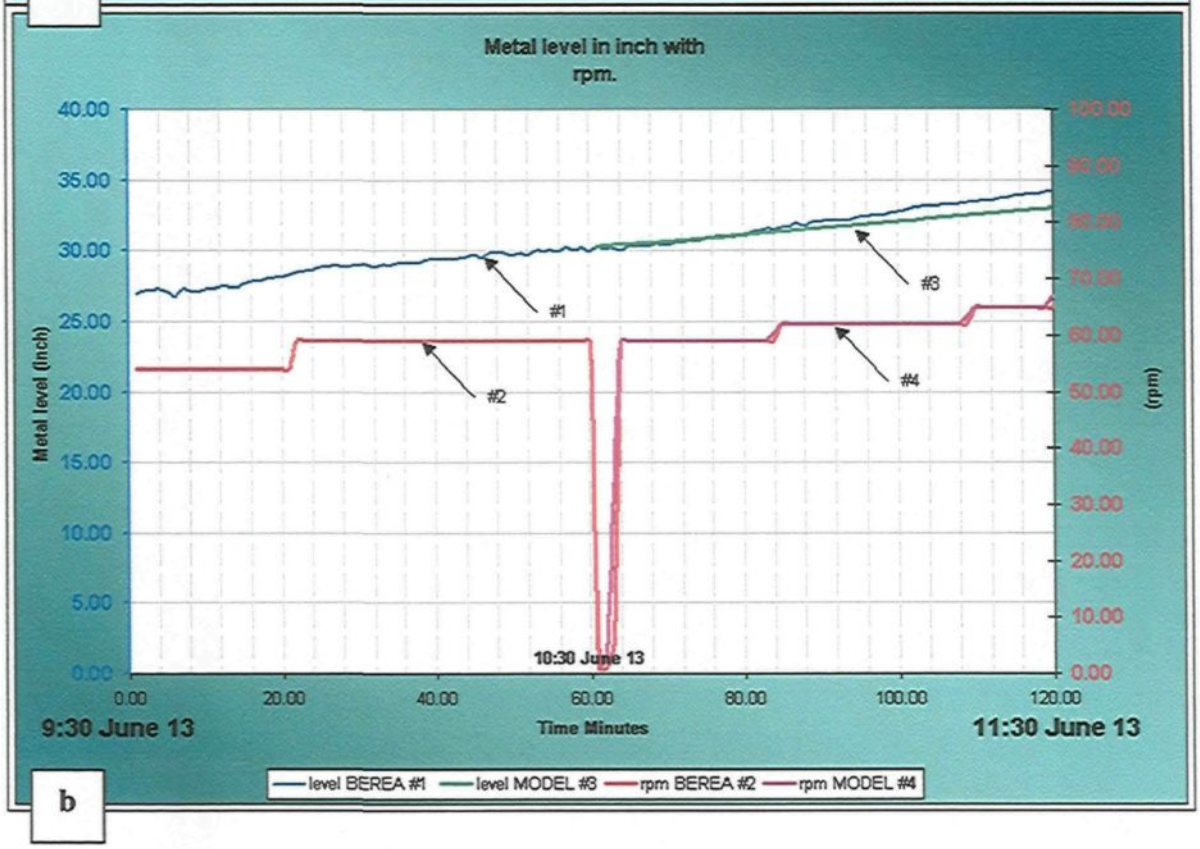
Metal level in inch with
rpm.
Metal level (inch)
(rpm)
#1
#2
#3
#4
10:30 June 13
9:30 June 13
Time Minutes
11:30 June 13
level BEREA #1
level MODEL #3
rpm BEREA #2
rpm MODEL #4

b

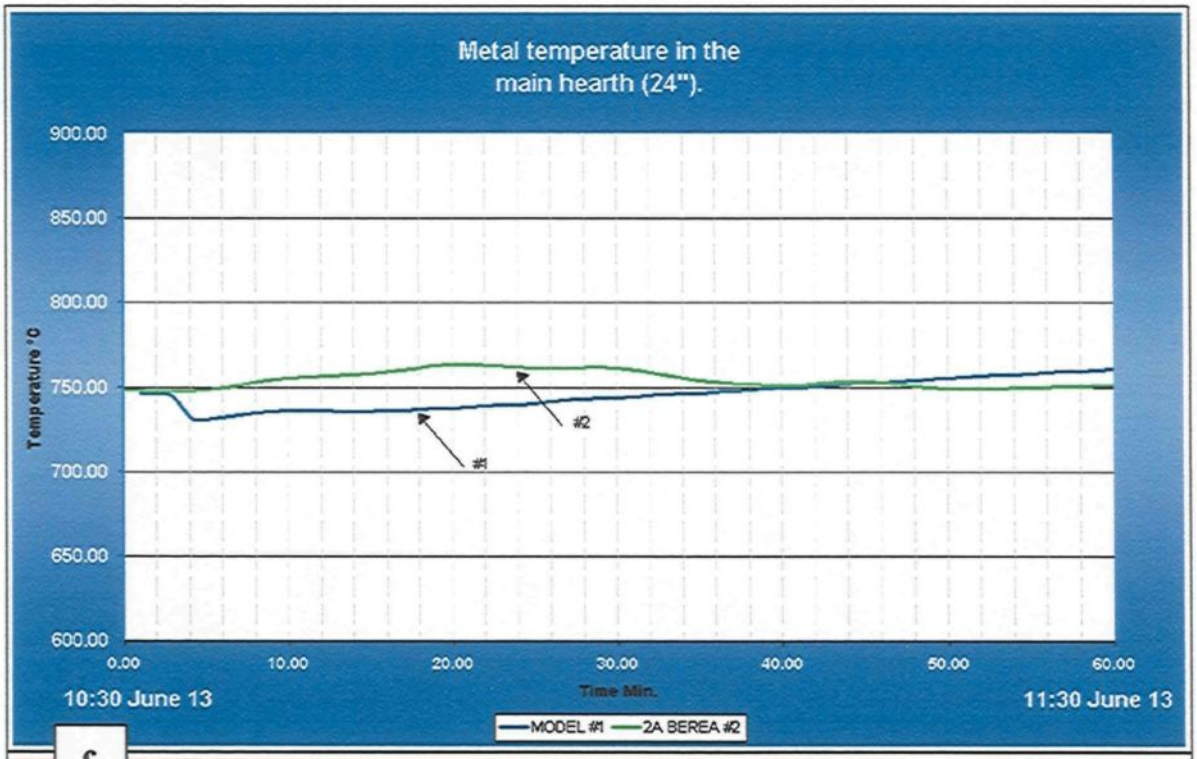
Metal temperature in the
main hearth (24").
900.00
850.00
800.00
750.00
700.00
650.00
600.00
Temperature °0
0.00
10.00
20.00
30.00
40.00
50.00
60.00
Time Min.
#1
#2
10:30 June 13
11:30 June 13
MODEL #1
2A BEREA #2

c

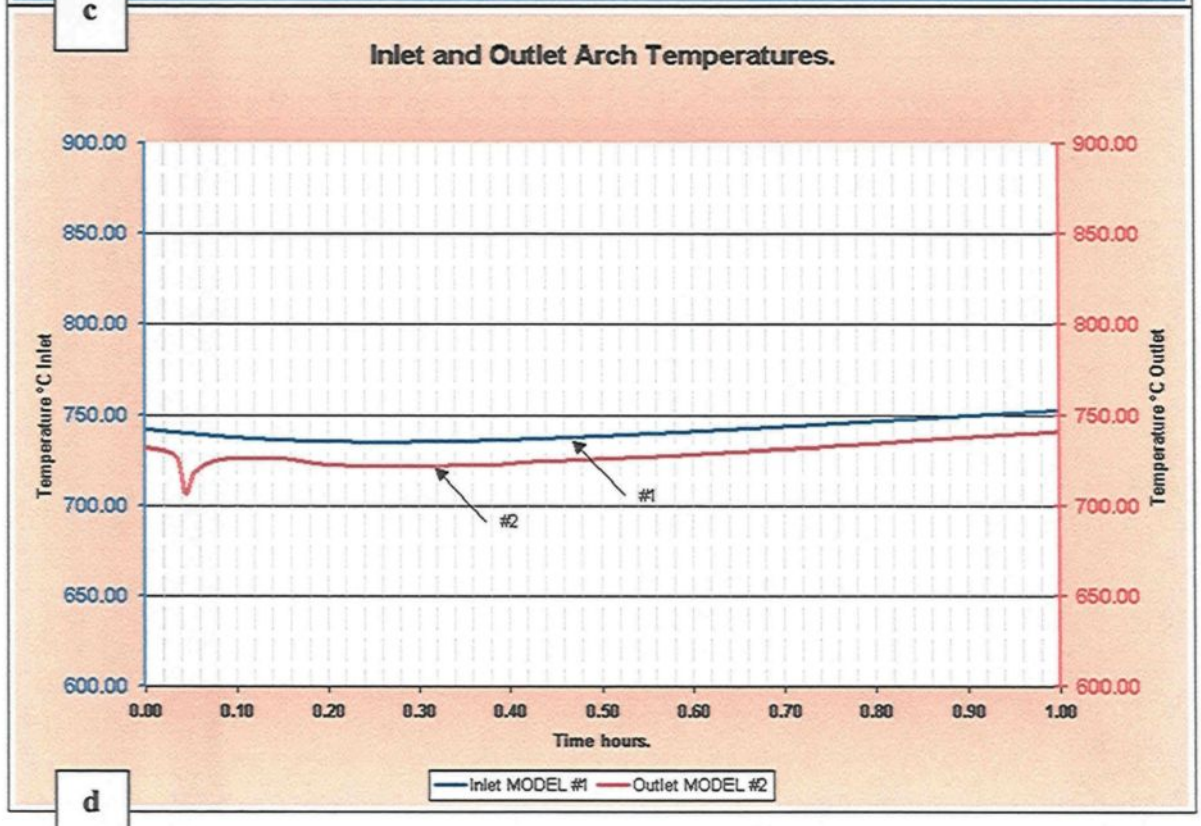
Inlet and Outlet Arch Temperatures.
900.00
850.00
800.00
750.00
700.00
650.00
600.00
Temperature °C Inlet
Temperature °C Outlet
0.00
0.10
0.20
0.30
0.40
0.50
0.60
0.70
0.80
0.90
1.00
Time hours.
#1
#2
Inlet MODEL #1
Outlet MODEL #2

d

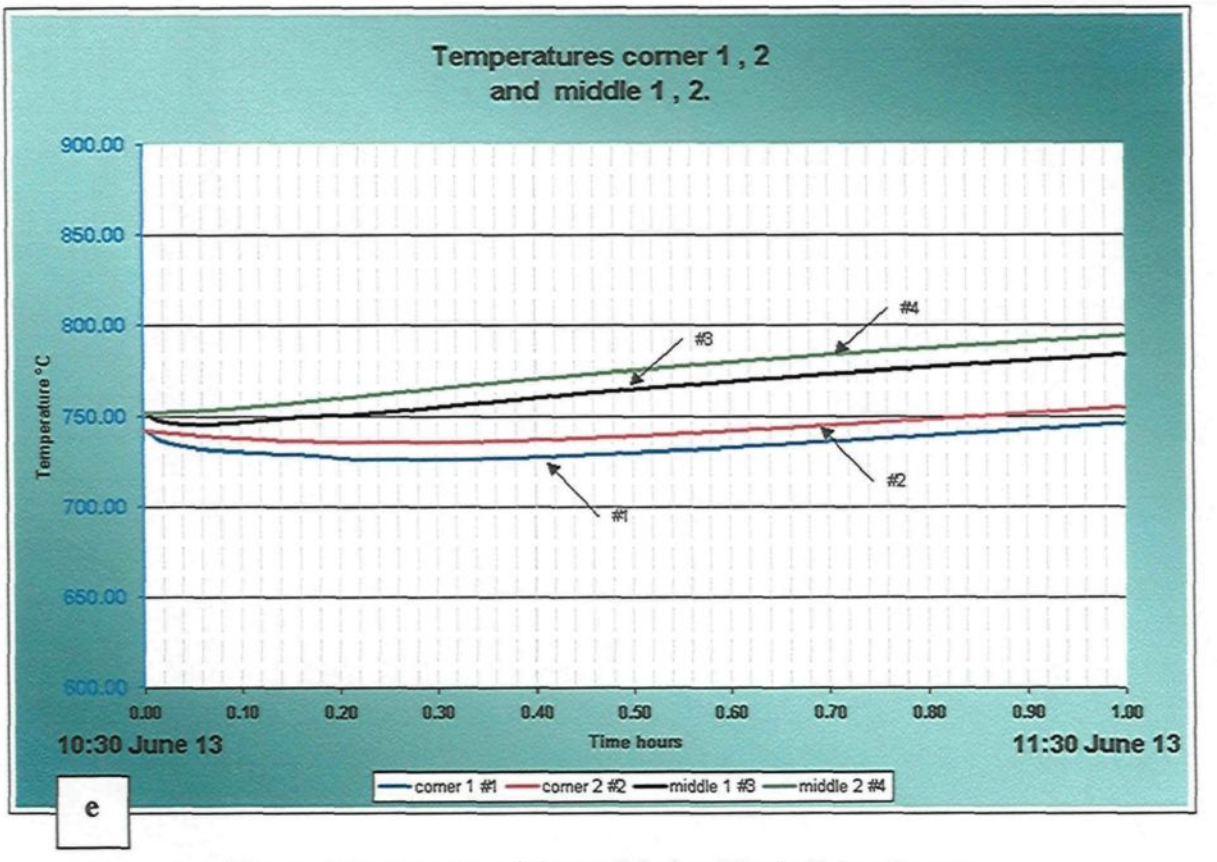

Figure 5.7 : Results of the Validation Work Using Test A
On Furnace 2A of Berea Plant

5.4 Validation with the Test B on the 2A Berea Furnace

A second validation work was started based on the plant data taken during the week of June 12, 2000 on Furnace 2A in the Berea plant. Four tests were performed (Tests A, B, C and D). Test B was done on June 13 in the afternoon. For the validation, the period from 12:00 to 16:00 p.m. was used. The results of the validation work using Test B are presented in this section.

For the validation work, the control emulator in the model was deactivated. The shred flow rate, the fuel flow rate and impeller rpm were taken directly from the plant data.

Figures 5.8 (a), (b) and (c) show the plant data and the data used in the model for these variables. Consequently, the control action on the furnace was implicitly included in the model. Initial values of a number of parameters such as the metal level were taken from the plant data as well. Initial conditions in the furnace are crucial for the success of the simulation. The plant data were studied in detail in an effort to understand the conditions in the furnace at the beginning of the test. Some of the discrepancies between the model predictions and the plant data may be due to difficulty in specifying the initial conditions.

Some of the results are shown in Figure 5.8 (c) metal level, (d) metal temperature in the main hearth at 24-inch depth (where the metal temperature was measured with a thermocouple), (e) roof temperature. The metal level is overestimated by about one inch before tapping (Figure 5.8 c). This corresponds to 2-3% of the metal in the furnace and it is significant. The source of error might be in the model or in the measurement itself when the level is high. The metal temperature predictions are reasonable (Figure 5.8 d); but the predictions indicate slightly higher temperatures. The last figure (Figure 5.8 e) shows the roof temperature predicted by the model and compares it with the measured value. The positions of the thermocouples used for the furnace control is of utmost importance. A well-positioned thermocouple in the metal will give a good indication of the heat content of the metal. It is also important to position the refractory thermocouple properly. Depending on its depth from the surface in the refractory, it will respond differently to temperature changes. The discrepancy seen in the Figure 5.8e may be due to problems in positioning or specifying the initial conditions properly.

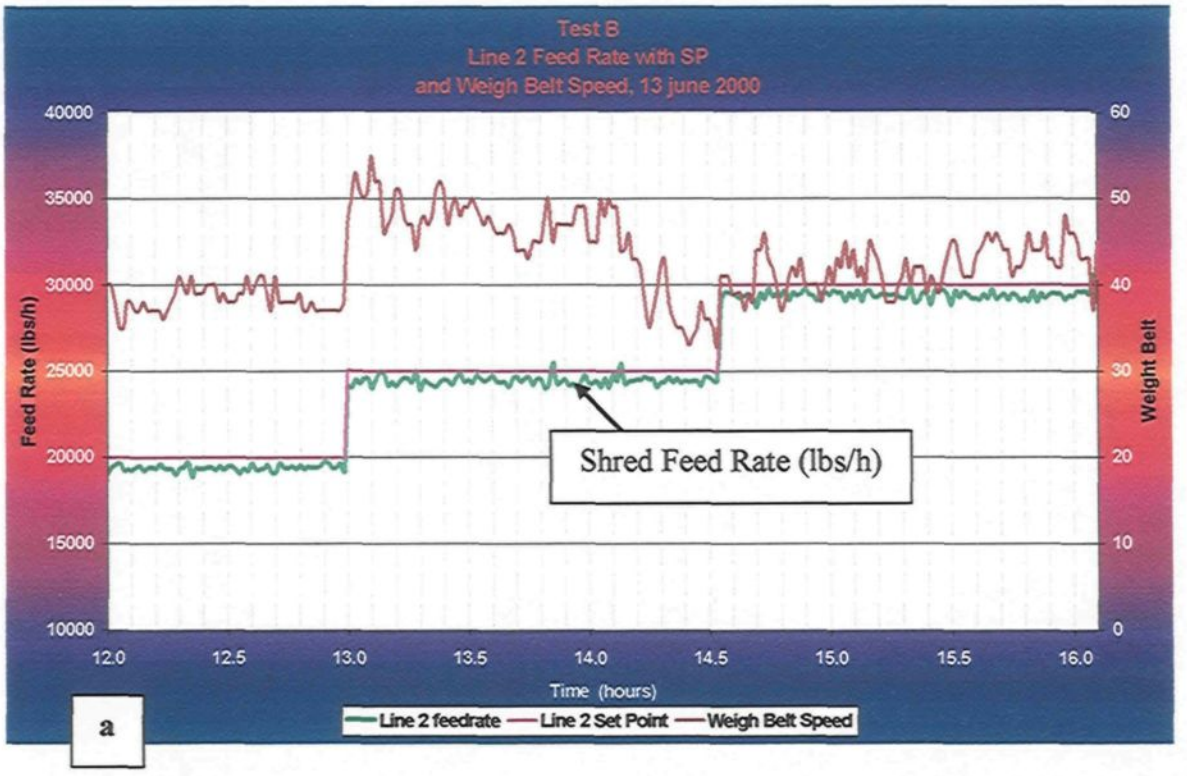
Test B
Line 2 Feed Rate with SP
and Weigh Belt Speed, 13 june 2000
Feed Rate (lbs/h)
Weight Belt
Shred Feed Rate (lbs/h)
Time (hours)
Line 2 feedrate
Line 2 Set Point
Weigh Belt Speed

a

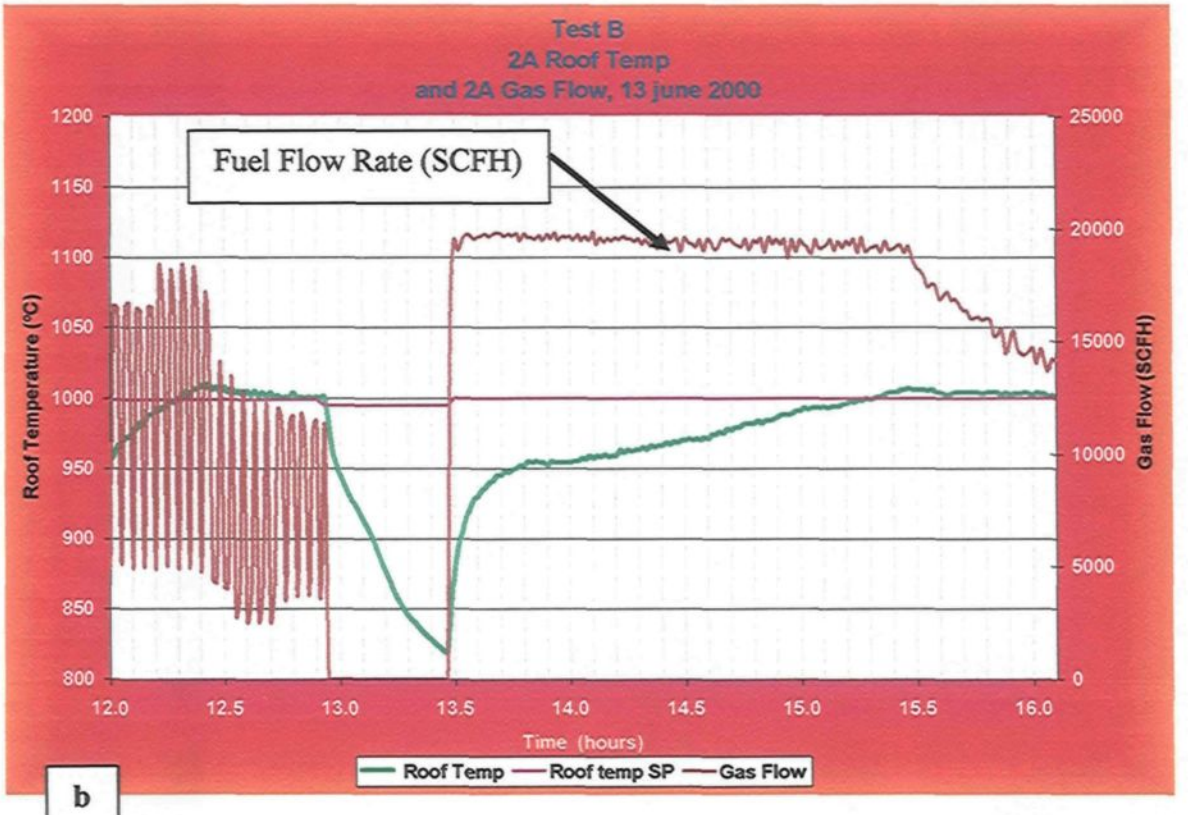
Test B
2A Roof Temp
and 2A Gas Flow, 13 june 2000
Fuel Flow Rate (SCFH)
Roof Temperature (°C)
Gas Flow (SCFH)
Time (hours)
Roof Temp
Roof temp SP
Gas Flow

b

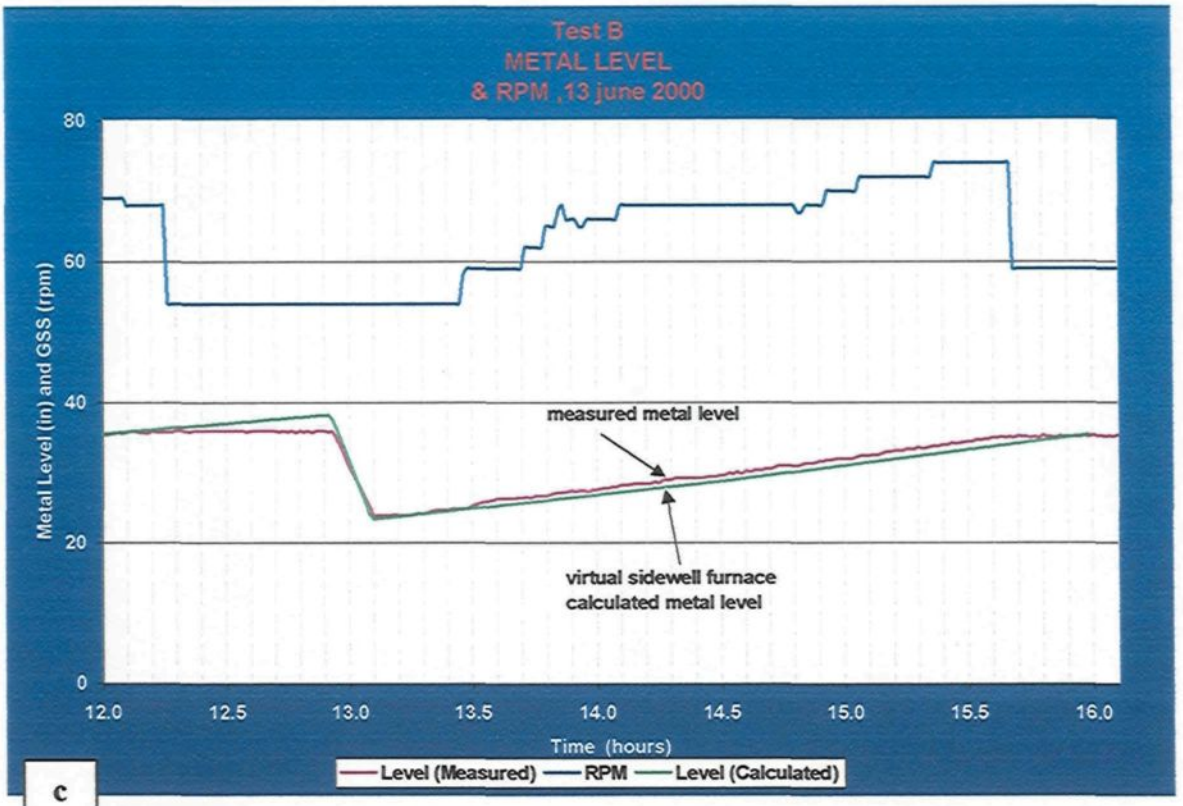
Test B
METAL LEVEL
& RPM ,13 june 2000
Metal Level (in) and GSS (rpm)
80
60
40
20
0
12.0
12.5
13.0
13.5
14.0
14.5
15.0
15.5
16.0
Time (hours)
measured metal level
virtual sidewell furnace
calculated metal level
Level (Measured)
RPM
Level (Calculated)

c

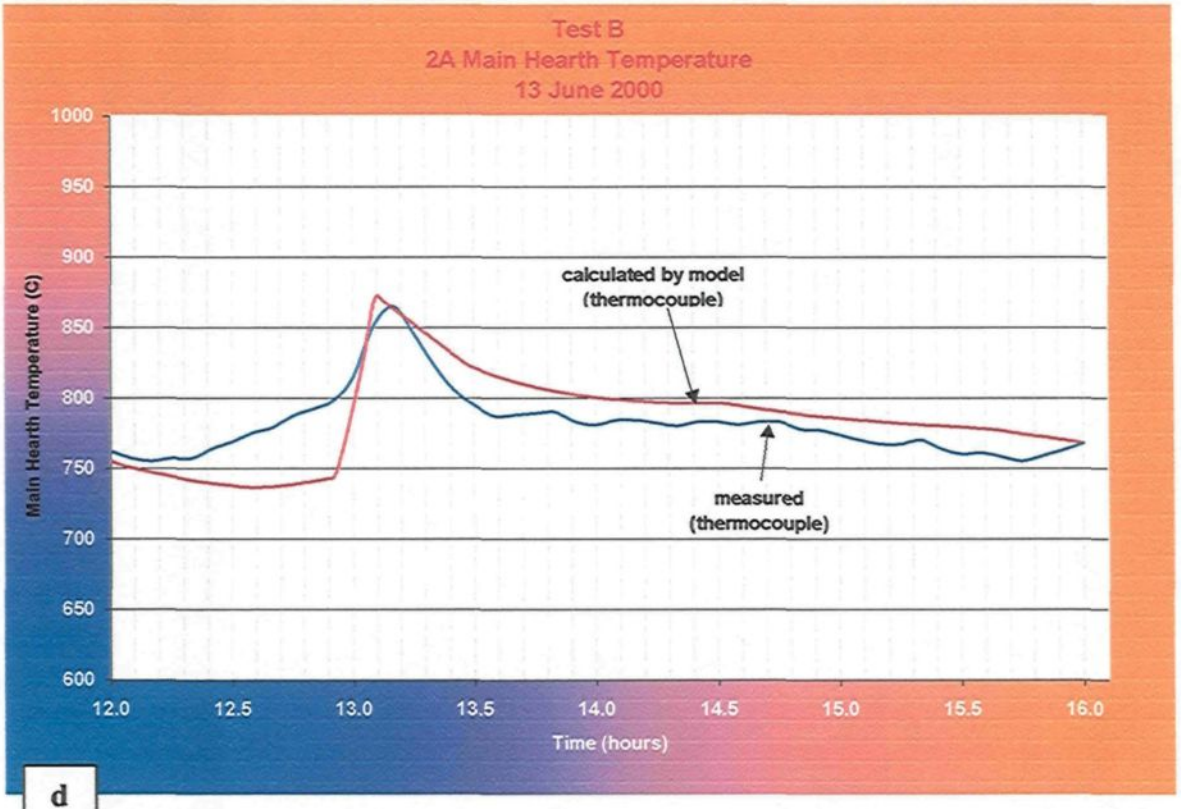
Test B
2A Main Hearth Temperature
13 June 2000
Main Hearth Temperature (C)
1000
950
900
850
800
750
700
650
600
12.0
12.5
13.0
13.5
14.0
14.5
15.0
15.5
16.0
Time (hours)
calculated by model
(thermocouple)
measured
(thermocouple)

d

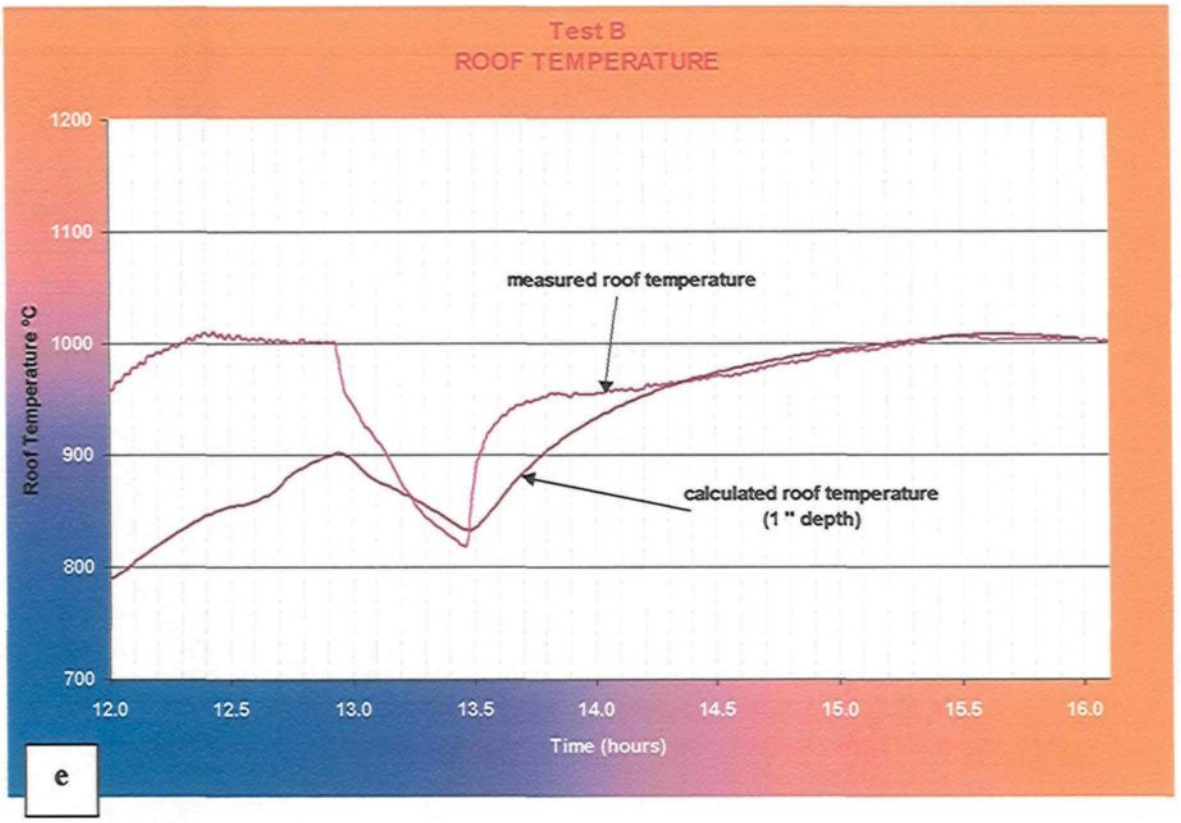

Figure 5.8 : Results of the Validation Work Using Test B
On Furnace 2A of Berea Plant

5.5 Case Studies Done with the Model

The dynamic model combined with the control emulator and the interface has been transferred to industry and is being used in a number of plants for different purposes (performance assessment, testing different operating conditions, energy consumption estimates, etc.). A number of studies were performed and effects of the following factors on the furnace performance were determined: Thermocouple position in the liquid metal; rotational speed of the impeller; roof temperature of the refractory in the combustion chamber; preheating of sows, shred and combustion air; metal setpoint temperature[43-47].

Recommendations were made to the industry based on the results. A number of studies are presented in the following sections.

5.5.1 Effect of Fuel Flow Rate on Shred Melting Capacity

One of the effective ways of increasing the shred melting capacity is to increase the burner power, that is, the fuel flow rate. In order to determine the impact of fuel flow rate on shred melting capacity, three cases were simulated for the furnace described in Table 1.1. Under normal operating conditions, shred feed rate is 19,000 lbs/h. The controller was off, and the heating was adjusted so that the metal would reach 805°C at the end of 4 hours. This could be done with a fuel flow rate of 16,000 SCFH. No event other than shred melting was allowed. In the other two cases, the fuel flow rate was decreased in one and increased in the other by 25%, and the shred feed rate was adjusted in such a way that the metal was heated similarly to 805°C in 4 hours. The results are shown in Table 5.1.

Table 5.1 : The Effect of Fuel Flow Rate on Shred Melting Capacity

Case No.	Fuel Flow Rate (SCFH)	Shred Flow Rate (lbs/h)	Remarks and Results
1	12,000	13,500	• Fuel flow rate is reduced by 25% • Same metal temperature after 4 hours of heating. • Shred feed rate decreases by 29%.
2	16,000	19,000	• Base Case. • 4 hours of operation.
3	20,000	23,700	• Fuel flow rate is increased by 25% • Same metal temperature after 4 hours of heating. • Shred feed rate increases by 24.5%.

The shred feed rate as a function of fuel flow rate is shown in Figure 5.9. As expected, the relationship is not linear. A decrease of 25% in fuel flow rate causes a reduction of 29% in shred melting capacity. An increase of 25% in fuel flow rate results in an increase of 24.5% shred melting capacity (see Figure 5.10). These results are in agreement with the ones discussed in Chapter 3 for the effect of fuel flow rate on the heat transfer to metal. Heat flux increases with increasing fuel flow rate, but the furnace efficiency decreases. The above non-linear relationship is a reflection of this trend.

Various model predictions are presented in Figure 5.11 for the comparison of three cases: (a) metal temperature measured by the thermocouple, (b) roof temperature of the refractory measured by the thermocouple, (c) fuel flow rate and total fuel consumption, and (d) the liquid metal level. The metal temperatures are similar as it was the basis for comparison in this study. Higher flow rates lead to higher refractory temperatures. At some point, further increase in fuel flow rate may not be possible since there is a maximum refractory temperature beyond which refractory failure may occur. This imposes a limit on how much the fuel flow rate can be increased in an existing furnace. Obviously, fuel consumption increases with higher fuel flow rates. Naturally, when the shred feed rate is higher, the level increases more rapidly. Therefore, by increasing fuel flow rate, higher amount of shred can be melted within a given time period; or a given amount of shred can be melted in a shorter period of time which increases productivity.

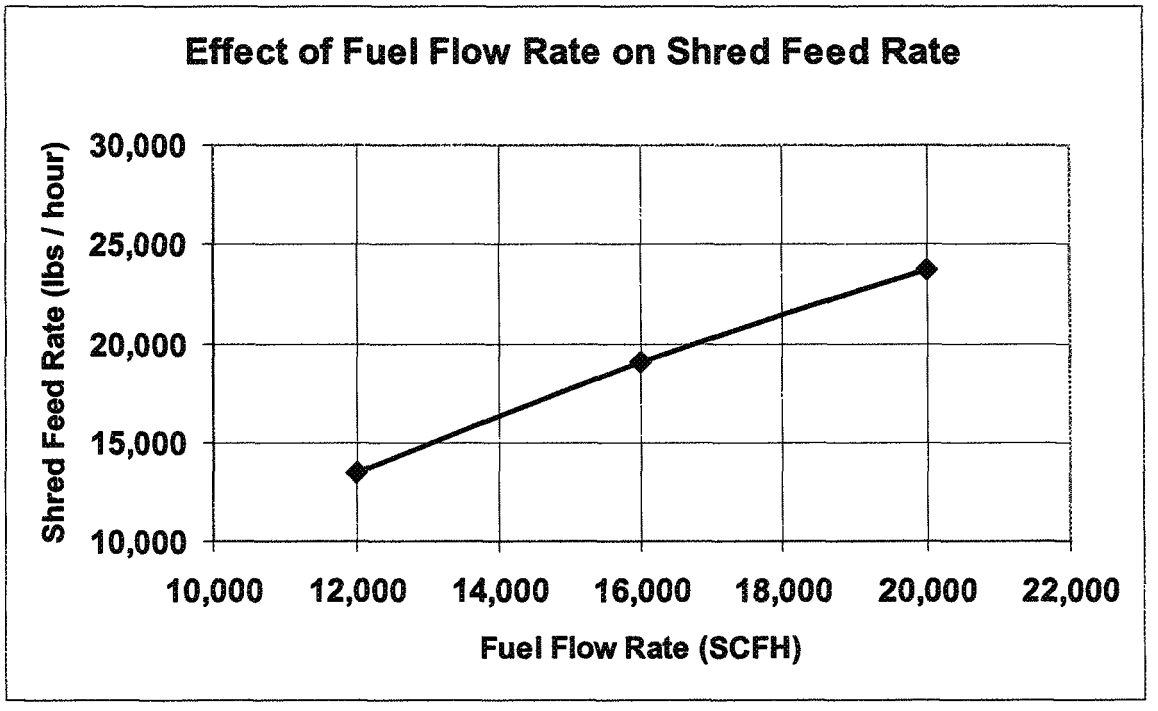

Figure 5.9 : Shred Melting Capacity as a Function of the Fuel Flow Rate.

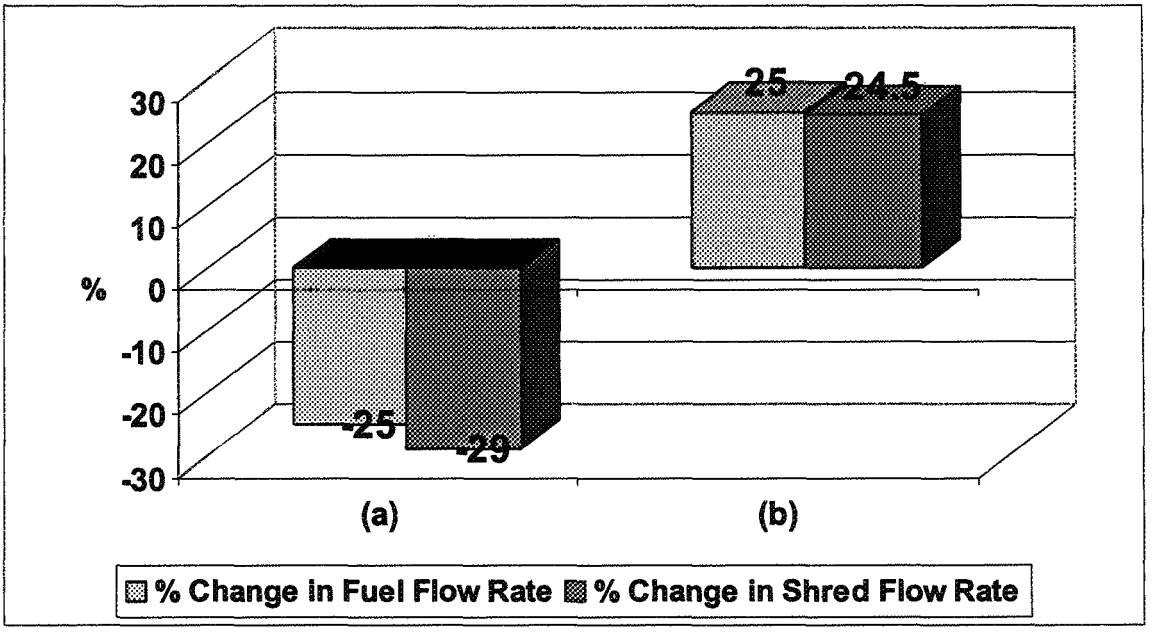

Figure 5.10 : Impact of Fuel Flow Rate on Shred Melting Capacity in Percentages: (a) 25% Decrease, and (b) 25% Increase in Fuel Flow Rate.

(a)

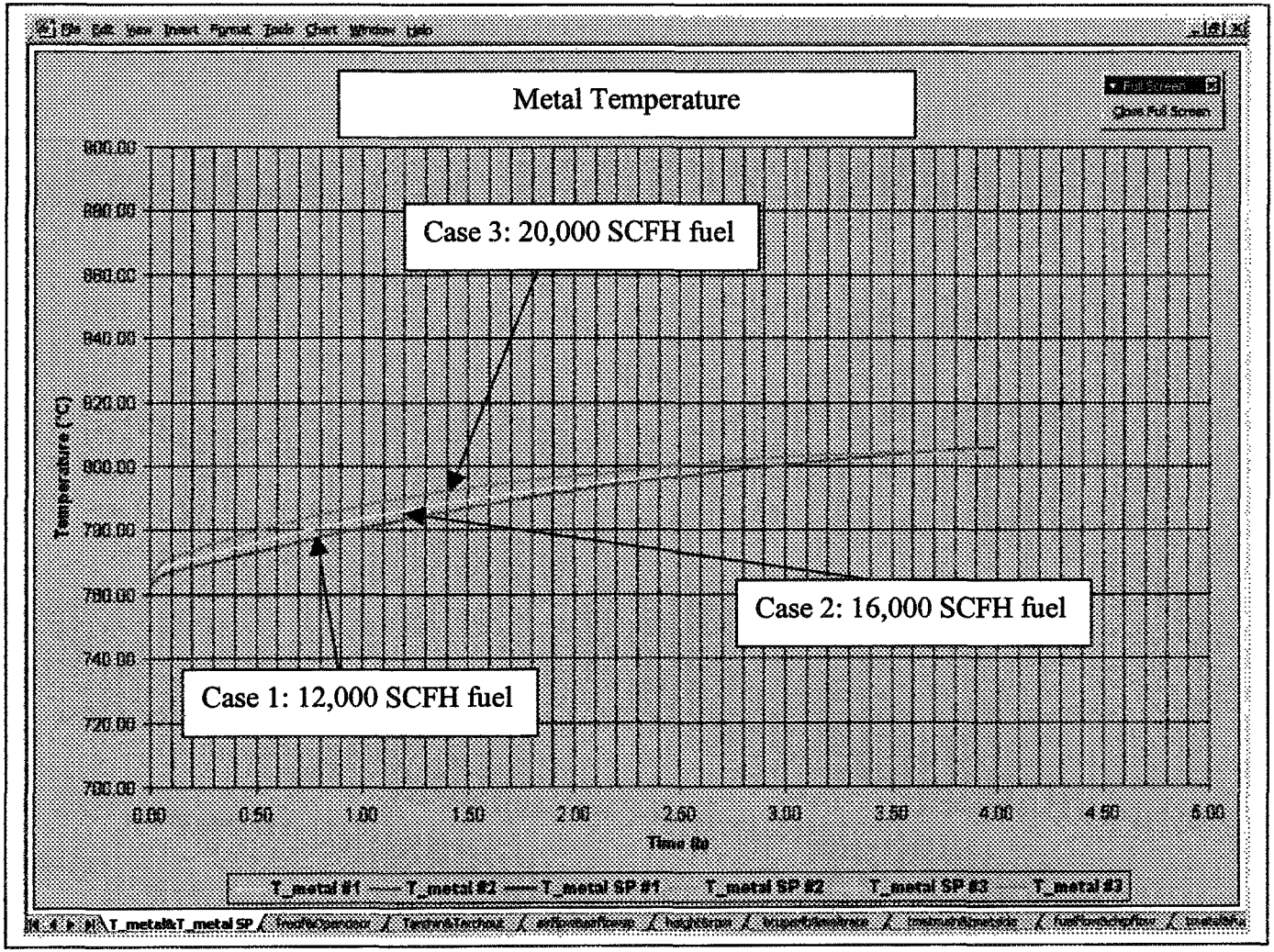
Metal Temperature
Case 3: 20,000 SCFH fuel
Case 2: 16,000 SCFH fuel
Case 1: 12,000 SCFH fuel
Temperature (°C)
Time (s)
T_metal #1
T_metal #2
T_metal SP #1
T_metal SP #2
T_metal SP #3
T_metal #3

(b)

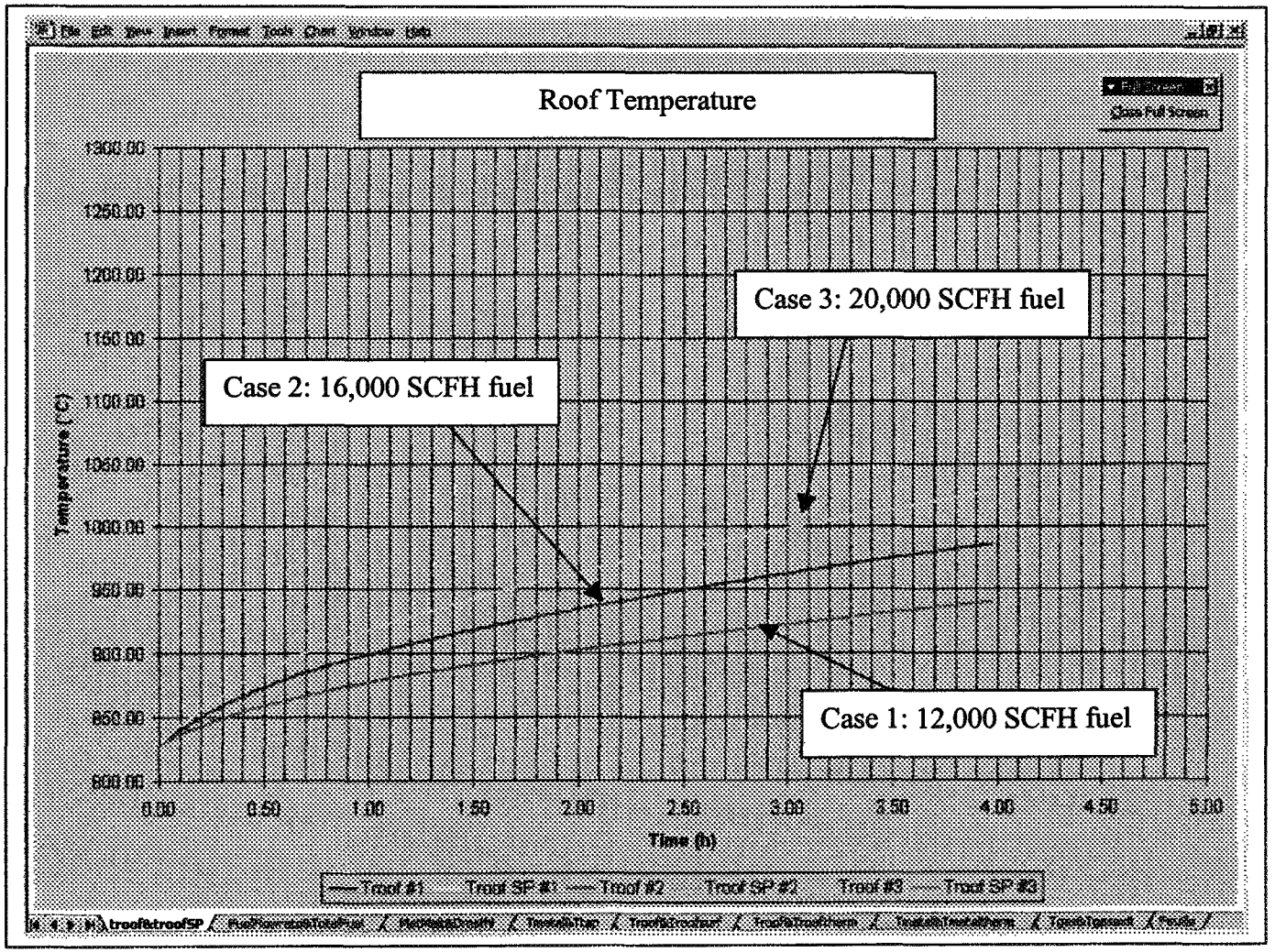
Roof Temperature
Case 3: 20,000 SCFH fuel
Case 2: 16,000 SCFH fuel
Case 1: 12,000 SCFH fuel
Temperature (C)
1300.00
1250.00
1200.00
1150.00
1100.00
1050.00
1000.00
950.00
900.00
850.00
800.00
0.00
0.50
1.00
1.50
2.00
2.50
3.00
3.50
4.00
4.50
5.00
Time (h)
Roof #1
Roof SP #1
Roof #2
Roof SP #2
Roof #3
Roof SP #3

(c)

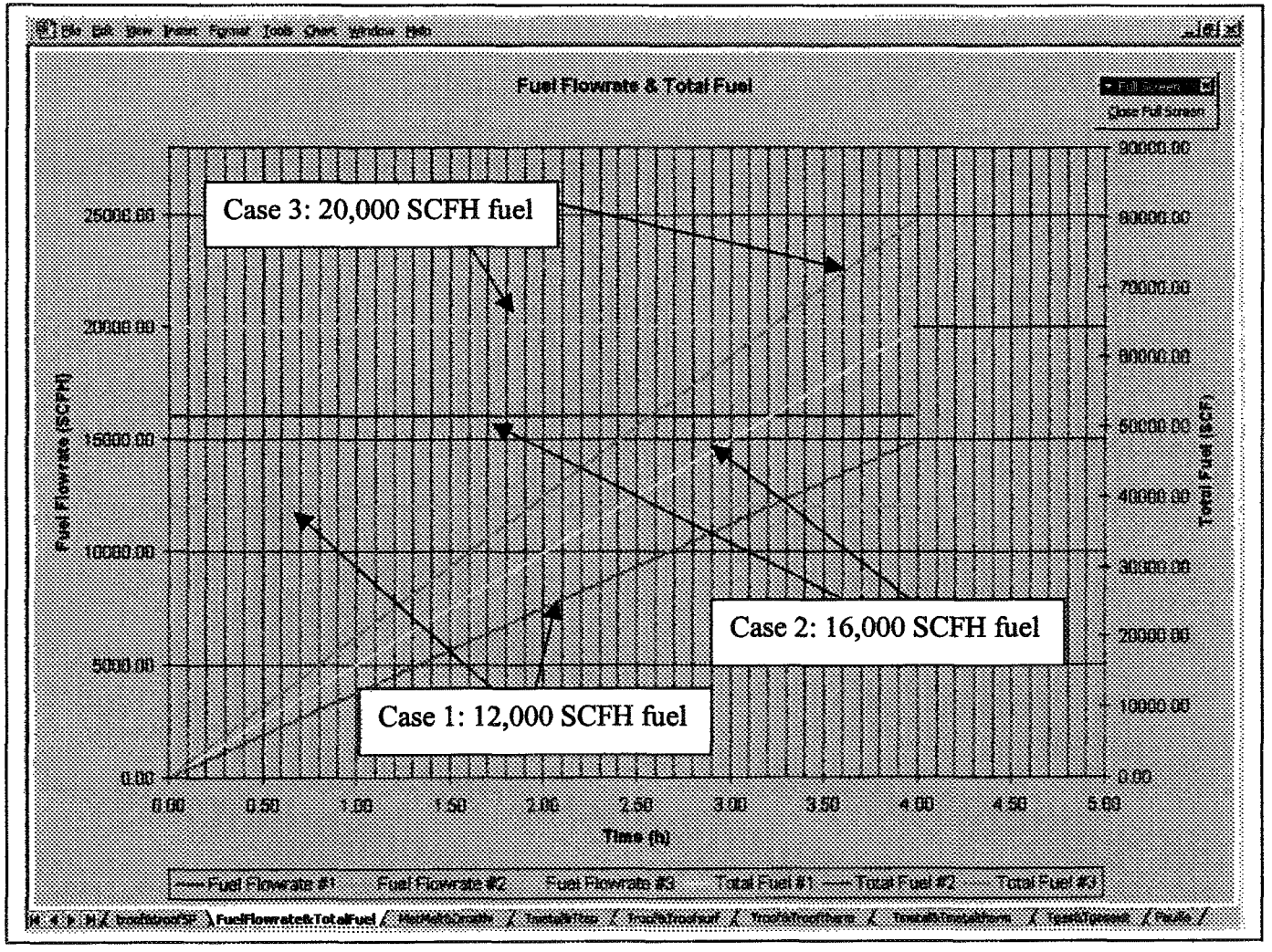
Fuel Flowrate & Total Fuel
Case 3: 20,000 SCFH fuel
Case 2: 16,000 SCFH fuel
Case 1: 12,000 SCFH fuel
Fuel Flowrate (SCFH)
Total Fuel (SCF)
Time (h)
25000.00
20000.00
15000.00
10000.00
5000.00
0.00
30000.00
25000.00
20000.00
15000.00
10000.00
5000.00
0.00
0.00
0.50
1.00
1.50
2.00
2.50
3.00
3.50
4.00
4.50
5.00
Fuel Flowrate #1
Fuel Flowrate #2
Fuel Flowrate #3
Total Fuel #1
Total Fuel #2
Total Fuel #3

(d)

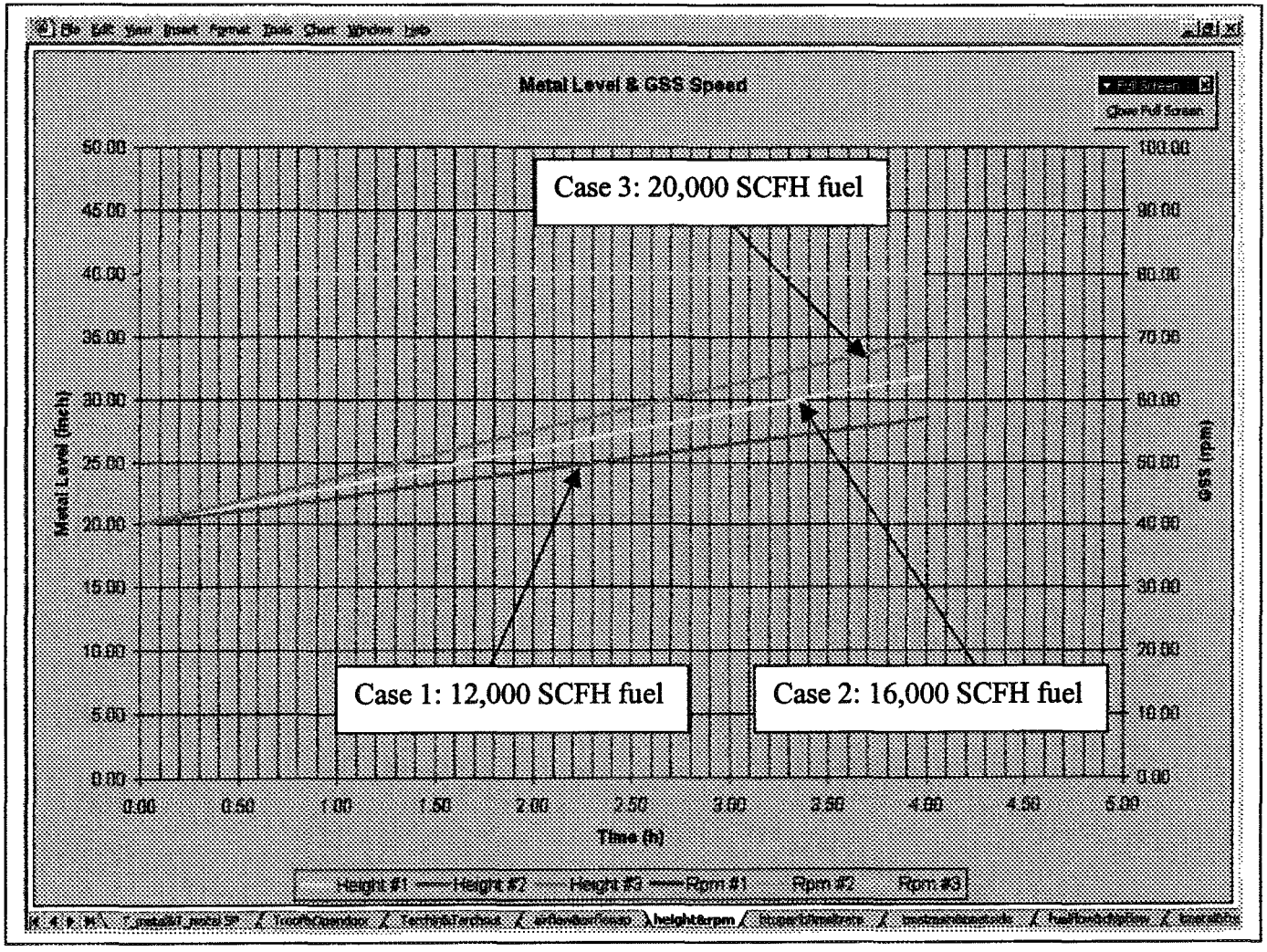

Figure 5.11: Impact of Fuel Flow Rate on Shred Melting Capacity: Comparison of Results for the Three Cases.

5.5.2 Effect of Dross Thickness on Furnace Operation

The impurities and oxides form a floating layer on the liquid metal called dross. This layer entraps some liquid metal as well. Its properties are not very well known. It is estimated that the amount of dross forms is about 1.5% of the metal melted. Its thermal conductivity is assumed as 3-5 W/m K. From time to time, dross is removed by skimming. This is done to avoid the accumulation of large amounts of dross. Also, the thermal conductivity of liquid aluminum is in the order of 125 W/m K, which means the conduction of heat from the metal surface to the interior of the liquid metal is much more efficient without the dross layer. Usually the thickness of dross layer is not uniform, and not the entire surface is covered with dross; but as an approximation in the case of this simplified model, the dross layer is uniformly distributed over the metal surface. Still, the results clearly demonstrate the negative effect of dross formation on furnace performance. Two studies were carried out in order to assess this effect.

Effect of the rate of dross formation (as % of metal melted): Two simulations were done using 0.5 and 2.5%. Results are given in Table 5.2. The shred feed rate is kept at 19,000 lbs/h and the fuel flow rate is maintained at 16,000 SCFH. Higher percentage results in more dross formation. When this layer gets thicker, the temperature difference between the top and bottom of the dross layer increases reducing the heat transfer to liquid metal. Then the metal is heated less efficiently and the refractory is heated to higher temperatures.

Table 5.2 : The Effect of Dross Formation Rate

Case No.	% (Dross Generated as % of Metal Melted)	Metal Temperature After 4 Hours (°C)	Refractory Temperature After 4 Hours (°C)	Results and Remarks
1	0.5	813	960	• Higher metal temperature. • Lower refractory temperature.
2	2.5	797	1012	• Lower metal temperature. • Higher refractory temperature

Figure 5.12 shows the model predictions: (a) the dross thickness, (b) metal temperature measured by the thermocouple, and (c) refractory roof temperature measured by the thermocouple. When the rate is 2.5 %, the dross layer thickness increases more rapidly. The temperature difference between the top and bottom surfaces of the dross layer increases yielding higher temperatures for the top surface. This reduces the heat transfer to metal resulting in lower temperatures for the liquid metal as well as a rapid rise in the refractory temperature. At a certain dross thickness, the limit may be reached where the temperature on the top surface of the dross layer approaches those of the gas and the refractory, thus, reducing the heat transfer so significantly that it may not be possible to maintain the temperature in the liquid bath and to melt the solid charge at the same time. Then the metal will start to cool down. At this point, the operation has to be stopped for skimming.

(a)

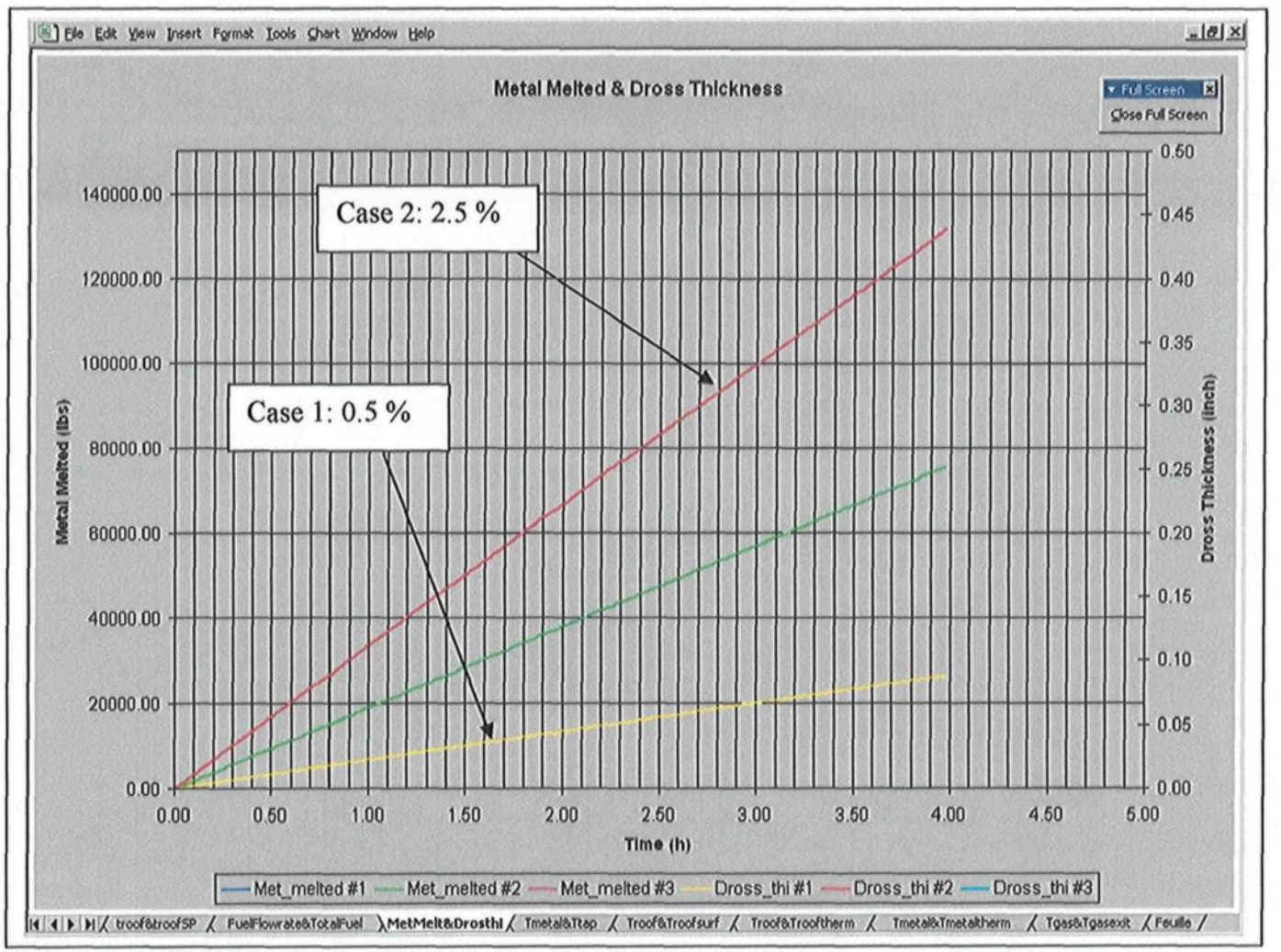
File Edit View Insert Format Tools Chart Window Help
Metal Melted & Dross Thickness
Full Screen
Close Full Screen
Case 2: 2.5 %
Case 1: 0.5 %
Metal Melted (lbs)
Dross Thickness (inch)
Time (h)
140000.00
120000.00
100000.00
80000.00
60000.00
40000.00
20000.00
0.00
0.60
0.45
0.40
0.35
0.30
0.25
0.20
0.15
0.10
0.05
0.00
0.00
0.50
1.00
1.50
2.00
2.50
3.00
3.50
4.00
4.50
5.00
Met_melted #1
Met_melted #2
Met_melted #3
Dross_thi #1
Dross_thi #2
Dross_thi #3
troof&troofSP
FuelFlowrate&TotalFuel
MetMelt&Drosthi
Tmetal&Ttap
Troof&Troofsurf
Troof&Troofthern
Tmetal&Tmetaltherm
Tgas&Tgasexit
Feuille

(b)

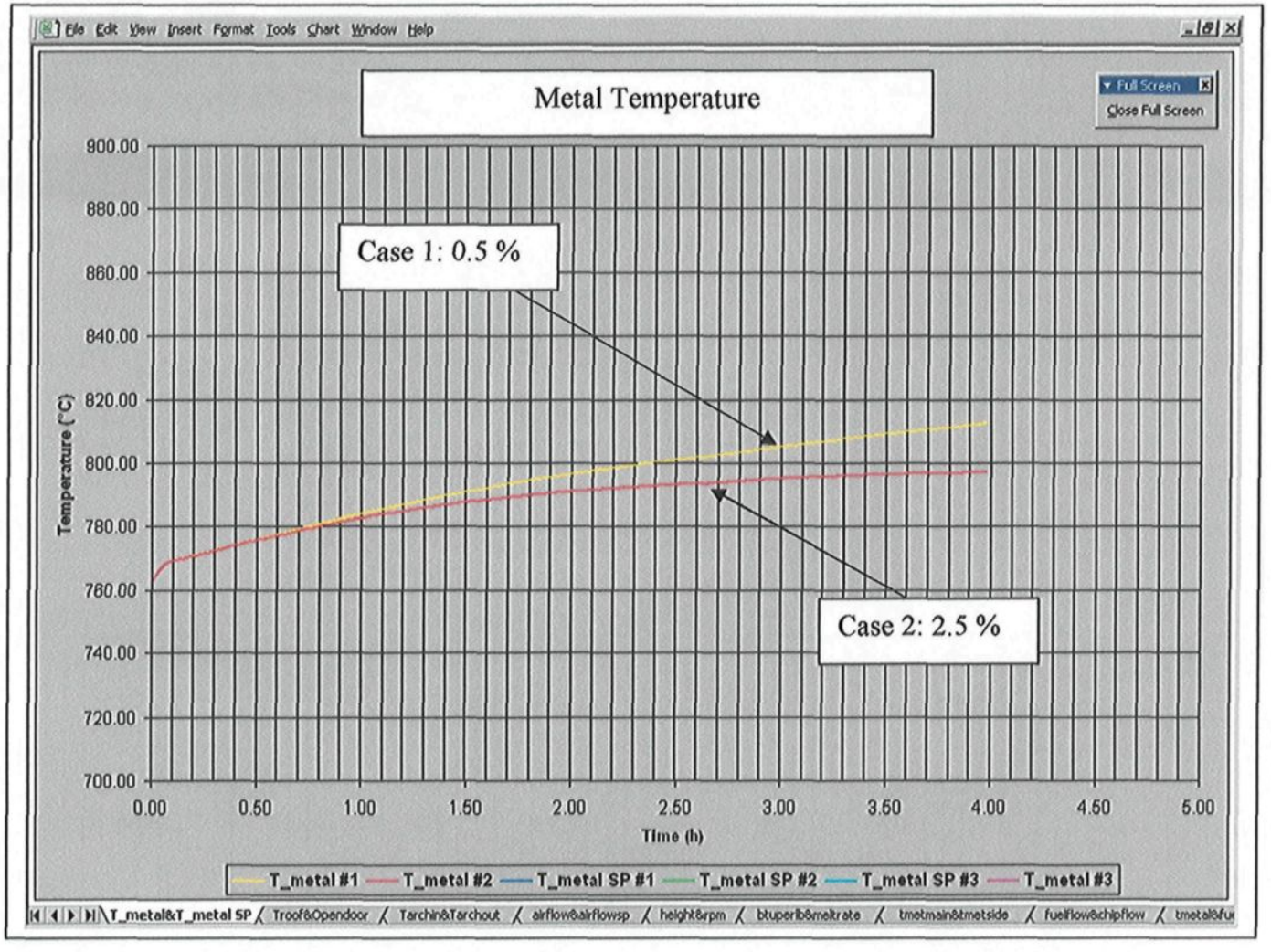
File Edit View Insert Format Tools Chart Window Help
Full Screen
Close Full Screen
Metal Temperature
Case 1: 0.5 %
Case 2: 2.5 %
Temperature (°C)
900.00
880.00
860.00
840.00
820.00
800.00
780.00
760.00
740.00
720.00
700.00
0.00
0.50
1.00
1.50
2.00
2.50
3.00
3.50
4.00
4.50
5.00
Time (h)
T_metal #1
T_metal #2
T_metal SP #1
T_metal SP #2
T_metal SP #3
T_metal #3
T_metal&T_metal SP
Troof&Opendoor
Tarchin&Tarchout
airflow&airflowsp
height&rpm
btuperlb&meltrate
tmetmain&tmetside
fuelflow&chipflow

(c)

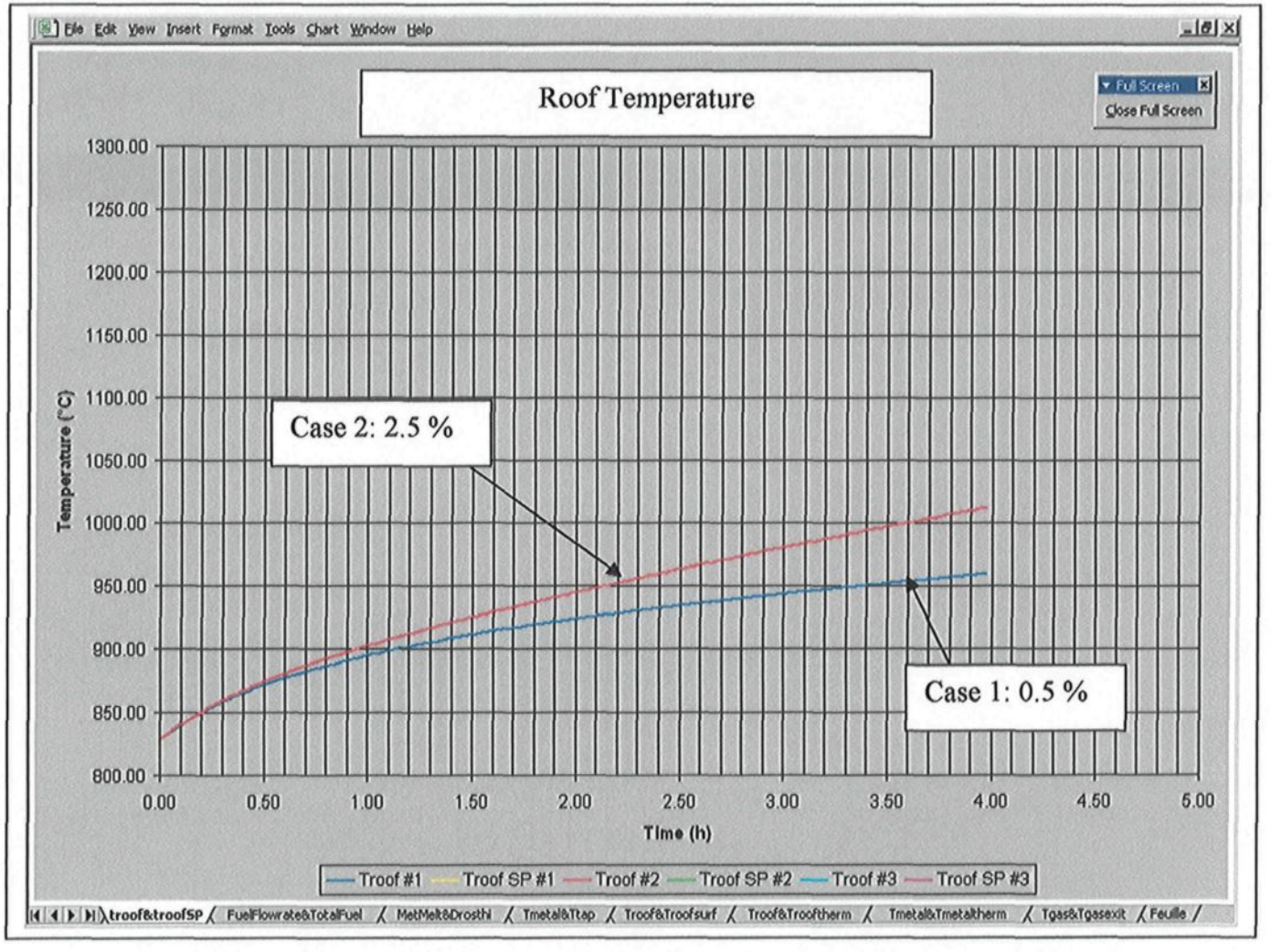

Figure 5.12: Impact of Dross Formation Rate on Furnace Performance: Comparison of Results for the Two Cases.

Effect of initial dross layer thickness: The objective of this study is again to demonstrate the negative effect of the dross on furnace performance. Two cases were simulated starting with different initial dross thickness. The shred rate was kept at 19,000 lbs/h. The fuel flow rate was adjusted in such a way that the metal was heated the same way for the two cases. The results are given in Table 5.3.

Table 5.3 : Effect of Initial Dross Thickness

Case No.	Initial Dross Thickness (inch)	Specific Energy Consumption (Btu/lb)	Refractory Temperature After 4 Hours (°C)	Results and Remarks
1	0.0	867	986	• Base Case. • Lower refractory temperature.
2	0.2	916	1033	• Higher refractory temperature. • Fuel consumption, and, consequently, specific energy consumption increase by 5.6%.

The refractory temperature rises more rapidly for Case 2 as expected. The fuel consumption and specific energy consumption increase by 5.6%. The model predictions are shown in Figure 5.13: (a) dross thickness, (b) metal temperature measured by the thermocouple, (c) refractory roof temperature measured by the thermocouple, and (d) the fuel flow rate and the total fuel consumption. It is important to carry out skimming in the furnace at appropriate intervals.

(a)

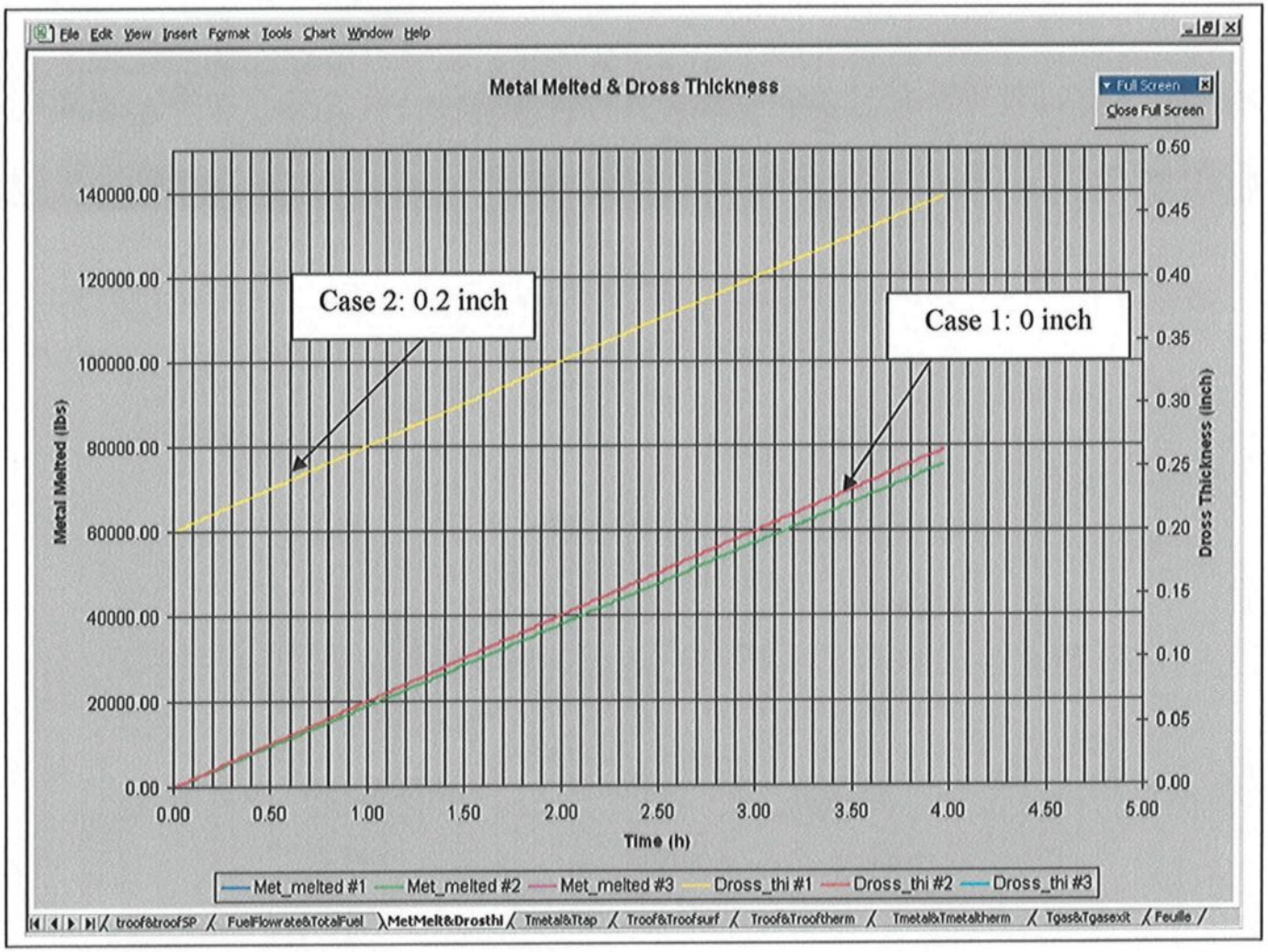
File Edit View Insert Format Tools Chart Window Help
Metal Melted & Dross Thickness
Full Screen
Close Full Screen
Case 2: 0.2 inch
Case 1: 0 inch
Metal Melted (lbs)
Dross Thickness (inch)
Time (h)
0.00
20000.00
40000.00
60000.00
80000.00
100000.00
120000.00
140000.00
0.00
0.50
1.00
1.50
2.00
2.50
3.00
3.50
4.00
4.50
5.00
0.05
0.10
0.15
0.20
0.25
0.30
0.35
0.40
0.45
0.50
Met_melted #1
Met_melted #2
Met_melted #3
Dross_thi #1
Dross_thi #2
Dross_thi #3
troof&troofSP
FuelFlowrate&TotalFuel
MetMelt&Drosthi
Tmetal&Ttap
Troof&Troofsurf
Troof&Troofthem
Tmetal&Tmetalthem
Tgas&Tgasexit
Feuille

(b)

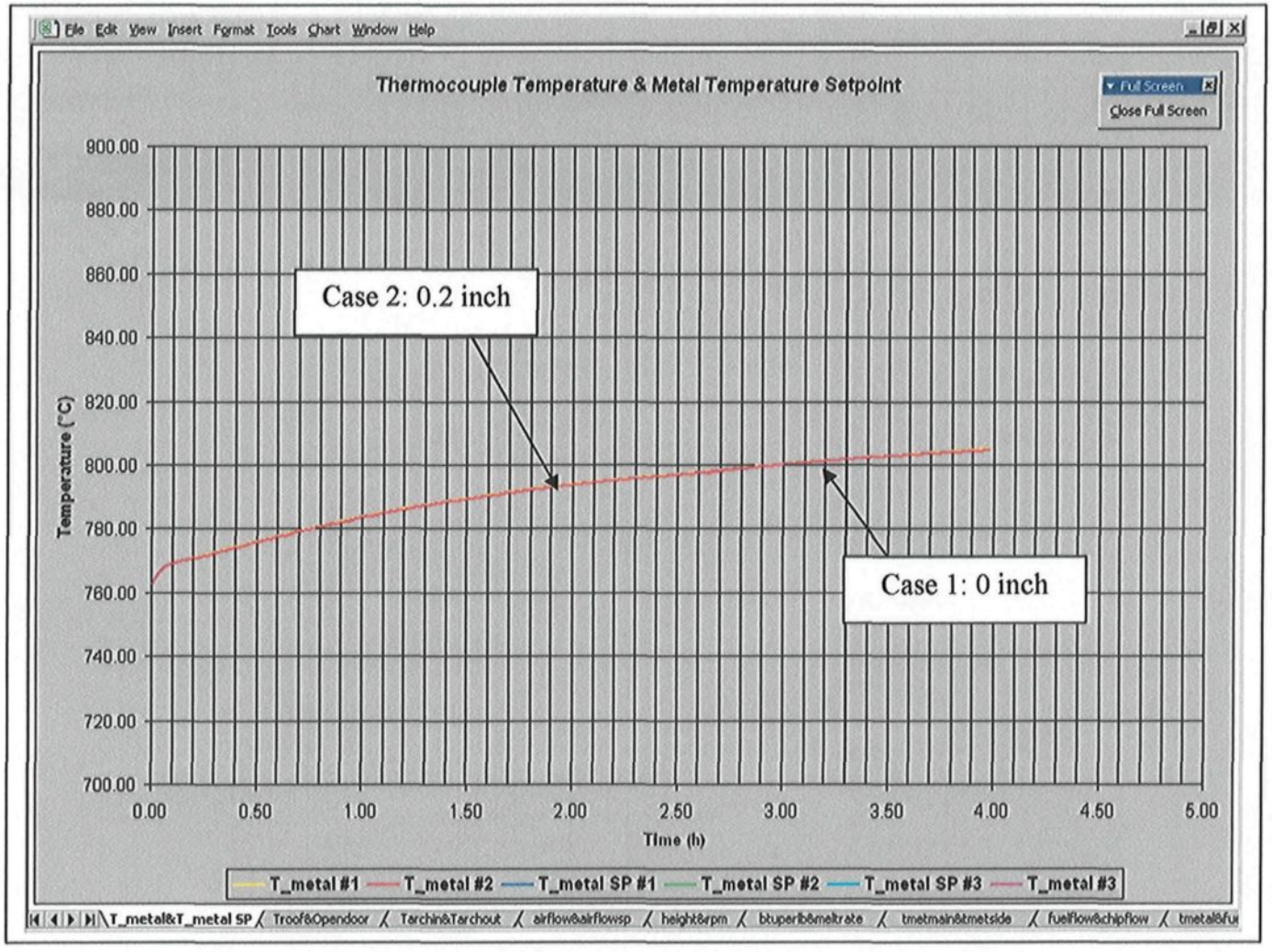
File Edit View Insert Format Tools Chart Window Help
Thermocouple Temperature & Metal Temperature Setpoint
Full Screen
Close Full Screen
Case 2: 0.2 inch
Case 1: 0 inch
Temperature (°C)
900.00
880.00
860.00
840.00
820.00
800.00
780.00
760.00
740.00
720.00
700.00
0.00
0.50
1.00
1.50
2.00
2.50
3.00
3.50
4.00
4.50
5.00
Time (h)
T_metal #1
T_metal #2
T_metal SP #1
T_metal SP #2
T_metal SP #3
T_metal #3
T_metal&T_metal SP
Troof&Opendoor
Tarchin&Tarchout
airflow&airflowsp
height&rpm
btuperlb&meltrate
tmetmain&tmetside
fuelflow&chipflow

(c)

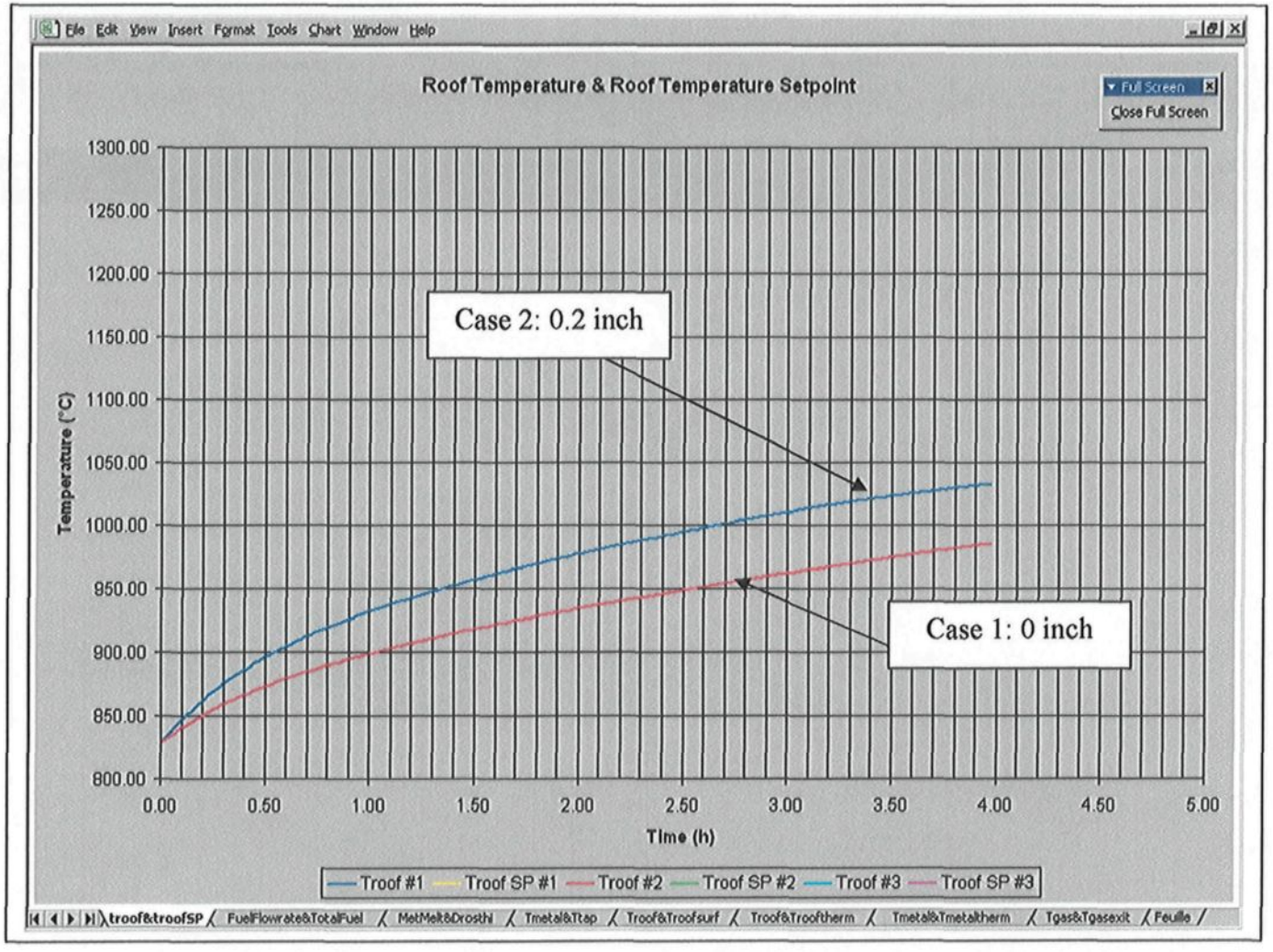
File Edit View Insert Format Tools Chart Window Help
Roof Temperature & Roof Temperature Setpoint
Full Screen
Close Full Screen
1300.00
1250.00
1200.00
1150.00
1100.00
1050.00
1000.00
950.00
900.00
850.00
800.00
Temperature (°C)
0.00
0.50
1.00
1.50
2.00
2.50
3.00
3.50
4.00
4.50
5.00
Time (h)
Case 2: 0.2 inch
Case 1: 0 inch
Troof #1
Troof SP #1
Troof #2
Troof SP #2
Troof #3
Troof SP #3
troof&troofSP
FuelFlowrate&TotalFuel
MetMelt&Drosthi
Tmetal&Ttap
Troof&Troofsurf
Troof&Troofthern
Tmetal&Tmetaltherm
Tgas&Tgasexit
Feuille

(d)

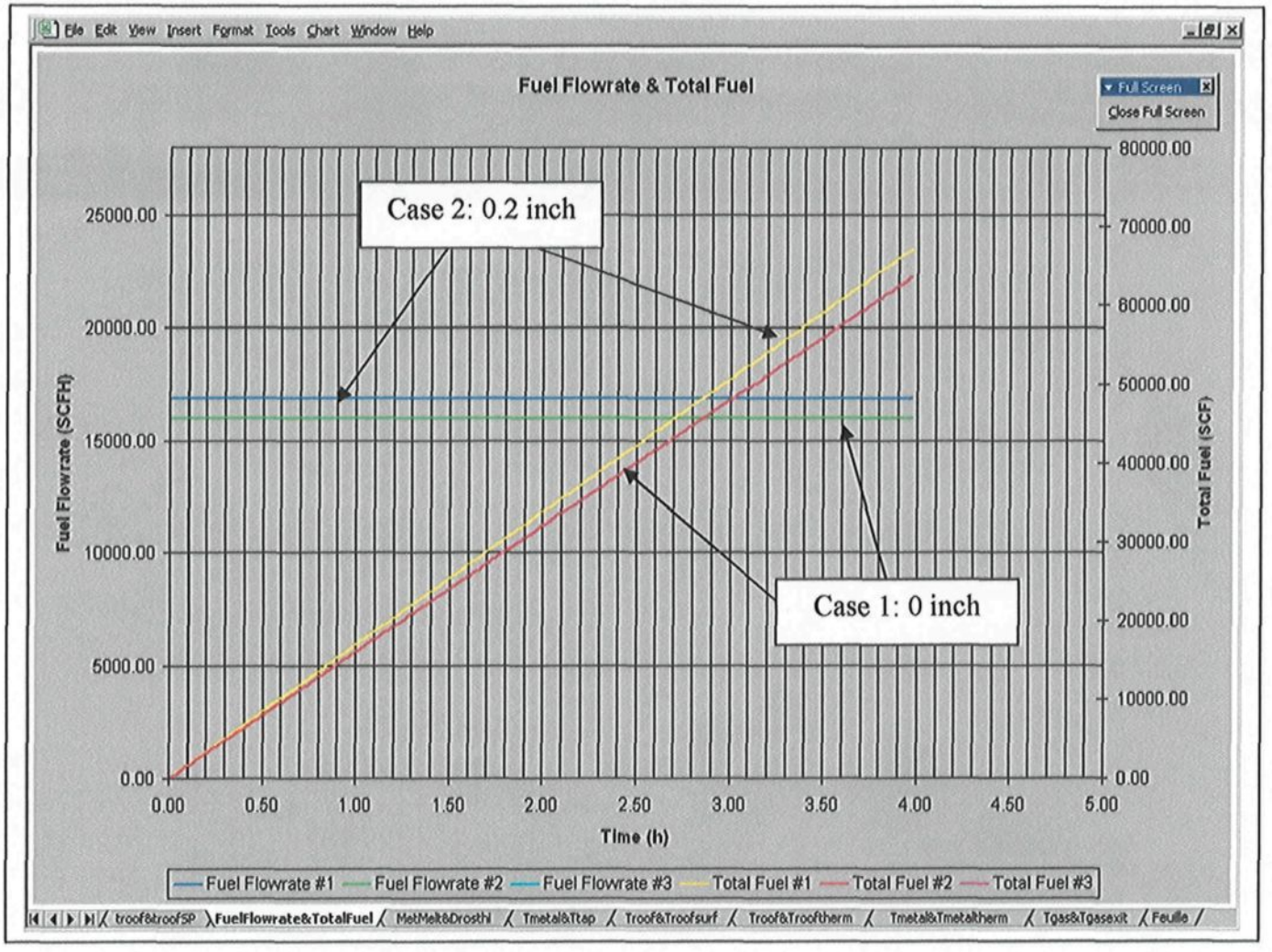

Figure 5.13: Impact of Initial Dross Thickness on Furnace Performance: Comparison of Results for the Two Cases.

5.6 Conclusions

The dynamic model accounts for all the important phenomena occurring in the sidewell furnace and has been used to carry out a large number of studies to improve the furnace operation and control. The overall findings can be summarized as follows:

1. The metal thermocouple should be placed near the inlet arch. The metal temperature measured here represents the average metal temperature better, and a better control is achieved by not over or under-heating the metal.
2. The maximum refractory temperature should be set as high as possible to increase production by either decreasing the melting period (shorter batches) or increasing the melting capacity.
3. Preheating the combustion gas or any solid charged to the furnace increases the energy efficiency, and, thus, furnace performance.
4. Maintaining as high a rotational impeller speed as possible improves the furnace operation by increasing the two important flow characteristics: circulation between the main hearth and side well and mixing in the main hearth.
5. The heat transfer to metal, and consequently, the shred melting capacity can be improved by increasing the fuel flow rate at the expense of furnace efficiency.
6. Dross layer has a negative impact on furnace operation and should be removed appropriately.
7. The model is being used for many other studies in an effort to improve and optimize the sidewell furnaces.

CHAPTER 6

CONCLUSIONS AND RECOMMENDATIONS

6.1 Conclusions

The current project is the first comprehensive study on sidewell furnaces. Many important phenomena have been investigated in detail. Four different models were developed as tools to study and to optimize the design parameters as well as the control and operation of the sidewell furnaces:

1. A 3D steady-state flow model for the metal using CFX,
2. A combustion chamber model based on one-gas-zone model,
3. A 3D transient heat transfer model for the metal, and
4. A global dynamic model of the furnace with a control emulator.

Each of these models consists of a number of coupled sub-models ranging from zero dimensional and steady-state to three dimensional and transient in nature. Each one was built to study different aspects of the sidewell furnace design and operation. The models built for control purposes are usually zero dimensional, or one-dimensional at the most. The sidewell simulator built in this project, which combines a dynamic furnace model with a control emulator, solves for the heat transfer in the liquid metal bath in three dimensions. This was made possible by imposing the flow, which was calculated by the

three-dimensional flow model, in the dynamic model. This is an original approach which can be adopted to other types of modelling work.

The results of each model are discussed and the conclusions are presented in the relevant chapters. The overall conclusions are given below:

1. There is an optimum ratio for the dimensions of the different geometrical components of the furnace.
2. The impeller has an optimum position. The circulation rates decrease when it is moved away from that position.
3. The pump angle has an optimum value and may affect the circulation in the furnace adversely if it is not positioned properly.
4. Baffle type has a strong effect on circulation rates. Rectangular baffles give better circulation, and less susceptible to penalties (decrease in circulation) if the impeller is not at the optimum position.
5. It is important to have reasonable metal circulation rates between the side well and the main hearth as well as reasonable levels of mixing in the main hearth. The heat transfer depends strongly on these variables.
6. Good mixing and circulation rates result in improved heat transfer efficiencies which could lead to energy savings or increased production.
7. The preheating of the shreds, sows and combustion air increases the furnace efficiency. Air preheating can be realized relatively easily using the regenerative burners.

8. The maximum refractory roof temperature should be set as high as physically possible. It creates great potential for increased production.
9. Thermocouple locations (both refractory and metal) are very important for appropriate temperature readings as well as proper control of the furnace.
10. The furnace control is adequate; however, there seems to be room for improvement.

The combustion chamber model is a simple one, but it takes into account all the important phenomena and represents the current enclosure reasonably well. However, in order to improve the design of the combustion chamber (burner configuration, dimensions, chimney position, fuel type, various emissions, etc.), a more detailed model would be needed.

The models have been validated using data from the water model and plants. It is difficult to carry out detailed measurements in sidewell furnaces. The data that are normally measured during operation were available from plants. They were used for the validation. All the model predictions were in good agreement with the laboratory and plant data. Many of the recommendations from this project have been or are in the process of being implemented in the plants.

6.2 Recommendations

A significant amount of work has already been done on sidewell furnaces in this project. Development in two areas could lead to further improvement of the furnace design and operation. The first one is, as mentioned previously, the design of the combustion chamber. The second is the review of the control strategy. The cascade controller seems to be adequate, but it usually works in a manner similar to on/off type controller. It is

important to review and evaluate this in order to verify and improve, if necessary, the furnace control. The recommendations can be summarized as follows:

1. For new furnaces, recommended design criteria can be used.
2. For existing furnaces, recommendations can be implemented as much as possible.
3. It would be advisable to form a committee of experts and to review the control strategy used.
4. The combustion chamber can be modelled in more detail to improve design and operation as well as burner configuration.
5. The dynamic model can be modified slightly and adapted to other furnaces. There is potential for the development of a more general tool.
6. The model's interface can be further improved to facilitate its access to potential users.

APPENDIX 1

SUMMARY

Aluminum recycling has many positive effects on economy and environment. It helps conserve the natural resources, decrease the energy consumption by 95%, and reduces the cost of aluminum. Today, recycling is a major component of the aluminum industry. The beverage cans constitute the most important category of recycled material in quantity and quality. In general, the shredded cans are melted in sidewell furnaces.

Recycling industry is growing very rapidly. To remain competitive, the industry has to optimize its performance by lowering the energy costs and maximizing the productivity. For this reason, a project has been undertaken for the development of models for sidewell furnaces. Using these models, the parameters affecting the operation and design of these furnaces can be studied. Thus, the objective of the current project is to develop tools that could be used to improve and optimize the sidewell furnaces. These tools are:

- A 3D general mathematical model to carry out detailed studies to determine the best furnace geometry, and best impeller and pump positions in order to improve the melt rate and metal circulation,
- A simplified dynamic mathematical model to assess different control strategies and operating conditions.

The furnace consists of two parts: a side well where the decoated and shredded chips of cans are fed and a main hearth where the heat is provided for the system. The inlet and outlet arches provide the metal circulation between these two sections. In the side well, an impeller is installed for quick submergence of shreds. A baffle is located next to the impeller to increase the metal circulation. In some plants, a jet pump is also installed in the main hearth to provide good mixing in the liquid metal.

The performance of a melting furnace can be characterized by energy efficiency and melt rate. These parameters depend strongly on the effective transfer of heat from the combustion chamber where it is generated to the point of utilization. The heat is required to maintain the liquid metal at a certain temperature as well as to melt the shred fed to the side well and the solid metal charged to the main hearth.

The project consists of four parts. The first part is the development of a 3D model to calculate the isothermal flow field in the liquid metal. The partial differential equations of continuity, momentum in three directions, and the turbulence are solved using the commercial code CFX. A large number of simulations were carried out to study the effects of different parameters on metal flow. Based on the results, the pump and impeller positions, the type and length of the baffle, the arch dimensions, the width of the side well, and the dimensions of the main hearth were optimized so as to provide an improved circulation in the liquid metal.

The second part is the modelling of the combustion chamber. A one-gas-zone model was developed to calculate the heat transfer to metal surface (as well as to refractories) by radiation and convection. This model does not give detailed temperature and heat flux

distributions; however, it is simple and accounts for all the important phenomena in the combustion chamber. Also, the computation time is very short. A parametric study has already been carried out to determine the effects of different factors on the heat transfer to metal. The results show that the heat transfer to metal surface can be improved by increasing the fuel flow rate or the combustion air temperature. The fuel flow rate has a significant impact, but the furnace efficiency decreases with increasing fuel flow rate. The preheating of the combustion air, however, increases the heat transfer as well as the furnace efficiency. It is also important to provide appropriate mixing in the metal bath to maintain as low a surface temperature as possible to improve the heat transfer to metal.

The third part is the global modelling of the furnace in 3D. Due to the dynamic character of the process, transient heat transfer in the liquid metal is also incorporated into the metal bath model of the first part. Then the model is coupled with the combustion chamber model of the second part. In order to run the model in a reasonable time, the isothermal flow field calculated in the first part is imposed and only the transient enthalpy equation is solved in the metal bath. The results indicate that the forced convection is a very important factor. The temperature gradient decreases with increasing flow through the arches and circulation in the main hearth. The average gradient is reduced by 50 % (from about 80°C to 40°C) by adding the baffle, and by 80-90% (from about 80°C to 10°C) with the addition of a baffle and a pump.

The fourth part of the project is the development of a dynamic model to improve the control and the process itself. The sidewell furnace is a highly dynamic system, and everything varies with time. To study the actual operation, a dynamic model is necessary.

The model is constructed based on a modular structure in two parts: one for the metal and one for the combustion chamber. The two parts are built separately and then coupled resulting in the global model. The interface between the models is located on the metal surface. It is a simplified model, but it accounts for all the important phenomena and all the events taking place in the furnace. This model serves as a virtual furnace. A control emulator is added, and a simulator for the sidewell furnaces is thus created. A user-interface is also constructed to facilitate the use of the simulator, and it is transferred to industry for different applications. Many studies have already been carried out. The effects on the furnace performance have been studied for the thermocouple position, maximum allowable refractory temperature, preheating of the metal charged and the combustion air. The improvements obtained from the results of these studies have been, or are being, implemented in the plants.

All the models have been validated using the experimental data from the laboratory and the plants. All the model predictions have been confirmed by plant observations or data.

APPENDIX 2

CONSERVATION EQUATIONS AND FINITE VOLUME TECHNIQUE

A.2.1 Conservation Equations

The conservation equations can be derived by writing the differential equations for a fixed differential control volume[12,48-50]. The mass balance is called the continuity equation:

$$\frac{\partial \rho}{\partial t} + \nabla \bullet (\rho \vec{V}) = 0 \qquad [A.2.1]$$

The momentum equation for laminar flow can also be obtained directly from the second law of Newton written for a unit volume:

$$\rho \frac{d\vec{V}}{dt} = \sum f \qquad [A.2.2]$$

where $d\vec{V}/dt$ is the total acceleration:

$$\frac{d\vec{V}}{dt} = \frac{\partial \vec{V}}{\partial t} + u\frac{\partial \vec{V}}{\partial x} + \mathrm{v}\frac{\partial \vec{V}}{\partial y} + w\frac{\partial \vec{V}}{\partial z} \qquad [A.2.3]$$

and the resultant force is the sum of body and surface forces:

$$\sum f = \rho \vec{g} - \nabla P + \nabla \bullet \tau \qquad [A.2.4]$$

The first term on the right hand side is the gravity force (body force), and the second and third terms are the pressure and viscous forces (surface forces) where τ represents the viscous stresses (a tensor). Equation [A.2.3] can be written as:

$$\rho\frac{d\vec{V}}{dt}=\rho\frac{d\vec{V}}{dt}+\vec{V}\left[\frac{\partial\rho}{\partial t}+\nabla\bullet(\rho\vec{V})\right]= \\ \frac{\partial}{\partial t}(\rho\vec{V})+\frac{\partial}{\partial x}(\rho u\vec{V})+\frac{\partial}{\partial y}(\rho v\vec{V})+\frac{\partial}{\partial z}(\rho w\vec{V}) \qquad [A.2.5]$$

The general momentum equation for laminar flow becomes:

$$\left[\frac{\partial}{\partial t}(\rho\vec{V})\right]+\left[\frac{\partial}{\partial x}(\rho u\vec{V})+\frac{\partial}{\partial y}(\rho v\vec{V})+\frac{\partial}{\partial z}(\rho w\vec{V})\right] \\ -[\nabla\bullet\tau]=[\rho\vec{g}-\nabla P] \qquad [A.2.6]$$

The first term on the left hand side is the transient term, the second and third terms are convection and diffusion terms, the term on the right hand side is the source term.

If the flow is Newtonian, the viscous stresses are proportional to the strain rate and the viscosity:

$$\nabla\bullet\tau=\nabla\bullet(\mu\nabla\bullet\vec{V}) \qquad [A.2.7]$$

Substituting Equation [A.2.7] into [A.2.6] results in the Navier Stokes equations.

The energy equation is given by:

$$\frac{\partial(\rho H)}{\partial t}+\nabla\bullet(\rho\vec{V}H)-\nabla\bullet(k\nabla T)=\frac{\partial P}{\partial t} \qquad [A.2.8]$$

where H is the total enthalpy defined as:

$$H=h+\frac{1}{2}\left|\vec{V}\right|^2 \qquad [A.2.9]$$

h is the static (thermodynamic) enthalpy, and the second term is the kinetic energy contribution. For incompressible and weakly compressible flow (Mach number < 0.3), the kinetic energy term is negligible; then h becomes equal to H. The thermodynamic enthalpy is related to temperature and pressure through a constitutive equation.

For turbulent flow, Reynolds time averaging is used[12,16,50]. Every variable is defined as the sum of time averaged value plus the fluctuating component. For example, u velocity component is written as u=ū+u'. When these variables are substituted into the momentum and energy equations, additional terms are obtained. In momentum equation, the diffusion term becomes:

$$\nabla(\mu \nabla \bullet \vec{V} - \rho \overline{V_i' V_j'}) \qquad [A.2.10]$$

The second term is called the Reynolds or turbulent stresses. These are actually the convective acceleration terms (not stresses) which account for the contributions of fluctuating velocity components over and above those caused by the fluctuations at the molecular level. They have the mathematical effect of stresses and occur right next to the laminar Newtonian stresses; and this gives rise to the universal use of the above terminology. Here the turbulence modelling comes in. Many models have been developed to represent the Reynolds stresses. In the present project, the K-ϵ model is used. Two additional partial differential equations are solved for K, the kinetic energy of turbulence, and ϵ, the rate of dissipation of turbulence. The diffusion term is redefined using an effective viscosity which is the sum of molecular and turbulent viscosities:

$$\begin{aligned} \nabla \bullet \tau_{eff} &= \nabla \bullet (\tau + \tau_t) \\ &= \nabla \bullet (\mu_{eff} \nabla \bullet \vec{V}) = \nabla \bullet \left[(\mu + \mu_t) \ \nabla \bullet \vec{V} \right] \end{aligned} \qquad [A.2.11]$$

The turbulent viscosity is calculated from K and ϵ:

$$\mu_t = C_\mu \rho (K^2 / \varepsilon) \qquad [A.2.12]$$

In the energy equation, the diffusion term becomes:

$$\nabla \bullet (k \nabla T - \rho \overline{V_i' H}) \qquad [A.2.13]$$

Here the second term is called the Reynolds or turbulent fluxes. Again similar to the momentum equation, these terms reflect the fact that the convective transport due to turbulent velocity fluctuations will enhance mixing over and above that caused by thermal fluctuations at the molecular level. In turbulent flow, the total enthalpy is defined as:

$$H = h + \frac{1}{2} \left| \vec{V} \right|^2 + K \qquad [A.2.14]$$

which now includes the turbulent kinetic energy contribution. The diffusion term is rearranged as:

$$\nabla \bullet \left[(\frac{k}{c_p} + \frac{\mu_t}{\sigma_H}) \nabla H \right] \qquad [A.2.15]$$

Again, for incompressible and weakly compressible flow, H can be taken equal to h neglecting the kinetic energy terms. σ_H is known as the turbulent Prandtl number.

For further details for the turbulence models, the reader is referred to references 12, 16, 48-50.

A.2.2 Finite Volume Technique

All the conservation equations of momentum, energy and mass transport (not the equation of continuity) can be represented in the following form[16] (see Equations [A.2.6] and [A.2.8] for momentum and energy):

$$\frac{\partial}{\partial t}(\rho \phi) + \nabla \bullet (\rho \vec{V} \phi) - \nabla \bullet (\Gamma \nabla \phi) = S_{\phi} \qquad [A.2.16]$$

where ϕ is the general variable (velocity components, enthalpy or species concentrations), and the term on the right hand side is the source term which represent gravity and pressure forces as well as any other force such as coriolis and centrifugal forces. In the case of an impeller, a term is added in the source which represents the force applied onto the fluid by the impeller blades. This will be discussed in more detail in Appendix 3.

There are mainly two numerical methods to solve these equations: finite volume and finite element methods[14-15]. CFX is based on the finite volume method[16]. The calculation domain is divided into a number of discrete finite volumes called cells. Each term in the above equation is integrated over the finite cell volume. The integration of the convection terms needs to be carried out carefully depending on the flow regime. The partial differential equations are converted to a set of algebraic equations. Solution gives the distributions of dependent variables over the discretized domain. Based on the velocity and density distributions (of course, density is constant for incompressible and weakly compressible flow), the mass balance is verified for each cell using the equation of continuity. This is done by calculating the mass residuals for the cells. Ideally, the residuals should be zero but they rarely are. Iterations are required to obtain the solution. As the

solution approaches the final result, mass residuals should decrease. This is called convergence. The iterations are stopped when the residuals are reduced below a certain tolerance. If the mass residuals are increasing, the solution is said to be diverging. Precautions have to be taken to avoid divergence. For further details concerning the numerical solution of transport equations, see references 14-16, 53, 72.

APPENDIX 3

MATHEMATICAL REPRESENTATION OF THE IMPELLER

A.3.1 Force Applied by an Impeller Blade onto the Fluid

The rate of change of momentum is equal to a force. That is why the momentum equation can be derived directly from the second law of Newton (see Appendix 2). In the case of an impeller, there is a momentum transfer from the blades to the fluid. A quantity of fluid with a mass flow rate $\dot{m}$ crossing an area A_n has a rate of change of momentum given by:

$$df_n = d\dot{M} = \dot{m}\,dV = \rho\, A_n\, V\, dV \qquad [A.3.1]$$

If this momentum change is caused by a blade sweeping through the fluid, a blade coefficient similar to the drag coefficient is added:

$$df_n = C_B\, \rho\, A_n\, V\, dV \qquad [A.3.2]$$

Integration of this equation gives:

$$f_n = \frac{1}{2} C_B\, \rho\, A_n\, V^2 \qquad [A.3.3]$$

During this momentum transfer, the fluid velocity increases from its initial value before the contact with the blade to a value equivalent to the blade velocity. Therefore, the integral

limits are from the fluid velocity to the blade velocity, both normal to the blade area. Thus, the force applied by the blade in the normal direction is[27]:

$$f_n = \frac{1}{2} C_B \rho A_n \left[(V_b|_n)^2 - (V_f|_n)^2 \right] \qquad [A.3.4]$$

The impeller velocity tangent to the blades can be found by taking the cross product of the angular velocity and the position vector. Dot product of the resultant vector with the unit vector normal to the blade area gives the desired blade velocity in the normal direction:

$$V_b|_n = (\vec{w} \times \vec{r}) \bullet \vec{\lambda} \qquad [A.3.5]$$

Similarly, the dot product of the fluid velocity with the same unit vector yields the desired fluid velocity in the normal direction:

$$V_f|_n = \vec{V}_f \bullet \vec{\lambda} \qquad [A.3.6]$$

The unit vector normal to the blade area is defined in terms of its directional cosines:

$$\vec{\lambda} = \cos\gamma_x \, \vec{i} + \cos\gamma_y \, \vec{j} + \cos\gamma_z \, \vec{k} \qquad [A.3.7]$$

where γ_x, γ_y, and γ_z are the angles between the normal and the x, y, and z axes. Substituting [A.3.5] and [A.3.6] into the Equation [A.3.4], the normal force can be re-written as:

$$f_n = \frac{1}{2} C_B \rho A_n \left\{ \left[(\vec{w} \times \vec{r}) \bullet \vec{\lambda} \right]^2 - \left[\vec{V}_f \bullet \vec{\lambda} \right]^2 \right\} \qquad [A.3.8]$$

This is the force applied by the impeller onto the fluid. It should be noted that it is possible to arrive at different equations if different hypotheses are used in the treatment of velocity in Equation [A.3.3]. The blade coefficient has to be adjusted and assigned proper values coherent with the hypotheses. Also, only the normal force is calculated and the tangential

force on the blade surface is neglected since it depends on the first power of velocity as opposed to the second power dependence of the normal force.

A.3.2 Source Terms in Momentum Equation

The blade area has to be calculated per unit volume, and it is given by:

$$A_n = n / 2 \pi r \qquad [A.3.9]$$

where n is the number of blades. The components of the normal force in coordinate axes are found by multiplying it with the normal unit vector:

$$\vec{f} = f_n \vec{\lambda} = f_x \vec{i} + f_y \vec{j} + f_z \vec{k} \qquad [A.3.10]$$

The source terms in the x-, y-, and z-momentum equations can now be written as[26]:

$$S_u = f_x \qquad S_v = f_y \qquad S_w = f_z \qquad [A.3.11]$$

The above approach has been used for a number of systems successfully. It is always possible to represent the impeller and its geometry as rigorously as one wishes. This requires many computational cells and is desirable when one is interested only in the impeller itself. If a large system is being modelled, detailed representation of the impeller would lead to excessive number of cells, and, consequently, prohibitive computation times. In these cases, impeller has to be represented properly but using much smaller number of cells; that is where reliable models such as the one given above need to be implemented.

APPENDIX 4

PHYSICAL MODELLING OF SIDEWELL FURNACES

A.4.1 Water Model Design and Similarity Criteria

Physical modelling was needed to test some of the observations from the plants and the predictions of the 3D mathematical model for the liquid metal flow. A project was undertaken to build a pilot size physical model of the sidewell furnace given in Table 1.1 of Chapter 1. The objective was to provide data for the validation of the mathematical model and to determine its reliability. Due to space limitations and availability of resources, the pilot system was set up at a scale of 0.3. This is a reasonable size; it is large enough to represent the process properly and is not too small to modify the relative importance of different phenomena taking place in the actual system. For example, if the liquid depth is reduced too much (if it becomes too shallow), the wall effects (roughness, shear stress) may govern the flow pattern rather than the geometry, impeller and the pump.

In physical modelling, respecting the similarity between the model and the actual system is important[12]. First criterion is the geometric similarity: this ensures that the model has the same length scale as the system. The dimensions of the sidewell furnace was scaled down by 0.3, except for the impeller dimensions (diameter and blade height) for which the

ratio was 0.24 (due to availability of resources). The difference in ratios (0.3 versus 0.24) is small, and geometric similarity can be assumed respected.

The second criterion is the kinematic similarity: the ratio for the length and time scales has to be the same which ensures that the velocity-scale ratio remains the same as well. For free surface flows, the Froude number is the dimensionless number which provides the kinematic similarity:

$$Fr = V^2 / g L \qquad [A.4.1]$$

Since the gravitational acceleration cannot be modified, the Froude number is a purely kinematic parameter since it contains characteristic length and velocity.

The third criterion is the dynamic similarity. For this, the model and the system should have the same length-scale ratio, time-scale ratio and the force-scale or mass-scale ratios. This means that geometric similarity must exist; also dynamic similarity, simultaneous with the kinematic similarity, should be respected. Then the body and surface forces will be in the same ratio and have equivalent directions. The Reynolds number is the dimensionless number that characterizes the flow and is a dynamic similarity parameter:

$$\mathrm{Re} = L V / \upsilon \qquad [A.4.2]$$

For free surface flows, the Froude number defined by Equation [A.4.1] is necessary as well. For the impeller and the pump, the attempt was made to use these two numbers for similarity, but it is not possible to have both respected. More information on similarity of systems is available in a number of refrences[12, 49-50].

In order to carry out measurements, the liquid in the model has to be transparent to be able to visualize the flow. Water is in general chosen due to its availability,

transparency, safety, etc. Liquid aluminum flow in the sidewell furnace is Newtonian like water. The kinematic viscosity of water is 1×10^{-6} m^2/s at 25°C, and the kinematic viscosity of aluminum is 1.8×10^{-6} m^2/s at 750°C. Even though the values are not the same, the difference is not drastic; this allows the use of water for modelling aluminum in many studies.

A.4.2 Similarity Criteria for Impeller[30-31,38,49]

The primary function of the impeller is the submergence of the shred fed to the side well. The vortex shape has to be maintained to achieve this. The characteristic velocity for an impeller is the tangential (linear) velocity at the tip which is equal to the radius times the rotational speed "ω". The characteristic length is the impeller diameter "d". The Reynolds number for an impeller is defined as:

$$\mathrm{Re}_I = d^2\,\omega / \nu \qquad [A.4.3]$$

For the model and the system to be similar, the following should hold true:

$$\frac{\omega_2}{\omega_1} = \left(\frac{\nu_2}{\nu_1}\right)\left(\frac{d_1}{d_2}\right)^2 \qquad [A.4.4]$$

The Froude number for the impeller is given by:

$$Fr_I = \frac{d\omega^2}{g} \qquad [A.4.5]$$

and the following condition should be satisfied for similarity:

$$\frac{\omega_2}{\omega_1} = \left(\frac{d_1}{d_2}\right)^{1/2} \qquad [A.4.6]$$

When the numbers are substituted in Equations [A.4.4] and [A.4.6], the following are obtained, respectively:

$$\omega_2 \cong 9\,\omega_1 \qquad [A.4.7]$$

$$\omega_2 \cong 2\,\omega_1 \qquad [A.4.8]$$

The industrial impeller rotational speed is in range of 50-90 rpm. As seen above, it would be very difficult to keep the Reynolds number the same. Such high speeds would create instability in the side well of the model not to mention the formation of an undesirably large vortex. Due to equipment limitations, the rotational speeds of 100 to 120 rpm were used. The Froude number was respected to some extent.

A.4.3 Similarity Criteria for Pump[30-31]

The pump is essentially used to increase mixing in the main hearth. The characteristic velocity for a pump is the discharge velocity "*V*" and the characteristic length is the diameter of the discharge area "*D*". The Reynolds number for a pump is given by:

$$\mathrm{Re}_p = D\,V / \upsilon \qquad [A.4.9]$$

For the model and the system to be similar, the following should hold true:

$$\frac{V_2}{V_1} = \left(\frac{D_1}{D_2}\right)\left(\frac{\nu_2}{\nu_1}\right) \qquad [A.4.10]$$

The Froude number for the pump is given by:

$$Fr_p = V^2 / D\,g \qquad [A.4.11]$$

and the following condition should be satisfied for similarity:

$$\frac{V_2}{V_1} = \left(\frac{D_2}{D_1}\right)^{1/2} \qquad [A.4.12]$$

The pump that was used (that was available) had a half the diameter of the actual pump. When these numbers are substituted in Equations [A.4.10] and [A.4.12], the following results are obtained, respectively:

$$V_2 = V_1 \qquad [A.4.13]$$

$$V_2 = 0.7\ V_1 \qquad [A.4.14]$$

The industrial pump is an intermittent one which pulls a quantity of liquid aluminum for a period of time followed by a period of push generating an average discharge velocity in range of 3 to 4 m/s. The geometric ratio is 0.5 for the pump diameter compared to 0.3 for the furnace geometry and 0.24 for the impeller. This difference is partially compensated from the similarity point of view by having Reynolds and Froude numbers giving similar ratios for the pump discharge velocity. In the experiments, the pump discharge velocity was maintained between 3 and 4 m/s.

A.4.4 Validation of Mathematical Model

As discussed in the sections above, it was not possible to respect all similarity criteria due to limitations on equipment and resources. Also, in general, it is almost impossible to have absolute similarity between a model and the actual system. The results of the experimental work on the physical model confirmed all the tendencies predicted by the model. In order to verify the degree of reliability, the mathematical model was modified to simulate the physical model as it is (with the exact model dimensions and the appropriate water properties). Some of the cases were simulated and compared with laboratory data. The agreement was excellent as shown in Chapter 2. In fact, the experimental results of the

physical model, predictions of the mathematical model and observations (as well as some data) from the plant were all in good agreement showing the same trends and tendencies.

The velocities in the water model were measured using a helical anemometer. It had a 5 cm diameter and an error of 0.1 rpm. Its diameter was about one fifth of the water height, but this was the only one available at the time of measurements. A grid with a pointer was set up on top of the furnace to determine the measurement position and angle. The angle was determined by a freely moving pointer which was placed at the measurement location before the anemometer was positioned accordingly. In general, the measurements were stable except for the cases where there seemed to be too much turbulence. These were indicated in the original reports[30-31].

APPENDIX 5

MATHEMATICAL MODELLING OF COMBUSTION CHAMBERS AND DESCRIPTION OF ONE-GAS-ZONE MODEL

A.5.1 Modelling Combustion Chambers

The combustion chambers can be divided into two broad categories: those in which the primary interest is the transfer of heat from the hot combustion products to some charge or surface such as in furnaces and boilers; and the others where the conversion of heat to work is the major concern such as in internal combustion engines and gas turbines. For the latter group, the accuracy of heat transfer calculation is of secondary importance; what is important is the determination of accurate flow field and pressure distribution to be able to find the work the system could provide. For the first group, however, the heat transfer has to be calculated accurately in order to design and operate them properly.

A detailed calculation requires the solution of all conservation equations including turbulence, combustion and radiation. All phenomena occurring in a combustion chamber can be represented by differential equations except for the radiative heat transfer which is expressed in the form of integro-differential equations. Different numerical methods have to be used to solve these two sets of equations; and this creates a compatibility problem[34]. Earlier on, some researchers opted for the simplification of one part while treating the other

part in great detail due to limited capacity of computational resources. One school concentrated on developing methods for the solution of partial differential equations while treating the radiative transfer in an approximate manner by using, for example, the flux methods[51]. They obtained detailed distributions of velocity, temperature and concentrations; however, the radiative heat transfer calculation was compromised. The other school put more emphasis on the radiative heat transfer calculations while imposing a flow and combustion pattern to avoid solving the differential equations of motion[52]. This method gave detailed temperature and heat flux distributions accurately; however, it required the predetermination of flow and combustion profiles. In recent decades, with the development of high capacity (speed and memory) computers, it became possible to solve both parts rigorously and to couple them to obtain the complete solution[34, 52].

Not all engineering problems call for such detailed approaches. In some cases, complex reacting flow can be simplified by assuming a well-mixed or a plug-flow system. In a well-mixed enclosure, no gradients exist. The gas in the enclosure has a single temperature and leaves the furnace at that same temperature. Many furnaces used in chemical and metallurgical industries approach this state due to high-momentum burners creating a well-mixed environment; however, the gradients always exist. To account for the departure from ideal well-mixed enclosure, different values are assigned to the gas and exit temperatures. Also, by separating the sink (charge) and refractory surfaces, allowance can be made for non-isothermal walls[37-38]. These types of models are referred to as "one-gas-zone" models and give reasonably good results. In the plug-flow model, all transversal gradients are assumed negligible, and variation is allowed only in the axial direction (in the

main flow direction). These types of models are quite suitable for long enclosures such as kilns. For further information on the modelling of combustion chambers, the reader is referred to other references[38, 53-54].

A.5.2 Radiative Heat Transfer in Combustion Chambers[38, 55-57]

There are major differences between thermal radiation and other modes of heat transfer. The radiative transfer is a function of temperature to the fourth power whereas conductive and convective transfer is a function of temperature to the first power. Therefore, in high temperature systems, radiation becomes the dominant mode. Also, heat transfer by conduction and convection depends entirely on local conditions while radiation involves the heat exchange of every part with all other parts of the enclosure. Due to its interactive nature, radiation requires an integral analysis as opposed to the differential analysis used for conduction and convection.

Some methods treat radiation as a local phenomenon, and this allows a differential analysis to be carried out for radiative exchange as well. This is the case with flux methods. Such an approach makes the radiative heat transfer calculation compatible with the solution of partial differential equations of momentum, heat and mass transport. Flux methods are valid for dark (highly absorbing) gas medium in which the radiative transfer takes place through a diffusion type process.

Hottel and his co-workers developed the zone method[38]. The system is divided into a number of divisions called zones with uniform properties. Then a radiant energy balance is written for each zone including the radiative interchange of that zone with all the other zones. This results in a set of algebraic equations which, upon solution, yield the radiative

heat flux distributions in the system. This method treats radiation as a global phenomenon and gives accurate results so long as sufficient number of zones is used. Solution of radiative exchange equations requires the predetermination of total interchange factors. These factors can be calculated using the determinant technique as suggested originally by Hottel. In this technique, there are limitations on zone sizes, and sometimes it becomes very difficult to calculate them due to geometric complexity. Total interchange factors can also be found using the Monte Carlo technique, which can easily be adapted to complex geometries and non-uniform medium properties[34,52]. Zone method combined with the Monte Carlo technique is probably the most elegant and accurate way of calculating radiative heat transfer in combustion enclosures.

Monte Carlo is a ray-tracing technique. There are other methods such as imaginary planes, discrete transfer and discrete ordinate methods which fall in between the flux and zone methods. Discrete transfer and discrete ordinate methods seem to give good results since they are based on ray-tracing technique and try to account for the interactive and global nature of radiation as well. For more details, the reader is referred to references[58-65].

A.5.3 Radiative Properties of Combustion Products

A reliable representation of the radiative properties of the combustion products is an essential part of the radiative heat transfer analysis in combustion chambers. In fossil-fuel fired furnaces, there are two sources of thermal radiation within the combustion products: gaseous species and suspended solid particles. These two sources exhibit entirely different emission characteristics. While emission from gaseous species is of molecular in nature and, consequently, concentrated within discrete bands in the infrared spectrum, particulate

emission is continuous over the entire spectrum. The major combustion products which contribute to radiative transfer are: carbon dioxide and water vapor (gases); soot, char, and ash (particulate matter). A recent study[66] has reviewed all the work on gases in this area, and the reader is referred to this study as well as the following references[67-70].

A.5.4 One-Gas-Zone Model

For completeness, some of the equations given in Chapter 3 are repeated here. This is a steady-state model. Natural gas is the fuel and is assumed 100% methane. The reaction, input and output molar and mass flow rates of chemical species are shown in Table A.5.1. The gas temperature is a weighted average of the adiabatic flame temperature and the gas exit temperature:

$$T_g = a_T\, T_e + (1 - a_T)\, T_{ad.fl.} \qquad [A.5.1]$$

The value of "a_T" depends on how well mixed the enclosure is. Its value is around 0.6 to 0.75 for most industrial furnaces. The total input into the furnace is given by:

$$Q_{in} = m_f\, \Delta H_{fuel} + m_f\, C_{p,f}\, (T_{fuel} - T_{amb}) + m_{air}\, C_{p,air}\, (T_{air} - T_{amb}) \qquad [A.5.2]$$

The adiabatic flame temperature is calculated from:

$$Q_{in} = m_{prod}\, C_{p,prod}\, (T_{ad.fl.} - T_{amb}) \qquad [A.5.3]$$

using the ambient temperature as the reference temperature.

All the interchange factors are summarized in Table A.5.2. Number 1 indicates the refractory surface and number 2 indicates the metal surface. The heat balance on the refractory can be written as:

$$\begin{aligned}(GS1R + GS1H)\, \sigma\, (T_g^4 - T_{s_1}^4) = (S_1\, S_2\, g)\, \sigma\, (T_{s_1}^4 - T_{s_2}^4) \\ + UA_1 (T_{s_1} - T_{amb})\end{aligned} \qquad [A.5.4]$$

If the term for the heat loss to environment is neglected to get an approximate value of temperature for the refractory surface, the following expression is obtained:

$$T_{s_1}^4 = \frac{\left[(GS1R + GS1H)\, T_g^4 + (S_1\ S_2\ g)\, T_{s_2}^4\right]}{(GS1R + GS1H + S_1\ S_2\ g)} \qquad [A.5.5]$$

The heat balance for the gas is given by:

$$\begin{aligned} Q_{in} &= (GS1R + GS1H)\,\sigma\,(T_g^4 - T_{s_1}^4) \\ &+ (GS2R + GS2H)\,\sigma\,(T_g^4 - T_{s_2}^4) \\ &+ m_{prod}\ C_{p.prod}\ (T_e - T_{amb}) \end{aligned} \qquad [A.5.6]$$

The metal surface temperature is an input to the model, thus a known variable. Based on these equations, the following iterative solution procedure is used to find the gas and refractory temperatures. Steps 1 to 5 are for initial estimates, then, Steps 6 to 8 are used till convergence is obtained. In Step 9, the maximum refractory temperature is verified.

1. Calculate adiabatic flame temperature from [A.5.2] and [A.5.3].
2. Estimate the initial gas exit temperature:

   (metal surface temperature + 100°C)
3. Find initial gas temperature using Equation [A.5.1].
4. Find all the approximate interchange factors. They all depend on the gas emissivity which itself depends on the gas and metal surface temperatures as well as gas composition.
5. Substitution of the expression for the approximate refractory temperature given in [A.5.5] into [A.5.6] yields:

$$\left[\frac{(GS1R+GS1H)\,(S_1\,S_2\,g)}{GS1R+GS1H+S_1\,S_2\,g}+(GS1R+GS1H)\right]\sigma\,(T_g^4)$$

$$+\left[\frac{m_{prod}\,C_{p,prod}}{a_T}\right](T_g)$$

$$-\left\{\begin{array}{l}\left[\frac{(GS1R+GS1H)\,(S_1\,S_2\,g)}{GS1R+GS1H+S_1\,S_2\,g}+(GS1R+GS1H)\right]\sigma\,(T_{s_2}^4)\\ \\ +\left[m_{prod}\,C_{p,prod}\,(\frac{1-a_T}{a_T}\,T_{ad.fl.}+T_{amb})+Q_{in}\right]\end{array}\right\}=0 \qquad [A.5.7]$$

for the approximate gas temperature (since the refractory temperature is approximate). This equation can be put into the form:

$$T_g^4+b\,T_g+c=0 \qquad [A.5.8]$$

This is a non-linear equation. The approximate gas temperature is found by the Richmond iteration method[71-72] (extension of Newton's method) using equations [A.5.9] and [A.5.10] ("n+1" new iteration, "n" old iteration):

$$\begin{aligned} f(T_g)&=T_g^4+b\,T_g+c=0\\ f'(T_g)&=4\,T_g^3+b\\ f''(T_g)&=12\,T_g^2\end{aligned} \qquad [A.5.9]$$

$$T_g^{n+1}=T_g^n-\frac{2\,f(T_g^n)\,f'(T_g^n)}{2\left[f'(T_g^n)\right]^2-f(T_g^n)\,f''(T_g^n)} \qquad [A.5.10]$$

6. A good estimate for the gas temperature is now available. Equation [A.5.4] is put into the same form as Equation [A.5.8] for the refractory temperature:

$$[GS1R + GS1H + S_1\ S_2\ g]\sigma\ (T_{s_1}{}^4)$$

$$+[U\ A_1](T_{s_1}) \qquad [A.5.11]$$

$$-[(GS1R + GS1H)\ \sigma\ T_g^4 + (S_1\ S_2\ g)\ \sigma\ T_{s_2}^4 + U\ A_1\ T_{amb}] = 0$$

and the refractory temperature is calculated using the Richmond iteration method given above.

7. A good estimate for the refractory temperature is now available. Equation [A.5.6] is put into the same form as Equation [A.5.8] for the gas temperature:

$$[GS1R + GS1H + GS2R + GS2H]\sigma\ (T_g{}^4)$$

$$+\left[\frac{m_{prod}\ C_{p,prod}}{a_T}\right](T_g)$$

$$-[(GS1R + GS1H)\ \sigma\ T_{s_1}^4 + (GS2R + GS2H)\ \sigma\ T_{s_2}^4 \qquad [A.5.12]$$

$$+ m_{prod}\ C_{p,prod}\ (\frac{1-a_T}{a_T}\ T_{ad.fl.} + T_{amb})\ +\ Q_{in}] = 0$$

and the gas temperature is calculated using the Richmond iteration method given above.

8. Update the interchange factors using the new gas temperatures from Step 7. Repeat Steps 6 to 8 using the latest available values, and each time check if the gas temperature is converged. A tolerance of 0.1°C (absolute error) is used in the programme; it can be modified as desired.

9. Once the convergence is obtained, check if the calculated refractory temperature is higher than the maximum allowable value (not to have refractory failure). If lower, the calculation is finished. If higher, then reduce the fuel flow rate by 1%, and repeat the entire procedure. This repetition continues until the maximum refractory temperature condition is satisfied.

The gas emissivity in Table A.5.2 accounts for all the major combustion products[68]. The above procedure normally takes less than a second if the refractory temperature is not higher than the maximum value. If it is higher, it may take a few seconds.

Table A.5.1 Combustion Reaction, Reactants and Products

Reaction: $CH_4\ (m_f\ kg/s) + 2\ O_2\ (x\%\ excess\ air) \rightarrow CO_2 + 2\ H_2O$

	In		***Out***	
	n (kgmoles/s)	***m (kg/s)***	***n (kgmoles/s)***	***m (kg/s)***
CH_4	$(m_f / 16)$	m_f	0	0
O_2	$(m_f / 16)\ 2\ (1 + x/100)$	$n_{O_{2in}} \times 32$	$(m_f / 16)\ 2\ (x/100)$	$n_{O_{2out}} \times 32$
N_2	$(m_f / 16)\ 2\ (1 + x/100)\frac{79}{21}$	$n_{N_{2in}} \times 28$	$n_{N_{2out}} = n_{N_{2in}}$	$n_{N_{2out}} \times 28$
CO_2	0	0	$(m_f / 16)$	$n_{CO_{2out}} \times 44$
H_2O	0	0	$(m_f / 16)\ 2$	$n_{H_2O_{out}} \times 18$

Table A.5.2 Radiative and Convective Interchange Factors

(1 indicates refractory surface, 2 indicates metal surface)

Direct interchange between black surfaces:

$s_1\ s_1 = A_1 - A_2$

$s_1\ s_2 = s_2\ s_1 = A_2$

$s_2\ s_2 = 0$

ε_g gas emissivity $\quad \tau = 1 - \varepsilon_g$ gas transmissivity (assumed uniform)

Total interchange with gray gas between black surfaces

$S_1\ S_1 = (s_1\ s_1)\ \tau$

$S_1\ S_2 = S_2\ S_1 = (s_1\ s_2)\ \tau$

$S_2\ S_2 = 0$

Total interchange with gray gas between gray surfaces

$Term1 = A_1\ \varepsilon_1 / (1 - \varepsilon_1)$

$Term2 = A_2\ \varepsilon_2 / (1 - \varepsilon_2)$

$Term3 = (A_2 / (1 - \varepsilon_2)) - S_1\ S_2$

$Term4 = (A_1 / (1 - \varepsilon_1)) - S_1\ S_1$

$Term5 = Term1 \times Term2 - (S_1\ S_2)^2$

$S_1\ S_1\ g = Term1 \times (Term1 \times Term3 / Term5 - \varepsilon_1)$

$S_2\ S_2\ g = Term2 \times (Term2 \times Term4 / Term5 - \varepsilon_2)$

$S_1\ S_2\ g = Term1 \times Term2 \times S_1\ S_2 / Term5$

$G\ S_1 = A_1\ \varepsilon_1 - (S_1\ S_1\ g + S_1\ S_2\ g)$

$G\ S_2 = A_2\ \varepsilon_2 - (S_1\ S_2\ g + S_2\ S_2\ g)$

Total interchange factors for radiation and convection

$$GS1R = G\ S_1 \times \left\{ \left[1 - (T_{s_1} / T_g)^3 \right] / \left[1 - (T_{s_1} / T_g)^4 \right] \right\}$$

$$GS2R = G\ S_2 \times \left\{ \left[1 - (T_{s_2} / T_g)^3 \right] / \left[1 - (T_{s_2} / T_g)^4 \right] \right\}$$

$$GS1H = h_1\ A_1 \times \left[4\sigma \left\{ (T_{s_1} + T_g) / 2 \right\}^3 \right]$$

$$GS2H = h_2\ A_2 \times \left[4\sigma \left\{ (T_{s_2} + T_g) / 2 \right\}^3 \right]$$

APPENDIX 6

DESCRIPTION OF DYNAMIC SIDEWELL FURNACE MODEL, CONTROL EMULATOR AND INTERFACE

A.6.1 Numerical Solution of Ordinary Governing Differential Equations

Refractories: The 1D transient conduction equation for all the inside nodes within the refractories (combustion chamber and the metal) are written as[71]:

$$(-Fo)\,T_{n-1}^{t+1} + (1 + 2Fo)\,T_n^{t+1} + (-Fo)\,T_{n+1}^{t+1} = T_n^t \qquad [A.6.1]$$

using the backward finite difference scheme. The temperatures on the inside boundaries are known in the combustion chamber as well as in the metal bath. The temperatures on the outside are expressed in terms of the ambient temperature through the convective boundary condition. The above equation is written for the boundaries using known temperatures. The number of equations is equal to the number of unknowns. The resultant set of algebraic equations form a tri-diagonal matrix and is solved using Thomas algorithm[72].

Change in Metal Level: The total volume change as a function of time due to the addition of solid charge (shreds, sow, scrap) or transfer of metal to the holding furnace. This volume change at every time step is calculated from:

$$\Delta V = \sum m_i \,/\, \rho_i \qquad [A.6.2]$$

Due to the geometry of the furnace, the relationship between the change in volume and the change in metal height is not linear. The change in metal level is found from:

$$\Delta V = \left[l\,(w - H / \tan\theta) + \frac{h\,l}{\tan\theta} \right] \Delta h + \left[l / 2\tan\theta \right] \Delta h^2 \qquad [A.6.3]$$

Heat Balance in the Liquid Metal: All the heat inputs and outputs in a cell are calculated. These include: metal entering and leaving the cell, conduction (this is important due to very high thermal conductivity of aluminum), heat loss trough the refractories or to the environment, heat sink due to phase change of metal. Then the net change in accumulation term is determined:

$$\frac{\partial}{\partial t}(\rho\, V\, C_p\, T) = Q_{total} \qquad [A.6.4]$$

Using forward difference in time, the temperature at the new time level is determined from the previous one[72]:

$$T^{t+1} = \frac{(\frac{Q_{total}\,\Delta t}{\rho\, C_p\, V_{av}}) + (1 - \frac{\Delta V}{2V_{av}})\, T^t}{(1 + \frac{\Delta V}{2V_{av}})} \qquad [A.6.5]$$

where Vav is the volume averaged over the given time step. Because of the forward difference, the time step has to be very small to be able to have accurate results. Even though any value can be specified in the programme, one second is used in all simulations.

Dross Layer: The amount of dross formed is calculated from the amount of metal melted:

$$\dot{m}_{dross} = i\,\%\ of\ metal\ melted \qquad [A.6.6]$$

This percentage is empirical and 1.5 % seems to give the amount of dross generated in the plants. The thickness of dross layer is found from:

$$\frac{(\dot{m}_{dross} / \rho_{dross})}{A_{furnace}} = \Delta x_{dross} = f(t) \qquad [A.6.7]$$

Then the temperature difference between top and bottom surfaces of the dross is:

$$T_{top\ surface} = T_{metal\ surface} + Q(\Delta x / k) \qquad [A.6.8]$$

When the dross gets too thick, this difference could be significant and reduce the heat transfer considerably. The combustion chamber sees the top surface of the dross and receives that temperature as the boundary condition.

Melting of Solid Charge: Phase change is not solved intrinsically. The melting of the large solid blocks is assumed to occur in a certain (fixed) volume within the melt over a certain period of time. The shreds are too thin; therefore they are assumed to melt as soon as they are submerged. The sows are left on the inclined surface of the charge door for a period of time before they are pushed into the liquid metal. During their stay in the main hearth, they are preheated. Using lumped-capacitance method[71], it was calculated that they are heated up about 75 to 100°C in an hour:

$$\Delta T / \Delta T_i = \exp(-\frac{h\ A_s}{\rho\ V_c})\ t \qquad [A.6.9]$$

This number is consistent with the plant tests.

During tapping, the metal is transferred to another furnace. This is a complex process to include in the current simplified model. The tapping spout is close to the bottom; therefore it was assumed that the metal was removed from the bottom layer.

The numerical solution procedure can be summarized as follows:

1. The temperatures in the entire system are initialized. The flow pattern is introduced. All the events for the entire simulation period are programmed.
2. The time is increased using the time step (1 second).
3. The temperature profiles in all the refractories are calculated in the new time step.
4. The heat flux to the metal surface is determined from the combustion chamber model.
5. All the events are visited if they are to be included in this time step. Changes in metal volume, metal height, solid charge addition, metal transfer etc. are all verified and determined.
6. The transient heat balances for the cells in the liquid metal are solved using Equations [A.6.4] and [A.6.5], and the new metal temperature distribution is determined.
7. The procedure from Step 2 to Step 6 is repeated until the end of total simulation time.
8. Total mass and heat balances are calculated.

In the programme, at the end of the simulation, all the output files are prepared to display results through interface or excel. At the beginning, a subroutine verifies if the input data are consistent.

A.6.2 Control Strategy and Control Emulator

The dynamic model was developed by the author. The work on the control was done by other members of the group. The control emulator is briefly described here for the purpose of giving a complete picture. Cascaded control strategy shown in Figure A.6.1 was programmed and incorporated into the dynamic model. This is called the control emulator. The bath temperature controller, by its CO (controller output) action, adjusts the setpoint of the roof temperature controller TCroof. The roof temperature controller, by its CO (controller output) action, adjusts the setpoint of the air and gas flow controller (FC). For further details, the reader is referred to the original report[40-41].

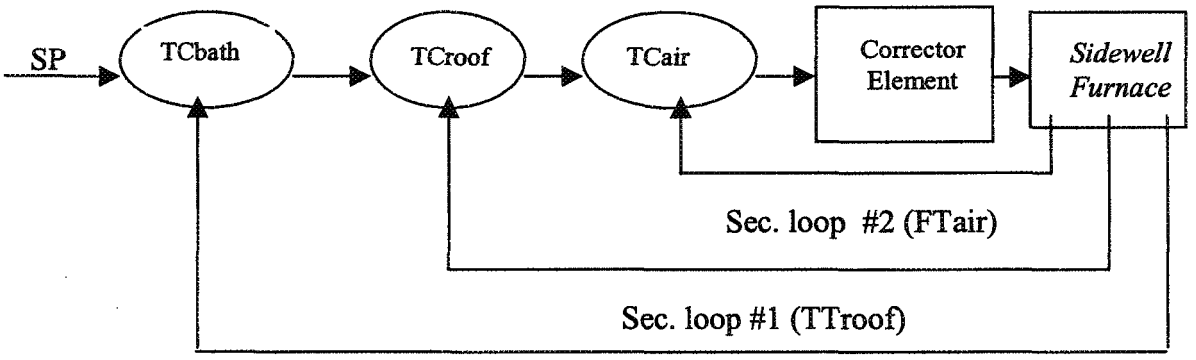

Figure A.6.1 : The Cascaded Control Strategy of the Sidewell Furnace Used in the Control Emulator.

The dynamic model together with the control emulator represents the real operation of a sidewell furnace virtually. Without these two components, the dynamic behavior of the furnace cannot be properly simulated. An example is given below to demonstrate the importance of the control emulator on the simulation.

Table A.6.1: Effect of Controller on Simulation (Effect of Maximum Roof Temperature on Production).

Case No.	Maximum Roof Temperature (°C)	Metal Temperature Setpoint (°C)	Remarks and Results
1	1050	800	• Base case. • Metal reaches 800°C and refractory reaches 1050°C after 5 hours.
2	1000	800	• Refractory reaches 1000°C after 2 hours and 40 minutes. • Controller reduces the fuel flow rate. • Metal cannot be heated any further.
Maximum Fuel Flow Rate: 15,500 SCFH Shred Feed Rate: 21,000 lbs/h			

Table A.6.1 compares two cases. In Case 1, the maximum refractory temperature is 1050°C. The fuel and the shred flow rates are adjusted in such a way that the metal and the refractories reach 800°C and 1050°C, respectively, in five hours. In Case 2, the maximum refractory temperature is reduced to 1000°C. In about 2 hours and 40 minutes, the refractory reaches the maximum temperature; the fuel flow is cut and the metal cannot be heated any further. The results are shown in Figure A.6.2 (a) metal temperatures and their setpoints, (b) refractory temperatures and their setpoints calculated by the control emulator, and (c) fuel flow rate and metal temperatures together. These figures clearly show the control action demonstrating its importance in simulating the operation of a furnace realistically. These results also indicate that the maximum refractory temperature should be set as high as possible (without refractory failure) to be able to achieve high heating rates in metal.

a

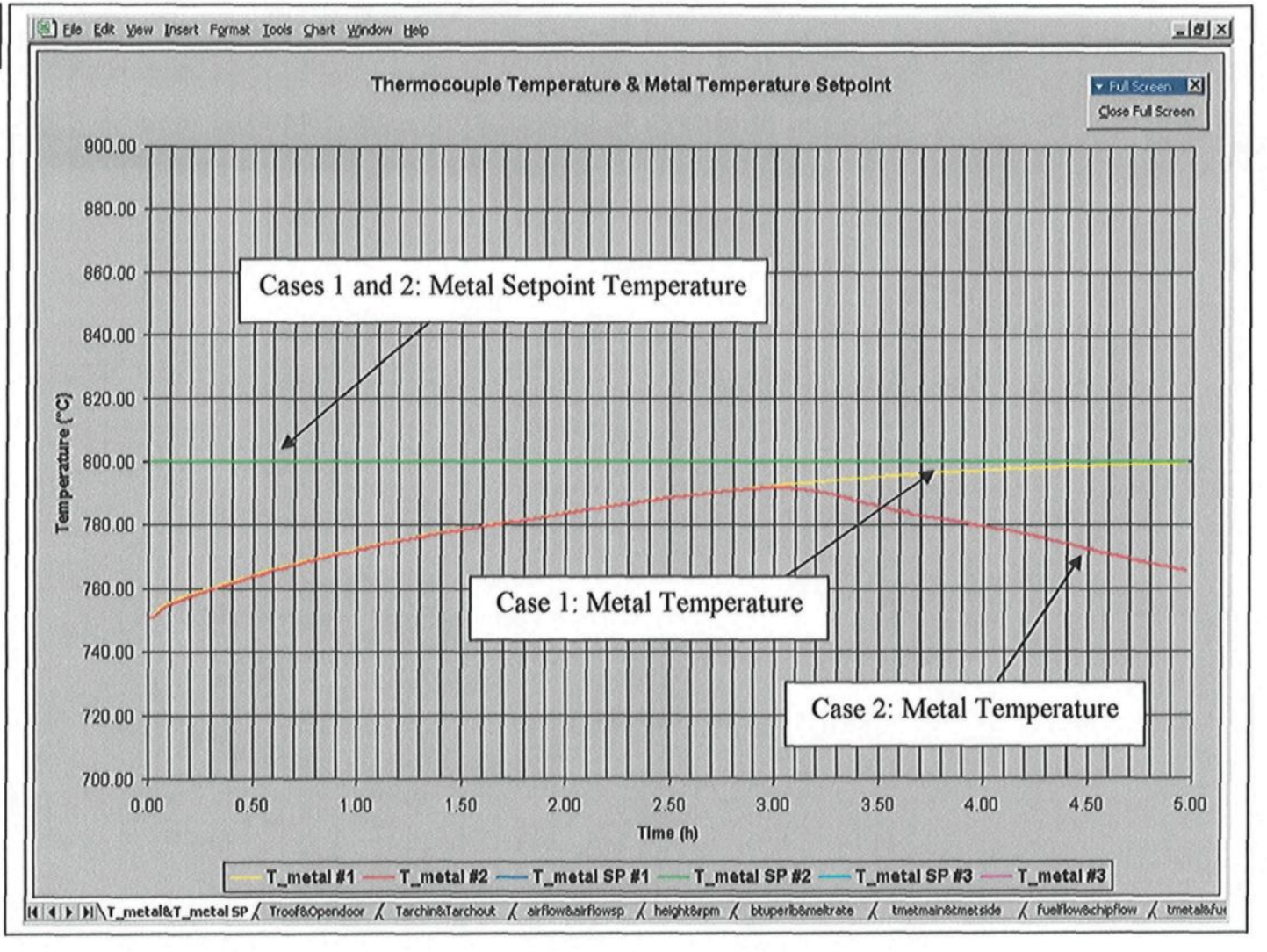
File Edit View Insert Format Tools Chart Window Help
Thermocouple Temperature & Metal Temperature Setpoint
Full Screen
Close Full Screen
900.00
880.00
860.00
840.00
820.00
800.00
780.00
760.00
740.00
720.00
700.00
Temperature (°C)
Cases 1 and 2: Metal Setpoint Temperature
Case 1: Metal Temperature
Case 2: Metal Temperature
0.00
0.50
1.00
1.50
2.00
2.50
3.00
3.50
4.00
4.50
5.00
Time (h)
T_metal #1
T_metal #2
T_metal SP #1
T_metal SP #2
T_metal SP #3
T_metal #3
T_metal&T_metal SP
Troof&Opendoor
Tarchin&Tarchout
airflow&airflowsp
height&rpm
btuperlb&meltrate
tmetmain&tmetside
fuelflow&chipflow

b

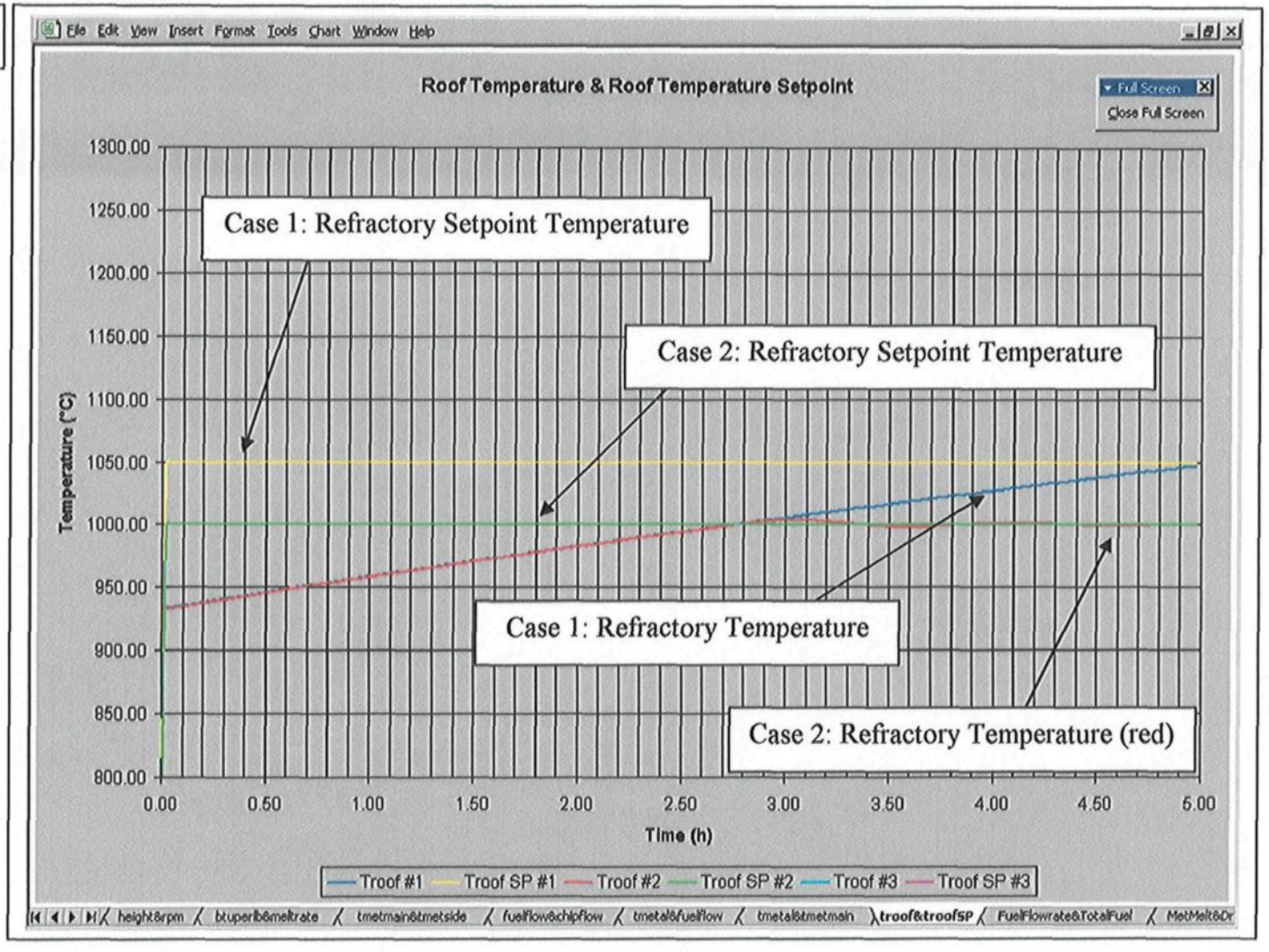
File Edit View Insert Format Tools Chart Window Help
Roof Temperature & Roof Temperature Setpoint
Full Screen
Close Full Screen
Case 1: Refractory Setpoint Temperature
Case 2: Refractory Setpoint Temperature
Case 1: Refractory Temperature
Case 2: Refractory Temperature (red)
Temperature (°C)
1300.00
1250.00
1200.00
1150.00
1100.00
1050.00
1000.00
950.00
900.00
850.00
800.00
0.00
0.50
1.00
1.50
2.00
2.50
3.00
3.50
4.00
4.50
5.00
Time (h)
Troof #1
Troof SP #1
Troof #2
Troof SP #2
Troof #3
Troof SP #3
height&rpm
btuperlb&meltrate
tmetmain&tmetside
fuelflow&chipflow
tmetal&fuelflow
tmetal&tmetmain
troof&troofSP
FuelFlowrate&TotalFuel
MetMelt&Dr

c

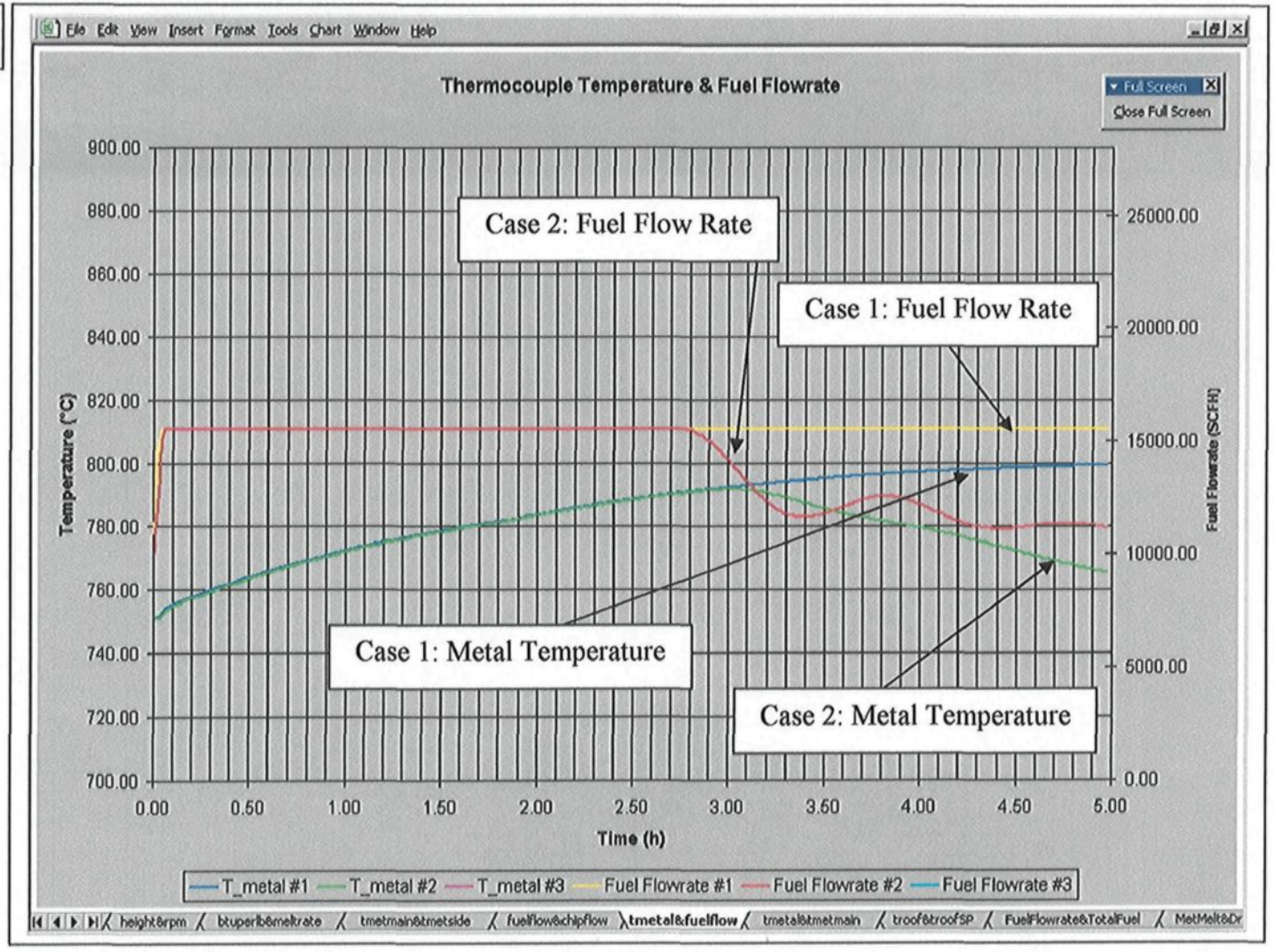

Figure A.6.2 : Example for the Effect of Controller on Sidewell Furnace Operation

A.6.3 Sidewell Furnace Simulator

The sidewell furnace simulator consists of the dynamic model combined with the control emulator and a user-friendly interface. There are nine input files as shown in Table A.6.2. The variables are grouped in six files depending on their role; and three of them are for the specification of variable input data: GSS (impeller) rpm, feed rate (shred flow rate), and gas flow (fuel flow rate). Some of the physical and thermodynamic data are not directly accessible; they are specified inside the programme. These files contain all the data required to run the programme.

Once the run is completed, the results can be displayed as an Excel file. Some selected results from a simulation are shown in Figure A.6.3. The simulation, itself, is not discussed here because the purpose is simply to demonstrate the presentation of results in the Excel format. Also, the control action is clearly seen in these figures. Up to three runs can be carried out and the results can be saved on the same excel file for comparative studies. This option was used to present the results shown in Chapter 5.

Figure A.6.4 displays some snapshots from a simulator run. A user manual and tutorial is available directly on the computer. At the end of the run, a short report is automatically prepared in Word format. The report summarizes the simulation and gives heat and mass balances. If there is an error in the specification of some variables, the simulation is stopped and the user is warned.

Table A.6.2 : Input Files for the Dynamic Sidewell Furnace Model

Furnace (a)

Value	Variable
7.0	Length of main hearth (m)
5.7	Width of main hearth (m)
0.97	Height of main hearth (m)
1.8	Width of side well (m)
45.0	Angle for the inclined side wall (degree)
1.7	Height of the combustion chamber (m)
0.9	Refractory emissivity
0.9	Metal surface emissivity
35.1	Heating value of fuel (natural gas) (MJ/kg)
11.34	Convective heat transfer coef., gas-metal (in comb cham) (W/m2-C)
11.34	Convective heat transfer coef., gas-refractory (in comb cham) (W/m2-C)
11.34	Convective heat transfer coef., (outside) (W/m2-C)
1000.0	Maximum refractory temperature (C)
25.0	Ambient temperature (C)
800.0	Maximum combustion air temperature for regenerative burner (C)
600.0	Minimum combustion air temperature for regenerative burner (C)
30.0	Cycle for regenerative burner (s)
60.0	Combustion air temperature for direct firing (C)
0.305	Refractory wall thickness for combustion chamber (m)
0.305	Refractory side wall thickness for metal section (m)
0.305	Refractory floor thickness (m)
0.61	Refractory hot wall thickness (m)
10.0	Percent excess air
500.0	Minimum exit gas temperature for full burner power (C)
1.5	Dross generation as % (mass) of metal melted

Thermocouples (b)

Value	Variable
0.61	Distance from max. metal level for metal thermocouple (m)
1.22	Distance from burner wall for metal thermocouple (m)
0.61	Distance from door for metal thermocouple (m)
44.5	Distance from the surface for roof thermocouple (mm)

Flow (c)

Value	Variable
BER_1A	Furnace to be simulated
0.9	Diameter of impeller (m)
80.0	rpm for the impeller
2.0	rpm: Constant (1), Variable (2), Stepwise (3), P.W. Equation (4)
0.1	Distance between impeller and bottom (m)
0.3	Distance between impeller and arch (m)
0.0	Shifted distance from optimum position (m)
2.0	Type of insert (Rectangular=1, Triangular=2, None=3)
0.3	Length of insert (m)
1.0	There is pump in the main hearth (No=1, Yes=2)
100.0	Pump orifice diameter (mm)
23.0	Pump capacity, average mass flow rate (kg/s)

Initial conditions (d)

Value	Variable
1.0	Furnace to be simulated (1-Existing, 2-New)
2.0	Initial conditions (Uniform=1, Non-uniform=2)
1.0	Controller in operation (Yes=1, No=2)
8655.0	Shred Feed rate (kg/h)
1.0	Shred Feed rate: Constant (1) or Variable (2)
152.6	Fuel flow rate (max. if controller in operation) (Nm3/h)
1.0	Fuel flow rate (if no controller): Constant (1) or Variable (2)
0.9	Initial metal height (m)
950.0	Initial refractory temp (C)
760.0	Initial average metal temperature (C)
2.54	Initial dross layer thickness (mm)
4.0	Total simulation time (h.min)

Events (e)

Value	Variable
0.0	Are sows fed to main hearth? (0=No, 1=Yes)
6.0	Number of sows placed in the main hearth
1.0	Mass of each sow (in metric tons - 1000kg)
350.0	Sow temperature (C)
0.3	Time when sows are placed in the furnace (h.min)
30.0	Duration the sows are left in combustion chamber (min)
0.0	Is scrap fed to side well (0=No, 1=Yes)
2.0	Tons of scrap placed in the side well (in metric tons - 1000kg)
50.0	Scrap temperature (C)
1.0	Time when scrap is placed in the side well (h.min)
0.0	Is skimming done in main hearth? (0=No, 1=Yes)
3.0	Time when skimming is done in main hearth (h.min)
10.0	Duration of skimming in main hearth (min)
1.0	Is tapping done? (0=No, 1=Yes)
0.56	Time when tapping is done
10.0	Duration of tapping (min)
45.4	Tons of metal removed during tapping (in metric tons - 1000kg)
60.0	Frequency of mixing in side well by well walker (min)
0.0	Is skimming done in side well? (0=No, 1=Yes)
2.0	Time when skimming is done in side well (h.min)
0.0	Is the burner operated in direct firing mode? (0=No, 1=Yes)
2.0	Time when the direct firing mode starts (h.min)
3.0	Time when the direct firing mode ends (h.min)
350.0	Shred temperature (C)

Controller (f)

Value	Variable
800.0	Metal set point temperature to calculate SP (Troof) (SP1)
2.0	Gain for Tbath (Kp1)
0.07	Reset for Tbath (Ki1)
0.1	Rate for Tbath (Kd1)
0.5	Gain for Troof (Kp2)
0.07	Reset for Troof (Ki2)
0.0	Rate for Troof (Kd2)
0.1	Gain for FIC (Kp3)
0.07	Reset for FIC (Ki3)
0.1	Rate for FIC (Kd3)

Feed Rate

(g)

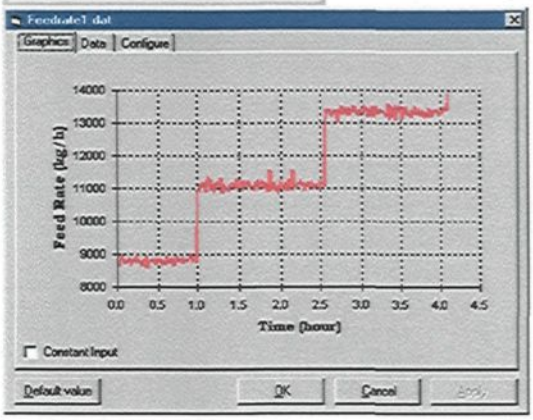

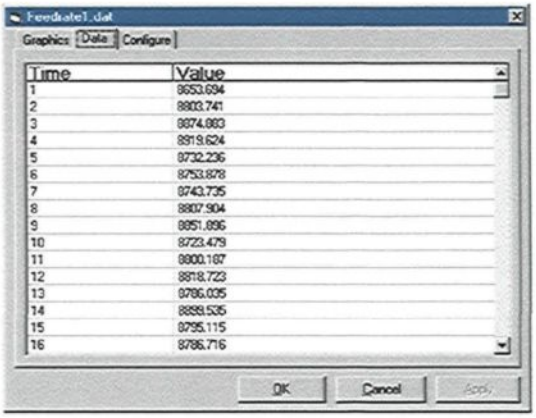

Gas Flow

(h)

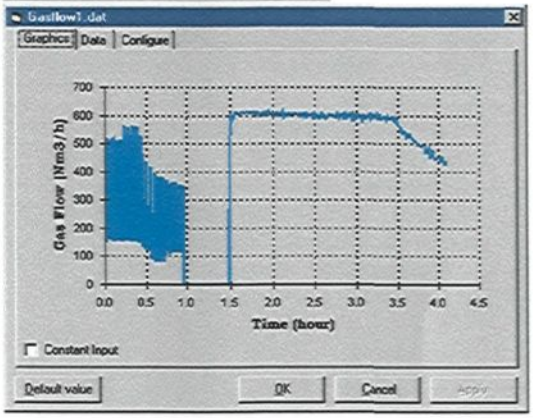

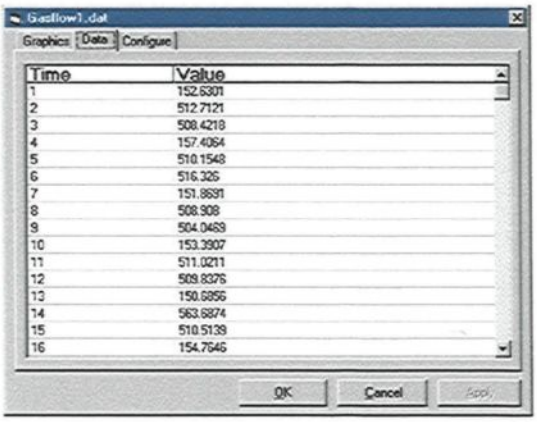

GSS rpm

(i)

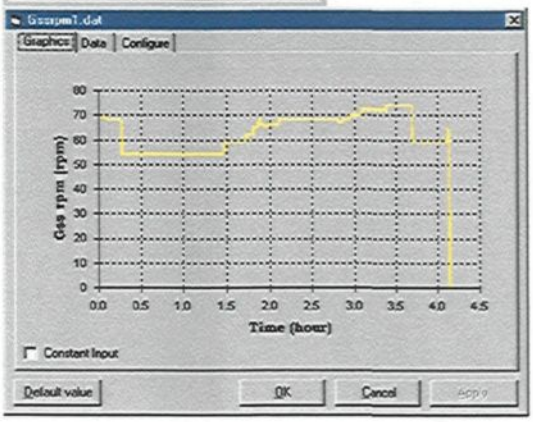

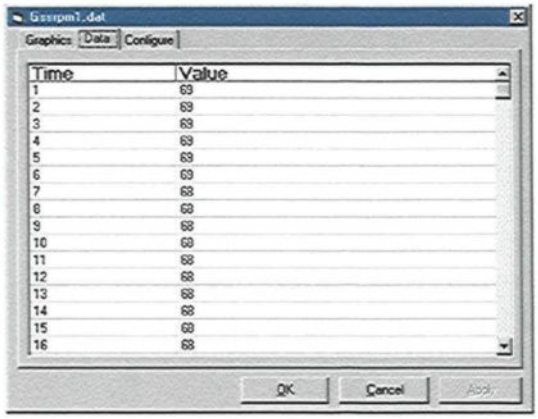

APPENDIX 7

SUMMARY OF ASSUMPTIONS USED IN THE MATHEMATICAL MODELS

A.7.1 Natural Convection

Natural convection was never considered in the liquid metal; however, this is a valid assumption. Natural convection occurs when there is heating in a fluid body. The creation of density differences leads to unstable flow patterns. This occurs if the heating is done at a position other than the top surface. Rising hot fluid is replaced by cold fluid with no definite flow pattern. In the liquid metal within the sidewell furnace, the temperature gradient hardly exceeds 100°C due to high thermal conductivities and forced convection (created by the impeller and the pump). The density variation is less than 2% and is insignificant for this application (much smaller differences in ocean water lead to great currents that circle the earth).

Also, when the heating is done from the top surface, no flow is created and a stable, nearly linear temperature profile is established by conduction in the fluid. Similarly in sidewell furnaces, liquid aluminum is heated from the top by the combustion chamber. No unstable flow pattern could ever form even if there were no impeller (or pump). In addition, forced convection (circulation between the main hearth and the side well as well as the metal circulation in the main hearth) is always present in the sidewell furnace. Without it,

the melting rate of a sidewell furnace would be negligibly small since the energy is provided by the combustion chamber in the main hearth whereas the charge is fed to the side well.

A.7.2 Three Dimensional Isothermal Flow Model for the Metal Bath (Chapter 2)

This isothermal flow model was used to study and optimize the geometrical parameters in the liquid bath. The assumption is, of course, that the flow is of utmost importance in heat transfer as discussed in detail in Chapter 2. This assumption has been validated by the results of Chapter 4 where the 3D transient heat transfer model showed clearly the strong relationship between the flow and furnace performance.

The metal surface was taken as flat. The vortex created by the impeller was not represented geometrically. The vortex depth changes with impeller rotational speed and impeller position. Therefore, to represent the vortex, a two-phase flow with adaptive grid system would have to be adopted. With the resources available, it was impossible to represent the entire liquid metal and the vortex in detail. In any case, the strength of vortex can be estimated based on the velocities around the impeller. The second implication of a flat surface is the absence of wave formation. The Froude number in the main hearth for a typical operation is less than the critical value for free surface flows which means there would be no wave formation. In order to keep dross formation to a minimum, it is better to maintain such a condition. Also in the modelling work, the objective was to study the entire furnace, and wave formation was never anticipated.

The metal level changes continuously in the furnace within a certain range (two thirds to full); however, a fixed metal height was considered in the model. Again, the

adaptive grid system would have to be used to simulate level changes which would have increased the simulation time considerably. The flow field was calculated for a number of different metal heights, and it was observed that the patterns were similar. Therefore, optimizing geometry using a fixed height was justified. Later on, for operation and control, a dynamic model was built in which case the level changes are important.

Impeller was represented by a force term in the source term of the momentum equation. This was necessary, again, to represent the entire furnace rather than the impeller in detail. As discussed previously, such representation was used successfully in many studies. The validation work based on the water model demonstrated the validity of this approach. The pump was represented as a jet (mass source inlet on the back wall). Again, the water model results showed that this was a good representation.

The K-ε turbulence model was used in the model. This representation has been used in numerous applications with success. It fails in swirling flows[53], but in the current application, there was no swirl. The reasonable predictions by the model in all the simulations are an indication for the reliability of the K-ε turbulence model.

CFX was used to solve the partial differential equations. Historically, the finite volume and finite difference methods were used to calculate coupled flow, heat and mass transfer problems whereas the finite volume method was used to analyse stress and vibrations in various structures. In the past few years, this has changed drastically. At the time, there were very few finite volume codes such as PHOENICS, FLUENT, and FLOW-3D (earlier version of CFX) which could handle the type of work required in this project. Among them, CFX (initially FLOW-3D) was the best in terms of representing complex

geometries and had an open structure in terms of inserting custom-made codes. Thousands of lines were inserted into the program for the appropriate representation of various phenomena.

The triangular insert was represented using a step-wise geometry in the mathematical model. This was done to have a reasonable number of blocks for geometrical representation which, otherwise, would increase the number of cells considerably. This changes the calculated flow pattern slightly, but it should not introduce any significant error because the predicted results were validated by the experimental data.

A.7.3 Simplified Combustion Chamber Model (Chapter 3)

This model was used to carry out a parametric study in the combustion chamber. All the important phenomena were represented. Only one gas zone exchanging heat with the surrounding refractories and the metal surface was considered. The gas had an effective temperature, and the temperature distribution within the gas could not be calculated with this model. The non-isothermal temperature distribution and gas flow patterns were all lumped into one factor, a_T, and it was determined by comparing the model predictions with the calculated data from the plant. A detailed model could have been built for the combustion chamber; in fact, that was the original plan. Later on, the dynamic model was thought to be more important, and detailed combustion chamber modelling was excluded from the current project.

The heating value of the fuel was supplied by the company. In order to simplify the calculations, natural gas was taken as 100% methane even though this value varies between 82 to 96% and the rest usually contains heavier hydrocarbons. The exact gas composition

was not always available. The energy released by the combustion was in fact correct, but the product gas composition was not accurate. Also, 100% combustion was assumed with carbon dioxide and water vapor as the reaction products. The variation in gas composition due to these assumptions is not significant, and its impact on gas emissivity is even smaller.

The gas as well as the refractory and the metal surfaces were considered gray. The absorption coefficient was calculated from the gas emissivity which, itself, was determined based on the calculated gas composition. Gray-gas assumption is approximate and results in very simple calculations. The exact values of the surface emissivities are not known, however they were assigned values which gave model predictions similar to calculated data. This may have corrected the inaccuracies caused by the gray-gas assumption.

The metal and refractory surface temperatures were considered uniform, and consequently a single value was calculated for the heat flux on each surface. A detailed combustion model would have given the temperature and heat flux distributions on the metal and refractory surfaces.

One-dimensional steady-state heat conduction was assumed in the refractories. Since the refractory thickness is much smaller than its other dimensions for industrial furnaces, this is a valid assumption that is used in many studies. Steady-state assumption is certainly valid for the purposes of the parametric study.

The power of this combustion chamber model is its simplicity and fraction-of-a-second computation time while representing all the relevant phenomena in detail.

A.7.4 Global Model with 3D Transient Heat Transfer in the Liquid Metal (Chapter 4)

This model was used to determine quantitatively the impact of metal flow on the heat transfer in the liquid metal bath. The combustion chamber model of Chapter 3 was coupled with a 3D transient heat transfer model for the metal. The same assumptions discussed above for the combustion chamber are applicable here as well. One important point is the steady-state refractory assumption. This is valid as long as the temperatures in the combustion chamber vary slowly, however, this is not always the case during the operation of sidewell furnaces.

In the metal part, the flow was imposed assuming that the flow pattern remains the same. The flow was calculated once at the beginning based on the model of Chapter 2. Therefore, the assumptions discussed above for the metal flow model are also applicable here. The difference is the incorporation of the solution of transient enthalpy equation. The heat loss through the refractories in the metal part were calculated using an overall heat transfer coefficient. Again, a steady-state one-dimensional conduction was assumed for the refractories. Thus, the above comments for the combustion chamber refractories apply here as well.

Heat loss from the surface of the side well was also estimated and assigned a uniform value on the entire surface. The melting of metal was represented as a heat sink term and was not modelled in detail, again, to keep the calculations simple and the computation time reasonable. In the sidewell furnace, this is justified due to the very thin shreds fed to the side well and small amount of solid blocks fed to the main hearth.

This model was not exploited fully. More work can be done using this model on 3D transient heat transfer in the liquid metal with some minor modifications.

A.7.5 Dynamic Sidewell Furnace Model (Chapter 5)

This model was used to simulate the operation of the furnace. It also combines the combustion chamber sub-model with the liquid metal sub-model coupled through the interface at the metal surface.

The combustion chamber sub-model is similar to the one described in Chapter 3 except for the one-dimensional transient conduction through the refractories instead of a steady-state one. This is a more realistic approach since the furnace operation is always dynamic. The time constant of the gas is so small (in seconds compared to minutes in the metal and hours in the refractory) that it can be treated as steady state. This should not introduce any significant error.

The dynamic behavior of the liquid metal is represented appropriately. One-dimensional transient conduction is solved for the refractories in the metal part. The flow field calculated with the model of Chapter 2 is used to determine the imposed flow pattern here as well. Consequently, all the assumptions related to flow calculation are also valid here. The heat transfer calculation in the liquid metal is transient. Heat transfer through the dross layer is assumed steady. This is a valid assumption if dross layer is not very thick. As the thickness increases, this assumption becomes less accurate. This could be improved by making the analysis transient in the dross layer as well.

The sidewell furnace simulator, which combines the dynamic model with the control emulator, has been transferred to industry and is being used to improve the operation.

NOMENCLATURE

CHAPTERS 3 AND 4, APPENDIX 5

a_T	weighing factor ("well-mixedness" of a furnace)
A_1	total refractory surface area (m^2)
A_2	metal surface area (m^2)
$C_{p,air}$	air heat capacity (J/kg K)
$C_{p,f}$	fuel heat capacity (J/kg K)
$C_{p,prod}$	product heat capacity (J/kg K)
$GS1R$	total radiative interchange factor for gas-to-surface 1 (m^2)
$GS1H$	convective interchange factor for gas-to-surface 1 (m^2)
$GS2R$	total radiative interchange factor for gas-to-surface 2 (m^2)
$GS2H$	convective interchange factor for gas-to-surface 2 (m^2)
ΔH_{fuel}	heating value of fuel (J/kg)
$h_{c,m}$	convective heat transfer coefficient to metal (W/m^2 K)
$h_{c,r}$	convective heat transfer coefficient to refractories (W/m^2 K)
m_{air}	air flow rate (kg/s)
m_f	fuel flow rate (kg/s)
m_{prod}	flow rate of combustion products (kg/s)
Q_{dir}	direct heat transfer to metal (W)

$Q_{dir,con}$	convective component of the direct heat transfer to metal (W)
$Q_{dir,rad}$	radiative component of the direct heat transfer to metal (W)
Q_{exit}	chimney losses (W)
Q_{in}	total heat input to furnace (W)
Q_{ind}	indirect heat transfer from refractory to metal surface (W)
Q_{loss}	heat loss through the refractories (W)
Q_{met}	Total heat transfer to metal (W)
Q_{ref}	heat transfer to refractories (W)
$Q_{ref,con}$	convective component of the direct heat transfer to refractories (W)
$Q_{ref,rad}$	radiative component of the direct heat transfer to refractories (W)
S_1S_2g	total radiative interchange factor between surfaces 1 and 2 (m^2)
T_{air}	air inlet temperature (K)
T_{amb}	ambient temperature (K)
$T_{ad,fl}$	adiabatic flame temperature (K)
T_e	exit gas temperature (K)
T_{fuel}	fuel inlet temperature (K)
T_g	gas temperature (K)
T_{met}	metal surface temperature (K)
T_{ref}	refractory temperature (K)
$T_{ref,m}$	maximum refractory temperature (K)
T_{s_1}	refractory temperature (K)
T_{s_2}	metal surface temperature (K)

U	overall heat transfer coefficient (W/m^2 K)
$\%xair$	percent excess air
ϵ_g	gas emissivity
ϵ_r	refractory emissivity
ϵ_m	metal emissivity
η	furnace thermal efficiency
τ	gas transmissivity

CHAPTER 5

C_p	heat capacity (J/kg K)
k	thermal conductivity (W/m K)
m	mass flow rate (kg/s)
Q	heat flow rate (W)
t	time (s)
T	temperature (K)
V	volume of liquid metal (m^3)
x	axial coordinate (m)
α	thermal diffusivity (m^2/s)
ρ	density (kg/m^3)

APPENDIX 2

C_p	heat capacity (J/kg K)
$C\mu$	constant for the calculation of turbulent viscosity (dimensionless)
f	force per unit volume (N/m^3)
$\vec{g}$	gravitational acceleration $g_x \vec{i} + g_y \vec{j} + g_z \vec{k}$
h	enthalpy (static or thermodynamic) (J)
H	total enthalpy (J)
$\vec{i}, \vec{j}, \vec{k}$	unit vectors in x, y, z directions
k	thermal conductivity (W/m K)
K	kinetic energy of turbulence (m^2 / s^2)
P	pressure (Pa)
S_ϕ	source term in the general equation
t	time (s)
T	temperature (K)
u, v, w	velocity components in x, y, z directions (m/s)
$\vec{V}$	velocity vector (m/s) $u \vec{i} + v \vec{j} + w \vec{k}$
$\overline{V_i' V_j'}$	time average value of the product of V_i' and V_j'
V_i', H'	fluctuating component of V_i, H
x, y, z	coordinate axes (m)
ϵ	rate of dissipation of turbulence (m^2 / s^3)

μ	viscosity (kg/ms)
μ_{eff}	effective viscosity (kg/m s)
μ_t	turbulent viscosity (kg/m s)
ρ	density (kg/m^3)
σ_H	turbulent Prandtl number
ϕ	general dependent variable
τ	shear stress (N/m^2)
τ_t	turbulent stress (N/m^2)
Γ	total exchange coefficient
∇	operator $\partial/\partial x\,\vec{i} + \partial/\partial y\,\vec{j} + \partial/\partial z\,\vec{k}$

APPENDIX 3

A_n	area normal to the flow direction (m^2)
C_B	blade coefficient
$\vec{f}$	force applied by the impeller onto the fluid (N/m^3)
f_n	face normal to the blade surface (N/m^3)
$\dot{m}$	mass flow rate (kg/s)
$\dot{M}$	rate of change of momentum (kg m/s^2)
n	number of blades
r	blade radius (m)

$\vec{r}$	position vector (m)
S_u, S_v, S_w	source terms for u, v, w momentum equations
V	velocity in general (m/s)
V_b	blade velocity (m/s)
V_f	fluid velocity (m/s)
$\gamma_x, \gamma_y, \gamma_z$	angles of directional cosines
$\vec{\lambda}$	unit vector normal to the blade surface
ρ	fluid density (kg/m^3)
$\vec{w}$	rotational velocity (rad/s)

APPENDIX 4

d	impeller diameter (m)
D	pump discharge diameter (m)
Fr	Froude number
Fr_I	Froude number for impeller
Fr_p	Froude number for pump
g	gravitational acceleration (m/s^2)
L	characteristic length (m)
Re	Reynolds number
Re_I	Reynolds number for impeller
Re_p	Reynolds number for pump

V	velocity (m/s)
υ	kinematic viscosity (m^2/s)
ω	impeller rotational speed (rad/s)

APPENDIX 6

$A_{furnace}$	surface area of metal in main hearth (m^2)
C_p	heat capacity (J/kg K)
h	metal level at any time (m)
Δh	change in the metal level as a function of time (m)
H	maximum liquid metal level (m)
i %	percentage used to calculate dross generation based on the amount of metal melted
l	total length of main hearth and side well (m)
$\dot{m}_{dross}$	mass of dross layer at time t (kg)
m_i	metal melted or transferred (kg), i indicates shred, sows, scrap or transferred metal
Q	heat transfer through dross layer (W)
Q_{total}	net heat transfer for a given cell (W)
t	time (s)
T	temperature (K)
ΔT_i	initial temperature difference (K)
T_n^t	temperature of node n at time t (K)

V	metal volume (m^3)
ΔV	change in metal bath volume (m^3)
Δx_{dross}	dross thickness (m)
w	width of main hearth (m)
θ	angle of the side wall with the horizontal (°)
ρ_i	density (kg/m^3), i indicates shred, sows, scrap or transferred metal

REFERENCES

1. Kevorkijan, V., "The Recycle of Wrought Aluminum Alloys in Europe", J. of the Minerals, Metals, and Materials Society (JOM), vol. 54, no. 2, pp. 38-41, 2002.

2. Rombach, G., "Future Availability of Aluminum Scrap", Proceedings of the 131th TMS Annual Meeting, Seatle, Washington, Feb. 17-21, 2002, ed. W. Schneider, Light Metals 2002, pp. 1011-1018, 2002.

3. Steverson, W.B., "MRFs and UBCs: A Concern Yet an Oppurtunity', Proceedings of the 124th TMS Annual Meeting, Las Vegas, California, Feb. 12-16, 1995, ed. J.W. Evans, Light Metals 1995, pp. 1303-1307, 1995.

4. Herwich, G., Roth, D.J., "Compact Type Remelt Plant, An Efficient In-House Recycling System for the Extruder", Proceedings of the 120th TMS Annual Meeting, New Orleans, Louisanna, Feb. 17-21, 1991, ed. E. Roy, Light Metals 1991, pp. 801-804, 1991.

5. van Linden, J.H.L., "Aluminum Recycling – Everybody's Business, Technological Challenges and Opportunities", Proceedings of the 119th TMS Annual Meeting, Anaheim, California, Feb. 18-22, 1990, ed. C.M. Bickert, Light Metals 1990, pp. 675-682, 1990.

6. Rottwinkel, T., Sanhen, N., "Aluminum Recycling – A European Perspective", Proceedings of the 119th TMS Annual Meeting, Anaheim, California, Feb. 18-22, 1990, ed. C.M. Bickert, Light Metals 1990, pp. 683-689, 1990.

7. Whiteley, P.R., "Melting and Holding Furnace Design Concepts", Aluminum Melt Treatment and Casting, ed. M. Nilmani, 3rd Int. Australian, Asian, and Pacific Symposium, Melbourne, Australia, July 4-8, 1993.

8. Larouche, A., Chapdelaine, A., " Modelling Aluminum Melting Furnace Design and Operation with REFORM Software", Proceedings of the 31st Annual Conference of Metallurgists (CIM), Advances in Production and Fabrication of Light Metals and Metal Matrix Composites, Edmonton, Alberta, Aug. 23-27, 1992, ed. M.M. Avedesian, L.J. Larouche, J. Masounave, pp. 265-273, 1992.

9. van Linden, J.H.L., Hannula, R.E., "A Mathematical Model of the Aluminum Beverage Can Recycling System", Proceedings of the 110th TMS Annual Meeting, Chicago, Illinois, Feb. 22-26, 1981, ed. G.M. Bell, Light Metals 1981, pp. 813-825, 1981.

10. Warwick, O.H., "Fundamentals of Aluminum Remelt Furnace Design", Proceedings of the 2nd Int. Aluminum Extrusion Technology Seminar, vol. I, pp. 81-86, Atlanta, Ga., Nov 15-17, 1977.

11. Riverin, G., Stevens, W., Bristol, D., Kocaefe, Y.S., "Impact of Good Metal Circulation and Furnace Operation for Increased Performance for Sidewell Furnaces", Proceedings of the 126th TMS Annual Meeting, Orlando, Florida, Feb. 9-13, 1997, ed. R. Huglen, Light Metal 1997, TMS, 1997.

12. White, F.M., "Fluid Mechanics", McGraw Hill, Inc., New York, 1999.

13. Becker, H.A., "Physical Probes", Chapter Two, Instrumentation for Flows with Combustion, Academic Press, 1993.

14. Patankar, S.V., "Numerical Heat Transfer and Fluid Flow", Hemisphere Publishing Corporation, Mc-Graw Hill Book Company, New York, 1982.

15. Huebner, K.H., Thornton, E.A., "The Finite Element Method for Engineers", 2nd ed., John Wiley and Sons, Inc., New York, 1982.

16. AEA Technology, CFX-4.2: Solver, AEA Technology, Central House, 14 Upper Woburn Place, London, WC1H 0JN, 1997.

17. Bui, R.T., "Computational Modelling of Thermophysical Processes in the Light Metals Industry", Rev. Gen. Therm., vol. 36, pp. 575-591, 1997.

18. Waite, P., "A Technical Perspective on Molten Aluminum Processing", Proceedings of the 131th TMS Annual Meeting, Seatle, Washington, Feb. 17-21, 2002, ed. W. Schneider, Light Metals 2002, pp. 841-848, 2002.

19. Grossmann, I.E., Westerberg, A.W., "Research Challenges in Process Systems Engineering", AIChE J., vol.46, no. 9, pp. 1700-1703, 2000.

20. Fahrmann, M.G., Smith, G.D., "Capitalizing on Computational Tools in Industrial Alloy Development", J. of the Minerals, Metals, and Materials Society (JOM), vol. 54, no.1, pp. 42-44, 2002.

21. Stewart, D.L., "Aluminum Melting Technology – Current Trends and Future Opportunities", Proceedings of the 131th TMS Annual Meeting, Seatle,

Washington, Feb. 17-21, 2002, ed. W. Schneider, Light Metals 2002, pp. 719-724, 2002.

22. Alchalabi, R., Meng, F., "Furnace Operation Optimization via Enhanced Bath Circulation: Technologies for Production Increase and Dross Reduction", Proceedings of the 131th TMS Annual Meeting, Seatle, Washington, Feb. 17-21, 2002, ed. W. Schneider, Light Metals 2002, pp. 739-746, 2002.

23. Kocaefe, Y.S., Bui, R.T., Kocaefe, D., Riverin, G., Gariepy, B., "Metal Flow Modelling in Sidewell Furnaces", Proceedings of the 36th Annual Conference of Metallurgists (CIM), Light Metals 1997, Sudbury, Ontario, Aug. 17-20, 1997, ed. C.M. Bickert, R.I.L. Guthrie, pp. 653-664, 1997.

24. Kocaefe, Y.S., Bui, R.T., Kocaefe, D., Riverin, G., Gariepy, B., "Mathematical Modelling of the Metal Flow in Sidewell Furnaces", Communication presented at the 126th TMS Annual Meeting, Orlando, Florida, Feb. 9-13, 1997.

25. Thibault, M.A., Tremblay, F., Pomerleau, J.C., "Molten Metal Stirring: Alcan Jet Stirrers", Proceedings of the 120th TMS Annual Meeting, New Orleans, Louisanna, Feb. 17-21, 1991, ed. E. Rooy, Light Metals 1991, pp. 1005-1011, 1991.

26. Neff, D.V., "Molten Metal Pumping Systems – Current Applications and Benefits", Proceedings of the 116th TMS Annual Meeting, Denver, Colorado, Feb. 24-26, 1987, ed. R.D. Zabreznik, Light Metals 1987, pp. 805-812, 1987.

27. Pericleus, K., Patel, M., "The Source-Sink Approach in the Modelling of Stirred Reactors", Physico-Chemical Hydrodynamics, vol. 9, no. 12, pp. 279-297, 1987.

28. Bilodeau, J.F., Lakroni, C., Kocaefe, Y.S., "Modelling of Rotary Injection Process for Molten Aluminum Treatment", Proceedings of the 130th TMS Annual Meeting, New Orleans, Louisanna, Feb. 11-15, 2001, ed. J.L. Anjier, Light Metals 2001, pp. 1009-1015, 2001.

29. Kocaefe, D., Bui, R.T., Provencher, R., Bourgeois, T., "Simulating and Optimizing an Al-SiC Composite Mixing Tank", Proceedings of the 125th TMS Annual Meeting, Anaheim, California, Feb. 4-8, 1996, ed. W. Hale, Light Metals 1996, pp. 913-919, 1996.

30. Dube, J.M., "Modélisation physique d'un four de recyclage d'aluminium", Rapport final du Stage-projet, Department of Applied Sciences, University of Quebec at Chicoutimi, Dec. 1996.

31. Dube, J.M., "Modélisation physique d'un four à recyclage d'aluminium muni d'une pompe à injection de métal", Rapport no. GRIPS-97-01, University of Quebec at Chicoutimi, May 1997.

32. Kocaefe, Y.S., Bui, R.T., "3D Mathematical Modelling of Sidewell Furnaces: Effect of Design and Operating Conditions on Metal Flow", Report no. CHIP-39, University of Quebec at Chicoutimi, Submitted to Alcan, December 1998.

33. Rivard, T., Kocaefe, Y.S., "Étude paramétrique sur la géométrie d'un four de recyclage d'aluminium", University of Quebec at Chicoutimi, Submitted to Alcan, Rapport no. CHIP-30, Sept. 1997.

34. Kocaefe, Y.S., "Mathematical Modelling of the Interaction Between Flow and Radiative Transfer in Combustion Systems", M.Sc.E. Thesis in Chemical Engineering, University of New Brunswick, Dec. 1982.

35. Kocaefe, Y.S., Simard, G., Charette, A., Bui, R.T., " A General Model for a Coke Calcining Kiln", Proceedings of the Spring Technical Meeting of the Combustion Institute, Canadian Section, pp. 46.1-46.5, 1993.

36. Kocaefe, Y.S., Simard, G., Bui, R.T., Charette, A., Potocnik, V., Perron, J., "Analysing the Heat Transfer in a Coke Calcining Kiln", Proceedings of the 121th TMS Annual Meeting, San Diago, California, March 1-5, 1992, ed. E.R. Cutshall, Light Metals 1992, pp. 627-632, 1992.

37. Sarofim, A.F., Hottel, H.C., "Radiative Transfer in Combustion Chambers: Influence of Alternative Fuels", Proceedings of the 6th International Heat Transfer Conference, pp. 199-217, 1978.

38. Hottel, H.C., Sarofim, A.F., "Radiative Transfer", McGraw Hill, Inc., New York, 1967.

39. Kocaefe, Y.S., Bui, R.T., Charette, A., "3D Mathematical Modelling of Sidewell Furnaces: A Parametric Study on a Combustion Chamber Using One-Gas-Zone Model", Report no. CHIP-44, University of Quebec at Chicoutimi, Submitted to Alcan, June 1999.

40. Bui, R.T., Charette, C., Chiasson, P.O., Desrosiers, D., Doyon, S., Kocaefe, Y.S., Perron, J., Tikasz, L., Villeneuve, V., "Optimal Control of Sidewell Recycling Furnaces: A Progress Report for the April to August 2000 Period", Report no. LECAP-5, University of Quebec at Chicoutimi, Submitted to Alcan, August 2000.

41. Bui, R.T., Charette , A., Charette, C., Chiasson, P.O., Fillion, C., Kocaefe, Y.S., Perron, J., Tikasz, L., Villeneuve, V., "Optimal Control of Sidewell Recycling

Furnaces: A Progress Report for the August 2000 to December 2000 Period", Report no. LECAP-6, University of Quebec at Chicoutimi, Submitted to Alcan, February 2001.

42. Waite, P., "Berea Plant Tests to Determine Optimum GSS Speed", Technical Letter, Alcan, July 2000.

43. Kocaefe, Y.S., Perron, J., "Advanced Control of Sidewell Furnaces, Study 1: Thermocouple Position", Technical Letter, University of Quebec at Chicoutimi, Submitted to Alcan, March 2001.

44. Kocaefe, Y.S., Perron, J., "Advanced Control of Sidewell Furnaces, Study 2: Variable GSS Speed According to Peter Waite's Equation", Technical Letter, University of Quebec at Chicoutimi, Submitted to Alcan, March 2001.

45. Kocaefe, Y.S., Perron, J., "Advanced Control of Sidewell Furnaces, Study 3: Preheating of Shred, Sow, and Combustion Air", Technical Letter, University of Quebec at Chicoutimi, Submitted to Alcan, April 2001.

46. Kocaefe, Y.S., Perron, J., "Advanced Control of Sidewell Furnaces, Study 4: Impact of Maximum Roof Temperature", Technical Letter, University of Quebec at Chicoutimi, Submitted to Alcan, November 2001.

47. Kocaefe, Y.S., Perron, J., "Advanced Control of Sidewell Furnaces, Study 5: Impact of Lower Metal Setpoint Temperature", Technical Letter, University of Quebec at Chicoutimi, Submitted to Alcan, October 2001.

48. Slattery, J.C., "Advanced Transport Phenomena", Cambridge University Press, 1999.

49. Brodkey, R.S., Hershey, H.C., "Transport Phenomena (A Unified approach)", McGraw Hill, Inc., New York, 1988.

50. Bird, R.B., Stewart, W.E., Lightfoot, E.N, "Transport Phenomena", John Wiley and Sons, Inc., New York, 1960.

51. Siddall, R.G., "Flux Methods for the Analysis of Radiant Heat Transfer", J. of Institute of Fuel, vol. 47, pp. 101-109, 1974.

52. Steward, F.R., Guruz, K.H., "Radiative Heat Transfer in Absorbing, Emitting, and Scattering Media Using the Monte Carlo Method", Transactions CSME, vol. 3, pp. 10-16, 1975.

53. Gupta, A.K., Lilley, D.G., Syred, N., "Swirl flows", Abacus Press, 1984

54. Khalil, E.E., "Modelling of Furnaces and Combustors", Abacus Press, 1982.

55. Modest, F.M., "Radiative Heat Transfer", McGraw Hill, Inc., New York, 1993.

56. Brewster, M.Q., "Thermal Radiative Transfer and Properties", John Wiley and Sons, Inc., New York, 1992.

57. Siegel, R., Howell, J.R., "Thermal Radiation Heat Transfer", McGraw Hill, Inc., New York, 1972.

58. Goutiere, V., Liu, F., Charette, A., "An Assessment of Real Gas Modelling in 2D Enclosures", J. of Quantitative Spectroscopy and Radiative Transfer, vol. 64, no. 3, pp. 299-332, 2000.

59. Sakami, M., El Kasmi, A., Charette, A., " Analysis of Radiative Heat Transfer in Complex Enclosures with Obstacles Using the Modified Discrete Ordinates Method", J. Heat Transfer, vol. 123, no. 5, pp. 892-900, 2001.

60. Sakami, M., Charette, A., Le Dez, V., "Radiative Heat Transfer in 3D Enclosures of Comlex Geometry by Using the Discrete Ordinates Method", J. of Quantitative Spectroscopy and Radiative Transfer, vol. 59, no. 1-2, pp. 117-136, 1998.

61. Charette, A., Haidekker, A., Kocaefe, Y.S., "Application of Hybrid Zone-Monte Carlo Method to Curvilinear Grids", International Journal of Numerical Methods in Engineering, vol. 37, pp. 203-216, 1994.

62. Charette, A., Haidekker, A., Kocaefe, Y.S., "3D Comparative Behavior of Discrete Transfer and Imaginary Planes Methods for Furnace Modelling, Can. J. of Chem. Eng., vol. 70, pp. 1198-1207, 1992.

63. Charette, A., Larouche, A., Kocaefe, Y.S., "Application of the Imaginary Planes Method to 3D Systems", Int. J. Heat and Mass Transfer, vol. 33, no. 12, pp. 2671-2681, 1990.

64. Kocaefe, Y.S., Simard, G, Audet, D., Beaulieu, J., "Application of Parallel Computing for the Hybrid Zone-Monte Carlo Method Using PVM", edited by Editions Européennes Thermiques et Industries, Paris, 1995.

65. Lockwood, F.C., Shah, N.G., "A New Radiation Solution Method for Incorporation in General Combustion Prediction Procedures", 18th Symp. (Int.) on Combustion, pp. 1405-1414, 1981.

66. Goutiere, V., Charette, A., Kiss, L., "Comparative Performance of Non-Gray Gas Modelling Techniques", Numerical Heat Transfer, Part B: Fundamentals, vol. 41, no. 3, pp. 361-381, 2002.

67. Howell, J.R., "Thermal Radiation in Participating Media: The Past, the Present, and Some Possible Futures", Transactions ASME, vol. 110, pp. 1220-1229, 1988.

68. Steward, F.R., Kocaefe, Y.S., "Total Emissivity and Absorptivity Models for Carbon Dioxide, Water Vapor and Their Mixtures", Proceedings of the 8th Int. Heat Transfer Conference, pp. 877-883, 1986.

69. Modest, M.F., "The Weighted-Sum-of-Gray-Gases Model for Arbitrary Solution Methods in Radiative Transfer", Transactions ASME, vol. 113, pp. 650-656, 1991.

70. Soufiani, A., Djavdan, E., "A Comparison Between Weighted Sum of Gray Gases and Statistical Narrow-Band Radiation Models for Combustion Application", Combustion and Flame, vol. 97, 240-250, 1994.

71. Incropera, F.P., DeWitt, D.P., "Introduction to Heat Transfer", 2nd ed., John Wiley and Sons, Inc., New York, 1990.

72. von Rosenberg, D.U., "Methods for the Numerical Solution of Partial Differential Equations", 4th ed., Gerald L. Farrar and Associates, Inc., Tulsa, 1977.

(a)

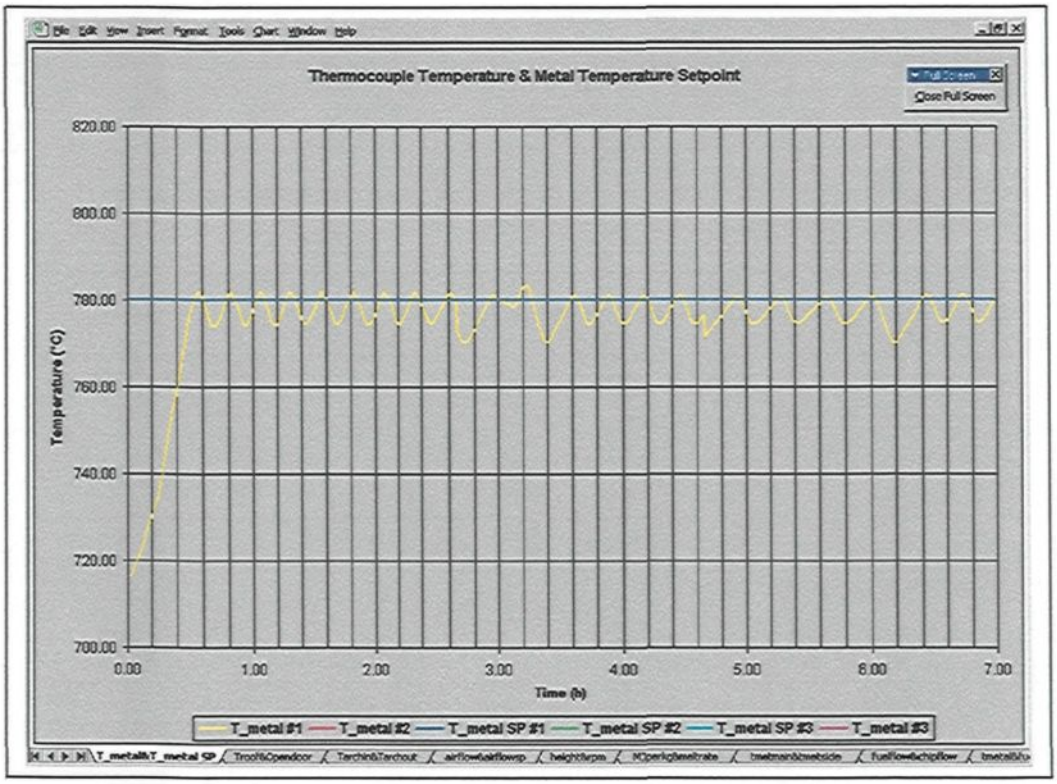
Thermocouple Temperature & Metal Temperature Setpoint
Close Full Screen
820.00
800.00
780.00
760.00
740.00
720.00
700.00
Temperature (°C)
0.00
1.00
2.00
3.00
4.00
5.00
6.00
7.00
Time (h)
T_metal #1
T_metal #2
T_metal SP #1
T_metal SP #2
T_metal SP #3
T_metal #3

(b)

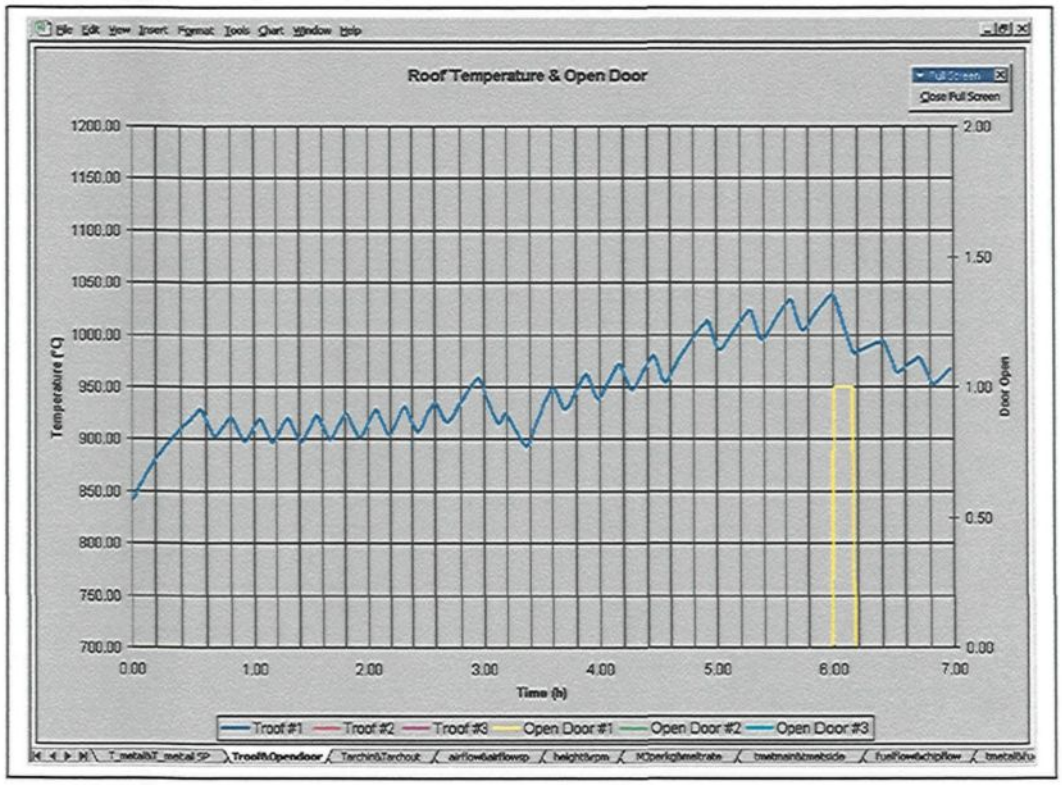
Roof Temperature & Open Door
Close Full Screen
1200.00
1150.00
1100.00
1050.00
1000.00
950.00
900.00
850.00
800.00
750.00
700.00
Temperature (°C)
2.00
1.50
1.00
0.50
0.00
Door Open
0.00
1.00
2.00
3.00
4.00
5.00
6.00
7.00
Time (h)
Roof #1
Roof #2
Roof #3
Open Door #1
Open Door #2
Open Door #3

(c)

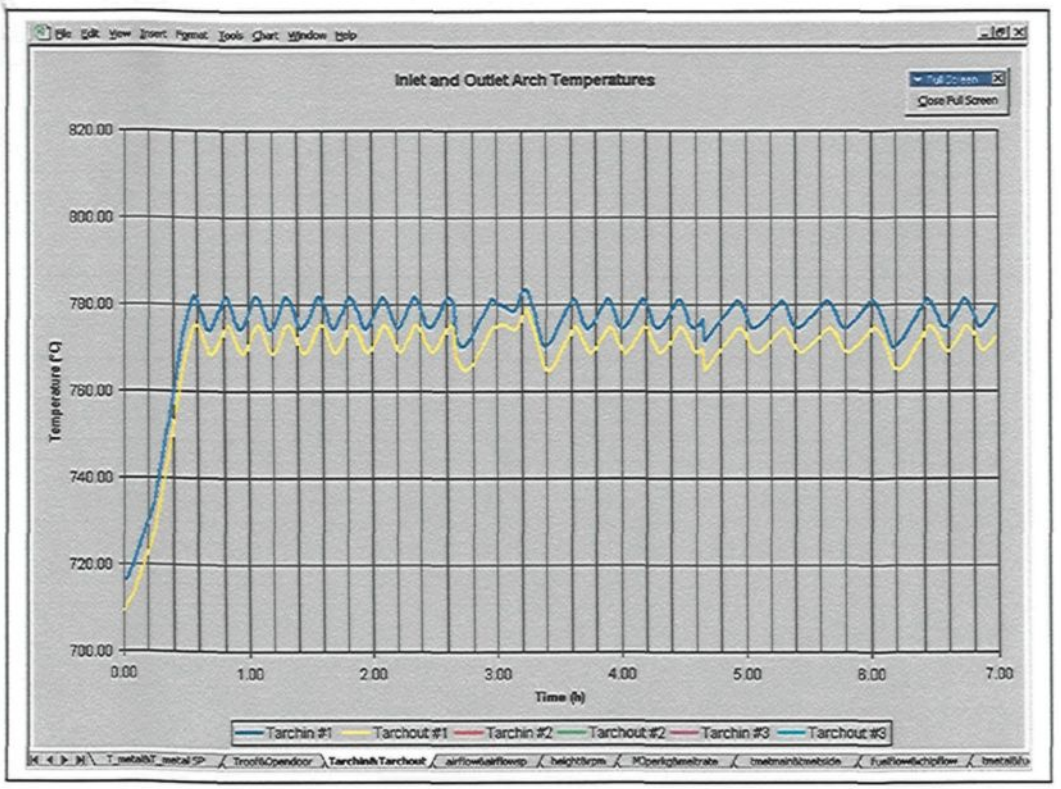
Inlet and Outlet Arch Temperatures
Close Full Screen
820.00
800.00
780.00
760.00
740.00
720.00
700.00
Temperature (°C)
0.00
1.00
2.00
3.00
4.00
5.00
6.00
7.00
Time (h)
Tarchin #1
Tarchout #1
Tarchin #2
Tarchout #2
Tarchin #3
Tarchout #3

(d)

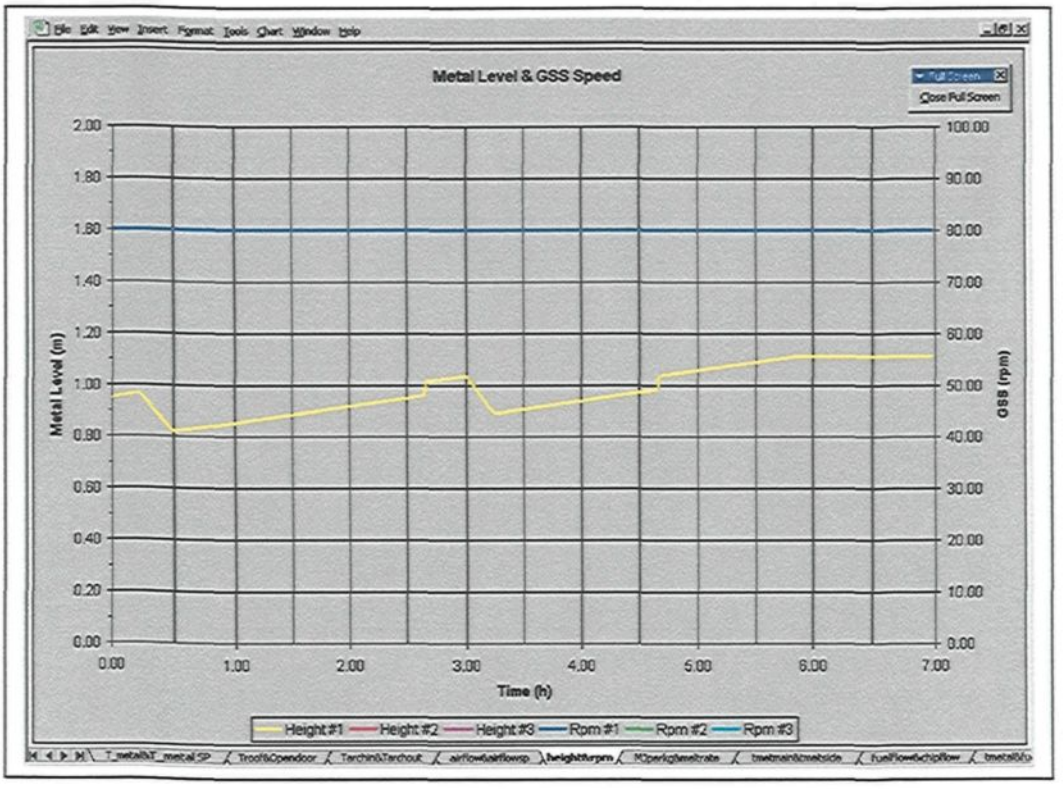
Metal Level & GSS Speed
Close Full Screen
2.00
1.80
1.60
1.40
1.20
1.00
0.80
0.60
0.40
0.20
0.00
Metal Level (m)
100.00
90.00
80.00
70.00
60.00
50.00
40.00
30.00
20.00
10.00
0.00
GSS (rpm)
0.00
1.00
2.00
3.00
4.00
5.00
6.00
7.00
Time (h)
Height #1
Height #2
Height #3
Rpm #1
Rpm #2
Rpm #3

(e)

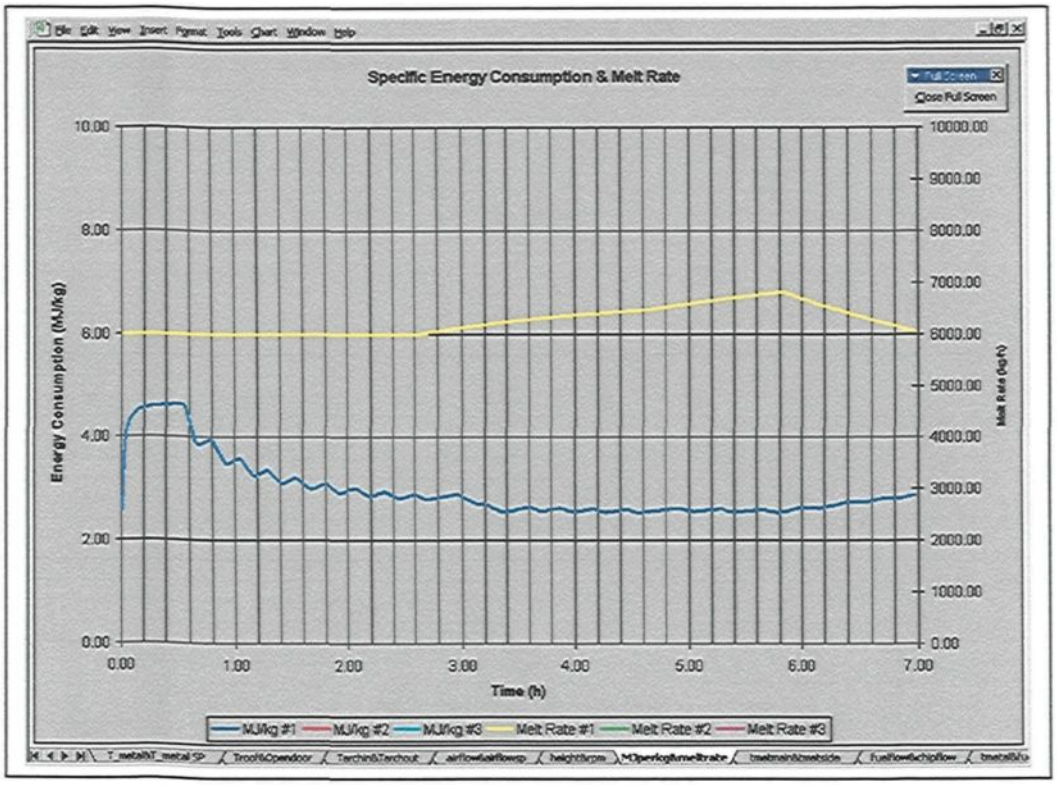
Specific Energy Consumption & Melt Rate
Full Screen
Close Full Screen
Energy Consumption (MJ/kg)
Melt Rate (kg/h)
Time (h)
10.00
8.00
6.00
4.00
2.00
0.00
10000.00
9000.00
8000.00
7000.00
6000.00
5000.00
4000.00
3000.00
2000.00
1000.00
0.00
0.00
1.00
2.00
3.00
4.00
5.00
6.00
7.00
MJ/kg #1
MJ/kg #2
MJ/kg #3
Melt Rate #1
Melt Rate #2
Melt Rate #3

(f)

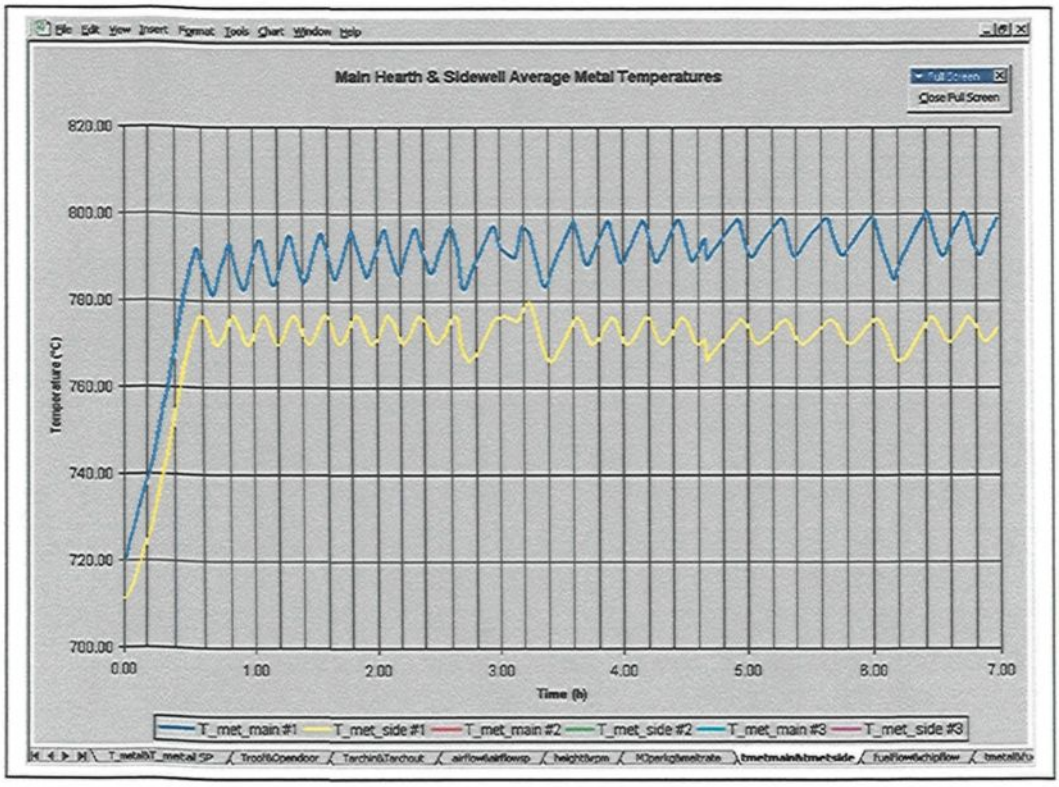
Main Hearth & Sidewall Average Metal Temperatures
Full Screen
Close Full Screen
Temperature (°C)
Time (h)
820.00
800.00
780.00
760.00
740.00
720.00
700.00
0.00
1.00
2.00
3.00
4.00
5.00
6.00
7.00
T_met_main #1
T_met_side #1
T_met_main #2
T_met_side #2
T_met_main #3
T_met_side #3

(g)

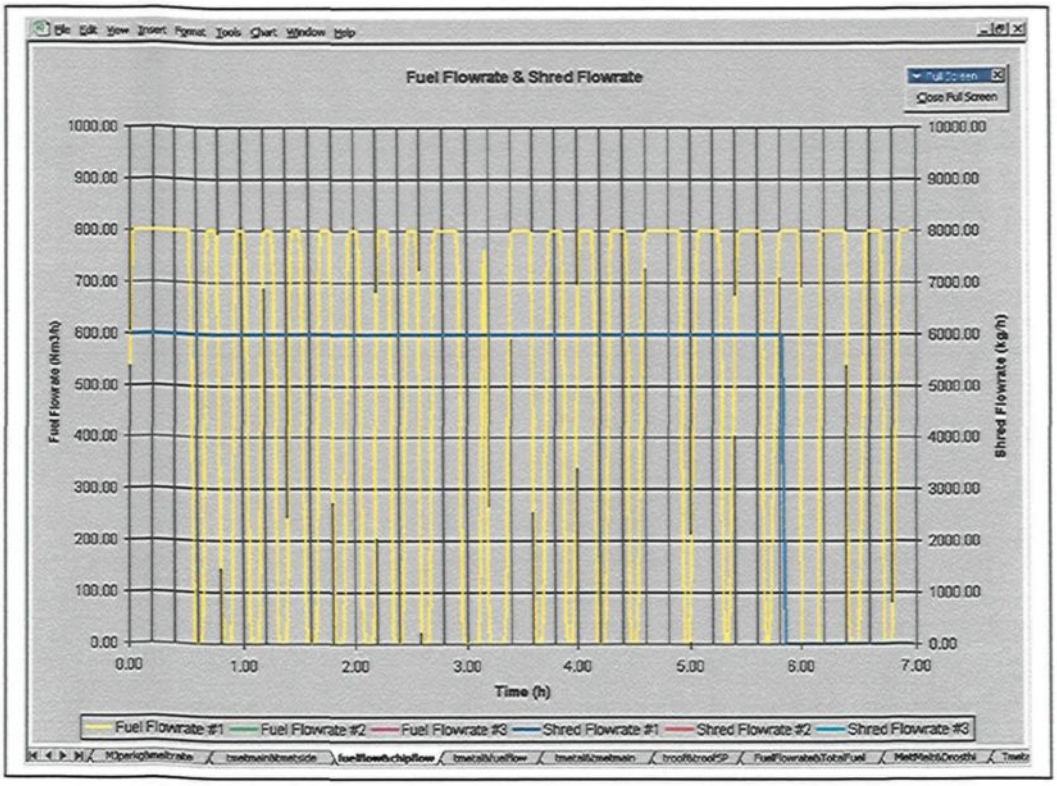
Fuel Flowrate & Shred Flowrate
Full Screen
Close Full Screen
Fuel Flowrate (Nm3/h)
Shred Flowrate (kg/h)
Time (h)
Fuel Flowrate #1
Fuel Flowrate #2
Fuel Flowrate #3
Shred Flowrate #1
Shred Flowrate #2
Shred Flowrate #3

(h)

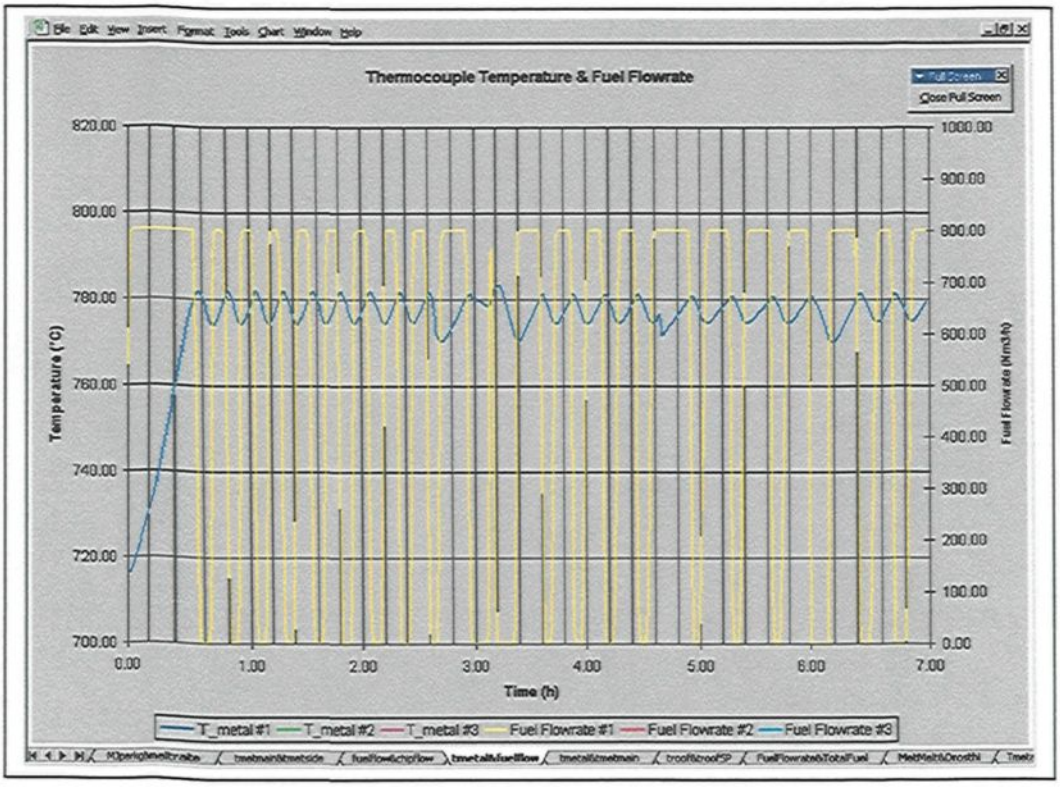
Thermocouple Temperature & Fuel Flowrate
Full Screen
Close Full Screen
Temperature (°C)
Fuel Flowrate (Nm3/h)
Time (h)
T_metal #1
T_metal #2
T_metal #3
Fuel Flowrate #1
Fuel Flowrate #2
Fuel Flowrate #3

(i)

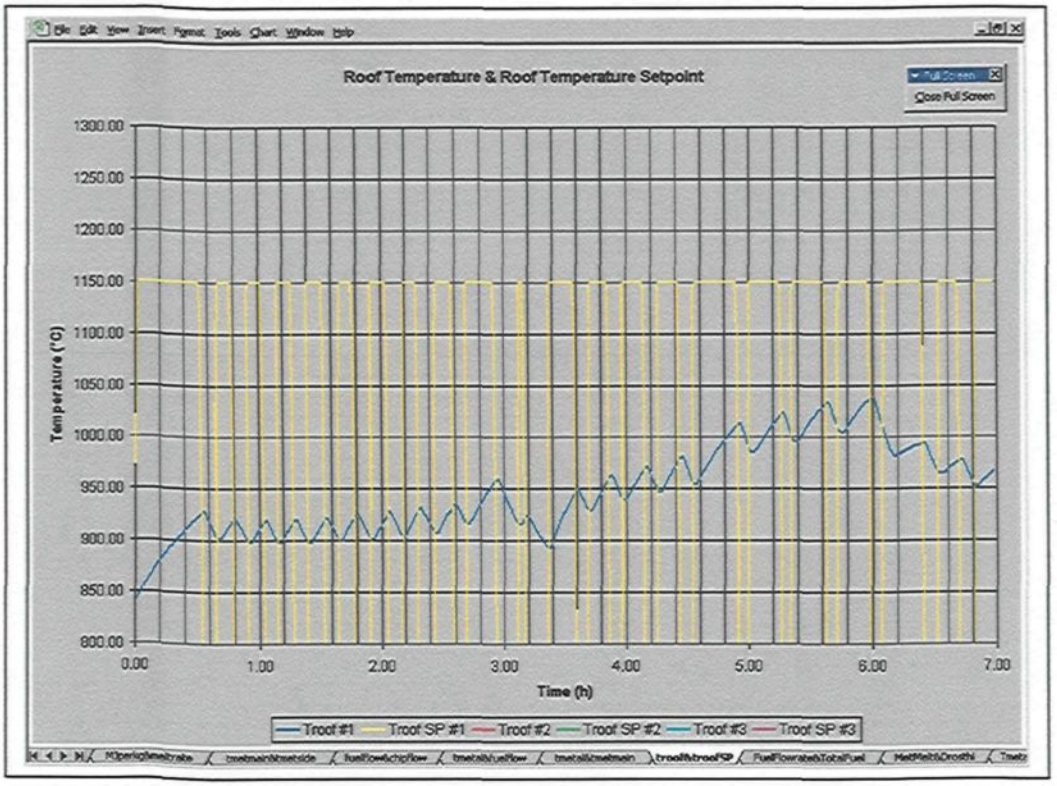
Roof Temperature & Roof Temperature Setpoint
Close Full Screen
Temperature (°C)
1300.00
1250.00
1200.00
1150.00
1100.00
1050.00
1000.00
950.00
900.00
850.00
800.00
0.00
1.00
2.00
3.00
4.00
5.00
6.00
7.00
Time (h)
Troof #1
Troof SP #1
Troof #2
Troof SP #2
Troof #3
Troof SP #3

(j)

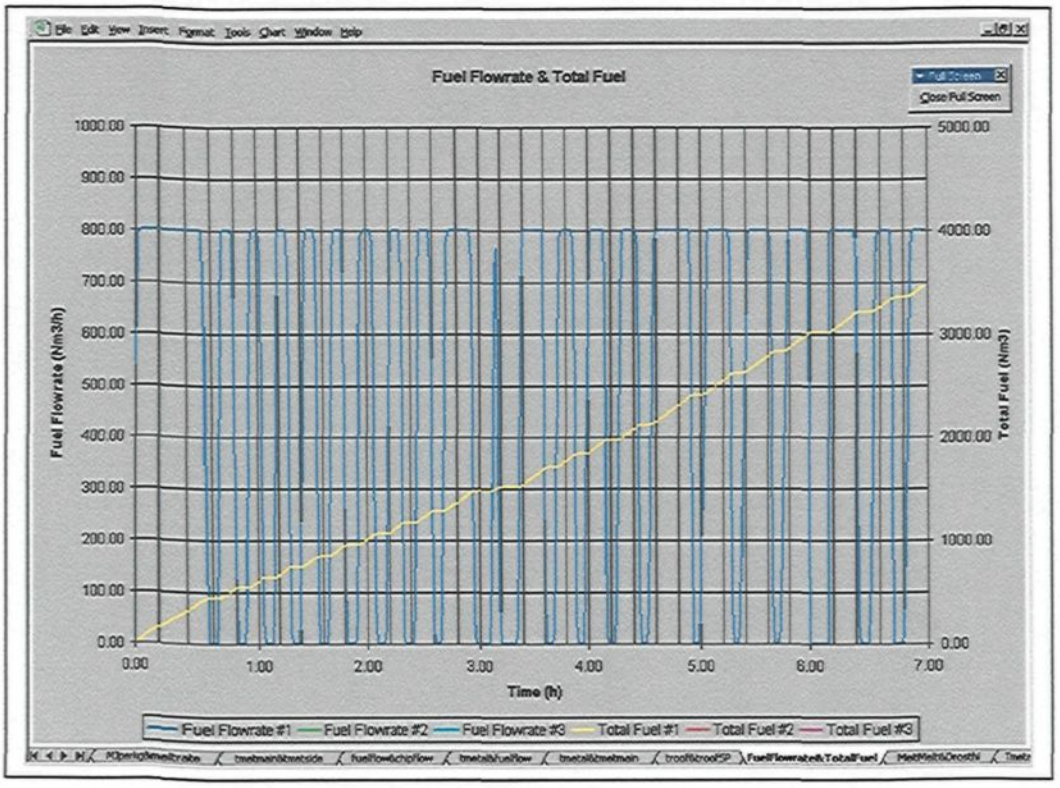
Fuel Flowrate & Total Fuel
Close Full Screen
Fuel Flowrate (Nm3/h)
Total Fuel (Nm3)
1000.00
900.00
800.00
700.00
600.00
500.00
400.00
300.00
200.00
100.00
0.00
5000.00
4000.00
3000.00
2000.00
1000.00
0.00
1.00
2.00
3.00
4.00
5.00
6.00
7.00
Time (h)
Fuel Flowrate #1
Fuel Flowrate #2
Fuel Flowrate #3
Total Fuel #1
Total Fuel #2
Total Fuel #3

(k)

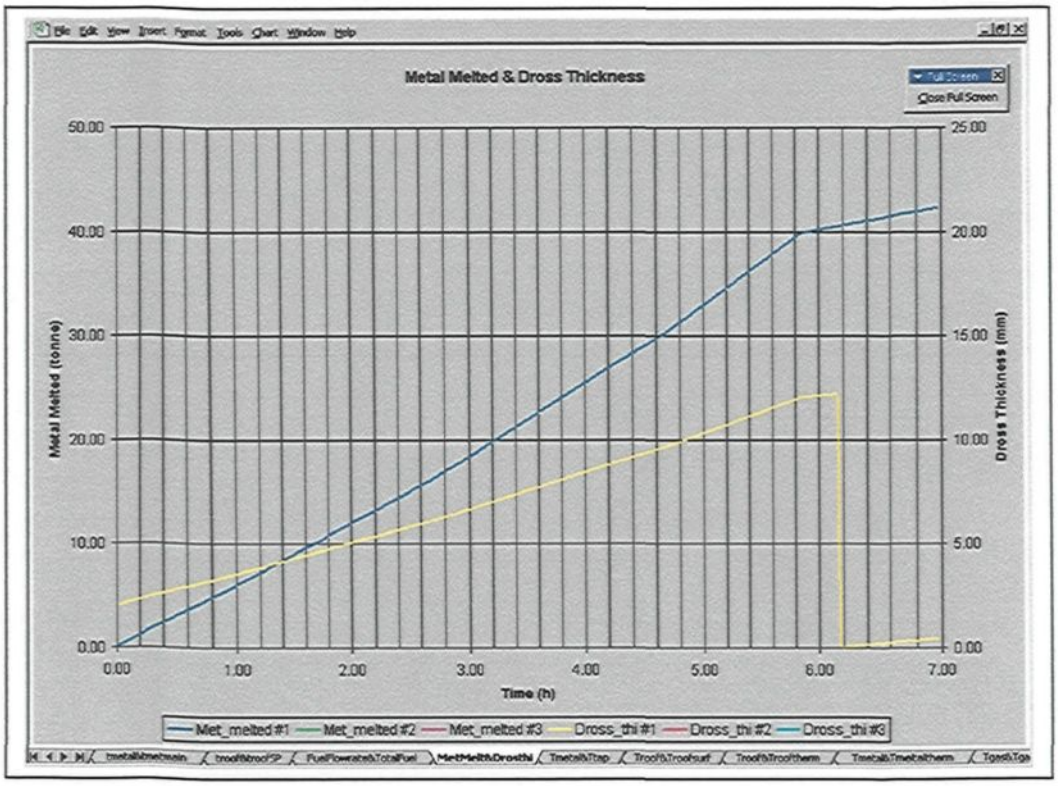

Figure A.6.3 : Some Selected Excel Files Created at the End of a Simulation (Each Graph is Identified Clearly Via A Title and Color-Coded Legend)

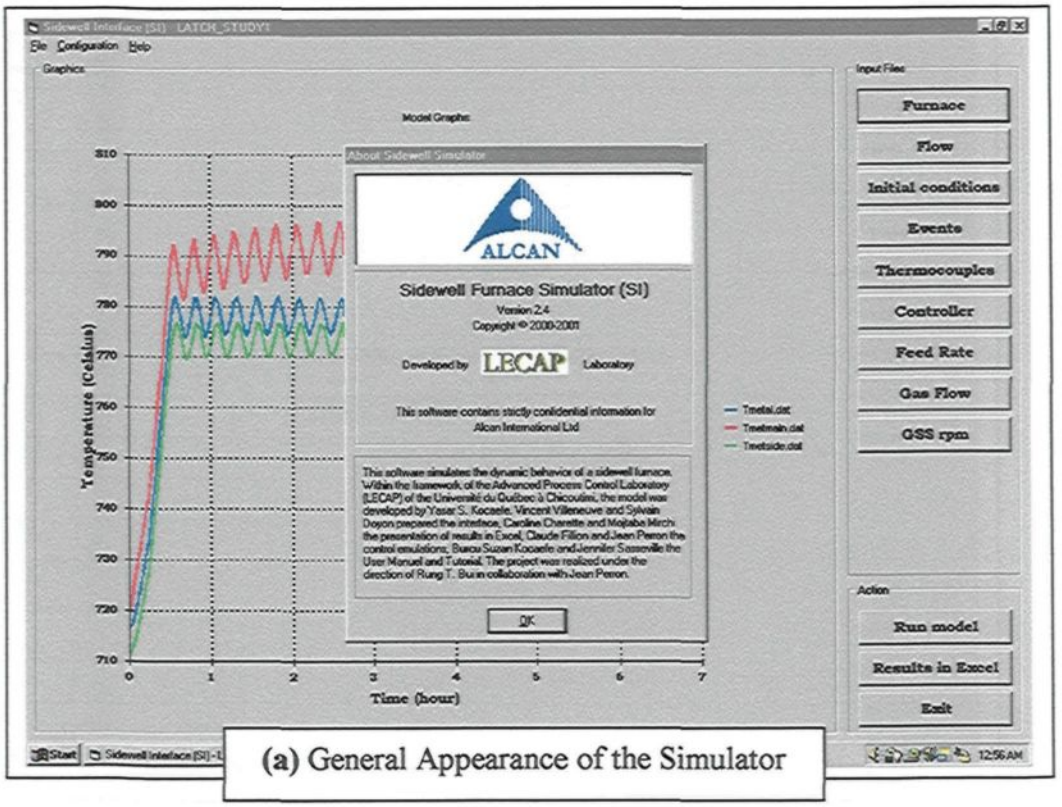

(a) General Appearance of the Simulator

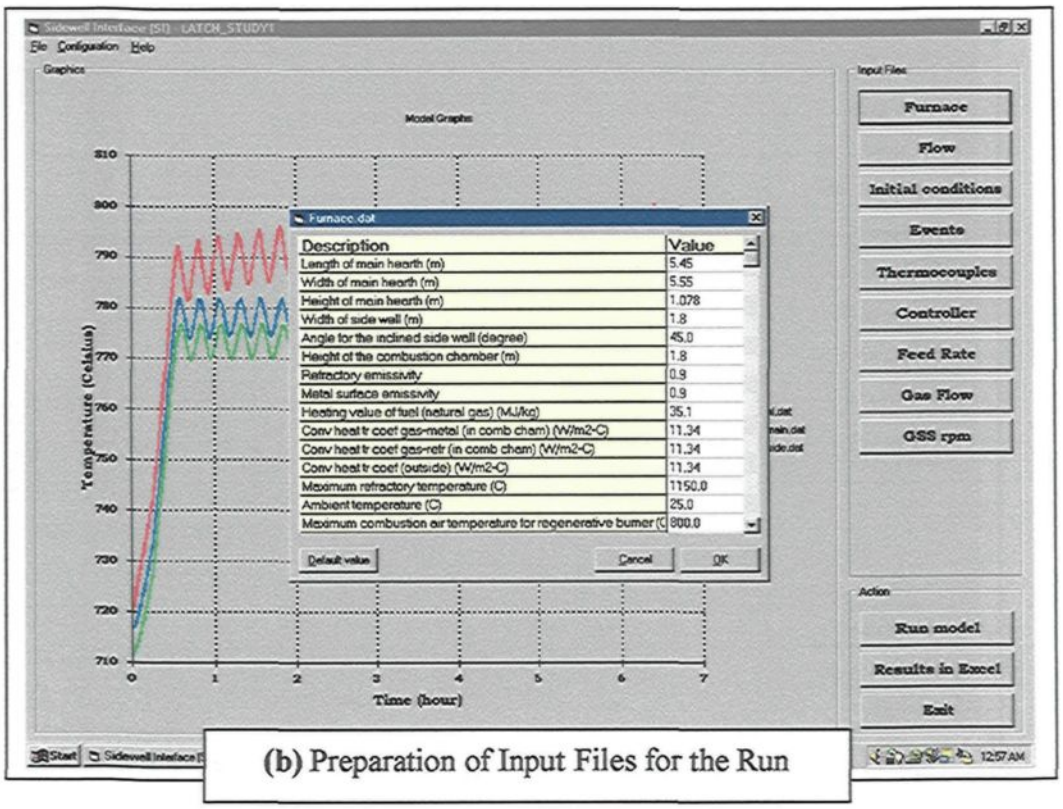

(b) Preparation of Input Files for the Run

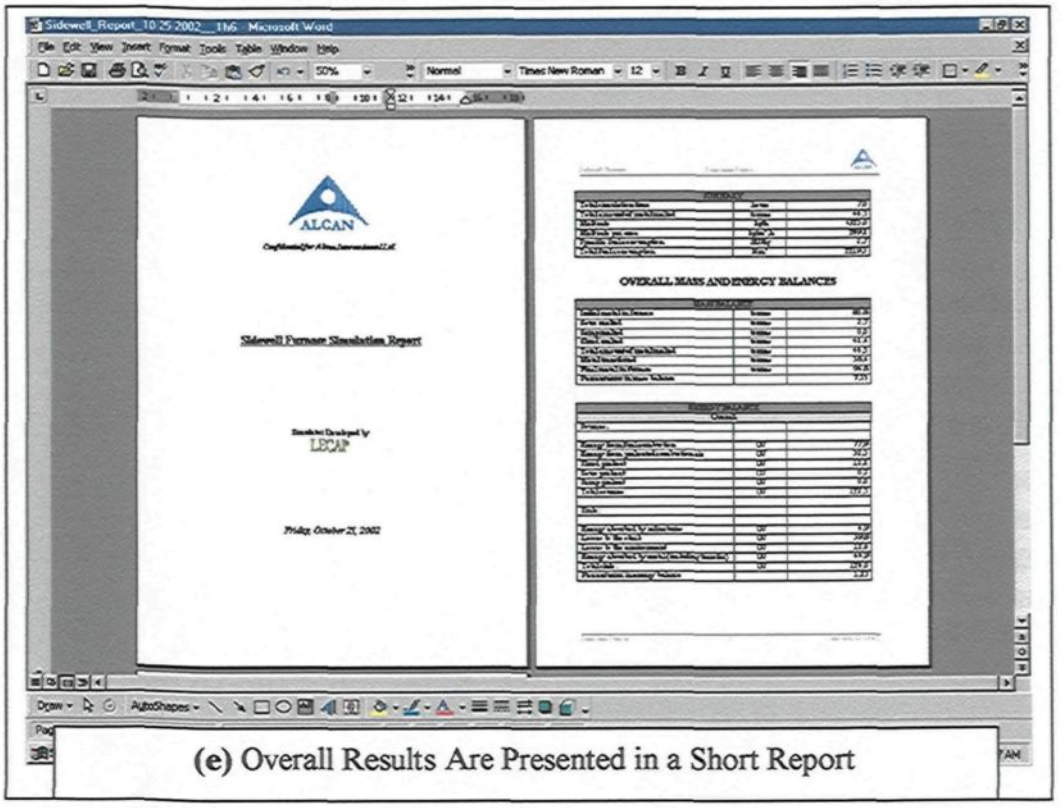

(e) Overall Results Are Presented in a Short Report

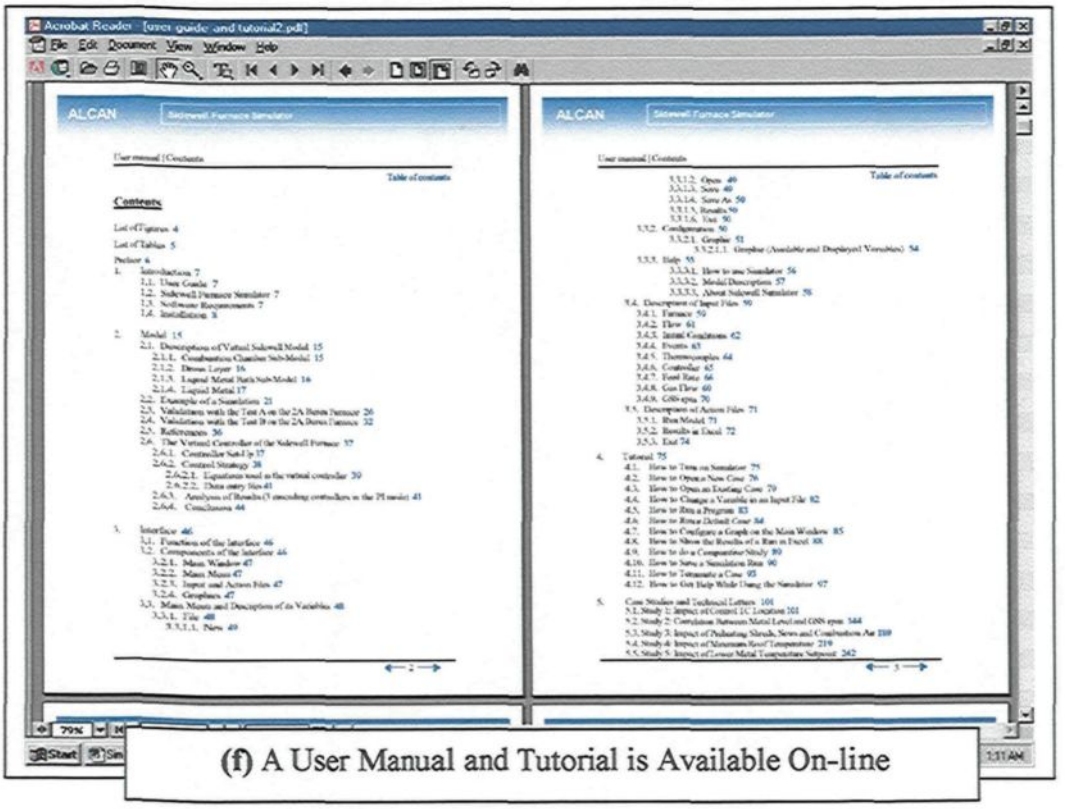

(f) A User Manual and Tutorial is Available On-line

Figure A.6.4 : Sidewell Furnace Simulator